UNIVERSITÀ
DEGLI STUDI
DI PADOVA

Sede Amministrativa: Università degli Studi di Padova

Dipartimento di Ingegneria Civile, Edile e Ambientale

CORSO DI DOTTORATO DI RICERCA IN: Scienze dell'Ingegneria Civile, Ambientale e dell'Architettura
CURRICOLO: Rischio, vulnerabilità, ambiente, salute e territorio
CICLO: XXXIV

LARGE DISPLACEMENT ANALYSIS OF MACRO-INSTABILITIES IN WATER RETAINING GEOSTRUCTURES

Coordinatore: Ch.mo Prof. Carmelo Maiorana
Supervisore: Ch.mo Prof. Paolo Simonini
Co-Supervisore: Ch.ma Dr. Francesca Ceccato
Co-Supervisore: Ch.ma Dr. Alba Yerro

Dottoranda : Veronica Girardi

Dedicated to my dad and my mum,

who pushed me to become an independent woman by means of studying and enriching my culture. This thesis is the result of will and perseverance.

Abstract

To conduct landslide risk assessment and structural health monitoring, it is important to understand the overall failure evolution process that ranges from small-strain initiation to large-strain post-failure run out. To achieve this goal and simulate such events, emerging large-strain numerical approaches, such as the Material Point Method (MPM), show promising potential as tools to model the entire instability mechanism, whilst successfully incorporating multi-phase interactions in granular porous media. In the specific context of water retaining geostructures stability predictions, the quantification of the mobilized soil mass and the run-out distance are not traditionally addressed. This is related to the common approaches in use, relying on the definition of the Factor of Safety (FS) using Limit Equilibrium Methods (LEM) and Finite Element Methods (FEM).

Based on these premises, this thesis work is focused on improving predictive numerical techniques for slope stability analysis, developing and using multiphase MPM approaches.

In Chapter 1 research context and motivations of the study are presented. The chapter is articulated in a brief review of river levee collapse mechanisms, stressing the accent on macro or global instability mechanisms, the ones considered in this thesis. Approaches from the literature used to study this complex problem are retraced, which include experimental approaches (small, large scale and centrifuge tests), study of case history, and numerical approaches (mostly LEM and FEM based analysis). An example of a typical levee safety analysis, based on the use of conventional numerical methods, is presented.

Chapter 2 focuses on the fundamentals of MPM, together with an overview of the current multiphase formulations of the method. This chapter provides a further contextualization of the research work.

At this point, the research activity is configured in a “testing” phase. An existing multiphase MPM formulation, the 2Phase Double Point approach, suitable for fully saturated soils and able to track relative displacements between fluid and solid, is considered. A well-known benchmark case, the soil column collapse, is investigated numerically and experimentally. Subsequently, the analysis moves to a large-scale problem, the failure of a levee due to rapid draw down. The results of the testing phase are presented in Chapter 3.

Based on the experience collected, and some limits identified in the saturated formulation used, a “development” phase starts (Chapter 4), focused on the implementation of an unsaturated MPM formulation with a complete set of hydraulic boundary conditions. The governing equations are derived from the balance equations of the solid and liquid phases that account for partial saturation effects, and the soil is discretized with a single set of material points that move according to the displacement of the solid phase. The implementation of different types of boundary conditions, such as transient hydraulic head, seepage face, and infiltration/evaporation, is discussed in detail. A validation procedure is put in place by considering 1D and 2D examples of seepage in different domains.

A numerical stability study is conducted for the first time for an unsaturated MPM formulation, given the explicit nature of the integration in the time scheme. Some preliminary criteria are obtained, relating the critical time step and the degree of saturation, and compared with the numerical simulation results. The formulation development and the study about the critical time step have a strong general validity for MPM users.

Finally, Chapter 5 is dedicated to applications of the newly developed formulation to several slope stability cases. At first, the method is applied to theoretical cases to simulate levee collapse due to rapid drawdown and rainfall. It these cases it emerges the capability of MPM in fully quantifying the displacements characterizing the slope's movement, giving further meaning to situations where $FS < 1$: it is possible to distinguish between load combinations inducing catastrophic collapse or small displacements.

Later, a large-scale slope failure experiment, carried out in 2009, is considered to test the formulation. Results are compared with the Limit Equilibrium Method (LEM), and an advanced constitutive model accounting for suction effect on strength parameters is used.

Additional applied cases are explored and presented in this thesis at a preliminary level: the investigation of a levee instability induced by toe uplift. This case considers a centrifuge experiment carried out in 2003 which is reproduced with MPM, with the aim of understanding the triggering mechanism and exploring the post failure behavior. The last two examples allows for reproducing massive collapse of the investigated earth structures.

The ease in employing the formulation in different cases, and the chance to perform whatever parametrical analysis, appears as a strong feature to extend in the future the use of this MPM formulation to several other applied cases where partially saturated slopes, artificial or natural, and other geotechnical problems of soil-water-structure interactions are investigated.

Conclusions and potential future developments conclude the thesis.

Contents

Listing of figures

Listing of tables

1

Research context and motivations

1 Introduction

River levees are earth embankments, also named flood embankments or dikes, designed to protect from flooding. Water tightness and stability are the primary functions of these earth structures. When levees collapse, economical and human lives losses are extremely impacting on the surrounding territories. In relation to this aspect, a progressive increase of failure events has occurred in the last century. This trend has pushed researchers to investigate the main causes of failure, with the aim of improving prediction techniques and consequent risk mitigation measures.

On a general level, it is well known that the global climate change, impacting on the hydrologic regimes and runoff capacity of rivers [1], is among the primary causes of the increasing failure rate. In addition, progressive urbanization of areas near levees, in relation to population growth, is determining an increased vulnerability, thus an increased risk.

On a more specific level, failure of levees is characterized by several complexities in relation with their geotechnical behavior as water retention earth structures. Among these complexities we can mention the understanding of the behavior of a levee in relation with its heterogeneous composition, or understanding in which extent certain combinations of hydraulic loads impact on the overall stability, how much is sptatially extended a levee breach, but also the impact of unsaturated soil state on the hydromechanical response during transient loading events.

When it comes to identifying and reproducing instability of levees, these challenging aspects need to be carefully studied and included in the description. Identification and reproduction are at the base of a correct prediction, allowing to control the structure behavior in time and to put in place suitable interventions.

In the following section, some major complexities associated to the understanding and prediction of river levees behavior are presented, to highlight the research context and the specific gap of knowledge target of this research work.

2 IDENTIFICATION AND REPRODUCTION OF FAILURE MECHANISMS IN FLOOD EMBANKMENTS

Researchers and geotechnical engineers, called to formulate hypothesis on failure causes and failure progression, have been developing models to explain the complex reality characterizing river levees along the years. In fact, to improve the understanding of failure causes, in several manuals and publication ([1, 2], among others) it is common to find a classification of levee's collapse mechanisms. These mechanisms depend on levee consistency, stratigraphy of foundation soils and hydraulic loads intensity. They are summarized in Fig. 1.1. For sake of simplicity, only static conditions are considered, since failure induced by shaking would require an in-depth treatment, out of this work scope.

1. External erosion

   The first three mechanisms, Fig. 1.1(a), (b), (c), are classified as external erosion phenomena. The first one, Fig. 1.1(a), overtopping and overflowing, is globally responsible of about 50 % of levee failures [3]. Most of the time, the direct consequence is a breach opening in the levee with rapid development and destruction of the entire section. Erosion of the first bank, reported in Fig. 1.1(c), also known as undercutting, develops when tangential forces exerted by the river flow exceed the erodibility threshold of the soil of the inner bank. Sediment transport can further contribute to the erosion process, together with the natural settlement of the river bed.

   Ultimately, the collapse of the inner slope usually occurs when the river level is decreasing. Another frequent phenomenon of erosion of the inner side occurs at the interface between the levee and man-made structures on it (see Fig. 1.1(b)), linked to the stiffness contrast between the materials.

2. Internal erosion

   The second subcategory is represented by internal erosion, reported in Fig. 1.1(d), (e), (f)). Internal erosion takes place either in the levee body or in the foundation soils and usually impacts on the landside stability. It is the result of progressive removal of fine particles due to seepage forces, hence the soil mixture tends to become progressively more permeable, thus favoring stronger seepage flows. It is recognized that there are four mechanisms of initiation and progression of internal erosion.

   Contact erosion, occurs at the contact between coarse and fine layers, with some washing out of fine particles, due to seepage forces parallel to the stratification.

   Migration erosion, suffosion, Fig. 1.1(d) is a not localized phenomenon whereby fine particles are transported through the voids of the solid matrix during seepage flow.

   Retrogressive erosion (piping, Fig. 1.1(e)), begins at a free surface on the downstream side of a dam or levee. The process progresses beneath the levee or dam. For this to occur, the levee or dam, or the cohesive strata, must form a roof for the eroding "pipe". The presence of backward erosion piping is often exhibited by the presence of sand boils at the downstream side of the dam or dike [4].

   Concentrated leak erosion, may occur through a crack or hydraulic fracture. Cracks or other continuous open paths for water may occur because of the collapse of settlement of poorly compacted fill in the embankment, around conduits and adjacent walls. They may also occur due to the action of animals burrowing into levees Fig. 1.1(f) and small dams and tree roots rotting in the dam and forming a hole [4]. Internal erosion can be associated also with through-penetrating structures, such as conduits associated with outlet works, in analogy with the previous case (b) of soil-structure interaction.

3. Macro or global instability

   Macro-instability is characterized by rotation and sliding of portions of the levee and its foundation on either landside Fig. 1.1(g) or riverside Fig. 1.1(h). The sliding can occur at the landside (during a high level of the outer water) or at the riverside (during a quick fall of the outer water level after a period of high water). Favorable conditions for this mechanism are represented by transient seepage in the levee, modifying the pore pressure distribution with an overall increase. This alteration of pore pressure results in a reduction of the effective stress, thus a progressive decrease of strength. When the maximum strength is exceeded, localized failure occurs, which can progress with the formation of slip surfaces along which rotation or roto-translation occurs. If in addition, the levee materials have experienced progressive damage with time, due to cycles of wetting and drying, cracks may be present, favoring the pressure increase, thus accelerating the phenomenon [1].

In the same category of macro-instabilities, it is possible to classify the instability induced by toe-uplift impacting on the levee external slope (see Fig. 1.1(i)). This mechanism occurs when a permeable layer of sand in the subsoil is covered by a relatively impermeable, weak and lightweight layer of clay/peat. In addition, the sand layer is in direct connection with the river, functioning as a water conduit. During extreme river levels, the water pressure in the deeper more permeable sand layer increases relatively fast, and as a result the upper clay/peat layers at the inner side can be lifted due to the upward water pressure. Under the lifting zone, a zone of constant pressure develops at the interface between sand and clays, and sliding of the top layer occurs. Lastly, the failure surfaces can extend on the landside and riverside, determining a well known block-shapes surface, which can involve total-height portions of the levee body.

Naturally, the above-mentioned mechanisms can also combine in some real scenario. Despite this classification, which summarizes the main physical aspects of each mechanism, a complete understanding of these failure events is not yet reached. These events depend on complex multiphase processes, before, during and after failure.

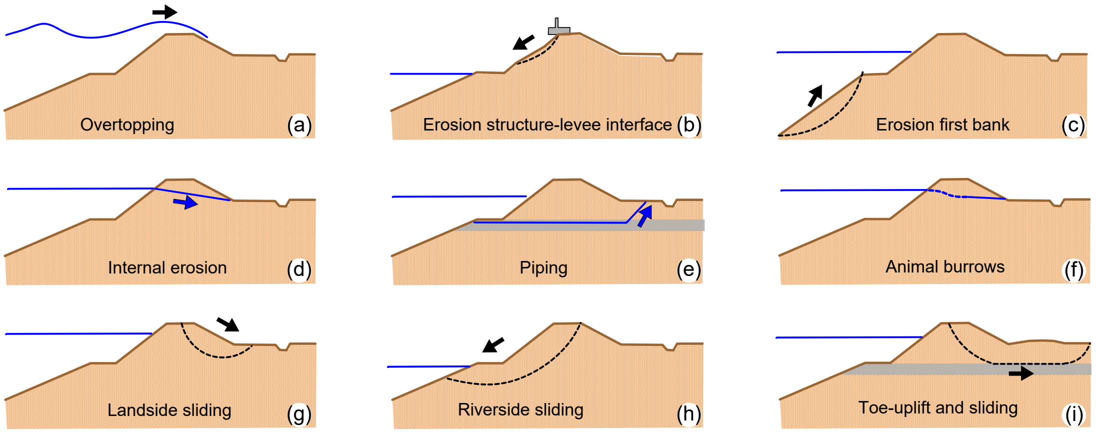

Figure 1.1: Principal levees collapse mechanisms: (a), (b), (c) External erosion related; (d), (e), (f) Internal erosion related and (g), (h), (i) Macro-instability, seepage related.

The focus of this research work is exploring a specific category of instability affecting levees and other water retaining geostructures: the macro-instabilities. Identification and reproduction are herein explained in relation to this category of instabilities. However, some considerations are valid also when considering other specific mechanisms.

In general, we can say that identification has two connotations: prior to the event, in the sense of detection/anticipation, and after the event, when causes and evolution of failure need to be reconstructed, considering the occurred soil mass movement. Failure of levees or portions of them due to a global or macro instability is most of the time rapid, characterized by extremely fast movement of soil masses with variable saturation. This rapidity poses difficulties in the detection prior to the event. Indeed, it is troublesome to track evolution of small displacements, or identify strain threshold which can be used as an indicator in time, like in landslides, before the event. Thus, design of specific monitoring and early-warning systems for levees is a challenging and up-to-date research branch working in parallel with the numerical modelling activity. Most of the time, rather than deformation, the focus is on hydraulic variables monitoring, since in many circumstances it's pointless to monitor deformation with conventional geotechnical instruments (like inclinometer), or use non-invasive techniques (like photogrammetry or geophysical tests). Seepage flow detection is hard to be performed even using conventional geotechnical instrumentation, such as pore pressure sensors, because its effect on pore water pressures is highly localized [5].

In light of the current limitations associated to in site instrumentation's prediction capacity and the economical constrains for the installation in these kilometric earth structures, it emerges that the use of numerical predictions is straightforward and more convenient.

The washing out of soil, when water previously retained is released on the landside, often erases every trace of the pre-existent structure, making it tough to understand causes of collapse, stratigraphy before the event and the predominant failure mechanism occurred. This aspect is peculiar of water retention earth structures and requires the development of numerical tools able to account for two main elements: full hydromechanical interactions, in saturated and unsaturated conditions, and large displacements. Multiphase interactions in unsaturated and saturated conditions determine hydraulic and mechanical response at the macro-scale. Often there are gaps between laboratory experiment conditions and real field, due to scale effects and heterogeneity of the involved soils [4], making troublesome understanding the actual phenomenon occurring at the macro scale. When considering for example a global stability assessment, it is common practice to perform uncoupled seepage and stability analysis. With this procedure, hydromechanical interactions between soil skeleton and pore fluid, governing the embankment response, are generally not considered, which often makes the results inaccurate and unreliable. For example, neglecting the suction effects in unsaturated soil behavior can introduce excessive underestimation of soil shear strength. In practice, unsaturated conditions are often neglected or loosely considered in an extremely crude manner. In the past two decades, the geotechnical research community has been determined to clarify the role of unsaturated soil behavior in the governing failure mechanism of water retention structures, with numerical and field studies [6, 7, 8, 9]. In this work particular importance is given to this aspect in the modelling activity, and an entire chapter will be dedicated to the development of a multiphase tool able to fully account for the unsaturated soil behavior.

The hydromechanical interactions in water retention earth structures like levees are a consequence of the hydrodynamic load system acting on them. This system needs to be carefully studied to understand its evolution with time, including the effects of climate change [9]. River level rise and infiltration due to rainfall induce variations in the phreatic level in the levee body, in turn affecting the effective stress state and the material strength. When considering a levee with a clay core, a high river level will mainly influence the phreatic level at the riverside. Due to the relatively short duration of a high river level, extreme rainfall has, for most clay dikes, a stronger influence on the phreatic level development. A worst-case scenario is the occurrence of a high water level after a period of extreme rainfall [10]. This scenario of combined hydraulic loads, rainfall and high river level, is not categorized among the principal instability mechanisms above-mentioned. However, it is reasonable to assume that a macro-instability can be triggered in an easier manner, and for lower river levels, if rainfall is contributing to the saturation. This occurrence will be carefully examined in the following chapters, and specific features developed to reproduce transient hydrodynamic load systems.

A challenging aspect in slope stability prediction includes the quantification of the mobilized soil mass and the run out distance, which are not traditionally addressed by practitioners. An example of a conventional numerical analysis for levees' safety assessment is carried out in the following Sec. 2.2, complemented by a brief list of limitations of the conventional approach used. Common approaches to perform safety assessment rely on the Factor of Safety (FS) definition by means of Limit Equilibrium Methods (LEM) and Finite Element Methods (FEM) [11]. FS is commonly defined as the ratio between maximum available shear strength and mobilized shear stress. This ratio does not provides information on deformations that can generate catastrophic consequences to the downstream communities. With LEM, FS is estimated on the basis of equilibrium considerations assuming an arbitrary failure mechanism and rigid-plastic soil behaviour. The fundamental shortcoming of limit equilibrium methods, which only satisfy equations of statics, is that they do not consider strain and displacement compatibility [12]. With the advent of FEM, the FS calculation has been enhanced considering the soil stress-strain behaviour [13]. Hence, the failure surface is a result of the model and does not need to be defined prior to the analysis. Moreover, the complex hydromechanical behaviour of the soil can be included at small-strain. However, modelling the deformations beyond the onset of failure is not possible with FEM since the method is limited to small deformations of the computational mesh elements. A more robust safety assessment should be based on the simulation of the entire failure mechanism from failure initiation to post-failure behaviour of the structure. This is of vital importance as the severity of floodplain inundation depends on the magnitude of the large deformations potentially experienced by flood embankments. Quantifying the deformations occurring in these structures, in terms of crest settlement and breach extension in longitudinal direction, is considered a key element to the design reliable risk assessments. The cost of river levees can be significantly reduced if targeted repairing or improvements could be designed based on the effect of the potential instability. This requires the simulation of large-strains, that is possible by using the Material Point Method (MPM) as shown in the following chapters of this thesis.

2.1 CURRENT APPROACHES TO STUDY AND PREDICT THE MACRO-INSTABILITY MECHANISMS

The current approaches to increase knowledge about macro-instability in river levees can be categorized in four main types:

1. Experimental approaches

   These approaches can be further subdivided in small scale and large scale. Small scale approaches can aid in clarifying some detailed physical processes governing the slope instability mechanisms ([14, 15]). Thus, these experiments have validity on several applied cases, not only considering levees. In particular, studies on the impact of rainfall on model slopes stability can provide guidance in treating similar issues for levee ([16, 17]) To bypass the problem of scaling laws, to extend considerations from small-scale to large scale, geotechnical centrifuge apparatus are used. This system allows for working on a small scale physical model but considering a real state of stress, thanks to the progressive gravity increase ([18, 19, 20]). Large scale approaches are based on the construction of real scale levees, both in the laboratory or in the field. As major drawback, they are limited by high costs. Among them, it's worthy to mention the experiences by [21, 22, 23, 24].

2. Monitoring approaches

   Monitoring system, as previously introduced, are mostly focused on pore pressure record, phreatic surface definition and evolution, together with the monitoring of unsaturated soil variables. Monitoring system can be installed in existing levee structure or in experimental slopes [21, 25, 26], and needs preliminary calibration steps. They can be categorized in localized system (like piezometers, tensiometers) or distributed systems (like optical fibers), but also they can be based on geophysical measurements [27]. Lastly, they can be suited to function as early warning systems [28].

3. Numerical approaches

   As previously mentioned, the most used numerical approaches are based on LEM and FEM. There are plenty of cases in the literature and in technical reports which report the use of these numerical techniques to assess levee's safety by computing the FS. The numerical methods can be employed to investigate experimental results, explain failure causes and mechanisms in relation to selected case studies, to understand failure with theoretical slopes with realistic solicitation scenario, to calibrate models, to make prediction and to assess the increase of safety with introduction of reinforcement measures. Very limited experiences with the use of large strain numerical models have been attempted before this research work [29, 30].

4. Probabilistic approaches

   Given the extent of the levee systems and the complexity of the interaction between the different potential modes of failure, stochastic methods are increasingly being applied in the context of risk analysis to assess potential for failure and to prioritize repairs and modifications [31]. Either analytical or numerical methods are used to assess safety in a conventional manner by defining the FS. However, a reliability analysis consists in accounting for parameters variability (material, geometry, boundary conditions, failure modes) in the computation of FS. Thus, the condition of $FS \leq 1$ is also expressed by a cumulative distribution function, also named fragility curve. If considering a single failure mode, it is possible to determine the impact of each property or parameter on the failure mode. Whereas, if several failure modes are considered, the failure mechanism with the highest probability to occur can be identified.Fragility curves for different failure mechanisms can also be combined in a single composite fragility curve. Probabilistic approaches combined with FEM seepage and LEM based safety assessments can be found in [31, 32, 33, 34] Differently, other authors employ FEM or Random Finite Element Method [35, 36, 37, 38].

5. Review of case studies

   The review of case studies allows for understanding increase, and it has relevant impact on the national and international level. Procedure of investigations, and definitions of material parameters, methodologies to approach to the failure analysis, are introduced and represent a reference for future studies. In addition, they provide support for improvement of design and safety assessments based on current legislations. There are several experiences in the literature, some popular cases occurred on the national territory and outside can be found in [6, 9, 39, 40, 41, 42]. Recently, a first attempt to build an international levee failure database was done by [43].

   The research work object of this thesis is focused on numerical approaches improvement. Small and large scale experimental data are used to apply the numerical tool which will be developed. Alternatively, it is possible to apply the numerical tool to a case study. For a better understanding of the state of the art of conventional procedures for safety assessment of levees, an example of workflow to investigate a levee section stability is presented in the following section.

2.2 AN EXAMPLE OF WORKFLOW TO ASSESS LEVEE SAFETY WITH A CONVENTIONAL NUMERICAL ANALYSIS

The safety analysis herein presented consider a typical levee section of the lower Tagliamento river, in the north-east of Italy. An investigation campaign is carried out in 2020 on a levee stretch of approximately 30km (starting from the river estuary and going toward the north) considering only the right orographic side. As previously introduced, a progressive level of detail is used for the investigation of levee geometrical features, consistency state, i.e. physical and mechanical properties.

To start, all the available information about the study area are collected. Inspections are conducted along the entire levee stretch to acquire information about the levee consistency (from the "outside") and to check for the presence of localized phenomena, like animal burrows or erosion near the inner banks. Animal burrows are not clearly visible and erosion is limited to two locations where the flood plain has an extension of hundreds of meters. Thus, the erosion phenomenon is far from the levee toe. This is more of a hydraulic engineering problem, which has been partially solved in the area with boulder shore revetments.

Concerning geometry, a topographic survey is compulsory to proceed with the investigation design and build following numerical models. In the case study under analysis, a topographical survey was carried out approx 10 years earlier to the study.

Morphology of the river and geology of the area are collected from geological reports. The lower course of Tagliamento river has a predominant meandering form, compared to the upper course with a typical braided channel morphology.

The history of levees' construction, damages and subsequent interventions, is reconstructed based on reports filed at the local authorities in charge of the earth structure. It emerges that the construction of the levees starts around the 1850, and the majority of the reinforcement interventions dates back to the second half of the 1900s. All this information is vital to identify those stretches with a pre-existent vulnerability in relation to the river morphology, levee geometry and local heterogeneity, and to be aware of recurrent instability types (for example if there has been evidence of piping). In this area, old document report few cases of piping which occurred in not a recent past, and the officer in charge of regular levee inspections doesn't report any event in the last 40 years. Breaches during extreme flooding events are recorded in the previous century, but with no specification of the main collapse mechanisms and the extension of failure. It is to note that the orographic left side of the Tagliamento river has been more impacted by flood events of the last century compared to the right side. In particular, in 1966 an intense pluviometric event which impacted on the entire national territory, induced severe damages on the levees on the left side and consequent flooding of the surrounding areas. After this event, the levees on both sides were reinforced with different interventions: heightenings, diaphragms in the levee body and at the toe, concrete revetments on the inner slope. These interventions, with no full continuity along the investigated stretch (and poorly documented), result in a situation extremely varied, which overlaps to the potential spatial heterogeneity of this long stretch.

It is of good practice to ascertain if results of antecedent geophysical or geotechnical surveys are available before a new investigation design, to optimize the resources and acquire initial knowledge. In fact, two survey campaigns are carried on in 2009 and 2013 (for the latter see [44]) but in very short portions of the levee.

Based on all the collected information, geophysical tests, fast and non-invasive, are performed. They consist in EMI (ElectroMagnetic Induction) along the entire stretch, from north to the mouth, followed by ERT (Electrical Resistivity Tomography) along longitudinal and transversal sections (length of each section is approx 100m). These last, for a total amount of 25 sections, are concentrated in a shorter portion of the stretch, as indicated with a red trait in Fig. 1.2. The ERT locations are chosen based on the EMI results, and the potentially critical locations identified during the initial recognition. The main outcomes from the EMI investigations consist in a zonation in homogeneous stretches based on the resistivity parameters: the levees near the mouth, for an extension of approx 10km are characterized by low resistivity, while the top portion levees are characterized by increasing values of resistivity (¿150 Ohm ·m). ERT sections show important variability, not only along the levee entire stretch in agreement with EMI values, but also in the singular section. To this aim, transversal sections are particularly useful, rather than longitudinal ones. The presence of a 2m layer of soil with high resistivity (150-200 Ohm ·m) is detected in most of the sections investigated (see Fig. 1.3), and in the foundation soils zones of high resistivity with apparent

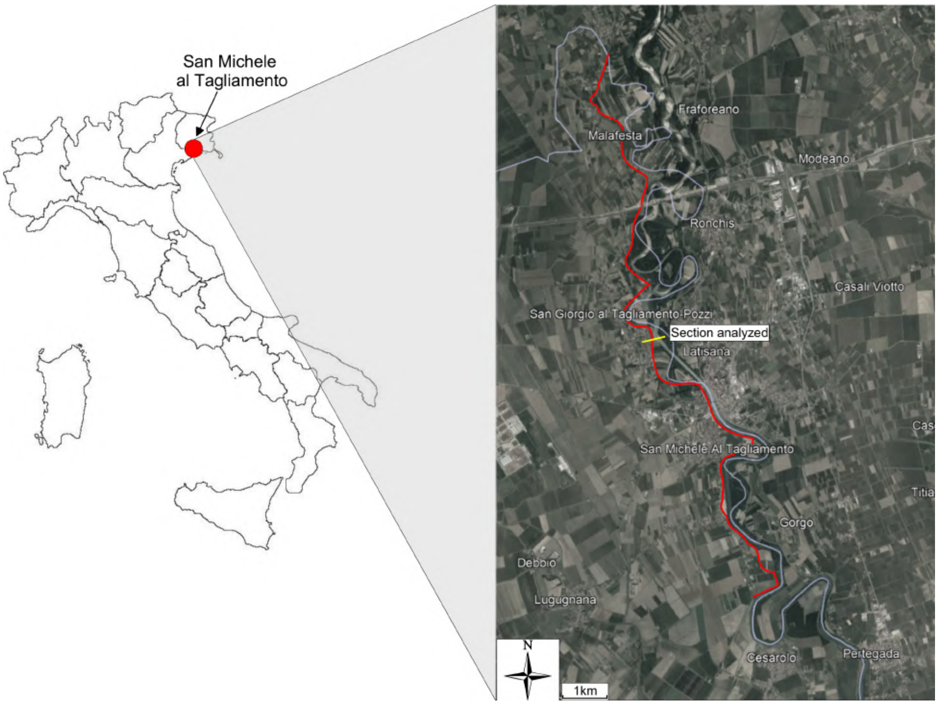

Figure 1.2: Test site location. On the satellite map, red lines outline levees stretch under analysis, while the yellow line trace the section whose safety is assessed.

spatial continuity from land side to river side are identified.

The results of the geophysical tests act as a support for the geotechnical investigations, which are concentrated along selected sections potentially at risk, based on the alleged stratigraphy and heterogeneity presence. A section located near San Giorgio al Tagliamento (a town in the territory of San Michele al Tagliamento) is considered in the following to explain geotechnical test carried on and safety analysis. In this section, the levee body has a height of 5.1m compared to the ground level at landside and a 2.3m retention wall is present on this same side, as visible in Fig. 1.5. On the landside, private properties are extremely close to the levee structure, while on the riverside the flood plain is cultivated, with a maximum extension of the flood plain in the order of 280m.

The purposed of the geotechnical tests is to allow for the subsoil geotechnical model definition. The subsoil geotechnical model is a representative scheme of a significant soil volume, subdivided in homogenous units considering physical and mechanical properties, and those units has to be characterized in relation to the specific geotechnical problem under analysis. Pore pressure and characteristic values of the geotechnical parameters have to be defined in the geotechnical model [45]. Characteristic values of geotechnical parameters are well-thought-out and cautious estimations for every limit state considered. Characteristic values need to be defined based on interpretation of results of specific laboratory tests on representative soil samples and of in site tests and measurements [45]. In addition, geotechnical tests allow for geophysical tests verification and calibration (see Fig. 1.3).

On the considered sample section and other selected sections, three CPTU (Cone Penetration Test with pore pressure measurement) are carried out, from the levee crest and at 20m distance from the levee axis on the riverside and on the landside. The central CPTU reaches a depth of 20m, while the lateral CPTUs are pushed at 15m. This combination of three tests on the same section allows for a better understanding of stratigraphic spatial variability in the section. For each CPTU a dissipation test is performed in a cohesive layer at variable depth. The tip resistance for the three tests is reported in Fig. 1.3; the pore pressure profile is not reported, given the execution inaccuracies (probably related to the filter not complete saturation) which result in a poorly representative profile. Tip resistance (and sleeve friction) give information about the stratigraphy, strength but also deformability and hydraulic parameters, when suitable correlations are employed. From the crest, a DMT (Dilatometer Test) is also carried out, reaching a max depth of 15m, to provide complementary data with the CPTU. The DMT outcomes have a particular capacity in detecting the state of stress in site, history of the deposits, strength and deformability. Both CPT and DMT can be equipped with geophones near their tip to measure soil dynamic parameters, like the shear wave velocity V_S and perform subsequent safety assessments in case of earthquake (for example liquefaction susceptibility or macro instability with simplified pseudo-static approaches). After in site-testing, soil sampling is performed along a borehole from the levee crest, up to 15m depth. Four undisturbed samples are collected along the vertical, together with all the disturbed material, for physical characterization.

The stratigraphy to be used in the following safety analysis is inferred considering CPTU, DMT data and granulometry tests (performed in the laboratory on the collected samples). The material index I_D from the DMT and the granulometric fraction percentages at every meter are reported in Fig. 1.4. The index I_D and

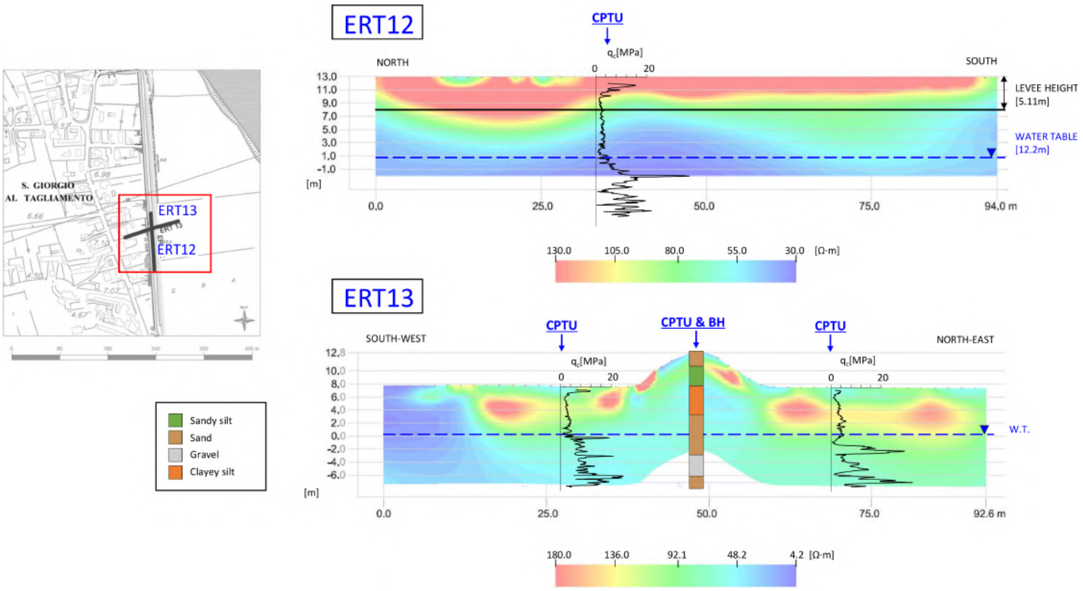

Figure 1.3: Overview of geophysical and geotechnical test results for rapid understanding of soil stratigraphy and geophysical tests verification.

the granulometric fraction show a soil profile in very good agreement: in the first two meters sand is predominant, which corresponds to the heightening realized around the 1970. Under this first unit, the materials of the original levee body are identifiable, a mixture of sand and silt, with a predominance of the latter, up to 9m depth. At this depth, sand fraction increases again and becomes predominant in the last 5m of the inspected stratigraphy. The presence of sand at depth is representative of this fluvial deposition environment, where sediment transport from the upper part of the river is recurring. Based on this information, and the spatial continuity of the soil layers detected from the three CPTU profiles, a simplified stratigraphy, with three main units, is considered for the safety analysis. The stratigraphy is made by three main formations: sandy silt for the levee body and the first 6m depth, silty sand (approx 1.5m) and sand (see Fig. 1.5). A maximum depth of 15m is considered sufficient for a representative outcome of a safety analysis. In terms of lateral extension, the model reach 100m on the landside and 280m on the riverside, including the lower inner bank. The software *Geostudio* [46] is used for the analysis which is articulated in two phases, uncoupled: first a transient seepage analysis, then a LEM based analysis, considering pore pressure distributions at every instant coming from the previous seepage analysis. The transient seepage analysis is carried out with SEEP/W, which is a FEM-based

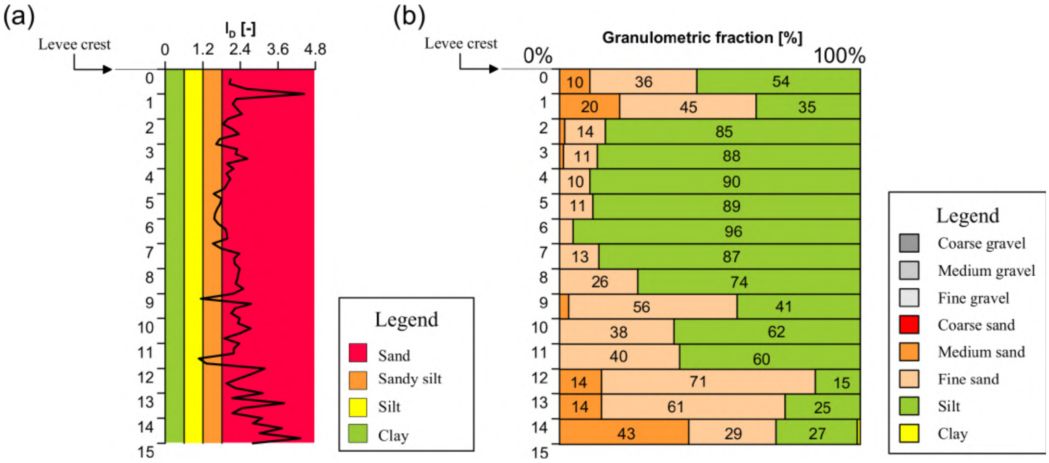

Figure 1.4: Stratigraphy of levee and foundation soils from in-site (DMT I_D index (a)) and laboratory test (granulometric fractions (b)).

solver. The continuity equation of the fluid in the porous media is considered as a governing equation, and the Darcy law is assumed for the flow regimes.

After the definition of surface and subsurface geometry, material properties should be assigned to the different units. It is possible to consider soil with unsaturated or fully saturated behavior. In absence of specific information coming from in-site or laboratory test on the unsaturated soil properties, like the experimental soil water retention curves (SWRC) or the hydraulic conductivity curve (HCC), it is decided to consider a saturated soil model, which requires as the most relevant input parameter the saturated hydraulic conductivity and to specify potential anisotropy of it. In the present case, hydraulic conductivity has been firstly estimated from in-site tests and lab tests (using a flow pump system during a consolidated undrained triaxial test). Then a more precise calibration is performed, using data coming from an open tube piezometer installed in the levee. Lastly, the hydraulic conductivity is considered isotropic. It should be specified that the SWRC, in absence of experimental calibration, can be estimated from the granulometry (see [47, 48]), however for the purpose of the study it was not required such a level of detail in the hyromechanical description. Information about the levee compressibility are retrieved from the DMT results, and assigned to each layer with the parameter M_V, inverse of the oedometric modulus. The hydraulic properties are summarized in Tab 1.1.

After material properties' specification, the hydraulic boundary conditions are assigned. On the landside a potential seepage face condition is assigned, while on the riverside a transient total head condition is imposed. The model is extended to 280m on the riverside, but the results are presented considering a reduced view of the model. Based on a hydraulic modelling preliminary to the geotechnical analysis, a peak hydrograph corresponding to a return time of 100yr is provided, with a growing phase of approximately 24hr and a more gentle decrease in 48hr. It is reported in Fig. 1.5. The initial condition is created by specifying the location of the water table, at the depth recorded during boreholes execution. Lastly, the model geometry needs to be discretized: a triangular mesh of 0.5m is considered for the top layer, while the underneath layers are discretized with a coarser mesh of triangles of 1m edge size. A total time of 72hrs is analyzed.

The results are used as input of the LEM analysis, which needs additional information to be specified: the strength parameters and the slip surface specification. Strength parameters are related to the failure criterion choice. A simple Mohr-Coulomb model is used, disregarding the potential increase in strength in the unsaturated zone above the phreatic surface. This is a conservative assumption. Drained parameters, friction angle and effective cohesion, are determined taking into account in-site tests and laboratory triaxial tests on undisturbed samples. The mechanical properties are summarized in Tab. 1.1. A circular slip surface is considered and by specifying ranges of entry and exit points on the ground surface, the software automatically chooses the slip surface and compute the relative FS. The soil mass above the slip surface is subdivided in slices, and static equilibrium equations are solved for each slice. The problem is statically undetermined, thus sub-methods has been developed in the mid 1900s to solve the problem based on additional assumptions. These assumptions consist in the selection of one or more static equations to solve (or to "respect") and in the specification of interslice forces ratios. In the present case, Morgestern-Price method is used which considers both equilibrium of forces and momentum. Hence, two factors of safety are computed, which vary depending on a function governing the variable inclination of the resultant ratio between horizontal and vertical interslice forces. The intersection between the two FS' curves defines the actual FS shown by the software. A LEM analysis is carried out for every instant of the transient seepage analysis. In Fig. 1.5 the surface associated to the minimum FS in time is reported, together with the value of FS. Lastly, the instant of occurrence is reported with a

Layer	M_v $[1/kPa]$	k $[m/s]$	γ $[kN/m^3]$	ϕ $[°]$	c' $[kPa]$
Sandy Silt	$7.67 \cdot 10^{-5}$	$5.0 \cdot 10^{-6}$	20.2	32	0.0
Silty sand	$6.49 \cdot 10^{-5}$	$2.0 \cdot 10^{-7}$	20.2	30	0.0
Sand	$3.20 \cdot 10^{-5}$	$3.0 \cdot 10^{-4}$	20.2	35	0.0

Table 1.1: Material parameters for transient seepage and LEM analysis.

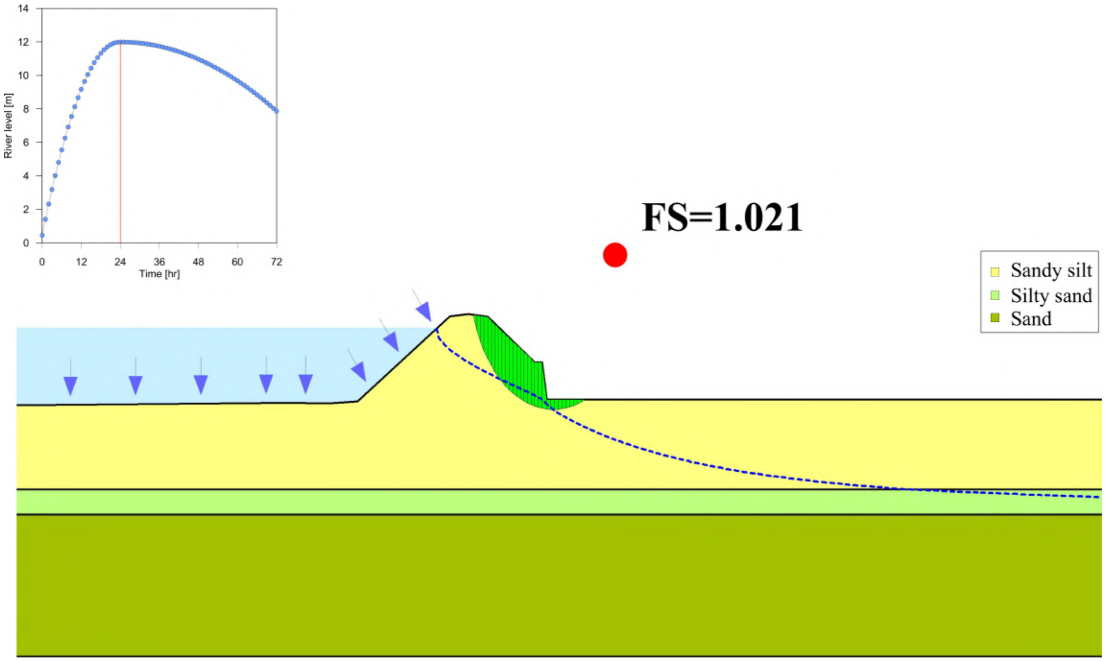

Figure 1.5: LEM analysis result at a levee section on the Tagliamento river.

red vertical line on the left-hand side hydrograph. This value of FS, immediately above 1, may be interpreted as a stable condition, however the strength reserves are practically absent, and each following solicitation or a potential localized damage not considered in the model, can represent a trigger for a full instability mechanism. Based on the current reference national law [45], this section is unsafe, since FS should be higher than 1.1 to consider the section as safe. Based on this result suggestions for future reinforcement interventions are provided. This type of result has certain limitations, listed in the following:

1. LEM is based on the hypothesis of rigid-plastic soil behavior, thus no state of stress in relation to the strain is accounted for in the analysis
2. The FS is considered the same along the entire slip surface extension, and this doesn't correspond to the real physics
3. The analysis is uncoupled, thus the multiphase interactions are not fully captured (just in simplified terms)
4. No displacements are quantifiable, the approach is purely based on forces (and momentum) computations. The actual soil mass movement can not be defined and subsequent considerations about areas impacted during the collapse are not traceable
5. No description of failure evolution in time (no post-failure). After FS¡1 the following modifications of it are not reliable and non precisely linked with the structure damage.

Based on this simple example of a conventional analysis, it appears appropriate and of paramount importance to improve numerical tools to overcome these limitations and provide higher quality predictions. In this manner, mitigation measures can be designed more efficiently, which is a fundamental aspect for these long extension structures. The development and use of the Material Point Method, in the field of levee safety, will be presented in the following chapters.

2

MPM multiphase formulations

1 FUNDAMENTALS OF THE MATERIAL POINT METHOD

The material point method (MPM) is a numerical technique capable of handling large deformations. As a continuum method, the study of deformation and forces, i.e. studying the mechanical behavior of bodies, is done considering conservation laws, like mass, momentum and energy balance. In most of MPM formulations, heat effects or any source of thermal energy is disregarded, and the mechanical work is the only considered source/sink of energy. The materials' behavior is described by a constitutive model, and compatibility equations are necessary to relate strain and velocity. In addition to the conservation equations, a set of initial and boundary conditions is necessary to solve any given problem. This set of equations and conditions is usually referred as a boundary value problem (BVP).

Equations sets characterizing BVPs are partial differential equations (PDE), which can be solved adopting suitable numerical techniques, like Finite Element Method (FEM) or Finite Difference method (FDM) among others. Galerkin FEMs [49, 50] are among the most popular techniques to solve a BVP in engineering disciplines. With these methods, the governing equations are transformed from a strong form (PDE) to a more convenient weak form (integral form). Then, making use of interpolation functions (also named shape functions) and a convenient spatial discretization with a computational mesh, the solution of the equations is obtained, as a nodal approximation of the actual solution.

MPM can be viewed as an extension of the FEM procedure. The weak form of the governing equations as well as the final system of equations posed at the nodes of the computational mesh are identical in both schemes. Nonetheless, MPM is a particle-based while FEM is a mesh-based method. If on one hand, in mesh-based methods the only space discretization entity is the mesh, on the other, in particle-based methods, a cloud of material points/particles discretizes the continuum body. All the physical properties are attached to the particles, not to the mesh elements. In some cases, in particle-based methods, the particles are the only entity, like in meshless methods as SPH (Smoothed Particle Hydrodynamic) [51, 52, 53]. In other cases, like in MPM, PFEM (Particle Finite Element Method) or FEMLIP, mesh and particles are both present [54, 55, 56, 57]. In this last case, the approximated solution is computed at the mesh nodes, however no permanent information is stored at the mesh level. To this aim, projection of nodal quantities to particles is done via shape functions.

To better understand the hystorical development of MPM, it is common to define this method in the framework of Lagrangian and Eulerian descriptions. In Lagrangian methods, the computational grid is embedded and deformed with the material [58]. There is no advection of mass flow across element boundaries, so no advection terms appear in the governing equations. It is easy to impose boundary conditions since element boundaries coincide with material interfaces. To avoid extreme distortion of the elements, thus introducing errors and preventing the convergence to the solution, remeshing may be necessary.

On the contrary, in Eulerian methods the material flows through the grid and this last is fixed. The volume of each element keeps constant during a simulation, but its density varies due to advection of mass [58]. In this case, interfaces and boundaries are more challenging to be tracked.

Finally, there are hybrid methods, like arbitrary Lagrangian-Eulerian (ALE) and Particle-in-cell (PIC) methods, which benefit from aspects of both the previous methods. In ALE methods, the computational mesh may be moved with the material like Lagrangian approach, or be held fixed in Eulerian manner, or be moved independently of material deformation to optimize element shapes and for a more accurate boundaries' description [59]. From PIC method, MPM has been developed. In fact, in PIC the computational cycle is divided into two phases, a

Lagrangian phase and an Eulerian phase. In the first Lagrangian phase, equations of motions are solved. In the Eulerian phase, the particles are moved and advection fluxes are considered, while the mesh is mapped back to the original configuration. MPM has been formulated in 1994 to solve solid mechanics problems, repurposing and improving many aspects of PIC and FLIP (an improvement of PIC using a fully Lagrangian formulation) [54].

MPM applies two levels of spatial discretization: (i) the body is discretized by a cloud of material points (MPs) which moves attached to the material and carry all the updated information such as velocities, strain, stresses, and history variables; and (ii) a fixed finite element mesh used to assemble and solve the system of balance equations. Large deformations are simulated by MPs moving through the computational background grid that covers the full problem domain (not only the bodies shape). This grid is used to solve the system of equilibrium equations, but since no information is stored at the mesh, the distortion or entanglement are completely avoided. The MPM computational scheme, presented in the following summary, can be divided in two phases, named Lagrangian (steps 1 and 2) and Eulerian or convective (steps 3 and 4), as in PIC.

1. At the beginning of a computational step, the material information, kinematic and stress variables are stored at the MPs. Therefore, this information need to be mapped from the MPs to the background mesh nodes by means of shape functions (Fig. 2.1(a))

2. The momentum balance equations can be solved at the nodes and the accelerations obtained (primary unknowns) (Fig. 2.1(b))

3. The kinematic quantities are updated at MPs, using interpolation functions. In this manner it's possible to update also strains and stress (secondary unknowns) at MPs, according to the constitutive models (Fig. 2.1(c))

4. The particle positions are updated, and the mesh is reset to the original location (Fig. 2.1(d)).

A strong point of MPM, included since its first formulation, is the adaptation to materials with history-dependent constitutive models. Since each material point is followed, history-dependent variables, such as plastic strain and strain-hardening parameters, can be associated with the material point for the complete evolution of the problem [54]. Geomaterials are typical history-dependent materials, and

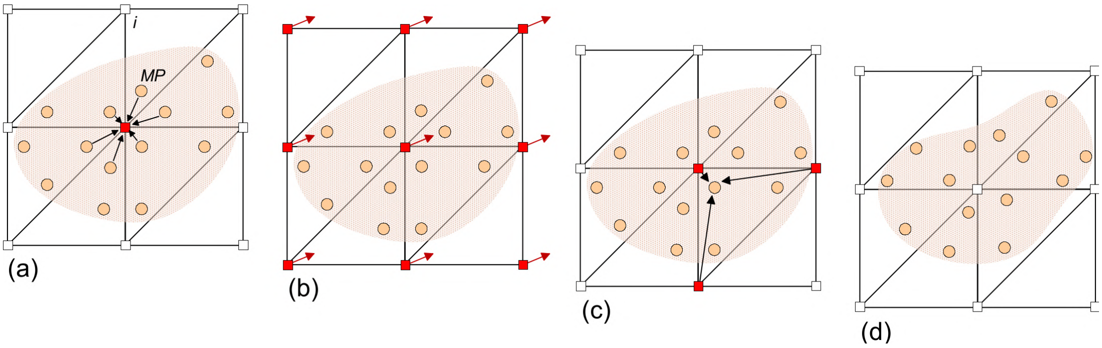

Figure 2.1: Computational scheme of MPM: (a) Information mapping to the nodes. (b) Resolution of momentum balance equations at the nodes. (c) MP quantities update. (d) MP housekeeping update. i stands for the node entity, while MP for the material point.

therefore in the last twenty years MPM has become increasingly popular in the field of geomechanics and geotechnical engineering. Among others, the applied cases explored are slope instabilities, failure of earth retaining structures, tunneling and underground collapses, soil penetration testing, pile installation, scour and internal erosion [60, 61, 62, 63, 64, 65, 66, 67].In addition to being characterized by large displacements, these applications often require the use of a multiphase description of soil.

Historically, [68] present several formulations for saturated and unsaturated soils referring to FEM implementations and discuss their applicability for different kinds of problems in geotechnical engineering. These formulations can also be extended for MPM. In fact, in Sec. 2 the current MPM multiphase formulations are presented to provide a framework for this research work.

Before we start covering the aspects of multiphase formulations, some of the principal implementation features of the MPM are introduced (considering a 1Phase material). The open-source software *Anura3D* (www.Anura3d.com) is the numerical tool selected for testing and development in this research work, hence, the mathematical framework herein presented, will refer mostly to it. *Anura3D* is based on a dynamic MPM formulation and an explicit in time integration scheme. It has been developed for the purpose of analyzing soil-water-structure interactions, so balance equations refer to the soil behavior as a porous medium. Constitutive laws are typical for soil and the principle of effective stress is included.

1.1 Dynamic formulation

The momentum conservation of the continuum can be written with the differential Eq. 2.1. A dynamic formulation is considered, which means that the acceleration term $\mathbf{a}$ is taken into account. In the same equation ρ stands for material density, $\boldsymbol{\sigma}$ is the stress tensor and $\mathbf{g}$ is the gravity vector

$$\rho\mathbf{a} = \nabla\boldsymbol{\sigma} + \rho\mathbf{g} \tag{2.1}$$

Boundary conditions correspond to the same types of FEM, i.e. Dirichlet (or essential) and Neumann (or natural). In the first case, the values of imposed velocity are directly injected in the system of discretized equations (usually displacements equal to zero in a prescribed direction). In the second case, Neumann conditions correspond to tractions applied along a portion of the border, and require the specification of an outward normal unit vector. The weak form equivalent to Eq. 2.1, considering a resolution domain Ω with traction boundary conditions τ applied on a portion of the boundary $\partial\Omega$, is given as

$$\int\limits_{V} \rho\mathbf{a}\cdot\mathbf{u}\,dV = \int\limits_{\partial\Omega} \tau \mathrm{d}\mathbf{u}\,\partial\Omega - \int\limits_{V} \sigma : (\nabla\mathbf{u})\,dV + \int\limits_{V} \rho\mathbf{g}\cdot\mathbf{u}\,dV \tag{2.2}$$

where $\mathbf{u}$ stands for the test function. At this point, the equation needs to be discretized. First an approximation of accelerations, velocity, displacements and test function vectors via shape functions $\mathbf{N}$ is introduced. For example,

$$\mathbf{v}(x,t) = \sum_{i=1}^{Ni} \mathbf{v}_i(t)\mathbf{N}_i(x,t) \tag{2.3}$$

The most distinguishing feature between FEM and MPM is the calculation of the numerical integration over the volume of a finite element. Meanwhile, in FEM the integrations are carried out using Gaussian quadrature points, in MPM they are calculated based on the material points which are not fixed like Gaussian points. The MP integration is applied by assuming that mass is concentrated at MPs location, thus

$$\rho(x,t) = \sum_{MP=1}^{n_{MP}} m_{MP}\,\delta(x - x_{MP}) \tag{2.4}$$

where m_{MP} and x_{MP} are the mass and the position of the material point, $\delta(\mathrm{x})$ is the Dirac delta function, and n_{MP} is the total number of material points. The final discretized form, considering approximated variables with shape functions and MP integration can be finally written in compact form as Eq. 2.5

$$\mathbf{Ma} = \mathbf{f}^{ext} - \mathbf{f}^{int} \tag{2.5}$$

where $\mathbf{a}$ is the nodal accelerations vector, $\mathbf{M}$ is the mass matrix, $\mathbf{f}^{ext}$ is the external force vector and $\mathbf{f}^{int}$ is the internal force vector, reported in Eqs. 2.6, 2.7, 2.8.

$$\mathbf{M} \approx \sum_{\mathrm{MP}=1}^{n_{\mathrm{MP}}} m^{\mathrm{MP}} \mathbf{N}_{MP} \tag{2.6}$$

$$\mathbf{f}^{\,\mathrm{ext}} \approx \int_{\partial\Omega_\tau} \mathbf{N}_{MP}^{\mathrm{T}} \tau \mathrm{d}\partial\Omega_\tau + \sum_{\mathrm{MP}=1}^{n_{\mathrm{MP}}} m_{\mathrm{m}}^{\mathrm{MP}} \mathbf{N}_{MP}^{\mathrm{T}} \mathbf{g} \tag{2.7}$$

$$\mathbf{f}^{\,\mathrm{int}} \approx \sum_{\mathrm{MP}=1}^{n_{\mathrm{MP}}} \mathbf{B}_{MP}^{\mathrm{T}} \sigma_{\mathrm{MP}} V_{\mathrm{MP}} \tag{2.8}$$

In Eq. 2.8, $\mathbf{B}_{MP}$ stands for the spatial derivative of the shape functions $\mathbf{N}_{MP}$, both particularized for the MP. Usually, the mass matrix is lumped to simplify the inversion procedure and solve the linear system of discretized equations. The type of shape functions used has a determinant impact on the simulation outcomes. In fact, one of the shortcomings of using linear shape functions is the phenomenon of volumetric locking in a nearly incompressible solid. Volumetric locking consists in an unrealistic stiff body response and an erroneous velocity field. In *Anura3D* linear shape functions are used, however a Nodal Mixed Discretization (NMD) technique [69] is put in place to tackle the issue. With this technique, the element volumetric behavior is averaged over the elements sharing its nodes via a least square smoothing process. This is why this technique is also referred as strain smoothing procedure. The effect of applying the NMD scheme is to increase the number of degrees of freedom per element [70].

Another well-known drawback related to linear shape functions in MPM is the cell-crossing instability. Whenever material points cross boundaries of any element in the computational background grid, a nonphysical unbalance force appears at the nodes that are shared between previous and new elements of that crossing MP [71]. This is directly depending on the gradient of the shape functions, constant but discontinuous at element borders. In turn, the gradient impacts on internal forces computation, resulting in significant oscillations of stress variables. In Anura3D a simplified approach allows mitigating this problem by averaging the stress of all the MPs in an element. Based on that, Gauss integration is adopted to determine the internal forces (as in FEM), in which a single point with an averaged stress is considered in each element. The calculation of the internal forces by means of the Gauss point integration is only considered in the elements located in the interior of the continuum. In *Anura3D* this procedure is commonly referred as *MPM-MIXED* since it uses both MPs and Gauss points [70]. This is not the only way to mitigate cell-crossing instability: other more sophisticated techniques has been proposed in the literature to mitigate locking, like the most popular Generalized Interpolation Material Point Method (GIMP) [72] and others [73, 74, 75, 76].

1.2 TIME INTEGRATION SCHEMES

The resolution of the Eq. 2.5 provides values of nodal acceleration at each time step of a simulation. At this point different time integration schemes are possible: explicit, implicit or semi-implicit.

In *Anura3D* an explicit Euler time scheme is adopted to compute velocity and displacements (Eqs. 2.9 and 2.10). The variables are given at time t^{k+1}, considering the solution at the previous time t^k and an increment of time Δt.

$$\mathbf{v}_i^{k+1} = \mathbf{v}_i^k + \Delta t\, \mathbf{a}^k \tag{2.9}$$

$$\mathbf{u}_i^{k+1} = \mathbf{u}_i^k + \Delta t\, \mathbf{v}^{k+1} \tag{2.10}$$

Explicit time schemes are conditionally stable, which means that Δt has a maximum value, usually named critical, above which the simulation doesn't converge anymore to the actual solution. The critical time step can be computed by solving an eigenvalue problem and imposing that the spectral ratio of the amplification matrix is equal to 1 (as reported for example in [71]). In this case, the amplification matrix is obtained by considering an appropriate system of equations, those stemming from the discretization of momentum balance equation and considering the explicit in time scheme. For one phase materials with linear elastic behavior the equation of the critical time step corresponds to the Courant Fredrich Levy (CFL) condition, i.e., Eq. 2.11

$$\Delta t_{crit} = \frac{Li}{\sqrt{\frac{E}{\rho}}} \tag{2.11}$$

where Li is the minimum mesh size, E is the Young modulus and ρ is the medium density. The denominator of Eq. 2.11 is the speed of compression waves. Other MPM codes benefit of explicit integration in time [77, 78, 79, 80].

On the other side, unconditionally stable implicit schemes, has also been proposed in the literature [81, 82]. In this case, momentum balance equation becomes implicit for velocity at time t^{k+1}, usually written as Eq. 2.12. The parameter μ allows the user to adjust between explicit and implicit: $0 < \mu < 1$ with $\mu = 0$ being fully explicit and $\mu = 1$ being fully implicit. The solution is obtained with an iterative procedure.

$$m_i^k \frac{\mathbf{v}_i^{k+1} - \mathbf{v}_i^k}{\Delta t} = \mu\, \mathbf{f}_i^{k+1} + (1-\mu)\mathbf{f}_i^k \tag{2.12}$$

In Eq. 2.12, $\mathbf{f}_i$ stands for internal force. External forces are not reported to simplify the presentation, but they can be easily combined with the internal forces. Some examples of current MPM codes relying on implicit schemes are [83, 84, 85]. Very recently a semi-implicit scheme has been proposed by [86] in a multiphase formulation. In fact, the effective stress is treated explicitly to avoid successive iteration associated with elastoplastic material responses, while the pore-pressure term is treated implicitly by solving the pressure Poisson equation.

1.3 NUMERICAL ALGORITHM: THE EXAMPLE OF *Anura3D*

At this point, after presenting the spatial and temporal discretization, it is possible to go through the steps of a typical MPM algorithm, for large strain problem analysis. The algorithm presented in the following is based on [87]. The main computational steps are listed below

1. The nodal mass is calculated using the shape functions and the lumped mass matrix at time t^k is formed. The internal and external forces are evaluated in the nodes (Eqs. 2.7, 2.8).

2. The momentum balance equation is solved, and the nodal accelerations $\mathbf{a}_i^k$ are determined
$$\mathbf{a}_i^k = \mathbf{M_i^k}^{-1}(\mathbf{f}_i^{ext,k} - \mathbf{f}_i^{int,k}) \tag{2.13}$$

3. The velocity at the material points is updated considering Eq. 2.14 as
$$\mathbf{v}_{MP}^{k+1} = \mathbf{v}_{MP}^k + \Delta t \sum_{i=1}^{n_i} \mathbf{N}i_{MP}^k \, \mathbf{a}_i^k \tag{2.14}$$

4. Updated nodal velocities are calculated taking into account Eq. 2.15 as
$$\mathbf{v}_i^{k+1} = \frac{1}{m_i^k} \sum_{MP=1}^{n_{MP}} \mathbf{N}i_{MP}^k \mathbf{v}_{MP}^{k+1} \tag{2.15}$$

5. Particle positions are updated considering Eq. 2.16 as
$$\mathbf{x}_{MP}^{k+1} = \mathbf{x}_{MP}^k + \Delta t \sum_{i=1}^{n_i} \mathbf{N}i_{MP}^k \, \mathbf{v}_i^k \tag{2.16}$$

6. The strain increment of a material points can be expressed as function of the nodal velocity, i.e. as function of the deformation gradient, as
$$\boldsymbol{\Delta}\varepsilon_{MP}^{k+1} = \Delta t \sum_{i=1}^{n_i} \mathbf{B}_{i,MP}^k \, \mathbf{v}_i^{k+1} \tag{2.17}$$

   where $\mathbf{B}_{i,MP}$ are shape function derivatives, evaluated at MPs.

7. The constitutive stresses are updated using a preselected material constitutive model.

8. The material properties are updated in the material points, such as volume and density, which are updated considering the increment of volumetric strain.

9. The computational grid is initialized for the next step, nodal values are discarded, and the material points carry all the updated information.

The structure of this algorithm is very similar in all the multiphase formulations of *Anura3D*, the major difference is the presence of one or two fluids, which impacts on the number of governing equations and the kinematic and stress variables that need to be computed accordingly.

2 MULTIPHASE FORMULATIONS

Soil as a porous media consists of a combination of three phases (ph): solid (S), liquid (L), and gas (G). The solid phase is made of solid grains that constitute the solid skeleton, while the fluid phases (i.e., liquid and gas) fill the pore space. The phases interact with each other determining the mechanic and hydraulic behaviour of the material.

Taking rigorously into account these interactions may be in many cases unacceptably complicated, computationally expensive, and even unnecessary for engineering applications [70]. For example, in numerical analyses of saturated soil, dealing with fully drained or fully undrained conditions means that the presence of water can be considered in a simplified way. In the first case, the excess pore pressure is assumed to be zero, thus the presence of the liquid can be neglected, and the solid skeleton can be regarded as 1Phase even though it is saturated.

In the second one, because of the negligible relative movement between solid and liquid, the equilibrium of the solid-liquid mixture can be considered rather than the equilibrium of solid skeleton and pore liquid as separate phases. The dissipation of pore pressure is not considered, given the fast time of load application. The analysis can be carried out considering total stress or effective stress. In undrained conditions, Eq. 2.18 is the momentum balance equation to solve

$$\rho_{sat}\mathbf{a} = \nabla\boldsymbol{\sigma} + \rho_{sat}\mathbf{g} \tag{2.18}$$

where $\mathbf{a}$ is the soil acceleration, $\boldsymbol{\sigma}$ is the total stress tensor and ρ_{sat} is the saturated soil density. Pore pressure increments for an effective stress analysis in undrained conditions are computed as

$$\dot{p_{\mathrm{L}}} = \frac{K_{\mathrm{L}}}{n}\dot{\varepsilon}_{\mathrm{vol,L}} \tag{2.19}$$

where $\dot{p_{\mathrm{L}}}$ is the derivative respect to time of liquid pressure, K_{L} is the liquid Bulk modulus, n the porosity and $\dot{\varepsilon}_{\mathrm{vol,L}}$ the time derivative of liquid volumetric strain.

Eq. 2.19 is valid under the assumption of weakly compressible fluid.

In all the other cases where partially drained conditions are recognized, a fully-coupled multiphase formulation is necessary to capture the soil behavior.

Two MPM frameworks have been presented to study fully-coupled multi-phase problems [88]: the single-point approach and the multi-point approach. The single-point framework represents the multi-phase soil mixture as a unique continuum represented with one set of MPs [86, 89, 90, 91]. During the calculation, all MPs move with the displacement of the solid skeleton represented using Lagrangian formulation and consequently the solid mass in the MP remains constant. Fluids' motion is described with respect to the moving solid skeleton. Saturated and unsaturated soil can be described with this approach.

The multi-point framework requires more than one set of MPs to represent different phases. In particular, the double-point approach for saturated soil is available in the literature and represents solid skeleton and liquid with two completely separate sets of MPs [92, 93, 94]. Each set of MPs moves accordingly to the displacement of the corresponding phase and carries the information of one phase only, hence solid and fluid are represented using Lagrangian formulation. In the double-point configuration presented in [92, 93], the soil is considered either fully dry or fully saturated. Very recently, [95] proposed an extension of this same approach to include hydro-mechanical interactions resulting from partially saturated conditions, where the liquid MPs carry information of the degree of saturation. Currently, the study of unsaturated soils using a three-point approach (i.e. three sets of MPs for solid, liquid and gas) has never been attempted yet.

Based on the existent formulations, Fig. 2.2 outlines the MPM soil descriptions, considering multiphase nature and MPs layers. A detailed comparison between saturated MPM formulations can be found in [96]. Once more, since *Anura3D* is the numerical tool selected for testing and development in this research work, the mathematical description of the following sections will be mostly focused on it.

2.1 SATURATED SINGLE POINT FORMULATIONS

The 2Phase Single Point MPM formulations (2P-SP) for saturated soils most of the time are based on two main approaches: the $\mathbf{v}_\mathrm{L} - \mathbf{v}_\mathrm{S}$ [80, 86, 89, 90, 97] and the $\mathbf{u}_S - \mathbf{p}_L$ [98, 99]. The first one is the most popular approach and the one

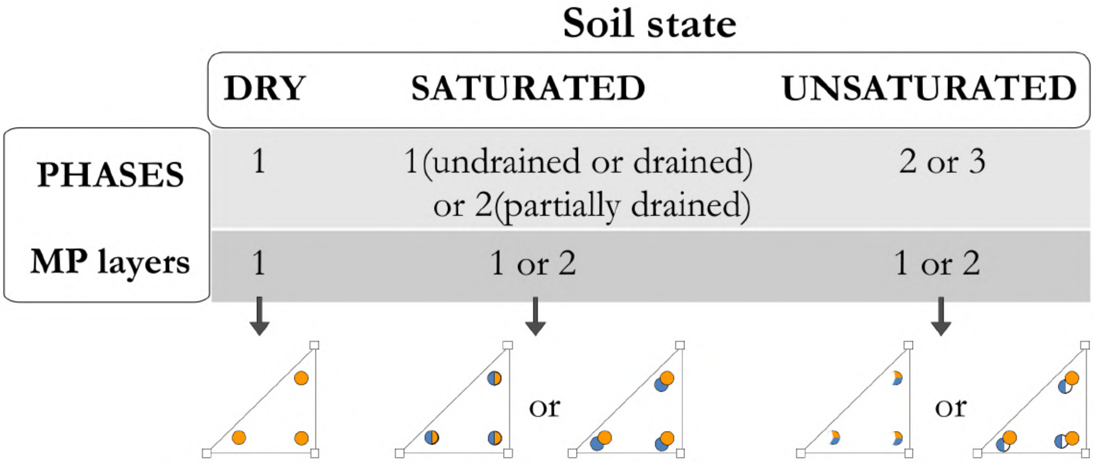

Figure 2.2: Soil states in MPM: distinction based on the number of phases and discretization in MP layers.

implemented in *Anura3D*. Each MP represents a portion of saturated porous media and carries the information of the solid (solid skeleton) and liquid in the pores (e.g., water). In this case, the MPs remain attached to the solid skeleton giving a Lagrangian description of the solid-phase movement, while the liquid-phase behavior is described with respect to the MPs by means of an Eulerian approach. In particular, the $\mathbf{v}_\mathrm{L} - \mathbf{v}_\mathrm{S}$ approach is implemented in *Anura3D*, based on the work of [97]. The set of governing equations includes momentum balance of the liquid and the mixture; mass balance, constitutive relations and compatibility equations, for each phase. The momentum balance equations (Eqs. 2.20, 2.21) are solved for the primary unknowns $\mathbf{a}_\mathrm{L}$ and $\mathbf{a}_\mathrm{S}$, accelerations of solid and liquid respectively.

$$\rho_L \mathbf{a}_L = \nabla p_L - \mathbf{f}_L^d + \rho_L \mathbf{g} \tag{2.20}$$

$$n_S \rho_S \mathbf{a}_S + n_L \rho_L \mathbf{a}_L = \nabla \cdot \boldsymbol{\sigma} + \rho_m \mathbf{g} \tag{2.21}$$

In Eqs. 2.20 and 2.21, ρ_L and ρ_S are liquid and solid density, while $\rho_m = n_S \rho_S + n_L \rho_L$ is the mixture density, i.e. saturated soil density; the liquid concentration ratio is $n_L = n$ and the solid concentration ratio is $n_S = (1 - n)$, where n is the porosity. The term $\mathbf{f}_L^d$ stands for liquid drag force, and in this formulation is expressed considering Darcy law (see Eq. 2.22).

$$\mathbf{f}_L^d = \frac{n_L \mu_L}{k_L}(\mathbf{v}_L - \mathbf{v}_S) \tag{2.22}$$

The intrinsic permeability is expressed as Eq. 2.23

$$k_L = \kappa_L \frac{\mu_L}{\rho_L g} \tag{2.23}$$

where κ_L is the hydraulic conductivity (for instance expressed in m/s) and μ_L is the dynamic viscosity of the liquid (for instance expressed in kPa $\cdot$ s). The mass balance equations for each phase are reported in Eqs. 2.24, 2.25

$$\frac{\mathrm{D}^{\mathrm{S}} n_{\mathrm{S}}}{\mathrm{D}t} + n_{\mathrm{S}} \mathrm{div}(\mathbf{v}_{\mathrm{S}}) = 0 \tag{2.24}$$

$$\rho_{\mathrm{L}} \frac{\mathrm{D}^{\mathrm{L}} n_{\mathrm{L}}}{\mathrm{D}t} + n_{\mathrm{L}} \frac{\mathrm{D}^{\mathrm{S}} \rho_{\mathrm{L}}}{\mathrm{D}t} + n_{\mathrm{L}} \rho_{\mathrm{L}} \mathrm{div}(\mathbf{v}_{\mathrm{L}}) + (\mathbf{v}_{\mathrm{L}} - \mathbf{v}_{\mathrm{S}}) \cdot \nabla(n_{\mathrm{L}} \rho_L) = 0 \tag{2.25}$$

The mass balance equations can be combined to obtain an expression for the liquid pressure increment (Eq. 2.26). In the latter, once again, a weakly compressible behavior is assumed for the liquid, i.e. $\frac{1}{\rho_{\mathrm{L}}} \frac{d\rho_{\mathrm{L}}}{dp_L} = -\frac{1}{K_L}$

$$\dot{p}_L = K_L \cdot \dot{\varepsilon}_{\mathrm{vol,L}} = K_L \cdot \frac{1}{n}[(1-n)\mathrm{div}(\mathbf{v}_{\mathrm{S}}) + n\,\mathrm{div}(\mathbf{v}_{\mathrm{L}}) + \nabla n\,(\mathbf{v}_{\mathrm{S}} - \mathbf{v}_{\mathrm{L}})] \tag{2.26}$$

The principle of effective stress is considered in this formulation, thus the total stress $\boldsymbol{\sigma}$ in 2.21 is expressed as Eq. 2.27

$$\boldsymbol{\sigma} = \boldsymbol{\sigma}' + p_L \mathbf{m} \tag{2.27}$$

where $\mathbf{m}$ is a unit vector. During a computational cycle, the increment of liquid pressure are computed with Eq. 2.26 and the pressure values updated, then the increment of effective stress are computed with a predefined constitutive model, implemented in incremental form as reported in Eq. 2.28

$$\dot{\boldsymbol{\sigma}'} = \mathbf{D} \cdot \dot{\boldsymbol{\varepsilon}} \tag{2.28}$$

where $\mathbf{D}$ is the tangent matrix.

Boundary conditions need to be specified for both phases: on the liquid, it is possible to impose pressure (analogous to traction for solid) or fix displacements in one or more directions (when both directions are fixed, the border is considered impermeable). Whereas on the solid, imposed traction or fixed displacements can be assigned, as previously introduced for the monophase formulation.

2.2 Saturated double point formulation

The 2Phase Double Point (2P-DP) formulation was initially presented by [100], and later extended by [79, 92] and [93, 101]. The formulation assumes that the soil is a superposition of two continuum media: the solid skeleton and the liquid phase. These are represented separately by two sets of Lagrangian MPs: solid material points (SMPs) and liquid material points (LMPs). The computational domain in which the material moves is as usual discretized with a finite element mesh. According to this framework, three possible domains can emerge:

- Porous medium in saturated conditions, when SMPs and LMPs share the same grid element
- Porous medium in dry conditions, when only SMPs are located in the grid element
- Free liquid, when only LMPs are located in the grid element.

The dynamic behavior of the continuum is described with the solid and liquid dynamic momentum balances (Eqs. 2.29 and 2.30), which are solved at the grid nodes for the acceleration of solid and liquid $\mathbf{a_S}$ and $\mathbf{a_L}$.

$$n_L \rho_L \mathbf{a_L} = \nabla \cdot \bar{\sigma_{\mathbf{L}}} - \mathbf{f}_{\mathrm{SL}} + n_L \rho_L \mathbf{g} \tag{2.29}$$

$$n_S \rho_S \mathbf{a_S} = \nabla \cdot \bar{\sigma_{\mathbf{S}}} + \mathbf{f}_{\mathrm{SL}} + n_S \rho_S \mathbf{g} \tag{2.30}$$

In the previous expressions

$$\bar{\sigma_{\mathbf{S}}} = \sigma' + n_S \sigma_{\mathbf{L}} \tag{2.31}$$

and

$$\bar{\sigma_{\mathbf{L}}} = +n_L \sigma_{\mathbf{L}} \tag{2.32}$$

correspond to the macroscopic partial stresses for solid and liquid phases, where $n_L = 1 - n_s$ is the liquid volumetric fraction (in the hypothesis of fully saturated soil $n_L = n$), σ' is the effective stress tensor, and $\sigma_{\mathbf{L}}$ is the stress tensor of the liquid phase. The force representing the interaction between solid and fluid, $\mathbf{f}_{\mathrm{SL}}$, assumes the expression proposed by [102] (Eq. 2.33)

$$\mathbf{f}_{\mathrm{SL}} = \mathbf{f}_{\mathrm{n}} + \mathbf{f}_{\mathrm{d}} = \sigma_{\mathrm{L}} \nabla n_{\mathrm{L}} + \mathbf{f}_{\mathrm{d}}. \tag{2.33}$$

In this expression, $\mathbf{f}_{\mathrm{n}}$ accounts for the porosity gradient. The second term, $\mathbf{f}_{\mathrm{d}}$, is a drag force, a function of the relative velocity between fluid and solid $(\mathbf{v}_L - \mathbf{v}_S)$. The drag law proposed by [103] is implemented in the 2P-DP formulation of *Anura3D*:

$$\mathbf{f_d} = \mathbf{f_1} + \mathbf{f_2} = \frac{\nu}{k_L} n_L^2 (\mathbf{v_L} - \mathbf{v_S}) + \beta n_L^3 \rho_l |\mathbf{v_L} - \mathbf{v_S}| (\mathbf{v_L} - \mathbf{v_S}). \tag{2.34}$$

It includes a linear term $\mathbf{f}_1$ (low-velocity regime) and a quadratic term $\mathbf{f}_2$ (high velocity regime). The former is a Stokesian drag term while the latter, named the non-Darcy flow coefficient, has been estimated by many authors both numerically and experimentally. It shows dependence on porous media features like permeability, porosity, and tortuosity [104, 105]. The formulation determines the empirical coefficient β using Ergun coefficients (Eq. 2.35) [106] $A = 150$, $B = 1.75$.

$$\beta = B / \sqrt{\kappa_L A n_L^3}. \tag{2.35}$$

The intrinsic permeability κ_{L} can evolve in time due to the variation of porosity. This is taken into account with a Kozeny-Karman formula (Eq. 2.36):

$$\kappa_{\mathrm{L}} = \frac{D^2}{150} n_{\mathrm{L}}^3 / (1 - n_{\mathrm{L}})^2. \tag{2.36}$$

In Eq. 2.36 D is the effective grain diameter and can be referred to D_{50}.

Granular materials can experience a transition between solid-like behavior to fluid-like behavior when the porosity and the shear rate increase. The 2P-DP formulation accounts for the phase transition process by a maximum porosity criterion. Below a threshold porosity value (n_{max}) solid-like behavior persists (*Solid state*) with positive effective stress, updated with constitutive relations typical of soils, like Mohr-Coulomb. Even in this formulation, solid stress is updated at the MPs level: the increment of stress is a function of the increment of strain, the effective stress current state and the state variables of the constitutive model in use. Conversely, above the maximum porosity, grains are supposed to be detached. Thus, the stress transmission is no more possible, the effective stress is zero and the soil behaves like a fluid (*Liquid state*), with an effective viscosity ν_{eq} (Eq. 2.37) [107], affected by the solid volumetric fraction $(1 - n_{\mathrm{L}})$.

$$\nu_{\mathrm{eq}} = \nu_{\mathrm{m}} \left(1 + \frac{5}{2}(1 - n_{\mathrm{L}}) + 5.2(1 - n_{\mathrm{L}})^2 \right) \tag{2.37}$$

In this formulation, the liquid phase is assumed weakly compressible and the stress increment is computed with Eq. 2.38

$$\dot{\sigma}_{\mathrm{L}} = \dot{p}_{\mathrm{L}}\mathbf{I} + \dot{\sigma}_{\mathrm{L,dev}} = K_{\mathrm{L}}\dot{\varepsilon}_{\mathrm{vol,L}}\mathbf{I} + 2\nu_{\mathrm{eq}}\dot{\varepsilon}_{\mathrm{L}}, \tag{2.38}$$

where $\mathbf{I}$ is the identity vector, K_{L} , $\dot{\boldsymbol{\varepsilon}}_{\mathrm{L}}$ and $\dot{\varepsilon}_{\mathrm{vol,L}}$ as previously defined. The expression of the volumetric component (Eq. 2.39) is obtained by rearranging the mass balance equations, again considering weakly compressible liquid. The complete mathematical developments can be found in [93].

$$\dot{\varepsilon}_{\mathrm{vol,L}} = \frac{1}{n}[(1 - n)\mathrm{div}(\mathbf{v}_{\mathrm{S}}) + n\,\mathrm{div}(\mathbf{v}_{\mathrm{L}}) + \nabla n\,(\mathbf{v}_{\mathrm{S}} - \mathbf{v}_{\mathrm{L}}) \tag{2.39}$$

Going back to the fluid transition, in elements with SMPs in *Solid state* the deviatoric part of the liquid stress tensor is assumed to be zero ($\dot{\sigma}_{\mathrm{L,dev}} = 0$). In *Liquid state*, i.e., as soon as fluidization occurs, the deviatoric component is computed considering Eq. 2.37 for the equivalent viscosity. It should be noted that in this simplified approach to reproduce fluidization, once the soil change to the *Liquid state*, it is not possible to reverse back to the *Solid state.*

Concerning boundary conditions, as in any other multiphase formulation, they need to be specified for each phase. These are fixity for the velocities (Dirichlet BC) or traction/pressure imposed (Neumann BC). When the *free surface* is considered, i.e., the boundary between free water and the atmosphere, the imposed pressure on the liquid is automatically equal to zero. The detection of the free surface of the liquid domain is based on a threshold value for the interpolated filling ratio η

at LMPs location, as expressed in Eq. 2.40. This threshold value $F_{FreeSurf}$ should be lower than 1, it is mesh-dependent and in simulations it is often set between 0.6 and 0.8.

$$\tilde{\eta}_{MP_L} < F_{FreeSurf} \tag{2.40}$$

This approach resembles the Volume of Fluid (VoF) method, where the physical volume fraction is used as an indicator to track the discontinuous volume change across the interface. The indicator function equals to unity at any point occupied by the fluid and zero elsewhere, and interface is detected if the value between zero and one [108], with a threshold value as previously specified.

In addition to these BCs, recently inflow/outflow BCs have been presented in the work by [109]. Specifically, in this implementation, the inflow boundary control the kinematics, i.e., velocity is imposed, while the outflow boundary has an imposed pressure. The MPs added or removed are related to an *ad-hoc* element layer, which has a fixed dimension. Due to this aspect, the implementation is not suitable to reproduce a transient total head condition, indeed corresponding to spatial variations of river levels. The 2P-DP formulation, as implemented in *Anura3D*, is tested in Chapter 3.

2.3 UNSATURATED SINGLE POINT

The single-point approach is the general framework selected to represent soils in unsaturated conditions. The current unsaturated single point formulations can be distinguished based on the number of computational phases described

1. Fully 3Phase formulation by [71, 110]
2. Simplified 2Phase formulations: [66, 111, 112, 113, 114, 115, 116, 117].

This distinction implies that in the 3Phase formulation three equations for each set of the governing equations (set of momentum balance, mass balance, constitutive equations and compatibility equations) are present. Whereas, in the 2Phase formulations, only two equations for each set are used. This is valid under the hypothesis of negligible density and pressure of the gas, $\rho_G = 0$ and $p_G = 0$, in turn, allowing for elimination of gas as a computational phase. Matric suction, $s = p_G - p_L$ can still be defined as $s = -p_L$.

The formulation developed by [116] is the object of Chapter 4, and there it will be explained in detail as it represents one of the principal activities of this research work. The 3Phase formulation ([71, 110]) is the first formulation developed to study unsaturated soil behavior. The momentum balance equations, relative to gas phase, liquid phase and mixture are reported in the strong form

$$\rho_G \mathbf{a}_G = \nabla p_G - \mathbf{f}_G^d + \rho_G \mathbf{g} \tag{2.41}$$

$$\rho_L \mathbf{a}_L = \nabla p_L - \mathbf{f}_L^d + \rho_L \mathbf{g} \tag{2.42}$$

$$n_S \rho_S \mathbf{a}_S + n_L \rho_L \mathbf{a}_L + n_G \rho_G \mathbf{a}_G = \nabla \cdot \boldsymbol{\sigma} + \rho_m \mathbf{g} \tag{2.43}$$

This formulation is fully dynamic, and all relative acceleration terms are fully accounted with the accelerations of each phase being the primary unknowns of the system, i.e. $\mathbf{a}_\mathrm{S}$, $\mathbf{a}_\mathrm{L}$ and $\mathbf{a}_\mathrm{G}$. The notation is the same as in the SinglePoint saturated formulation, the only new terms appearing are related to the gas phase, i.e. gas pressure p_G, gas density ρ_G, $\mathbf{f}_G^d$ gas drag force and ρ_m include a new term, $\rho_m = n_S\rho_S + n_\mathrm{L}\rho_\mathrm{L} + n_G\rho_G$. The porosity of the solid skeleton becomes $n = n_L + n_G$, and the volumetric concentration ratio of the fluid phases can be expressed in terms of the degree of saturation (S_L) and porosity as $n_L = nS_L$ and $n_G = n(1 - S_L)$, respectively for liquid and gas. Note that fully saturated conditions are the particular case when the degree of saturation S_L is one.

The fluid flow (either liquid or gas) is assumed laminar (as in the Single Point saturated formulation), and the liquid and gas drag forces ($\mathbf{f}_G^d$ and $\mathbf{f}_L^d$) are written taking into account validity of Darcy law, (Eq. 2.44). The subscript f denotes fluid phase, that can be either gas G or liquid L.

$$\mathbf{f}_f^d = \frac{n_f \mu_f}{k_f}(\mathbf{v}_f - \mathbf{v}_S) \tag{2.44}$$

Where μ_f and k_f correspond to the viscosity and intrinsic permeability of the fluids (i.e. $f = G, L$). The intrinsic permeability is defined in terms of hydraulic conductivity (κ_f), in analogy with 2.23

$$k_f = \kappa_f \frac{\mu_f}{\rho_f g} \tag{2.45}$$

In the formulations proposed by [66, 95, 112, 113, 114, 115, 116, 118] all dynamic terms, i.e., liquid and solid inertia, are considered and the main unknowns of the system are the accelerations of the solid and liquid phases ($\mathbf{a}_S$ and $\mathbf{a}_L$). The linear momentum of the liquid is identical to Eq. 2.42. The linear momentum of the mixture is equivalent to Eq. 2.43 but removing the dynamic term corresponding to the gas phase, which yields Eq. 2.46.

$$n_S \rho_S \mathbf{a}_S + n_L \rho_L \mathbf{a}_L = \nabla \cdot \boldsymbol{\sigma} + \rho_m \mathbf{g} \tag{2.46}$$

Very similarly, the formulation from [117] considers all dynamic terms and the solid and liquid accelerations as primary variables, but the momentum balance of the solid per unit of total volume (Eq. 2.47) is posed instead of the momentum balance of the mixture. **I** is the identity matrix.

$$n_S \rho_S \mathbf{a}_S = \nabla \cdot (\boldsymbol{\sigma} - n_L p_L \mathbf{I}) + (\rho_m - n_L \rho_L)\mathbf{g} + \mathbf{f}_L^d \tag{2.47}$$

Finally, the formulation by [111] neglects the relative acceleration of the liquid with respect to the solid skeleton. Therefore, all phases have the same acceleration $\mathbf{a}$ (i.e., acceleration of the system, $\mathbf{a} = \mathbf{a}_S = \mathbf{a}_L$). The momentum balances of the liquid, which is equivalent to the generalized Darcy equation (Eq. 2.48), and the mixture (Eq. 2.49) are the governing equations posed at the nodes of the computational mesh and the main unknowns are the acceleration of the system $\mathbf{a}$ and the liquid seepage velocity ($\mathbf{w} = nS_L(\mathbf{v}_L - \mathbf{v}_S)$).

$$\mathbf{w} = -\frac{\kappa_L}{\mu_\mathrm{f}}(\nabla p_L + \rho_L - \rho_L \mathbf{g}) \tag{2.48}$$

$$\rho_m \mathbf{a}_S = \nabla \cdot \boldsymbol{\sigma} + \rho_m \mathbf{g} \tag{2.49}$$

In the 3Phase MPM formulation [71, 110] the liquid and gas are considered to be a mixture of water and air, and mass exchange between liquid and gas phases is allowed to account for "water vapour" in the gas and "dissolved gas" in the liquid. Assuming incompressible solid grains ($\frac{\mathrm{D}^S \rho_S}{\mathrm{D}t} = 0$), the expressions for the mass balance of the solid is the same es Eq. 2.24 while for the fluids, the equations are written as Eqs. 2.50.

$$n\frac{\mathrm{D}^S(\rho_f S_f)}{\mathrm{D}t} + \nabla \cdot (\rho_f S_f n(\mathbf{v}_f - \mathbf{v}_S)) + \rho_f S_f \nabla \cdot \mathbf{v}_S = 0 \tag{2.50}$$

In those problems where the spatial variations of fluids mass in the soil are small ($\nabla(\rho_f S_f n) \approx 0$), [110] simplify the term with the gradient of the advective fluxes of the fluid phases (i.e. $\nabla \cdot (\rho_f S_f n(\mathbf{v}_f - \mathbf{v}_S))$) yielding to Eq. 2.51. The effect of neglecting part of the advective flow gradients is further discussed in Sec. 2.2.1.

$$n\frac{\mathrm{D}^S(\rho_f S_f)}{\mathrm{D}t} + \rho_f S_f n \nabla \cdot (\mathbf{v}_f - \mathbf{v}_S) + \rho_f S_f \nabla \cdot \mathbf{v}_S = 0 \tag{2.51}$$

The fluid mass balances are solved in the MPM computational cycle in terms of the variation of liquid and gas pressure ($\frac{\mathrm{D}^S p_L}{\mathrm{D}t}$ and $\frac{\mathrm{D}^S p_G}{\mathrm{D}t}$).

$$\frac{\mathrm{D}^S(\rho_f S_f)}{\mathrm{D}t} = \left(S_f \frac{\partial \rho_f}{\partial p_L} + \rho_f \frac{\partial S_f}{\partial p_L}\right)\frac{\mathrm{D}^S p_L}{\mathrm{D}t} + \left(S_f \frac{\partial \rho_f}{\partial p_G} + \rho_f \frac{\partial S_f}{\partial p_G}\right)\frac{\mathrm{D}^S p_G}{\mathrm{D}t} \tag{2.52}$$

The 2Phase MPM formulations neglect the gas density, and only the mass balances of the solid and liquid phases are required. All approaches consider the mass balance of the solid as presented in Eq. 2.24, but propose slightly different versions of the mass balance of the liquid. The formulation proposed by [66, 114] extends the previous works to account for internal erosion of the solid skeleton, based on the work from [119] for saturated conditions. The mass exchange between the solid and liquid phases is allowed according to an erosion law that controls the rate of eroded mass.

The system of governing equations is closed by compatibility equations and constitutive relations. Various hydro-mechanical stress frameworks are available in the literature to describe the behaviour of unsaturated soils [120]. They are inherited from the Bishop single effective stress approach [121] or from the independent stress variable approach [122]. The Bishop effective stress approach is the most commonly implemented in the MPM formulations [66, 95, 111, 113, 116, 117, 118]. The general form of the constitutive equation is presented incrementally as Eq. 2.28, where the effective stress essentially controls the stress state of unsaturated soil and is defined as Eq. 2.53. $\boldsymbol{\sigma}_{net}$ is the net stress ($\boldsymbol{\sigma}_{net} = \boldsymbol{\sigma} - p_G\mathbf{I}$), s is the matric suction and χ is an effective stress parameter generally assumed equal to S_L. Note that most of the works assume $p_G = 0$.

$$\boldsymbol{\sigma}' = \boldsymbol{\sigma}_{net} - \chi s\mathbf{I} \tag{2.53}$$

The independent stress variable approach is used in [110], where the net stress is defined more generally as Eq. 2.54. In this context, the stress state is described by two state variables (i.e. $\boldsymbol{\sigma}_{net}$ and s) and a double constitutive matrix is required (Eq. 2.55), where $\mathbf{h}$ is a constitutive vector controlling the influence of suction.

$$\boldsymbol{\sigma}_{net} = \boldsymbol{\sigma} - \max\{p_G, p_L\}\mathbf{I} \tag{2.54}$$

$$d\boldsymbol{\sigma}_{bet} = \mathbf{D} \cdot d\boldsymbol{\varepsilon} + \mathbf{h}ds \tag{2.55}$$

In addition to the constitutive equations, in any unsaturated formulation, the hydraulic model is required. The hydraulic model consists in two relations: Soil Water retention curve (SWRC) and hydraulic conductivity curve (HCC), respectively relating saturation degree with suction ($s = p_G - p_L$) and hydraulic conductivity with saturation degree.

Concerning boundary conditions, again they need to be specified for each phase, like in the previous saturated formulations. The same conditions are present for solid and liquid, plus the conditions for the gas are added, in terms of prescribed gas pressure or fixed gas displacements. Consistent research has been done in recent years to account for additional hydraulic boundary conditions that are relevant in several applications where earth structure/slopes/soil volumes are in contact with water or the atmosphere. These are infiltration/evaporation, potential seepage face and total head. In Chapter 4 the development and implementation of this full set of hydraulic boundary conditions is discussed in detail for the formulation by [116]. For the fully 3Phase formulations, these conditions are not implemented yet. Some of them are present in the other 2Phase formulations, but total head and seepage face are present only in the formulation object of this thesis work.

2.4 UNSATURATED DOUBLE POINT

Finally, the only available formulation for unsaturated soils that uses a double-point configuration [95] considers as governing equations, momentum balance of the liquid and the mixture. In addition, it rewrites the mass balance of the liquid Eq. 2.50 taking into account that the liquid mass is transported by the liquid material points. The material derivative can be described with respect to the liquid motion ($\frac{\mathrm{D}^L p_L}{\mathrm{D}t}$), and neglecting the gradient of porosity, it yields to Eq. 2.56. In this formulation, the gradients of degree of saturation and liquid density are implicitly accounted. The mass balance of the solid is posed exactly as Eq. 2.24.

$$n\frac{\mathrm{D}^L(\rho_f S_f)}{\mathrm{D}t} + \rho_f S_f(1-n)\nabla\cdot\mathbf{v}_S + \nabla\cdot\mathbf{v}_L = 0 \tag{2.56}$$

A weakly-compressible behavior is assumed for the liquid, and the variation of the liquid pressure ($\frac{\mathrm{D}^{S/L} p_L}{\mathrm{D}t}$) is derived again from the mass balance equations.

$$\frac{\mathrm{D}^{S/L}\rho_L S_L}{\mathrm{D}t} = \rho_L\frac{\mathrm{D}^{S/L}S_L}{\mathrm{D}t} - \frac{\rho_L}{K_L}\frac{\mathrm{D}^{S/L}p_L}{\mathrm{D}t} \tag{2.57}$$

Despite the sophisticated multipoint modelling, this formulation has simple hydraulic boundary conditions, i.e., imposed pressure or fixities, which limit the applicability to real scenarios of earth structures.

3 CURRENT APPLICATIONS OF MPM IN THE FIELD OF RIVER LEVEES

MPM has been applied to several geotechnical problems in the last decade [89, 123, 124, 125, 126], however in the field of levees, earth dams or dikes there are limited experiences. In relation to the collapse mechanisms introduced in Chapter 1, a levee overtopping has been analyzed in the work of [127] using the Double Point formulation. However, this is not a macro-instability mechanism. Suffusion (internal erosion) has been implemented in Single Point [64] and Double Point formulation [128]. The only examples about macro-instabilty are dikes instabilities with seepage flow in the work by [29] or without seepage in [129] and the reproduction of a centrifuge experiment where a soft clay dike is brought to failure by [30]. In these two examples, the unsaturated soil behavior has not been considered.

Based on the few examples analyzed with MPM and a rapidly increasing interest in these topics from the computational geomechanics community, it emerges that the present work is focused on the development of cutting-edge numerical tool and represents a pioneering study in the use of a displacements based approach to analyze the macro-instabilities undermining water retention earth structures safety.

3

Testing the 2Phase-Double point formulation in selected slope stability cases

1 INTRODUCTION

In this chapter, the 2Phase Double Point (2P-DP) formulation, suited for saturated soil and able to capture the relative displacement between the two phases, is tested in some selected slope stability problems. The aim of these studies is understanding the potential and limits of this approach while giving new insights about the analyzed phenomena.

The first example is the collapse of a soil column on a horizontal plane. This small-scale benchmark is commonly employed in geotechnical modelling to study the rheology of complex natural mixtures, as well as to calibrate major parameters controlling free surface earth fall behavior and potentially correlated debris flows. Small-scale laboratory experiments are designed and carried out to establish a reference case for the MPM numerical simulations. Unlike previous experiments of column collapse in completely submerged conditions, completely dry conditions, or with very small amount of fluid [see e.g. 130, 131, 132, 133, 134, 135, among others], the material is saturated and propagates in air. These conditions are closer to natural flow-like landslides. A plane strain numerical model is built, and the results are discussed with emphasis on the collapse dynamics, run-out, and size scale effects. In particular, the 2P-DP formulation is able to reproduce soil-fluid coupling in an advanced manner by considering a nonlinear drag force expression and phase transition from solid to liquid state. These two aspects and their impacts on propagation and run-out distance are investigated in this study.

Afterwards, a different problem is considered to test the formulation. Unlike the first case, the second is at the engineering scale: the failure of a levee section due to rapid drawdown. This case is treated in a simplified manner, by progressively removing liquid material points (LMPs) to mimic the emptying process. The aim of this second example is to show the power of MPM in quantifying failure and post-failure behavior. This kind of analysis can provide a safety assessment not only in qualitative terms by expressing a factor of safety (FS), but rather in quantitative terms, thanks to the full displacement analysis. To make this aspect more clear, a comparison with analysis based on LEM and FEM is carried out.

The examples presented in this chapter are taken from two papers coauthored by the thesis author [136, 137]. In the first paper, the study of the column collapse is enriched with a comparison between 2P-DP MPM and a micromechanical numerical approach, i.e., the DEM (Discrete element method) coupled with LBM (Lattice Boltzman method). Some of the most relevant findings arising from the comparison will be briefly presented.

2 SATURATED GRANULAR COLUMN COLLAPSE IN AIR

Many hazardous natural phenomena like debris flow, avalanches and submerged landslides are characterized by rapid movement of a mixture of solid particles and fluid. During motion the two phases can separate. Depending on the flow velocity and the mixture characteristics, the front can be dominated by the solid phase (granular front) or the liquid phase (fluid front). The interactions between these phases govern the propagation of the mixture, and this behavior is still poorly understood.

The numerical simulation of these phenomena is attractive, because it allows the use of numerical models in the context of hazard assessment and mitigation. On the other side, experimental data helps to calibrate numerical models, validate

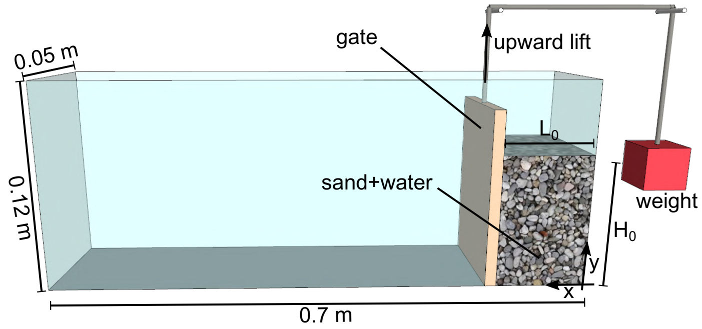

Figure 3.1: Illustration of the experimental setup used for column-collapse tests, from [136].

them and develop the intuition needed for the derivation of fundamental governing equations [130]. A commonly employed small-scale model for the study of flow-like landslides is the column collapse. The results of an experimental and numerical study of this specific problem are herein presented.

2.1 Experimental study

The sketch of the experimental configuration is illustrated in Fig. 3.1. It consists of a standard glass flume 0.70 m-long, 0.05 m-wide, and 0.12 m-high, closed at one end. The flume is equipped with a movable vertical gate at a distance of $L_0 = 0.04$ m from the closed end: in this way, a storage partition is created, where the saturated granular mixture is placed. By modifying the filling height, columns with different aspect ratios can be prepared. The channel base and the lateral walls are made of glass, while the gate is made of plexiglass.

The gate and the opening mechanism have been designed to address both water tightness before collapse and sudden gate uplift. The first is crucial to avoid partial desaturation prior to the collapse, thus an immiscible fluid (vaseline) was used to coat the interfaces between gate and flume sides; in addition, the same fluid favors the fast uplift of the gate, triggering the propagation of the saturated mixture in a way that can be well described by the sudden removal of fixities in the numerical models. The granular material (an artificial sand) has a uniform granulometric distribution with mean diameter $D = 2.5 \cdot 10^{-3}$ m and grain density $\rho_S = 2625$ kg/m^3. The fluid phase is water dyed with a natural colorant in order to improve the visualization of the fluid motion.

The preparation method of the saturated sample aims at controlling the initial volumetric fractions of the components. At the beginning, the column volume is

Conditions	H_0 [m]	L_0 [m]	a [-] number
Saturated and Dry	0.07	0.04	1.75
	0.06	0.04	1.50
	0.05	0.04	1.25
	0.04	0.04	1.00
	0.03	0.04	0.75

Table 3.1: Summary of experimental tests. The aspect ratio is computed as $a = H_0/L_0$.

filled with $2 \cdot 10^{-5}$ m^3 of water. Subsequently, a controlled amount of granular material is gently poured with a spoon immersed in the water to allow deposition without compaction and to avoid gas bubble inclusion. Soil layering continues until the column reaches the desired initial dimensions. If necessary, the water level is adjusted using a syringe. The liquid volume V_L and the solid mass m_s are carefully measured; the porosity is computed from the liquid volume as in Eq. 3.1

$$n_{V_L} = V_L/(H_0 L_0 W) \tag{3.1}$$

and subsequently cross-checked with a second equation (Eq. 3.2), based on solid mass

$$n_{m_s} = 1 - m_s/(\rho_s H_0 L_0 W) \tag{3.2}$$

In Eqs. 3.1, 3.2 H_0 is the initial column height, L_0 initial column base dimension parallel to x-axis (see Fig. 3.1 for the reference system) and W is the other base dimension of the column, corresponding to the flume thickness. Some differences were reported in the initial aggregation state due to the operator influence on the preparation procedure, however, the initial porosity values were always bounded between 0.39 and 0.43, with an average of 0.40.

The experimental tests considered are summarized in Tab.3.1. The initial column basal dimensions are fixed, since they are related to the apparatus configuration, while the height of the column is varied between $H_0 = 0.03$ m and 0.07 m, obtaining different aspect ratios $a = H_0/L_0$. Three tests for each configuration are carried out to verify the repeatability of the results and estimate the experimental error.

The process is recorded with a high-resolution and high-speed camera (500frames/s) placed at the channel side and aligned with the horizontal channel axis. The apparatus is illuminated by a constant artificial LED light, as visible in Fig. 3.2. The videos are elaborated with a MATLAB code, which extracts the frames and

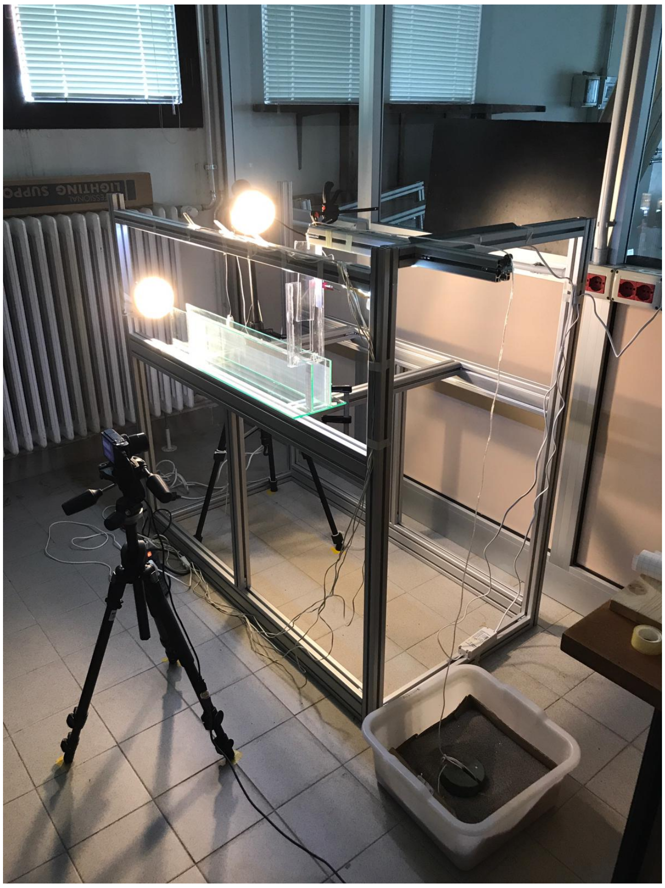

Figure 3.2: Complete apparatus set up ready for column collapse tests.

detects the edges of the column, creating the corresponding coordinates data set [138]. Note that with this procedure only the lateral profile of the column can be observed. Fig. 3.3 provides an overview of the collapse evolution for $a = 1.5$, with four extracted frames overlapping with the detected profiles (in red). Time is normalized with respect to a reference time, defined in accordance with previous numerical studies on dry and submerged granular column collapse [135, e.g.]: $t_{\mathrm{ref}} = \sqrt{H_0/g}$ for dry conditions and $t_{\mathrm{ref}} = \sqrt{H_0/g'}$ for saturated conditions. The reduced gravity $g' = g(\rho_{\mathrm{S}} - \rho_{\mathrm{L}})/\rho_{\mathrm{S}}$ accounts for the buoyancy effect in the ambient fluid [135, 139].

When the gate is lifted, at the column foot, both grains and water starts moving forward (Fig. 3.3(a)). Then, the top part heads toward the flume base, slipping along a failure surface progressively evolving with time (Fig. 3.3(b), (c)), which separates the flowing layer from the underneath static region. Finally,

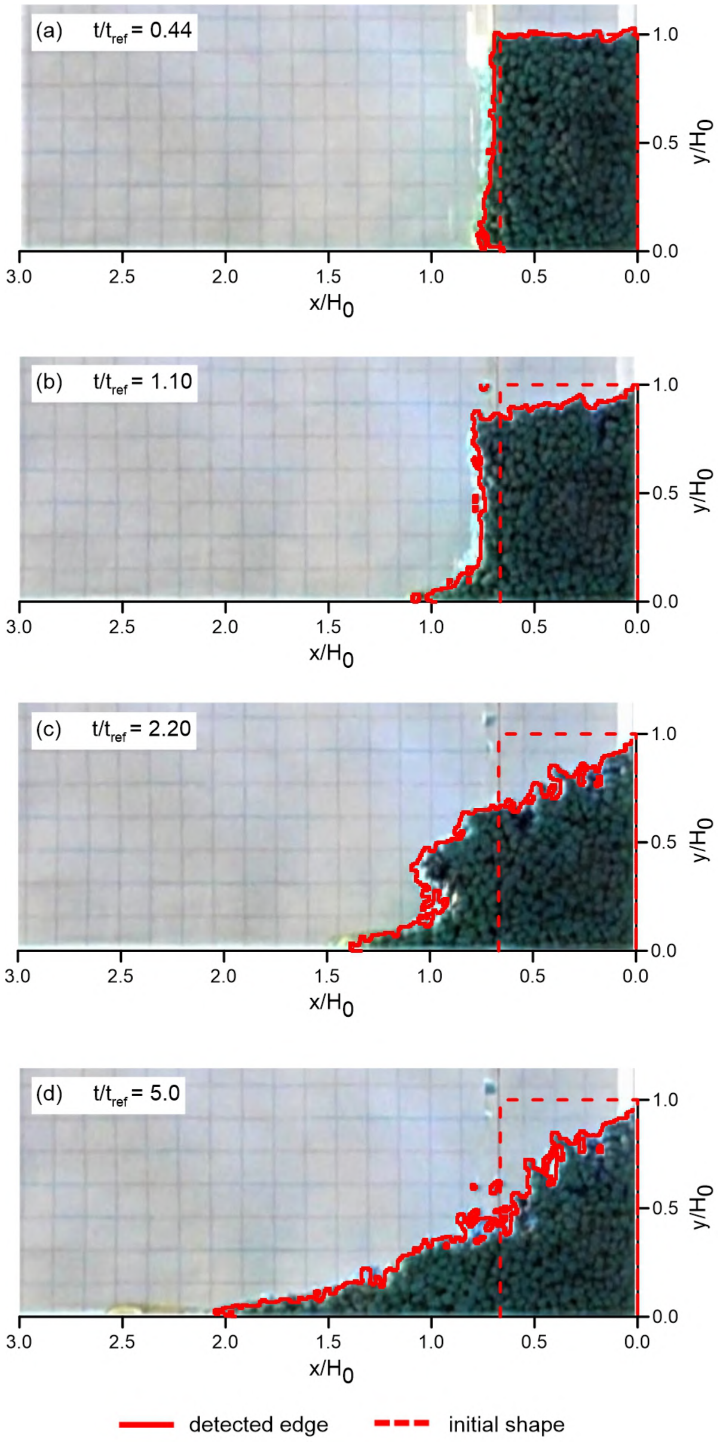

Figure 3.3: Frames of the saturated soil collapse experiment ($a = 1.5$) with edge detection at different time instants, from [136].

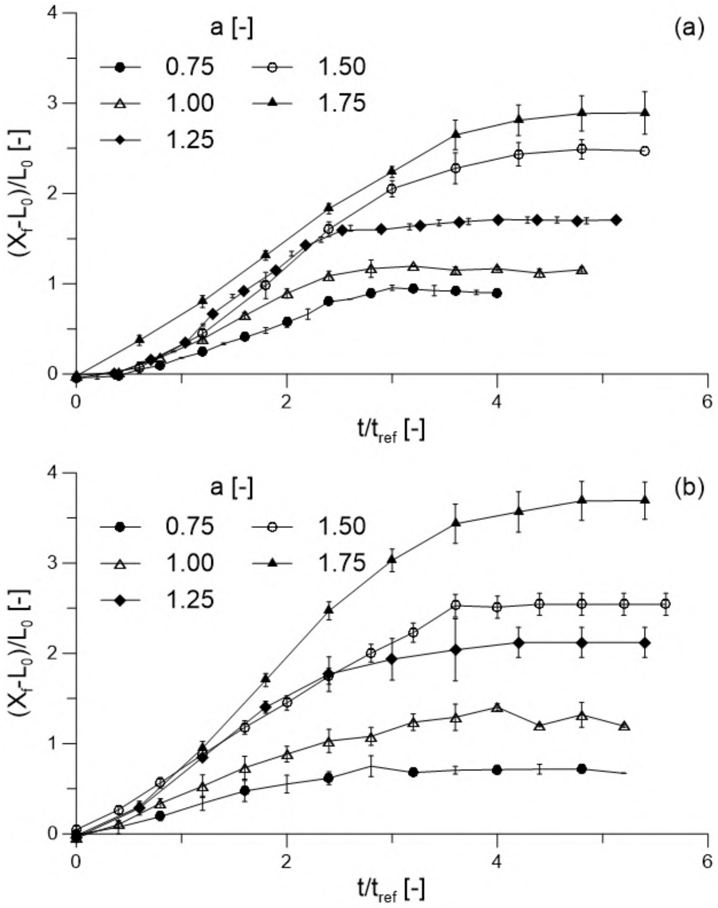

Figure 3.4: Time evolution of normalized front position for dry (*a*) and saturated cases (*b*), from [136].

the granular front decelerates and stops, while water filters through the solid phase (Fig. 3.3(d)). A comparison with tests of column collapse in dry conditions is also presented. Fig. 3.4 plots the evolution of the normalized front position $(X_f - L_0)/L_0$ as function of the normalized time t/t_{ref} for different aspect ratios in dry and saturated conditions. The evolution of the process and the run-out are very similar in dry and saturated conditions for $a \leq 1.0$. In contrast, the process is slightly faster in terms of normalized time and the run-out is longer in saturated conditions for $a > 1.0$. Overall, it is possible to identify, according to previous publications [132, 140, 141], three phases during the collapse: firstly, a transient acceleration phase of $\sim 0.8 t_{ref}$, then a constant velocity interval $\sim 2 t_{ref}$ and lastly the deceleration phase, which can last up to $\sim 6 t_{ref}$.

2.2 Set up and calibration of numerical model

A two-dimensional MPM model is set up, considering plain strain conditions. Frictional effects of the lateral boundary are neglected, and these are assumed small at the symmetry plane of the experiment. The bottom boundary is fixed (i.e., fully rough), while roller boundary conditions are applied at the other surfaces. A linear-elastic perfectly-plastic model with a Mohr-Coulomb failure criterion is used.

The MPM model applies a structured mesh with element size of $4 \cdot 10^{-3}$ m; 12 LMPs and 12 SMPs are assigned to each initially active element. A small value of local damping (0.02) is used to stabilize the results [142]. This damping is not an input of the constitutive relation, instead it is an additional force included in the momentum balance, proportional to the system unbalance force ($\mathbf{f}^{ext} - \mathbf{f}^{int}$), to the nodal velocity vector and to a damping coefficient (in this case equal to 0.02). This small damping coefficient does not significantly influence the run-out.

The influence of element size, MPs number, and local damping has been deeply discussed in previous works [143] considering dry column collapse simulated with a 1Phase approach. It was shown that mesh refinement improves the definition of the failure surface, while having a small effect on the runout. These considerations are confirmed for the 2P-DP MPM model considered in this study. Moreover, the mesh refinement impact on the computational time, since the critical time step is directly proportional to the mesh size, and more precisely to the minimal length of a element. The mesh chosen optimizes computational time and allows for a satisfactory reproduction of the experiment.

However, while in the dry case increasing the number of MPs does not improve significantly the results, with the 2P-DP approach, the use of only 3 MPs/elem sometimes leads to numerical instabilities, and better results are obtained with 12 MPs/elem. A larger number of MPs reduce the quadrature error [144] and the occurrence of elements filled with only a small number of MPs, which seems to be essential for the stability of 2P-DP MPM. A further increase of the number of MPs increases the computational cost without improving the results.

The boundary conditions for the liquid are identical to those of the solid. A simple Newtonian model is used to describe the material. In the 2P-DP MPM model, a reduced value of the bulk modulus ($2 \cdot 10^{7}$ Pa) compared to pure water

Soil density	ρ_S	2600	$[kg/m^3]$
Initial porosity	n	0.4	[-]
Friction angle	ϕ	35	[°]
Cohesion	c'	0.0	[kPa]
Young modulus	E	$1 \cdot 10^7$	$[kPa]$
Poisson's ratio	ν	0.3	[-]

Table 3.2: Material and strength parameters for SMPs in the column collapse model.

is used to speed up the calculation. A cavitation threshold is imposed in MPM to overcome numerical difficulties ("explosion" of MPs since the very beginning of the simulation), thus only positive pressures are allowed. In fact, introduction of negative pressure would require a suitable adaptation of the entire formulation to reproduce the unsaturated behavior. For instance, the mass balance equation should be consistently adapted, to account for the partially saturated state of the soil, impacting on the fluid quantities in the pores and volumetric strain evolution. The method has been extensively tested in the classical 1Phase (liquid) dam-break problem, showing good agreement with experimental results and other numerical methods [145, 146]. Following the experimental configuration, a mean diameter of $2.5 \cdot 10^{-3}$ m is used to update the intrinsic permeability and the drag force with Eq. 2.34 and Eq. 2.36. The initial porosity is set to 0.4.

Before studying the saturated conditions, a preliminary calibration of the material parameters governing the behavior of the solid phase is carried out based on dry column collapse tests. A reference height $H_0 = 0.06$ m is considered for calibration. A series of parametric analyses has been performed to calibrate the macroscopic friction angle, showing that $\phi = 35°$ gives the best results. Tab.3.2 lists the chosen set of parameters for the model. The simulation result that gives the best fit to the experimental data is illustrated in Fig. 3.5. The model based on DEM-LBM is also calibrated based on these experimental results.

2.3 NUMERICAL RESULTS

The current section presents the numerical results obtained in saturated conditions for the cases summarized in Tab.3.1. The results are analyzed in light of the experiment outcomes.

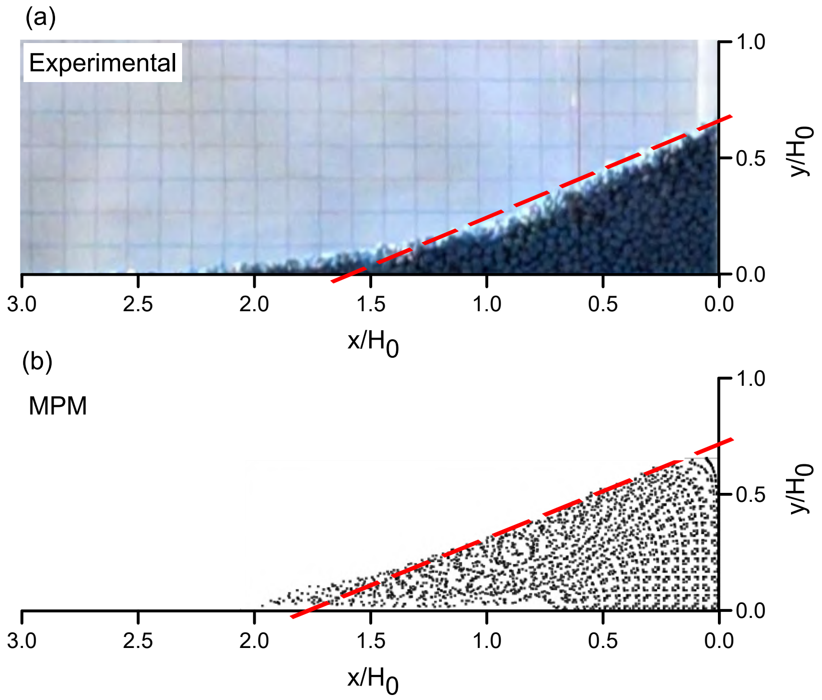

Figure 3.5: SMPs strength parameters' calibration. Final configuration of dry column collapse: experimental (a) vs. numerical results (b), adapted from [136].

2.3.1 Initialization

In the numerical model, the initial stress state is initialized during a gravity loading step in which gravity is applied while preventing horizontal displacement of both sides of the column. In Fig. 3.6(a) liquid pressure and Fig. 3.6(b)vertical effective stress are reported. The horizontal fixity on the left boundary (visible in Fig. 3.6) is then removed and the failure of the column is initiated.

2.3.2 Collapse dynamics and deposition

Figs.3.7 and 3.9 present the results obtained for the case $H_0 = 0.06$ m, which corresponds to a time scale of $t_{\mathrm{ref}} = 0.1$ s.

In Fig. 3.7 the collapse dynamic is captured by plotting SMPs displacements, using a color legend and scaling them compared to the initial column height, while LMPs are represented by blue dots. In the four normalized time instants selected it is evident that liquid and solid front are progressing in parallel, and only after $t/t_{ref} = 1$ the liquid flows out and propagates much further than the solid phase.

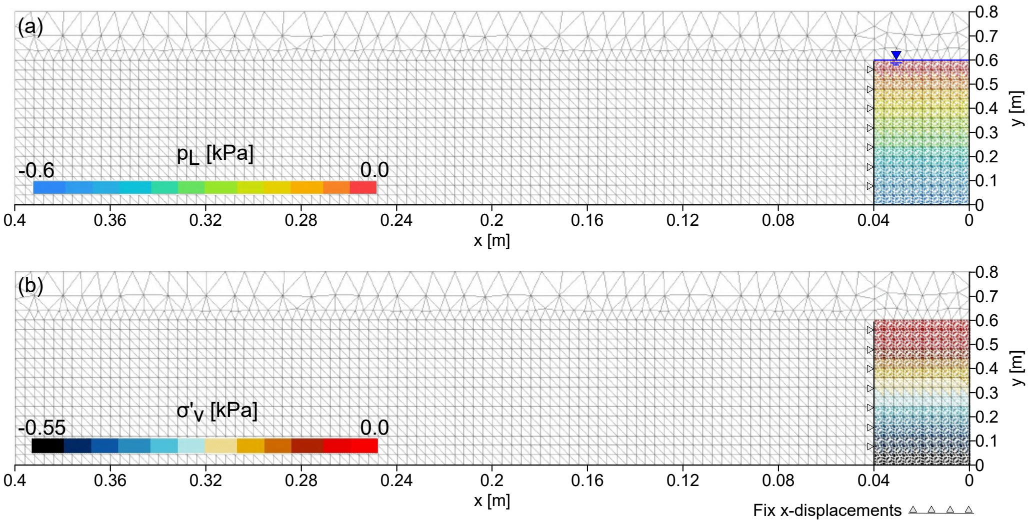

Figure 3.6: Results of the initialization phase, before column "release". Liquid pressure distribution (a) in LMPs and vertical effective stress in SMPs (b). The horizontal fixity imposed only in this phase is indicated with roller boundary symbols.

These results are analysed together with the experimental results. In fact, the selected times are very close to the experimental times of Fig. 3.3. Thus, after a first qualitative assessment, it appears that the shape of the moving soil mass resembles the experiment, apart from the top part, which is strongly influenced by the partially saturated state. For the cases $H_0 = 0.03m$, $0.05m$, and $0.07m$ ($a = 0.75$, 1.25, and 1.75, respectively) the time-evolution of the normalized solid front position is shown in Fig. 3.8 comparing numerical and experimental results. The position of the front in the numerical simulations is defined as the horizontal coordinate $X_{\mathrm{f,S}}$ overtaken by 0.5% of the total solid mass. From direct observation, the fluid front appears to be slightly ahead of the granular front in all tests. MPM correctly reproduces this behavior, see Fig. 3.8.

As previously mentioned, a comparison with a different numerical technique has been carried out during this study, using coupled DEM-LBM. The simulations based on this approach have been performed with an in-house code [147] by a colleague. The comparison with the MPM results is interesting because it helps shed light on this complex dynamic process and at the same time provide a characterization based on elements not present in a macro-mechanic continuum approach, like the MPM. In Fig. 3.9 grey points indicate the position of the solid

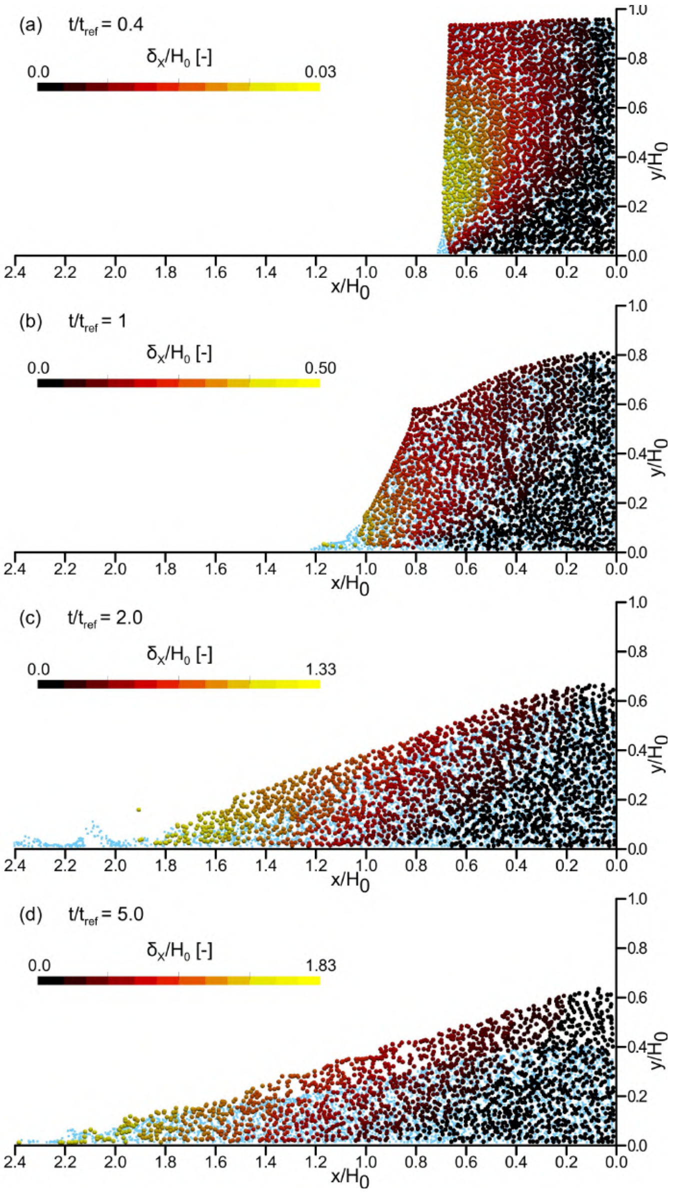

Figure 3.7: Numerical results at four time instants $t/t_{\mathrm{ref}} = 0.4; 1; 2; 5$. Blue circles indicate the position of the liquid phase (LMPs) while a colour scale is used to visualize the normalized solid displacements.

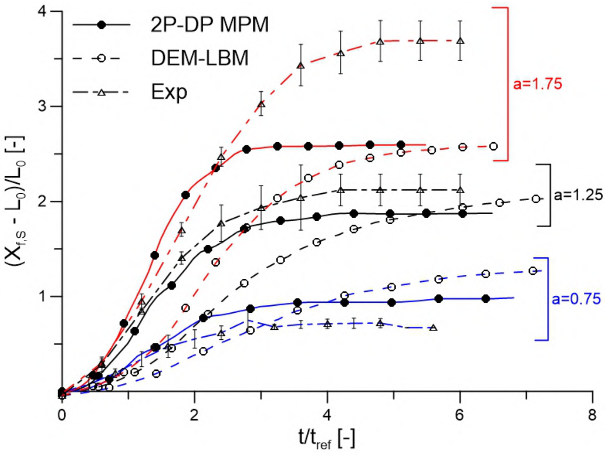

Figure 3.8: Evolution of normalized front position in time for different aspect ratios. Numerical results (holow circles for DEM-LBM and full circles for 2P-DP MPM) and experimental results (triangles) in saturated conditions, from [136].

phase (SMPs) while a colour scale is used to visualize the normalized fluid speed $v_{\mathrm{L}}/(g(H_0)^{0.5}$. The MPM model (panels *a*-*c*) predicts a faster collapse, with higher front velocity and, as previously mentioned, no clear separation between granular and liquid fronts. In the DEM-LBM model (panels *d*-*f*), the collapse develops more slowly and the formation of a granular front is recognizable up to $t/t_{ref} = 5$. After this time, the water slowly flows out of the soil. The difference in collapse speed can be explained as due to three simultaneous effects. Firstly, DEM-LBM is more dissipative, because it resolves the energy losses due to granular collisions. These are not directly considered in the Mohr-Coulomb model applied in 2P-DP MPM [148]. Second, DEM-LBM can account for negative pore pressures when the granular skeleton dilates. Conversely, in the 2P-DP MPM formulation the excess pore pressure can only be positive due to numerical difficulties. Thus, in the pure-continuum model the changes in pore pressure can promote granular mobility, but cannot reduce it. Since granular columns in loose packing are considered here, this effect must be limited. Third, DEM-LBM considers the confining effect of the lateral walls, but this is minor compared to other contributes.

The phase transition aspect can now be considered. In the experiments, after gate opening, the granular material collapses and water tends to flow out of the sample. At the same time, the top part of the column desaturates. When the granular material mobilizes, the grains closer to the free boundary accelerate, with the superficial layer of material moving towards fluidized conditions. The change

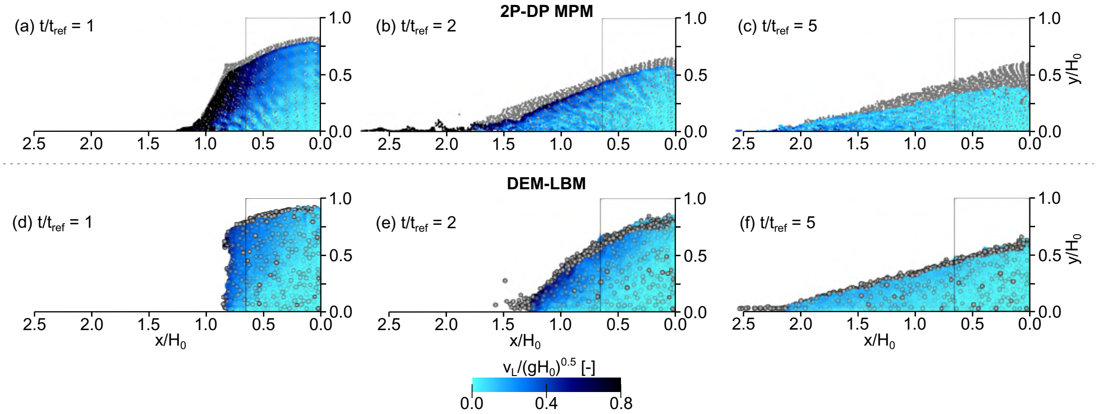

Figure 3.9: Numerical results at three time instants $t/t_{\mathrm{ref}} = 1; 2; 5$. Grey circles indicate the position of the solid phase (SMPs) while a colour scale is used to visualize the normalized fluid speed $v_{\mathrm{L}}/(g(H_0)^{0.5}$, from [136].

of state in the medium can be observed thanks to the phase status definition. It appears as a decrease of the mean effective stress due to the lack of confinement at the top and lateral boundary of the column. At these locations, the effective porosity increases, bringing (eventually) the solid to the fluidized state. In this state, soil effective stress is zero, and its presence in the fluid phase increases the apparent viscosity, according to Eq. 2.37. The boundary between the fluidized and non-fluidized state is $n_{\max}$, which is a model parameter. Fig. 3.10 shows the phase status at SMPs at $t/t_{\mathrm{ref}} = 2$ for $n_{\max} = 0.5$ and $n_{\max} = 0.8$. This parameter affects the soil profile slightly, but does not seem to be relevant for the run-out and collapse dynamics. Concerning deposition, Fig. 3.11 shows the final shape of the deposit for different initial column heights obtained with MPM (red-yellow dots) and DEM (gray circles). The black line indicates the experimental profile. The final shape of the solid deposit in MPM is approximately a straight line, while in DEM-LBM it is convex. This effect is due to the discrete description of the granular assembly in DEM-LBM. There is a relatively good agreement between the two numerical models.

The discrepancies with the experimental results are mainly due to the behavior of the top part of the column. This is in partially saturated conditions, and not completely dry as assumed by the numerical models. In the experiments, some grains and fluid remain attached to the lateral walls due to the fluid surface tension. These are recognized by the edge detection algorithm. This effect is pronounced only within the area covered by the initial position of the column, which is shown

(a) n_{max}=0.5

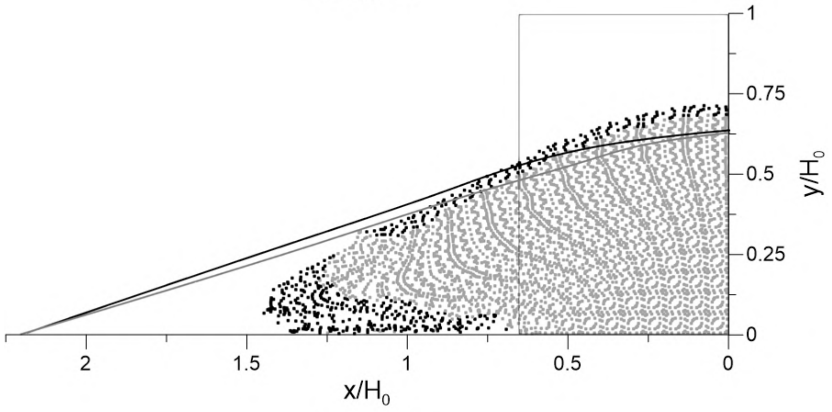

(b) n_{max}=0.8

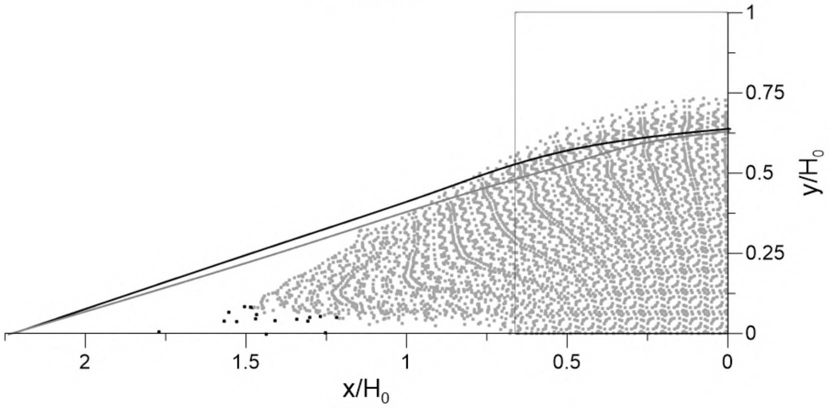

Figure 3.10: Phase status of SMPs at $t/t_{\mathrm{ref}} = 2$ in case (*a*) $n_{\max} = 0.5$ and (*b*) $n_{\max} = 0.8$. Black points are in fluidized state, grey points are in solid state. The grey and black lines indicate the final deposition for $n_{\max} = 0.5$ and $n_{\max} = 0.8$ respectively, from [136].

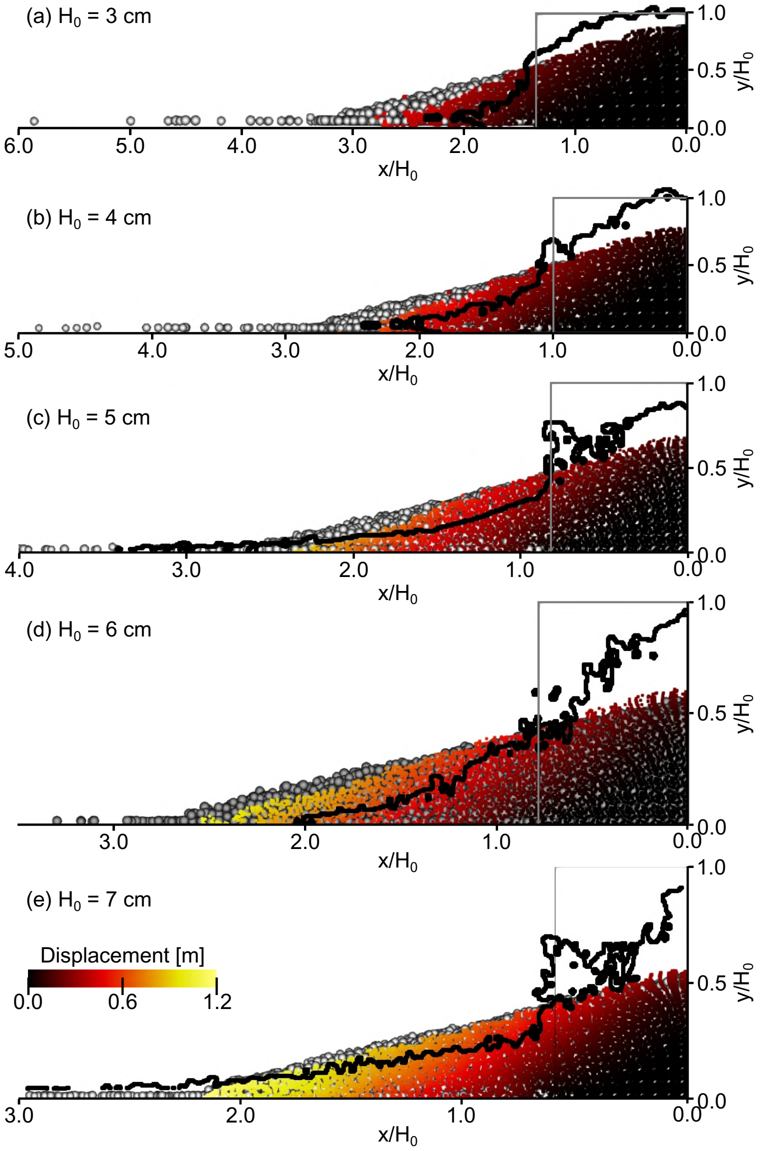

Figure 3.11: Final configuration of the saturated column collapses for $H_0 = 0.03, 0.04, 0.05, 0.06, 0.07\ \mathrm{m}$ (red or yellow dots stands for SMPs, gray circles for DEM particles and the black line is the experimental profile), from [136].

in Fig. 3.11 with a hollow rectangle. Outside of this area, the surface detection is fair.

2.3.3 DRAG FORCE IMPACT ON PROPAGATION

In multiphase continuum methods the definition of the drag force is an essential ingredient of the model. The ratio between the quadratic and the linear term in Eq. 2.34 is proportional to a modified particle Reynolds number $\mathrm{Re_p}$ [139] defined as:

$$\frac{f_2}{f_1} \approx \mathrm{Re_p} = \frac{D\rho_\mathrm{L}||\mathbf{v}_\mathrm{L} - \mathbf{v}_\mathrm{S}||}{\nu_\mathrm{m}} \tag{3.3}$$

For low $\mathrm{Re_p}$, the quadratic term f_2 is negligible compared to the linear term f_1. In the following, the reference velocity for the solid phase is assumed $v_\mathrm{S,ref} = \sqrt{g'H_0}$, which is a reasonable reference value for the solid front velocity as shown in [135]. The reference velocity for the liquid phase is assumed $v_\mathrm{L,ref} = \sqrt{gH_0}$, which is the free fall velocity. Note that $v_\mathrm{L,ref} - v_\mathrm{S,ref}$ does not represent any true relative velocity between phases during the collapse, but it is considered as a representative parameter of the solid-fluid interaction.

In order to explore the importance of the quadratic term in Eq. 2.34 we performed parametric analyses increasing the size of the column up to a factor of 100 while keeping $a = 1.5$. The liquid viscosity ν_m is varied between 0.001 Pa·s and 0.1 Pa·s and the grain size D between 0.0025 m and 0.25 m while keeping $\rho_\mathrm{L} = 1000$ kg/m^3 and $\rho_\mathrm{S} = 2600$ kg/m^3.

Fig. 3.12 illustrates the results for two different values of the particle Reynolds number $\mathrm{Re_p} = 4 \cdot 10^3$ and $\mathrm{Re_p} = 4 \cdot 10^5$, showing the position of LMPs and SMPs at different time instants. The results obtained using the linear and the quadratic term in Eq. 2.34 are shown in panels (*a-f*). Those obtained using only the linear term are shown in panels (*g-l*).

In the case $\mathrm{Re_p} = 4 \cdot 10^3$, shown in Fig. 3.12 (*a-c*,*g-i*), there is no clear separation between fluid and solid fronts. Neglecting the quadratic term of the drag force does not significantly alter the results. In contrast, for $\mathrm{Re_p} = 4 \cdot 10^5$, Fig. 3.12 (*d-f*,*j-l*), the fluid can easily flow out of the mixture, and in this case the effect of the quadratic term is significant.

The results of the parametric analyses showed that the importance of term f_2 in Eq. 2.34 becomes significant for the relative position between fluid and solid front approximately for $\mathrm{Re_p} > 4 \cdot 10^4$. This means that an appropriate formulation of the drag force is crucial to capture correctly the solid-fluid interaction in these phenomena, especially for high Reynolds numbers.

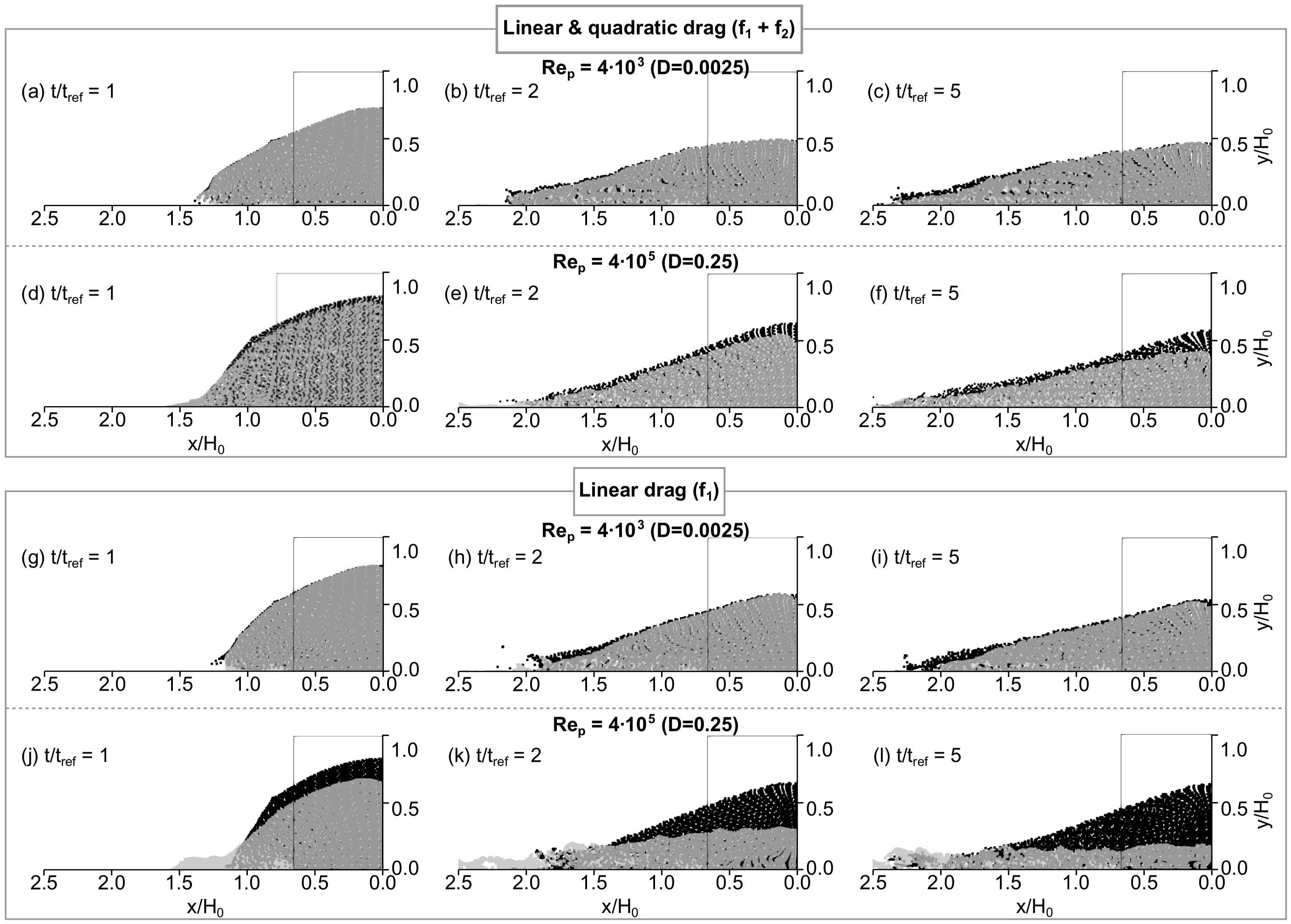

Figure 3.12: MPM simulations: Position of LMPs (grey) and SMPs (black) at different time instants using linear and quadratic terms in Eq. 2.34 (*a-f*) or only linear term (*g-i*). Comparisons for $Re_\mathrm{p} = 4 \cdot 10^3$ (*a-c*) and (*g-i*) and $Re_\mathrm{p} = 4 \cdot 10^5$ (*d-f*) and (*j-l*), from [136].

3 Levee failure induced by rapid drawdown

This section considers the effect on the stability of a levee or dam of a rapid decrease of water level, occurring in the river or reservoir retained by the considered levee. The treatment of this engineering problem with the 2P-DP formulation is an evident simplification, since the partially saturated state of soil, its variations during the drawdown and the impact on the flow process are not fully captured. It is a preliminary study, to better understand the importance and the practical consequences of developing an MPM unsaturated formulation, as presented in the following Chapter.

3.1 Preliminary conventional analysis

The geometry of the levee section is presented in Fig. 3.13(a). The levee is 4m high, with slope inclinations equal to 28° and 32°, respectively on the riverside and the landside. In addition, the initial and final river levels are indicated in the same figure. The initial water level in the reservoir is $H = 3m$ and it is decreased to $H = 0m$ in 30 minutes. The decrease is linear, as visible in the hydrograph in Fig. 3.13(b).

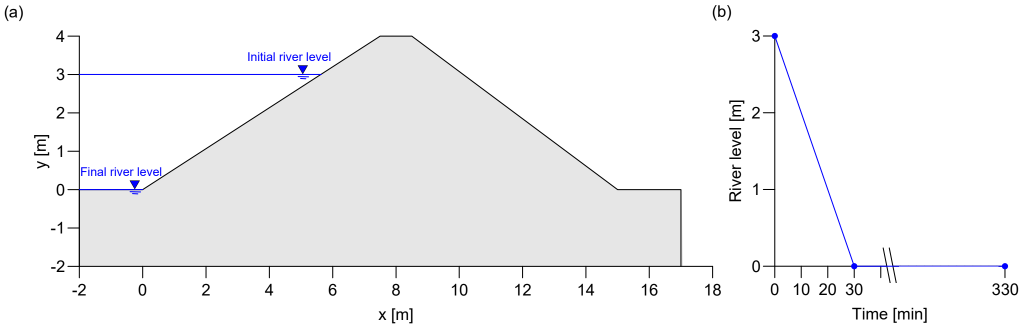

Figure 3.13: Levee section considered for the drawdown analysis(a), with indication of initial and final water levels. Hydrograph applied in the simulations(b).

The stability of the earth structure after rapid drawdown is customarily investigated coupling transient seepage analyses and LEM or applying a $phi-c$ reduction approach in finite element models. In both models the constitutive model adopted is a simple Mohr-Coulomb with strength parameters friction angle $\phi = 28°$ and effective cohesion $c' = 2kPa$. In Fig. 3.14 the results obtained with LEM using

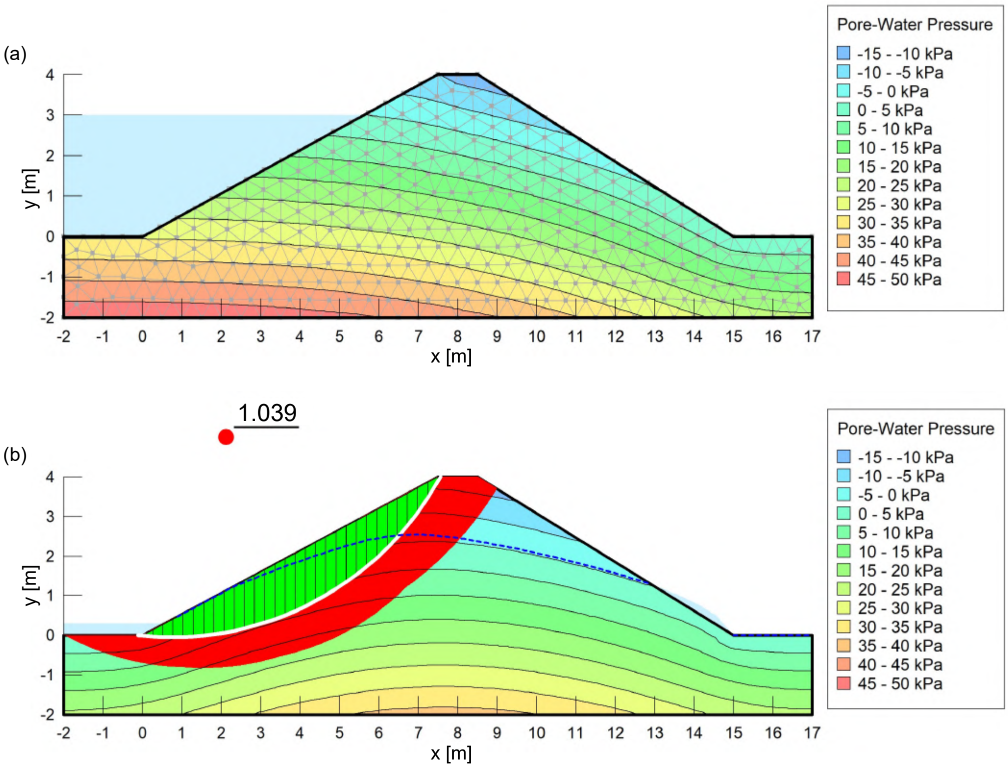

Figure 3.14: Drawdown stability analysis. (a) Pore pressure distribution prior to the drawdown, (b) Pore pressure distribution at 27 minutes, slip surface with minimum factor of safety $FS = 1.039$ and safety map.

the software *Geostudio* [46] are presented. The initial piezometric line and the pore pressure distribution are determined with a steady state seepage analysis, considering saturated hydraulic conductivity $K_{sat} = 4 \cdot 10^{-6} m/s$. The mesh for the seepage analysis is made with triangular elements of edge size equal to 0.5m. Fig. 3.14(a) shows the initial pore pressure distribution, before the drawdown. In the next phase, the water level is decreased linearly to $H = 0$ in 30 minutes and the pore pressure distribution is computed with a transient seepage analysis. At the end of the drawdown, the Bishop method is applied to determine the safety factor, which is 1.039 at 27 minutes (Fig. 3.14(b)). The slope is at the limit of static equilibrium, sensitive to instability mechanisms due to a minimal subsequent increase in solicitation or resistance reduction. Fig. 3.15 shows the results obtained with the FEM code Plaxis2D [149] (just the internal slope is depicted). The $phi - c$ reduction method is applied at the end of the seepage analysis and provide a safety factor of $FS = 0.987$. With this method the factor of safety correspond to the strength reduction factor SRF which is defined as in Eq. 3.4

$$SRF = \left(\frac{tan\phi'}{tan\phi'_f}\right) = \left(\frac{c'}{c'_f}\right) \tag{3.4}$$

where ϕ'_f and c'_f are the soil parameters at "failure". In this situation, the numerical FEM solution doesn't converge anymore.

The displacement contour indicates the potential sliding surface, but the calculated maximum displacement of 12mm shouldn't be considered representative of any realistic condition of failure. The advantage of FEM over LEM is that the sliding surface is a result of the analysis and does not have to be specified a priori. These methods provide an estimate of the safety factor, and the sliding mechanism but do not give any information on the displacements. To evaluate the failure process, the 2Phase double-point approach can be applied as shown in the next section.

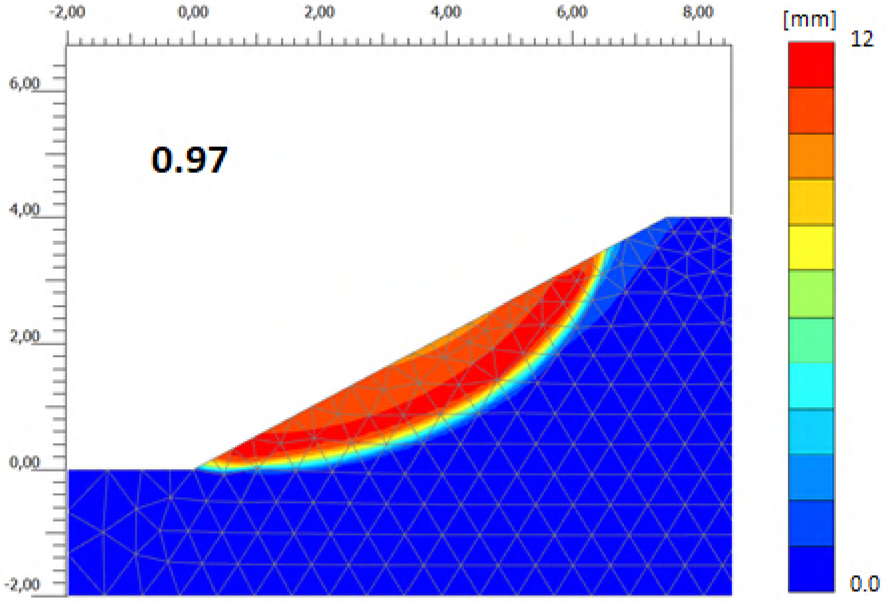

Figure 3.15: Drawdown stability analysis with FEM and $phi - c$ reduction method, from [137].

In order to reduce the computational cost, only the river-side slope is considered. The geometry and discretization of the problem are shown in Fig. 3.16. The mesh is realized with linear triangular elements. The initial number of MP per element is: 3 LMPs and 3 SMPs for the saturated soil area, 3 LMPs in the free water area and 3 SMPs in the dry soil area. The lower boundary is fixed for the solid phase, and horizontal displacements are prevented at the lateral boundary. All boundaries are impermeable for the liquid phase. The material parameters are summarized in Tab.3.3. The water level is assumed initially horizontal and stresses are initialized with a quasi-static gravity loading phase. The drawdown is simulated removing progressively the LMPs in the free water area in 5 load steps reaching H=0m in 30 minutes, then the simulations proceeds for 5 hours to visualize the evolution of displacements. During these 5 hours the LMPs keep to be removed in front of the slope, to maintain the outflow and the liquid pressure to zero on the slope border, to mimic a potential seepage face condition.

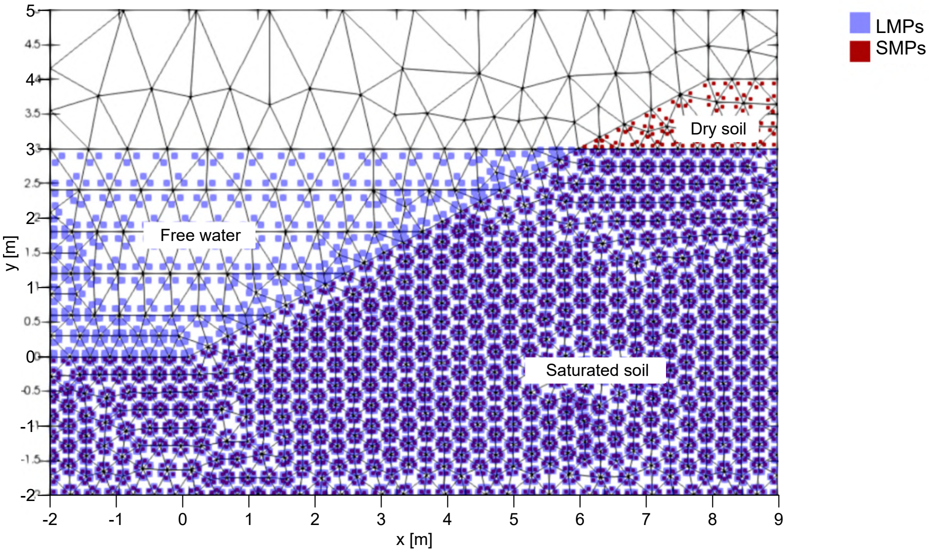

Figure 3.16: Geometry and discretization of the MPM model for the drawdown (displacements based) analysis, from [137].

Soil density	ρ_S	2650	$[kg/m^3]$	Liquid density	ρ_L	1000	$[kg/m^3]$
Porosity	n	0.4	[-]	Liquid Bulk modulus	K_L	$8 \cdot 10^4$	$[kPa]$
Friction angle	ϕ	28	[°]	Liquid dynamic viscosity	μ_L	$1 \cdot 10^{-6}$	$[kPa \cdot s]$
Cohesion	c'	2	[kPa]	Intrinsic permeability	k	$4.08 \cdot 10^{-12}$	$[\mathrm{m}^2]$
Young modulus	E	$3 \cdot 10^4$	$[kPa]$				
Poisson's ratio	ν	0.3	[-]				

Table 3.3: Material and strength parameters for the 2P-DP drawdown analysis.

3.3 RESULTS

Fig. 3.17 shows the displacement of SMPs and the position of LMPs at different time instants. At the beginning of the drawdown the displacements are very small, the failure surface begins to develop when the water level is lowered at 0.6m and at t=26.7min the maximum superficial displacement is 0.18m. The slope rapidly stabilizes at a new deformed configuration: at t=33.3min the maximum displacement is only 0.20m, and after 5 hours it reaches the value of 0.21m. The shape of the failure surface agrees well with the FEM results. The MPM results show that in this example, seepage due to water drawdown induces the development of a failure surface; however, the displacements remain relative small and a new stable configuration is reached. Different scenarios can be investigated with this approach and parametric analyses can be performed. For example, decreasing the friction angle to 24°, the factor of safety obtained with LEM at the end of the drawdown reduces to 0.93. In this case, the failure surface develops earlier and the maxim displacement reaches 0.60m at the end of the simulation (Fig. 3.18). In this example, the 2P-DP MPM analysis, shows how a safety factor lower than 1 can lead to limited displacements of the slope that will reach a new final configuration without severely compromising the ability to absolve its function in the short term. Different scenarios could be investigated modifying the geometry and mechanical behavior of the soil, thus offering valuable results for risk assessment. However, in terms of limitation of the 2P-DP formulation, it emerges that the lack of suitable hydraulic boundary conditions and a description of the unsaturated soil behavior are limiting the capability of reproduction. Evolution of hydraulic and mechanical parameters are not fully captured, especially considering the importance of describing the unsaturated state for water retention earth structures. These considerations prepare the ground for the development of an unsaturated formulations object of the following chapter.

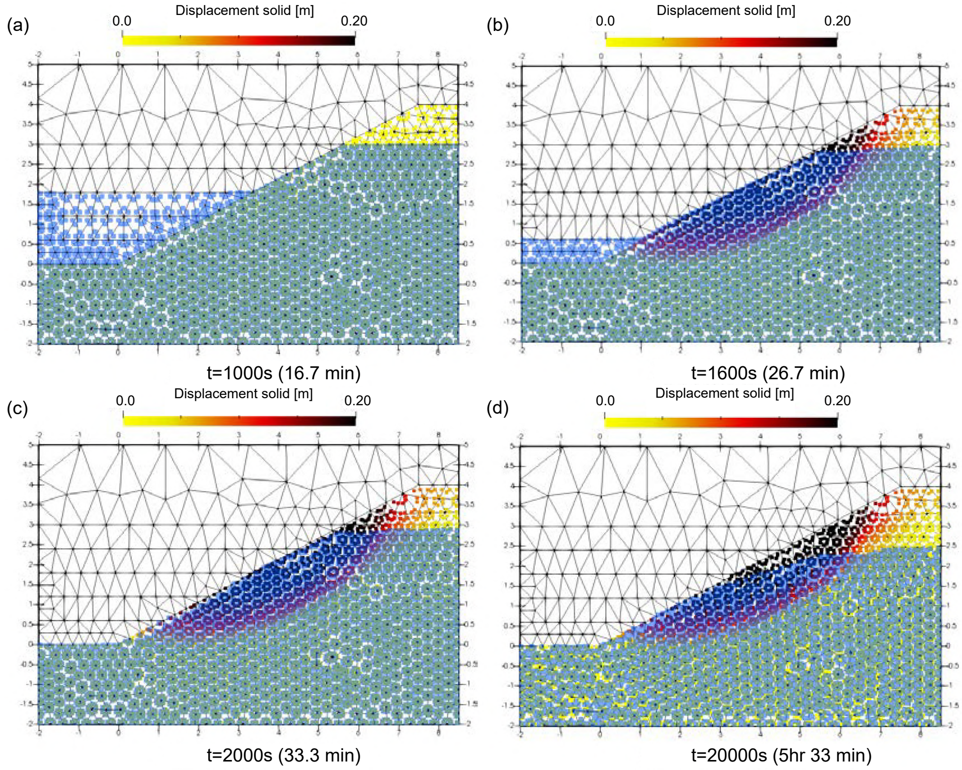

Figure 3.17: Solid displacements at different time instants during drawdown. LMPs are represented by blue dots, from [137].

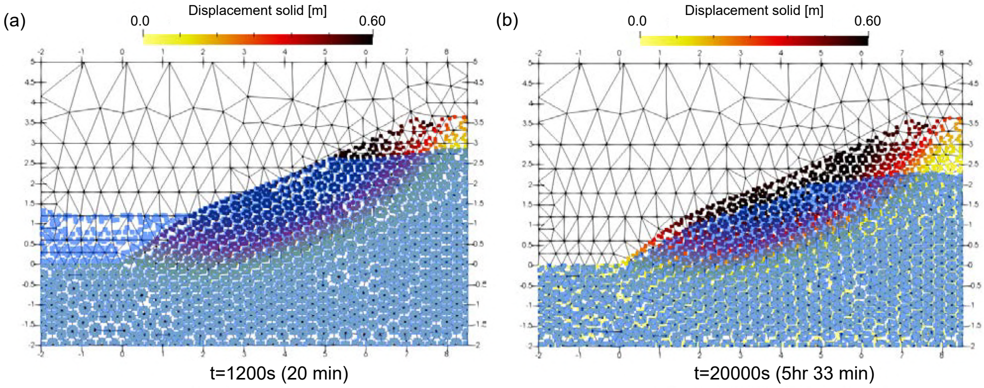

Figure 3.18: Solid displacement for $\phi = 24°$. LMPs are represented by blue dots, from [137].

4

Developing a 2Phase Single Point MPM formulation for unsaturated soil

1 INTRODUCTION

This chapter is focused on the 2Phase Single Point formulation developed during this thesis work. After the main hypothesis, the governing equations are presented. The innovative aspect of this formulation is the implementation of transient hydraulic boundary conditions. Validation with 1D and 2D cases is presented. Lastly, a preliminary study about numerical stability in unsaturated conditions is introduced. The contents of this chapter refer to three papers coauthored by the thesis author [115, 116, 150].

2 GOVERNING EQUATIONS

In the formulation here presented, named *2Phase with suction*, the following assumptions are adopted:

1. Gas pressure is neglected ($p_G = 0$)
2. Gas density is negligible compared to liquid and solid ones ($\rho_G \approx 0$)
3. Compressibility of solid grains is negligible compared to solid skeleton one ($\rho_S \approx 0$)

4. Isothermal conditions.

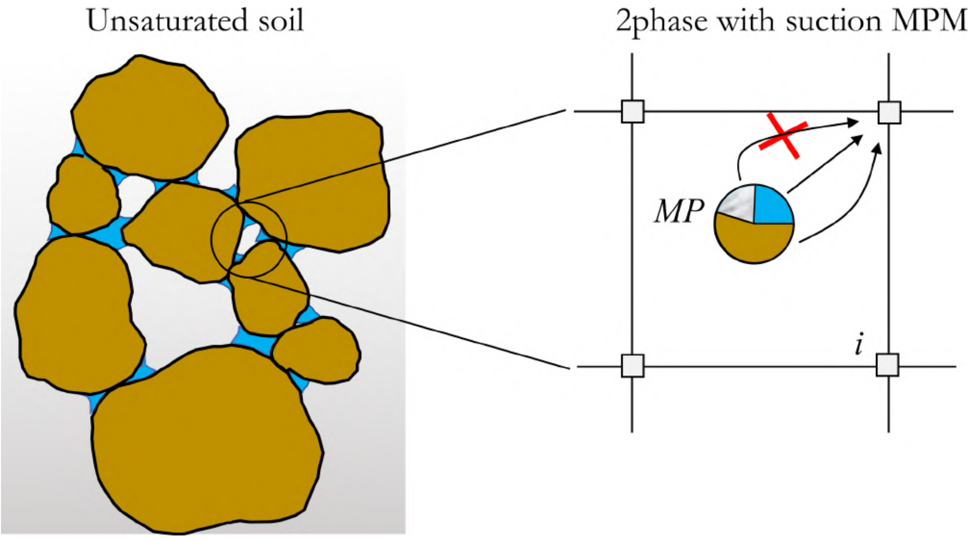

Figure 4.1: Unsaturated soil schematization in the 2Phase with suction MPM formulation. MP stands for Material Point while i stands for node.

2.1 MOMENTUM BALANCE EQUATIONS

The formulation is derived considering dynamic momentum balance of the liquid phase, dynamic momentum balance of the mixture, and mass balances and constitutive relationships of both phases involved (i.e. solid and liquid). All dynamic terms are taken into account; acceleration of the solid skeleton $\mathbf{a}_\mathrm{S}$ and acceleration of the pore liquid $\mathbf{a}_\mathrm{L}$ are the primary unknowns.

Unsaturated conditions are accounted, considering that the liquid phase does not entirely fill the voids. The balance equations of gas phase are neglected, thus the presented formulation can be considered 2Phase and is an extension of the one presented in [97] and [113]. The idealization behind this formulation is presented in Fig. 4.1. The momentum balance of the liquid phase per unit of liquid volume is given in Eq. 4.1

$$\rho_\mathrm{L}\mathbf{a}_\mathrm{L} = \nabla p_\mathrm{L} - \mathbf{f}_\mathrm{L}^\mathrm{d} + \rho_\mathrm{L}\mathbf{g} \tag{4.1}$$

where ρ_L is the liquid density, $\mathbf{f}_\mathrm{L}^\mathrm{d}$ is the drag force which accounts for solid-fluid interaction, p_L is the liquid pressure and $\mathbf{g}$ is the gravity vector.

The flow is considered laminar and stationary in the slow velocity regime. Hence, the drag force is governed by Darcy's law (Eq. 4.2)

$$\mathbf{f}_{\mathrm{L}}^{\mathrm{d}} = \frac{n_{\mathrm{L}}\mu_{\mathrm{L}}}{\kappa_{\mathrm{L}}}\left(\mathbf{v}_{\mathrm{L}} - \mathbf{v}_{\mathrm{S}}\right) \tag{4.2}$$

where μ_{L} is the dynamic viscosity of the liquid, κ_{L} is the liquid intrinsic permeability, n_{L} is the liquid volumetric fraction and $\mathbf{v}_{\mathrm{L}}$, $\mathbf{v}_{\mathrm{S}}$ are the absolute liquid and solid velocities respectively. The isotropic intrinsic permeability of the liquid κ_{L} can also be expressed in terms of Darcy permeability, or hydraulic conductivity, k_{L} (Eq. 4.3).

$$\kappa_{\mathrm{L}} = k_{\mathrm{L}}\frac{\mu_{\mathrm{L}}}{\rho_{\mathrm{L}}g} \tag{4.3}$$

The mixture dynamic momentum conservation can be written as Eq. 4.4,

$$n_{\mathrm{S}}\rho_{\mathrm{S}}\mathbf{a}_{\mathrm{S}} + n_{\mathrm{L}}\rho_{\mathrm{L}}\mathbf{a}_{\mathrm{L}} = \mathrm{div}(\sigma) + \rho_{\mathrm{m}}\mathbf{g} \tag{4.4}$$

where ρ_{S} is the solid grain density, n_{S} is the volumetric concentration ratio of solid, and $\rho_{\mathrm{m}} = n_{\mathrm{S}}\rho_{\mathrm{S}} + n_{\mathrm{L}}\rho_{\mathrm{L}}$ is the density of the mixture. Note that $n_{\mathrm{S}} = 1 - n$ and $n_{\mathrm{L}} = S_L n$, where n is the porosity of the solid skeleton and S_L is the degree of saturation.

σ is the total stress tensor, which can be computed with the Bishop's effective stress equation for unsaturated soils and has the form of Eq. 4.5, where χ is an effective stress parameter, here assumed equal to S_L, and $\mathbf{m}$ is the unit vector, equal to $(1\ 1\ 1\ 0\ 0\ 0)^{\mathrm{T}}$ in 3D. In this thesis, stresses and pressures are positive for tension, thus suction is equal to p_L.

$$\sigma = \sigma' + \chi p_L \mathbf{m} \tag{4.5}$$

2.2 Mass balance equations

The mass conservation of the solid phase is expressed as given in Eq. 4.6,

$$\frac{\partial(n_{\mathrm{S}}\rho_{\mathrm{S}})}{\partial t} + \mathrm{div}(n_{\mathrm{S}}\rho_{\mathrm{S}}\mathbf{v}_{\mathrm{S}}) = 0 \tag{4.6}$$

where $\mathbf{v}_{\mathrm{S}}$ is the velocity of the solid phase.

Similarly, the conservation of liquid mass can be written as Eq. 4.7,

$$\frac{\partial(n_{\mathrm{L}}\rho_{\mathrm{L}})}{\partial t} + \mathrm{div}(n_{\mathrm{L}}\rho_{\mathrm{L}}\mathbf{v}_{\mathrm{L}}) = 0 \tag{4.7}$$

where $\mathbf{v}_{\mathrm{L}}$ is the (true) velocity of the liquid phase

The material derivative with respect to the solid can be expressed as

$$\frac{\mathrm{D}^{\mathrm{S}}(\bullet)}{Dt} = \frac{\partial(\bullet)}{\partial t} + \mathbf{v}_{\mathrm{S}}\nabla(\bullet) \tag{4.8}$$

When considering incompressible solid grains and disregarding the spatial variations in density and porosity, the expressions for the conservation of mass of the solid and the liquid reduce to Eqs. 4.9 and 4.10 respectively.

$$\frac{\mathrm{D}^{\mathrm{S}}n_{\mathrm{S}}}{\mathrm{D}t} + n_{\mathrm{S}}\mathrm{div}(\mathbf{v}_{\mathrm{S}}) = 0 \tag{4.9}$$

$$\frac{\mathrm{D}^{\mathrm{S}}\left(\rho_{\mathrm{L}}n_{\mathrm{L}}\right)}{\mathrm{D}t} = (\mathbf{v}_{\mathrm{S}} - \mathbf{v}_{\mathrm{L}})\nabla(n_{\mathrm{L}}\rho_{\mathrm{L}}) - n_{\mathrm{L}}\rho_{\mathrm{L}}\mathrm{div}(\mathbf{v}_{\mathrm{L}}) \tag{4.10}$$

Including Eq. 4.9 into Eq. 4.10, taking into account the definitions of liquid volumetric concentration ratios in terms of porosity and degree of saturation, $n_L = S_L n$, and rearranging terms give Eq. 4.11

$$n\frac{\mathrm{D}^{\mathrm{S}}\left(\rho_{\mathrm{L}}S_{\mathrm{L}}\right)}{\mathrm{D}t} = \mathrm{div}\left[\rho_{\mathrm{L}}nS_{\mathrm{L}}(\mathbf{v}_{\mathrm{S}} - \mathbf{v}_{\mathrm{L}})\right] - \rho_{\mathrm{L}}S_{\mathrm{L}}\mathrm{div}(\mathbf{v}_{\mathrm{S}}) \tag{4.11}$$

Finally, the material derivative in Eq. 4.11 is solved assuming liquid pressure as state variable, which yields to Eq. 4.12.

$$n\left(S_{\mathrm{L}}\frac{\partial\rho_{\mathrm{L}}}{\partial p_{\mathrm{L}}} + \rho_{\mathrm{L}}\frac{\partial S_{\mathrm{L}}}{\partial p_{\mathrm{L}}}\right)\frac{\mathrm{D}^{\mathrm{S}}p_{\mathrm{L}}}{\mathrm{D}t} = \mathrm{div}\left[\rho_{\mathrm{L}}nS_{\mathrm{L}}(\mathbf{v}_{\mathrm{S}} - \mathbf{v}_{\mathrm{L}})\right] - \rho_{\mathrm{L}}S_{\mathrm{L}}\mathrm{div}(\mathbf{v}_{\mathrm{S}}) \tag{4.12}$$

The derivative of liquid density with respect of pressure is given by the state equation of liquid, Eq. 4.13, where K_L is the Bulk modulus of the liquid; while the derivative of the degree of saturation is given by the soil-water retention curve (SWRC). Eq. 4.13 states again the weakly compressible behavior of the liquid. This assumption is made to mitigate numerical instabilities arising at the incompressible limit. These numerical instabilities/inaccuracies are related to the low-order interpolation functions used in the present MPM formulation. The shape of Eq. 4.12 makes it look like the storage term accounts only for water compressibility and variation of degree of saturation with respect to the liquid pressure. Actually there is a third term, accounting for the compressibility of the solid, which is introduced in the final equation when the mass balance of the solid Eq. 4.9 is included into Eq. 4.10.

$$\frac{\partial \rho_{\mathrm{L}}}{\partial p_{\mathrm{L}}} = -\frac{\rho_L}{K_L} \tag{4.13}$$

When spatial variations of fluid mass in the soil are negligible, i.e $\nabla(\rho_L n S_L) \approx 0$, Eq. 4.12 can be simplified in Eq. 4.14

$$n\left(S_{\mathrm{L}}\frac{\partial \rho_{\mathrm{L}}}{\partial p_{\mathrm{L}}} + \rho_{\mathrm{L}}\frac{\partial S_{\mathrm{L}}}{\partial p_{\mathrm{L}}}\right)\frac{\mathrm{D}^{\mathrm{S}} p_{\mathrm{L}}}{\mathrm{D}t} = \rho_{\mathrm{L}} n S_{\mathrm{L}} \mathrm{div}(\mathbf{v}_{\mathrm{S}} - \mathbf{v}_{\mathrm{L}}) - \rho_{\mathrm{L}} S_{\mathrm{L}} \mathrm{div}(\mathbf{v}_{\mathrm{S}}) \tag{4.14}$$

This simplified form has been adopted also by [113]. [115, 151] showed that the use of Eq. 4.14 gives reasonably good results for applications where the degree of saturation varies in a limited range and the derivative of the SWRC is small. The effect of the gradient of advective fluxes in the fluid mass balance equations is discussed in Sec. 2.2.1 which is complemented with an illustrative example.

2.2.1 Discussion about gradient of advective fluxes in the mass balance equation

Eq. 4.11 can be written as Eq. 4.15, by expanding the gradient of the advective flux term.

$$n\frac{\mathrm{D}^S(\rho_L S_L)}{\mathrm{D}t} + \nabla(\rho_L S_L n)\cdot(\mathbf{v}_L - \mathbf{v}_S) + \rho_L S_L n \nabla\cdot\mathbf{v}_L + \rho_L S_L (1-n)\nabla\cdot\mathbf{v}_S = 0 \tag{4.15}$$

The first addend is related to the liquid mass change as a result of pressure and degree of saturation variation in time. All other terms explain the variation of liquid mass as a result of the liquid inflow/outflow gradients resulting from different mechanisms. In particular, the second term in Eq. 4.15 describes the variation of the liquid mass induced by a flow triggered by the fluid mass gradient; the third term describes the variation of liquid mass due to the divergence of the fluid velocity (equivalent to a volumetric deformation of the fluid); and the fourth term describes the variation of liquid mass due to the divergence of the solid velocity (equivalent to a volumetric deformation of the solid skeleton).

The mass balance equation is solved at the MP level, where the computation of the last two terms of Eq. 4.15 is straightforward because nodal velocities are already available during the traditional computational cycle. In contrast, the evaluation of the fluid mass gradient requires the additional step of mapping the quantity $\rho_L S_L n$ to the nodes and then calculate the gradient at the MP [71]. This is relatively simple and does not significantly increase the computational cost. The gradient of fluid mass can be calculated as Eq. 4.16. While the spatial gradient of liquid density ($\nabla \rho_L$) and porosity (∇n) can be assumed negligible in most cases, the gradient of the degree of saturation depends on the pressure gradient and the SWRC. The importance of the last term of Eq. 4.16 increases with pressure gradient and $\partial S_L / \partial p_L$.

$$\nabla(\rho_L S_L n) = S_L n \nabla \rho_L + S_L \rho_L \nabla n + n \rho_L \nabla S_L \tag{4.16}$$

To visualize the effect of this term, the evolution of suction in a 1m soil column during an infiltration test is considered. For $t = 0$, an initial suction s_0 is applied along the column. For $t > 0$, zero suction is imposed at the top boundary while the bottom is impervious. Gravity is neglected. The soil permeability is constant and the SWRC is linear (Eq. 4.27). Under these assumptions, an analytical expression that describes the evolution of the normalized suction along the column with time can be derived from the mass balance equation of the liquid following [152]

$$\frac{s}{s_0} = \frac{4}{\pi} \sum_{j=1}^{\infty} \frac{(-1)^{j-1}}{2j-1} \cos\left[(2j-1)\frac{\pi}{2}\frac{y}{h}\right] e^{-(2j-1)^2 T \pi^2/4} \tag{4.17}$$

The non-dimensional time factor T (Eq. 4.18) is defined as a function of the infiltration coefficient C_i (Eq. 4.19) and the drainage length (h).

$$T = \frac{C_i t}{h^2} \tag{4.18}$$

Solid density $[kg/m^3]$	ρ_S	2700
Liquid density $[kg/m^3]$	ρ_L	1000
Porosity [-]	n	0.3
Liquid bulk modulus $[kPa]$	K_L	80000
Liquid dynamic viscosity $[kPa \cdot s]$	μ_L	$1 \cdot 10^{-6}$
Intrinsic permeability liquid $[m^2/s]$	κ_L	$5 \cdot 10^{-11}$

Table 4.1: Material parameters for 1D infiltration example with applied pressure.

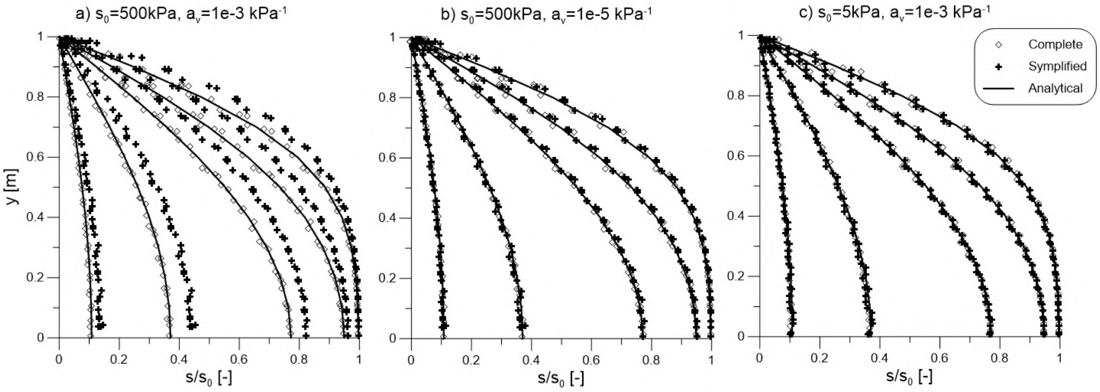

Figure 4.2: Evolution of normalized suction with depth. Comparison between numerical and analytical formulations.

$$C_i = \frac{k}{n\rho_L g\left(\frac{S_L}{K_L} + \frac{\partial S_L}{\partial p_L}\right)} = \frac{k}{n\rho_L g\left(\frac{S_L}{K_L} + a_v\right)} \tag{4.19}$$

Figure 4.2 compares the results obtained with the complete mass balance equation (Eq. 4.12, circles) and with the simplified mass balance equation (Eq. 4.14, cross symbol) considering different values of initial suction s_0 and $\partial S_L/\partial p_L = a_v$. For $s_0 = 500kPa$ and $a_v = 1 \cdot 10^{-3}$ (Fig. 4.2a) the simplified mass balance equation leads to a delay in the evolution of suction, while the complete mass balance equation gives results in very good agreement with the analytical solution. Decreasing the slope of the SWRC to $a_v = 1 \cdot 10^{-5}$ (Fig. 4.2b) or reducing the initial suction to $s_0 = 5kPa$, i.e. the pressure gradient, (Fig. 4.2(c) the two approaches give very similar results. Indeed, in these cases, the contribution of the last term of Eq. 4.16 is very small and neglecting the gradient of fluid mass is an acceptable simplification. For the range of pressure gradients and SWRC typical of many civil engineering applications, the error introduced using Eq. 4.14 is acceptably small.

In the following examples of this thesis, the more general Eq. 4.12 is used for liquid pressure updates.

2.3 COMPATIBILITY EQUATIONS

The compatibility equations allow obtaining the infinitesimal strain rate tensor of each phase at the MPs. These can be written in terms of the corresponding phase velocities as in Eqs. 4.20 and 4.21.

$$\frac{\mathrm{D}^S \boldsymbol{\varepsilon}_L}{\mathrm{D}t} = \frac{1}{2}\left[\nabla \cdot \mathbf{v}_L + (\nabla \cdot \mathbf{v}_L)^T\right] \tag{4.20}$$

$$\frac{\mathrm{D}^S \boldsymbol{\varepsilon}_S}{\mathrm{D}t} = \frac{1}{2}\left[\nabla \cdot \mathbf{v}_S + (\nabla \cdot \mathbf{v}_S)^T\right] \tag{4.21}$$

2.4 MECHANICAL CONSTITUTIVE EQUATION

In unsaturated soils, two stress variables can be used to capture the soil behavior, e.g. net stress $\sigma_{\text{net}} = \sigma - p_G$ and suction $s = p_L - p_G$. The incremental stress-strain equation becomes Eq. 4.22,

$$\frac{\mathrm{D}^{\mathrm{S}} \sigma_{\text{net}}}{\mathrm{D}t} = \mathbf{D}^{\text{ep}} \frac{\mathrm{D}^{\mathrm{S}} \varepsilon}{Dt} + \mathbf{h}' \frac{\mathrm{D}^{\mathrm{S}} s}{Dt} \tag{4.22}$$

where $\mathbf{D}^{\text{ep}}$ is the tangent stiffness matrix, $\mathbf{h}'$ is a constitutive vector. Both are defined by the constitutive model.

A great number of constitutive models for unsaturated soils have been presented in the literature [153, 154, 155, 156, 157, 158]. In this thesis, a suction-dependent Mohr-Coulomb failure criterion is employed in Chapter 5 as formulated by [159] in terms of net stress $\sigma_{\text{net}} = \sigma - p_G$ and suction $s = p_L - p_G$.

The parameters of the yield function are expressed as

$$c = c' + c_s \tag{4.23}$$

$$\phi = \phi' + \phi_s \tag{4.24}$$

where c_s and ϕ_s are the strength components depending on suction, and c' and ϕ'

are the effective strength parameters in saturated conditions. The components depending on suction are defined as

$$c_s = \Delta c_{max}(1 - e^{-Bs/p_{atm}}) \tag{4.25}$$

$$\phi_s = A(s/p_{atm}) \tag{4.26}$$

where B and A stand for calibration parameters, controlling c_s and ϕ_s rate of variation with suction, respectively, and Δc_{max} is the maximum increment of cohesion. The formulation doesn't pose any limit to the use of ulterior advanced constitutive models for unsaturated soils, which can more accurately capture some aspects of the soil behavior.

2.5 HYDRAULIC CONSTITUTIVE EQUATION

The relationship between pore liquid pressure and degree of saturation or liquid content is essential to model the behavior of unsaturated soil. This is given by the SWRC which can assume different analytical expressions [160, 161, 162]. In the following, two alternative relationships are used: (i) a linear relation (Eq. 4.27) where a_v is a constant parameter, S_{min} is the residual degree of saturation and S_{max} is the maximum degree of saturation, and (ii) the Van-Genuchten relationship [160] (Eq. 4.28) where p_{ref}, λ, are fitting parameters.

$$S_L = S_{min} + (S_{max} - S_{min}){p_L}^{a_v} \tag{4.27}$$

$$S_L = S_{min} + (S_{max} - S_{min})\left[1 + \left(\frac{p_L}{p_{ref}}\right)^{\frac{1}{1-\lambda}}\right]^{-\lambda} \tag{4.28}$$

Suction modifies the soil hydraulic conductivity and usually, unsaturated soils are less permeable than fully saturated soils. The ratio of the actual hydraulic conductivity to the saturated hydraulic conductivity (k/k_{sat}) is given by the hydraulic conductivity curve (HCC). A number of relationships has been proposed in the literature, however in this research, three HCCs are considered:

1. Constant permeability: this expression is appropriate if soil hydraulic conductivity is not expected to change significantly during the simulated process

$$\frac{k}{k_{sat}} = \text{const} \tag{4.29}$$

2. HCC function as proposed by [163] (Eq. 4.30) where r is a calibration parameter that usually varies from 2 to 4.

$$\frac{k}{k_{sat}} = S_L^r \tag{4.30}$$

3. HCC function as proposed by [164] (Eq. 4.31), where λ^* is commonly assumed identical to λ in the Van-Genuchten curve (Eq. 4.28).

$$\frac{k}{k_{sat}} = \sqrt{S_L}\Big[1 - \big(1 - S_L^{\frac{1}{\lambda^*}}\big)^{\lambda^*}\Big]^2 \tag{4.31}$$

3 MPM formulation

3.1 Weak form

The governing equations (liquid and mixture momentum balance) are transformed in the weak form, starting from a system of PDE to a system of integral equations among the domain. Test fields w and u are used in the framework of a virtual power formulation. Then, the divergence theorem is applied to bring out boundary conditions.

$$\int\limits_V \rho_{\mathrm{L}}\mathbf{a}_{\mathrm{L}} \cdot \mathbf{w} dV = \int\limits_V \Big[\nabla p_{\mathrm{L}} + \rho_{\mathrm{L}}\mathbf{g} - \frac{n_{\mathrm{L}}\mu_{\mathrm{L}}}{\kappa_{\mathrm{L}}}(\mathbf{v}_{\mathrm{L}} - \mathbf{v}_{\mathrm{S}})\Big] \cdot \mathbf{w} dV \tag{4.32}$$

The application of the divergence theorem to Eq. 4.32 results in Eq. 4.33

$$\begin{aligned}\int\limits_V \rho_{\mathrm{L}}\mathbf{a}_{\mathrm{L}} \cdot \mathbf{w} dV = \int\limits_{\partial\Omega_p} \widehat{\mathbf{p}}_{\mathrm{L}} \mathrm{d}\partial\Omega_{\mathrm{p}} - \int\limits_V p_{\mathrm{L}} \cdot \mathbf{w} dV + \int\limits_V \rho_{\mathrm{L}}\mathbf{g} \cdot \mathbf{w} dV - \\ \int\limits_V \Big[\frac{n_{\mathrm{L}}\mu_{\mathrm{L}}}{\kappa_{\mathrm{L}}}(\mathbf{v}_{\mathrm{L}} - \mathbf{v}_{\mathrm{S}})\Big] \cdot \mathbf{w} dV\end{aligned} \tag{4.33}$$

The mixture momentum balance equation in the weak form corresponds to Eq. 4.34

$$\int_V [(1-n)\rho_{\mathrm{S}}\mathbf{a}_{\mathrm{S}}]\cdot\mathbf{u}dV = \int_V \Big[-n_{\mathrm{L}}\rho_{\mathrm{L}}\mathbf{a}_{\mathrm{L}} + \nabla\sigma_{\mathrm{m}} + ((1-n)\rho_{\mathrm{S}} + n_{\mathrm{L}}\rho_{\mathrm{L}})\mathbf{g}\Big]\cdot\mathbf{u}dV \quad (4.34)$$

The application of the divergence theorem to Eq. 4.34 results in Eq. 4.35

$$\int_V [(1-n)\rho_{\mathrm{S}}\mathbf{a}_{\mathrm{S}}]\cdot\mathbf{u}dV = \int_V \Big[-(n_{\mathrm{L}}\rho_{\mathrm{L}}\mathbf{a}_{\mathrm{L}})\cdot\mathbf{u}dV + \int_{\partial\Omega_t} \tau \mathrm{d}u\partial\Omega_{\mathrm{t}} - \int_V \sigma_{\mathrm{m}} : (\nabla u)dV + \int_V [((1-n)\rho_{\mathrm{S}} + n_{\mathrm{L}}\rho_{\mathrm{L}})\mathbf{g}]\cdot\mathbf{u}dV \quad (4.35)$$

Where $\widehat{\mathbf{p}}_{\mathrm{L}}$ is the prescribed liquid pressure in the boundary $\partial\Omega_p$ and τ is the prescribed traction vector in the boundary $\partial\Omega_\tau$.

3.2 DISCRETIZED EQUATIONS

The discretized equations (Eqs. 4.36, 4.37) are obtained using the Galerkin procedure, and approximating the acceleration and velocity fields by means of finite element shape functions $\mathbf{N}$. Then, the grid elements are utilized to decompose the integrals among the entire volume domain, and the MP numerical integration procedure (Chapter 2, 1.1) is adopted for every integral on the element volume.

$$\widetilde{\mathbf{M}}_{\mathrm{L}}\mathbf{a}_{\mathrm{L}} = \mathbf{f}_{\mathrm{L}}^{\mathrm{ext}} - \mathbf{f}_{\mathrm{L}}^{\mathrm{int}} - \mathbf{Q}_{\mathrm{L}}(\mathbf{v}_{\mathrm{L}} - \mathbf{v}_{\mathrm{S}}) \quad (4.36)$$

$$\mathbf{M}_{S}\mathbf{a}_{\mathrm{S}} + \mathbf{M}_{\mathrm{L}}\mathbf{a}_{\mathrm{L}} = \mathbf{f}^{\,\mathrm{ext}} - \mathbf{f}^{\,\mathrm{int}} \quad (4.37)$$

$\mathbf{a}_{\mathrm{L}}$, $\mathbf{a}_{\mathrm{S}}$, $\mathbf{v}_{\mathrm{L}}$, and $\mathbf{v}_{\mathrm{S}}$ are the nodal acceleration and velocity vectors; $\mathbf{M}_{\mathrm{S}}$, $\mathbf{M}_{\mathrm{L}}$, and $\widetilde{\mathbf{M}}_{\mathrm{L}}$ are solid and liquid lumped mass matrices (Eq. 4.38- 4.40); $\mathbf{f}_{\mathrm{L}}^{\mathrm{ext}}$, $\mathbf{f}_{\mathrm{L}}^{\mathrm{int}}$, $\mathbf{f}^{\,\mathrm{ext}}$, $\mathbf{f}^{\,\mathrm{int}}$ are internal and external nodal force vectors of the liquid phase and the mixture (Eqs. 4.41- 4.44), and $\mathbf{Q}_{\mathrm{L}}$ is the drag force matrix (Eq. 4.45).

$$\widetilde{\mathbf{M}}_{\mathrm{L}} \approx \sum_{\mathrm{MP}=1}^{n_{\mathrm{MP}}} \widetilde{m}_{\mathrm{L}}^{\mathrm{MP}}\mathbf{N} \quad (4.38)$$

$$\mathbf{M}_{\mathrm{L}} \approx \sum_{\mathrm{MP}=1}^{n_{\mathrm{MP}}} m_{\mathrm{L}}^{\mathrm{MP}} \mathbf{N} \tag{4.39}$$

$$\mathbf{M}_{\mathrm{S}} \approx \sum_{\mathrm{MP}=1}^{n_{\mathrm{MP}}} m_{\mathrm{S}}^{\mathrm{MP}} \mathbf{N} \tag{4.40}$$

$$\mathbf{f}_{\mathrm{L}}^{\mathrm{ext}} \approx \int_{\partial\Omega_p} \mathbf{N}^{\mathrm{T}} \widehat{\mathbf{p}}_{\mathrm{L}} \mathrm{d}\partial\Omega_{\mathrm{p}} + \sum_{\mathrm{MP}=1}^{n_{\mathrm{NP}}} m_{\mathrm{L}}^{\mathrm{MP}} \mathbf{N}^{\mathrm{T}} \mathbf{g} \tag{4.41}$$

$$\mathbf{f}^{\,\mathrm{ext}} \approx \int_{\partial\Omega_\tau} \mathbf{N}^{\mathrm{T}} \tau \mathrm{d}\partial\Omega_{\tau} + \sum_{\mathrm{MP}=1}^{n_{\mathrm{MP}}} m_{\mathrm{m}}^{\mathrm{MP}} \mathbf{N}^{\mathrm{T}} \mathbf{g} \tag{4.42}$$

$$\mathbf{f}_{\mathrm{L}}^{\mathrm{int}} \approx \sum_{\mathrm{MP}=1}^{n_{\mathrm{MP}}} \mathbf{B}^{\mathrm{T}} p_{\mathrm{L}}^{\mathrm{MP}} \mathbf{m} V_{\mathrm{MP}} \tag{4.43}$$

$$\mathbf{f}^{\,\mathrm{int}} \approx \sum_{\mathrm{MP}=1}^{n_{\mathrm{MP}}} \mathbf{B}^{\mathrm{T}} \sigma_{\mathrm{MP}} V_{\mathrm{MP}} \tag{4.44}$$

$$\mathbf{Q}_{\mathrm{L}} \approx \sum_{\mathrm{MP}=1}^{n_{\mathrm{MP}}} \mathbf{N}^{\mathrm{T}} \frac{n_{\mathrm{L}}^{\mathrm{MP}} \rho_{\mathrm{L}} g}{k_{\mathrm{L}}^{\mathrm{MP}}} \mathbf{N} V_{\mathrm{MP}} \tag{4.45}$$

N is the matrix of nodal shape functions and **B** is the matrix of the gradients of the nodal shape functions evaluated at local MP positions. The treatment of boundary conditions for unsaturated soils is described in details in Sec. 4. The phase mass of the MP is calculated as Eqs. 4.46- 4.49, where V_{MP} is the volume of the MP.

$$\widetilde{m}_{\mathrm{L}}^{\mathrm{MP}} = \rho_{\mathrm{L}} V_{\mathrm{MP}} \tag{4.46}$$

$$m_{\mathrm{L}}^{\mathrm{MP}} = n_{\mathrm{L}}^{\mathrm{MP}} \rho_{\mathrm{L}} V_{\mathrm{MP}} \tag{4.47}$$

$$m_{\mathrm{S}}^{\mathrm{MP}} = n_{\mathrm{S}}^{\mathrm{MP}} \rho_{\mathrm{S}} V_{\mathrm{MP}} \tag{4.48}$$

$$m_{\mathrm{m}}^{\mathrm{MP}} = \rho_{\mathrm{m}} V_{\mathrm{MP}} \tag{4.49}$$

Eqs. 4.36 and 4.37 are integrated in time using the Euler-Cromer explicit method. This time integration scheme is conditionally stable and the critical time step size is computed by considering the minimum value between the critical time computed with the criterion proposed by [165] and the one associated to consolidation processes. A review of critical time step criteria in saturated MPM formulations is presented in Sec. 7.2, followed by a preliminary study on the influence of unsaturated conditions on the critical time step.

The momentum balances (Eqs. 4.36 and 4.37) are discretised and solved at the nodes of the mesh as in [97]. Mass balances (Eqs. 4.9 and 4.12) and constitutive equations (Eqs. 4.22) are posed locally at the MPs to update secondary variables.

3.3 NUMERICAL ALGORITHM

The formulation presented in previous section is implemented in the open source code *Anura3D*. The numerical algorithm is based on the modified lagrangian algorithm originally proposed by [87] for one-phase material, and successfully extended to multiphase materials (see e.g. [97, 110]). The MPM solution scheme for each time step can be summarised as follows.

1. Liquid momentum balance equation (Eq. 4.36) is assembled and solved for the liquid nodal acceleration $\mathbf{a}_\mathrm{L}$
2. Mixture momentum balance equation (Eq. 4.37) is assembled and solved to obtain the nodal acceleration of the solid $\mathbf{a}_\mathrm{S}$
3. Velocities and momentum of the MPs are updated from nodal accelerations of each phase
4. Nodal velocities are calculated from nodal momentum and used to compute the strain increment at the MP location and the terms on the right-end-side of Eq. 4.12
5. Mass balance equation (Eq. 4.12) and soil stress-strain equation (Eq. 4.22) give the increment of pore pressure and effective stress respectively
6. State variables at MPs are updated. Degree of saturation and hydraulic conductivity are updated according to SWRC and HCC respectively
7. Displacement and position of each MP are updated according to the updated velocity of the solid phase
8. Nodal values are discarded, the MPs carry all the updated information, and the computational grid is initialised for the next time step.

The proposed formulation requires the definition of the following boundary conditions (BC):

1. Prescribed liquid displacement or velocity on $\partial\Omega_{v_\mathrm{L}}$ and prescribed pressure on $\partial\Omega_\mathrm{p}$, where $\partial\Omega = \partial\Omega_{v_\mathrm{L}} \cup \partial\Omega_\mathrm{p}$ and $\partial\Omega_{v_\mathrm{L}} \cap \partial\Omega_\mathrm{p} = 0$
2. Prescribed solid displacement or velocity on $\partial\Omega_\mathrm{u}$ and prescribed traction on $\partial\Omega_\tau$, where $\partial\Omega = \partial\Omega_{v_\mathrm{S}} \cup \partial\Omega_\tau$ and $\partial\Omega_{\mathrm{v_S}} \cap \partial\Omega_\tau = 0$.

Essential boundary conditions on $\partial\Omega_{v_\mathrm{L}}$ and $\partial\Omega_{v_\mathrm{S}}$ are imposed on the nodes of the computational grid. Natural boundary conditions on $\partial\Omega_\mathrm{p}$ and $\partial\Omega_\tau$ are included in the weak form of the momentum balance equations.

In typical problems with partially saturated soil in geomechanics, prescribed liquid velocity can be applied on infiltration boundaries as described in Sec. 4.2, and prescribed pressures can be applied either by defining a pressure load $\widehat{p}_L$ or by assigning a total hydraulic head $\widehat{H}$ as explained in Sec. 4.1. Assuming the validity of Bernoulli's equation and neglecting the kinematic head, the total hydraulic head can be written as

$$\widehat{H} = h_g - \frac{\widehat{p}_L}{\rho_L g} \tag{4.50}$$

where h_g stands for the potential head or geometric head and $\widehat{p}_L/(\rho_L g)$ is the pressure head. The minus sign in Eq. 4.50 is introduced because pressure is assumed negative for compression.

Sometimes, the boundary condition is part of the problem solution, i.e. it is not known a priori if the boundary belongs to $\partial\Omega_{v_\mathrm{L}}$ or $\partial\Omega_\mathrm{p}$. This is typical of free surface flows across porous media along the so-called *potential seepage face* [166, 167]. Moreover, the size of this boundary condition can evolve along time. This boundary condition can be applied as presented in Sec. 4.3. Figure 4.3 represents schematically how these BCs simulate different hydraulic loading acting on a levee.

In classical FEM, the application of prescribed boundary conditions is simple as these can be specified directly on the boundary nodes, which coincide with the boundary of the continuum body and are well defined throughout the computation. However, the computational mesh in MPM does not necessarily align with the

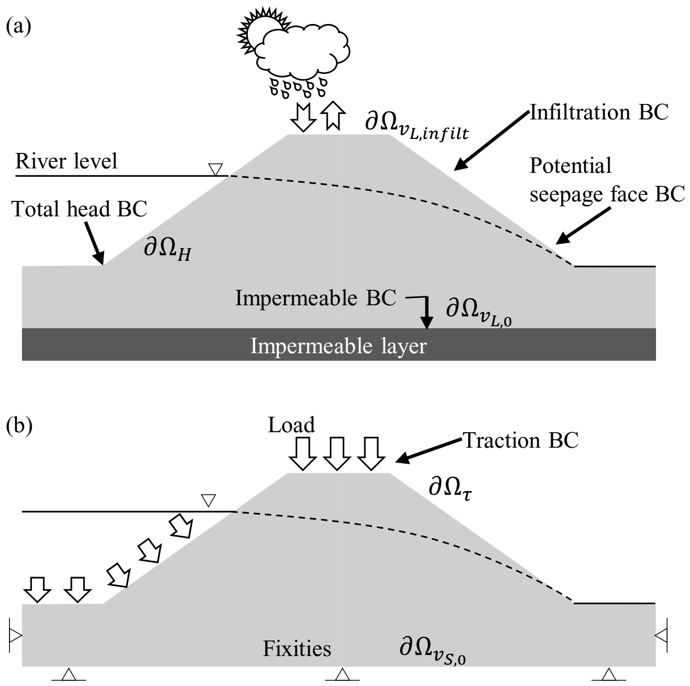

Figure 4.3: Typical boundary conditions for liquid phase (a) and mixture (b), from [150].

boundary of the material making the application of the prescribed boundary conditions more challenging.

In the numerical framework proposed here, zero-traction and zero-pressure boundary conditions are automatically enforced to be satisfied by the solution of equations of motion, but difficulties arise when dealing with non-zero boundary conditions. The nodes belonging to the boundary are determined with a procedure similar to the surface boundary algorithm presented in [79], here extended for unstructured mesh.

For each time step, firstly the active elements (i.e. elements containing MPs) adjacent to an empty element (i.e. element without MPs) are detected (*boundary elements*); then the nodes belonging to the element side adjacent to an empty element (*boundary side*) are marked as *boundary nodes*. The MPs next to the boundary side are identified as *boundary material points* as shown in Fig. 4.4. Finally, if the boundary node lies inside the area where a specified condition has to be applied, e.g. in the infiltration zone or on the potential seepage face, the corresponding boundary condition is applied.

Another difficulty with moving boundaries appears when prescribed velocity

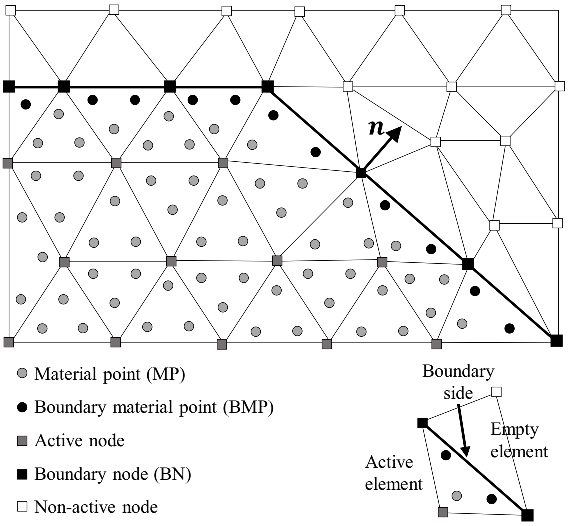

Figure 4.4: Definition of boundary nodes and boundary material points, from [116].

or traction (pressure) do not have a constant direction, but it is normal to the boundary. This means that if the shape of the contour changes, the direction of the applied condition has to be updated during the calculation. The normal direction at the node is determined by means of the gradient of mass as Eq. 4.51

$$\mathbf{n} \approx \frac{\sum_{\mathrm{MP}=1}^{n_{\mathrm{MP}}} m_m^{\mathrm{MP}} \mathbf{B}}{\|\sum_{\mathrm{MP}=1}^{n_{\mathrm{MP}}} m_m^{\mathrm{MP}} \mathbf{B}\|} \tag{4.51}$$

4.1 HYDRAULIC HEAD BC

Examples in which hydraulic head BC can be used are the seasonal fluctuations of groundwater tables [168], impoundement or drawdown of a water reservoir [169], the sudden increase of river levels due to an extreme flood event, the rupture of buried water pipes altering the surrounding water table distribution in a urban environment, or the effect of introducing a drainage system to stabilize a slope.

The hydraulic head BC is converted to an imposed pressure condition $\widehat{p_L}$, using Eq. 4.50 solved for the liquid pressure. This means that a hydrostatic approximation is adopted, neglecting local turbulence induced by the river flow or by the potential collapse of the internal bank. The element's nodes affected by this condition are detected with the algorithm introduced in the previous section.

A series of hydraulic head values in time, like the ones provided by water gauges readings, is assigned with an input file, and at each time step the current hydraulic head H_{curr} is computed by linear interpolation. The resulting nodal vector is part of the vector of external forces in the liquid momentum equation ($\mathbf{f}_{\mathrm{L}}^{\mathrm{ext}}$ in Eq. 4.36) and in the mixture momentum equation ($\mathbf{f}^{\mathrm{ext}}$ in Eq. 4.37) to account also for water weight.
Concerning the boundary nodes included in the hydraulic head BC but lying above H_{curr}, at first a "pressure approach" is implemented, and two scenarios considered: (i) constant pressure and (ii) linear pressure distribution (in suction), following the same hydrostatic gradient given by γ_W. In the case of a homogeneous slope in stationary flow regimes, it is common to introduce the unsaturated condition above the water table [170, 171], which reflects in the pore pressure distribution. Close to the phreatic surface, a linear increase of suction can be explained by the capillary rise controlled by the SWRC. The upper portion, closer to the interface with the atmosphere, is governed by climate conditions and suction depends on the water mass balance at the soil surface [171, 172]. The constant approximation reproduces this last effect, while the linear approximation simulates better the capillary effect. The drawback of the later approach is the overestimation of suction at higher locations.

In the literature, the BC above the river level has been reproduced in different ways. In some cases, an infiltration/evaporation BC is applied [171, 172] or a zero nodal flux is imposed [46], in other cases the condition has been approximated with the use of a potential seepage face [166, 173]. This last approach is followed in the second implementation, which can be considered an advancement of the pressure approach and will be used in the 2D seepage validation example of Sec. 6.2.

The two treatments of this boundary condition above H_{curr} are compared in the drawdown examples in Chapter 5.

4.2 INFILTRATION BC

This boundary condition is necessary to simulate rainfall or evaporation boundary condition. It consists in applying a prescribed specific discharge $q = \widehat{\mathbf{w}} \cdot \mathbf{n}$ along the boundary, where $\mathbf{n}$ is the outward normal unit vector (Eq. 4.51) and the seepage velocity $\widehat{\mathbf{w}}$ is defined as Eq. 4.52,

$$\widehat{\mathbf{w}} = n_L(\mathbf{v}_L - \mathbf{v}_S) \tag{4.52}$$

The application of this boundary condition is based on a predictor-corrector scheme: liquid and solid velocity are first predicted assuming zero-pressure boundary conditions at the infiltration boundary and then (eventually) corrected to ensure the prescribed infiltration rate. The procedure can be summarized in the following steps, also shown in Fig. 4.5:

1. $\mathbf{a}_{\mathrm{L}}^t$ and $\mathbf{a}_{\mathrm{S}}^t$ are computed by solving Eqs. 4.36 and 4.37 assuming $\widehat{p}_L = 0$ at the infiltration boundary
2. Nodal velocities are predicted as $\tilde{\mathbf{v}}_L^{t+\Delta t} = \mathbf{v}_L^t + \mathbf{a}_{\mathrm{L}}\Delta t$ and $\tilde{\mathbf{v}}_S^{t+\Delta t} = \mathbf{v}_S^t + \mathbf{a}_{\mathrm{S}}\Delta t$
3. Infiltration condition is checked. If the net infiltration discharge q_{net} (Eq. 4.53) is positive, ponding conditions occur and if fluid accumulation above the boundary is not allowed (it must remain at zero pressure) no correction is necessary. If the net infiltration discharge is negative, or liquid ponding is allowed above the surface, then liquid velocity must be corrected to ensure the correct infiltration rate

$$q_{net} = (n_L(\tilde{\mathbf{v}}_L^{t+\Delta t} - \tilde{\mathbf{v}}_S^{t+\Delta t}) - \widehat{\mathbf{w}}) \cdot \mathbf{n} \tag{4.53}$$

4. If necessary, the liquid nodal velocity is corrected by Eq. 4.54

$$\mathbf{v}_L^{t+\Delta t} = \tilde{\mathbf{v}}_L^{t+\Delta t} + \Delta\mathbf{v}_L \tag{4.54}$$

where $\Delta\mathbf{v}_L$ is derived by imposing $q_{net} = 0$ (Eq. 4.55) and it is given by Eq. 4.56

$$(n_L(\tilde{\mathbf{v}}_L^{t+\Delta t} + \Delta\mathbf{v}_L - \tilde{\mathbf{v}}_S^{t+\Delta t}) - \widehat{\mathbf{w}}) \cdot \mathbf{n} = 0 \tag{4.55}$$

$$\Delta\mathbf{v}_L = ((n_L(\tilde{\mathbf{v}}_L^{t+\Delta t} - \tilde{\mathbf{v}}_S^{t+\Delta t}) - \widehat{\mathbf{w}}) \cdot \mathbf{n})\mathbf{n} \tag{4.56}$$

5. The corrected liquid acceleration is computed as $\mathbf{a}_{\mathrm{L}}^t = (\mathbf{v}_{\mathrm{L}}^{t+\Delta t} - \mathbf{v}_{\mathrm{L}}^t)/\Delta t$
6. The MPM solution scheme can proceed with the convective phase as explained in steps 3-8 of Sec. 3.3.

Note that this boundary condition is applied at nodal level, thus nodal liquid volumetric fraction is necessary. This can be computed by mapping $n_L = nS_L$ from the MPs to the nodes of the mesh. This implementation is subsequently improved by taking inspiration from a recent formulation [117] similar to the one herein proposed. In this work the authors consider also a solid velocity correction such that Eq. 4.55 becomes

$$(n_L(\tilde{\mathbf{v}}_L^{t+\Delta t} + \Delta\mathbf{v}_L - \tilde{\mathbf{v}}_S^{t+\Delta t} - \Delta\mathbf{v}_S) - \widehat{\mathbf{w}}) \cdot \mathbf{n} = 0 \tag{4.57}$$

By imposing the conservation of the mixture momentum balance the solid velocity correction is computed as follows

$$\Delta\mathbf{v}_S = -\frac{m_L \Delta\mathbf{v}_L}{m_S} \tag{4.58}$$

and the liquid velocity correction becomes

$$\Delta\mathbf{v}_L = -\frac{(n_L(\tilde{\mathbf{v}}_L^{t+\Delta t} - \tilde{\mathbf{v}}_S^{t+\Delta t}) - \widehat{\mathbf{w}}) \cdot \mathbf{n})\mathbf{n}}{n_L\left(1 + \frac{m_L}{m_S}\right)} \tag{4.59}$$

where m_L and m_S are the liquid and solid nodal masses. This approach accurately ensures the conservation of momentum balance of the mixture at the boundary, i.e. the total stress remains constant at the ground level. The previous implementation, with the only correction of liquid velocity, implicitly assumes that the relative acceleration between solid and liquid is negligible and that the effective stress at the boundary is constant and equal to zero.

4.3 POTENTIAL SEEPAGE FACE BC

A *potential seepage face* can be defined as an interface between soil and atmosphere where the fluid is free to exit at zero pressure when the soil is saturated, but it cannot enter when the soil is partially saturated. An example of potential seepage face is the downstream surface of a river embankment (Fig. 4.3(a), or it can also arise in after a rapid drawdown of the river level. This boundary condition is necessary where it is unknown if the boundary is an essential or a natural boundary condition.

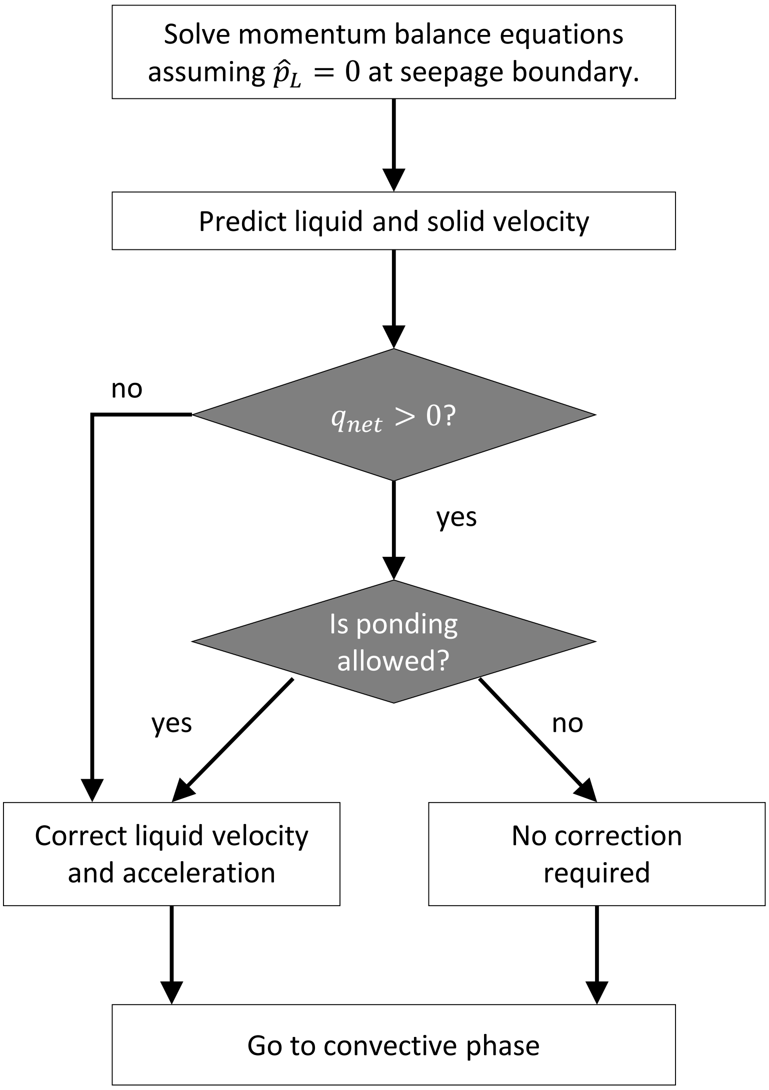

Figure 4.5: Flow chart of the infiltration boundary condition, from [116].

The implementation can be considered as a special case of the infiltration boundary condition described in Sec. 4.2, where $\widehat{\mathbf{w}} = 0$. Liquid and solid nodal velocities are predicted assuming zero-pressure at the potential seepage face (natural boundary condition). If $(n_L(\tilde{\mathbf{v}}_L^{t+\Delta t} - \tilde{\mathbf{v}}_S^{t+\Delta t})) \cdot \mathbf{n} > 0$ it means that fluid is flowing out of the soil at zero pressure and no correction is required. If $(n_L(\tilde{\mathbf{v}}_L^{t+\Delta t} - \tilde{\mathbf{v}}_S^{t+\Delta t})) \cdot \mathbf{n} < 0$, then fluid is flowing into the soil at zero pressure, thus liquid velocity must be corrected with Eqs. 4.54 and 4.56 in which $\widehat{\mathbf{w}} = 0$ (switch to essential boundary condition).

5 IMPROVEMENT OF INITIALIZATION PROCEDURE

5.1 NEW *K0*-PROCEDURE

At the beginning of every simulation it is required to initialize stress in the solid skeleton and liquid pressure. Stress distribution depends on solid weight and the deposition history, while liquid pressures depends on the water table location and the atmospheric condition history. The initialization procedure can be performed in two ways named gravity load and *K0*-procedure.

In both cases it is suggested to run one or more steps using the quasi-static calculation [70] to let the system reach a balanced configuration under the effect of the gravity vector and applied boundary conditions. If gravity load is used, stress is computed based on soil weight and the constitutive model under use. In this case, it is possible to assign an initial homogeneous value of liquid pressure to all the MPs.

On the other side, while using *K0*-procedure, it is additionally possible to specify the ratio between horizontal and vertical stress (*K0*), and the water table location. This is particularly important to "favour" the quasi-static convergence towards more realistic stress and liquid pressure gradients in the entire domain. In the present work *K0*-procedure has been improved in the following manner:

1. A non-horizontal soil surface can be specified for stress computation
2. A phreatic surface (not coinciding with the soil surface) can be specified at every location of the domain
3. A suction threshold above phreatic surface can be used, to limit the excessive suction values at soil surface (see Fig. 4.7)

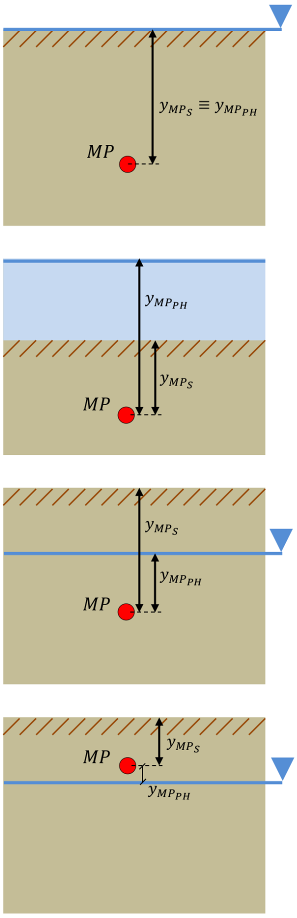

Case 1: Phreatic surface corresponds with soil surface

$$\sigma_y = -y_{MP_S} \cdot (\rho_{mix}\, g)$$
$$p_L = -y_{MP_{PH}} \cdot (\rho_L\, g)$$

Case 2: Phreatic surface is above soil surface

$$\sigma_y = -(y_{MP_S} \cdot \rho_{mix} + (y_{MP_{PH}} - y_{MP_S}) \cdot \rho_L)g$$
$$p_L = -y_{MP_{PH}} \cdot (\rho_L\, g)$$

Case 3: Phreatic surface and MP below soil surface

$$\sigma_y = -(y_{MP_{PH}} \cdot \rho_{mix} + (y_{MP_{PH}} - y_{MP_S}) \cdot \rho_{dry})g$$
$$p_L = -y_{MP_{PH}} \cdot (\rho_L\, g)$$

Case 4: Phreatic surface below soil surface but MP above it

$$\sigma_y = -y_{MP_S} \cdot (\rho_{dry}\, g)$$
$$p_L = +y_{MP_{PH}} \cdot (\rho_L\, g)$$

Figure 4.6: Stress and liquid pressure initialization with new *K0*-procedure in different cases.

In the scheme of Fig. 4.6 the stress and pressure computation based on soil and phreatic surface identification is presented. y_{MP_S} stands for the vertical distance between a MP and the soil surface, while $y_{MP_{PH}}$ is the distance of the MP from the phreatic surface. The phreatic surface should be most properly defined as a zero pressure surface, thus it is as a geometric entity corresponding to the phreatic surface in the soil but also to an external water level (like river or sea level). A simplified assumption in terms of dry soil weight is made to compute stress above the phreatic surface. Case 4 of Fig. 4.6 reproduce MPs liquid pressure computation above the phreatic surface in the case that a maximum value of suction is not specified.

The two options introduced in this work are presented in Fig. 4.7. In case (a) max suction is specified, the liquid pressure above phreatic surface is computed

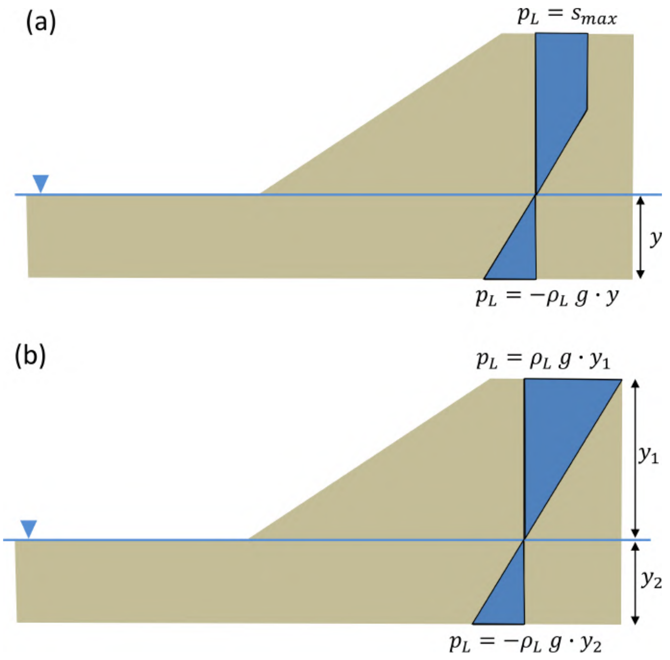

Figure 4.7: *K0*-procedure liquid pressure computation above phreatic surface: (a) linear until specified max suction is reached b) linear.

following the gradient of hydrostatic pressure, i.e. linear approximation, until the max suction value is met. Case (b) corresponds to the general case with no max suction value specification. It is important to underline two aspects: this implementation is currently valid just for 2D problems, however it can be easily extended to 3D problems to consider more complex domains.

K0-procedure should be always coupled with a quasi-static calculation, thus the stress and pressure assigned in the *K0* procedure are always modified during the computational step, given the present boundary conditions, the constitutive model and the Bishop principle of effective stress.

6 Validation

Validating the presented formulation is not straightforward because no analytical solution is available for coupled soil deformation-fluid flow in unsaturated conditions. To this aim, simple benchmarks where fixed solid skeleton (just flow problems) or small deformations can be considered. By comparing the results obtained by MPM and well-established FEM softwares, satisfying results could be achieved in terms of testing and validation, keeping in account slight differences in the implementations. In the choice of the benchmarks it is also fundamental to consider an optimized combination of material properties, range of saturation degree variation and mesh sizes, to limit excessive computational times in MPM. How these aspects can impact on the duration of an MPM simulation, will be covered in detail in Sec. 7.

In this section two simple benchmarks will be studied: (i) a 1D column infiltration in a fixed solid skeleton (Secs. 6.1.1) and (ii) a 2D seepage flow in a fixed solid skeleton levee (Sec. 6.2). The MPM results are compared with the ones provided by the commercial FEM code - SEEP/W by *Geostudio* [46].

6.1 INFILTRATION IN A 1D SOIL COLUMN

6.1.1 INFILTRATION IN RIGID SOLID SKELETON

A 1m-high soil column is considered with the material parameters listed in Tab. 4.2. For simplicity, the intrinsic permeability is assumed constant and equal to $\kappa_L = 1 \cdot 10^{-11} m^2$, corresponding to a hydraulic conductivity of $k = 1.0 \cdot 10^{-4}$m/s. Van-Genuchten SWRC is accounted (Eq. 4.28), with parameters $p_{ref} = 3kPa$, $\lambda = 0.7$, $S_{min} = 0.125$, $S_{max} = 1$. Liquid Bulk modulus K_L is reduced to a value of 80000 kPa compared to the real value for computational speed up and numerical stability. Notwithstanding, this value is sufficiently high compared to the soil compressibility. In the FEM software used for comparison this term is considered, and can be computed thanks to the following Eq. 4.60 (retrieved from [46]).

$$S_s = \rho_L g \, (\alpha + n\beta) = \rho \, g \, m_v \tag{4.60}$$

where S_s is the specific storage, α is the compressiblity of the soil structure, β is the compressiblity of the water, and m_v is the coefficient of volume change (ρ_L, n, g as defined above). Thanks to the specification of m_v it is possible to account for water compressibility values different from an assumed incompressible behavior.

The column is discretized with 20 rows of 2 square triangular elements filled with 3 MPs each (Fig. 4.8(a). The bottom and lateral boundaries are impervious, while a vertical infiltration rate $\widehat{w}_y = 1.0 \cdot 10^{-4}$ m/s is applied at the top boundary. An initial suction of 2kPa is assigned at $t = 0$s along the column, which corresponds to an initial degree of saturation $S_{L0} = 0.87$.

Solid density $[kg/m^3]$	ρ_S	2700
Liquid density $[kg/m^3]$	ρ_L	1000
Porosity [-]	n	0.4
Liquid bulk modulus $[kPa]$	K_L	80000
Liquid dynamic viscosity $[kPa \cdot s]$	μ_L	$1 \cdot 10^{-6}$

Table 4.2: Material parameters for 1D infiltration example and 2D seepage flow.

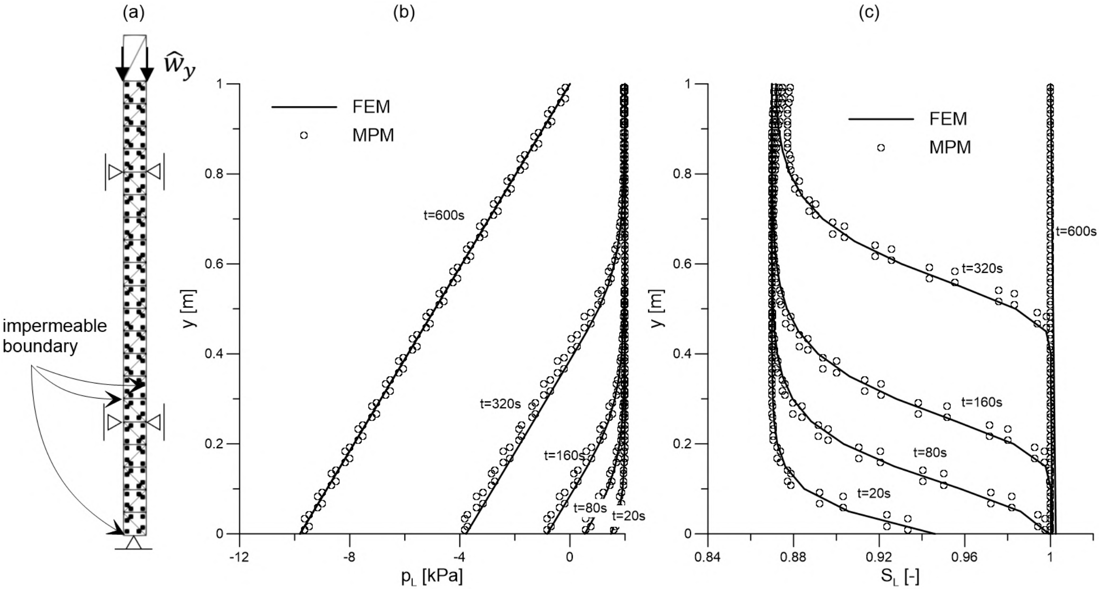

Figure 4.8: Geometry of the problem (a). Evolution of liquid pressure (b) and degree of saturation (c) along the column. Comparison between MPM and FEM, from [116].

The liquid infiltrates from the top and flows down though the column accumulating at the impervious bottom. Here suction starts decreasing and the soil saturates increasing S_L to 1. Fig. 4.8 plots the evolution of pore pressure and degree of saturation distribution along the column at different time instants. MPM results are in very good agreement with FEM. As expected, it can be noted that at long time ($t = 600s$) soil is saturated at the top boundary, i.e. $p_L = 0$, thus the infiltration BC switches from essential, i.e. applied infiltration velocity, to natural, i.e. zero-pressure, and the pore pressure does not increase further.

A small note: this case could have been considered also with a deformable solid skeleton. However, the major difference between the present unsaturated MPM formulations and most of the commercial codes FEM based is the computation of mixture weight above phreatic surface. In MPM this value is updated at every time step considering the actual saturation degree, while in the other cases the

Soil density	ρ_S	2700	$[kg/m^3]$
Liquid density	ρ_L	1000	$[kg/m^3]$
Porosity	n	0.4	[-]
Liquid Bulk modulus	K_L	80000	$[kPa]$
Liquid dynamic viscosity	μ_L	$1 \cdot 10^{-6}$	$[kPa \cdot s]$
Maximum degree of saturation	S_{max}	1.0	[-]
Minimum degree of saturation	S_{min}	0.1	[-]
Reference suction	p_{ref}	2.0	$[kPa]$
Lambda	λ	0.5	[-]
Saturated hydraulic conductivity	k_{sat}	$1.962 \cdot 10^{-4}$	[m/s]

Table 4.3: Material and SWRC parameters for the 2D seepage problem.

unsaturated weight is kept constant, with a predefined value since the simulation beginning. Given this aspect, it would be inaccurate to propose a validation example with MPM and one of these codes.

6.2 2D SEEPAGE FLOW IN A RIVER LEVEE

This case corresponds to a typical pre-failure transient seepage analysis. Geometry, initial water table position, and applied BCs are reported in Figure 4.9a. Two cross-sections, S1 and S2, are also sketched for the outcomes presentation. The progressive river-level rise is simulated with the total head BC. As a consequence, a seepage flow is induced in the levee body. On the land side, the seepage face BC ensures the free location of the phreatic surface exit point. The considered hydrograph is presented in Figure 4.9b. The river level reaches the peak height of 0.85m at 150s, followed by a gentle decrease. Tab.4.3 reports the material properties, for both solid and liquid phases. A reduced liquid bulk modulus K_L is used for computation speedup. In addition, the Van-Genuchten model (Eq. 4.28) is used for the SWRC and the corresponding parameters are presented in the same Tab. 4.3. The HCC is assumed constant, i.e. $k = k_{sat}$, not depending on saturation degree changes. The solid skeleton is fixed, i.e. soil deformability is neglected for a better comparison with FEM.

The spatial discretization consists of 3-node triangular linear elements of 0.05m side length, each filled with 3 MPs. The initial pore pressure distribution is hydrostatic, with water table position outlined in Figure 4.9a. The simulation time is 300s, and a mass scaling factor of 400 is used to optimize the computational

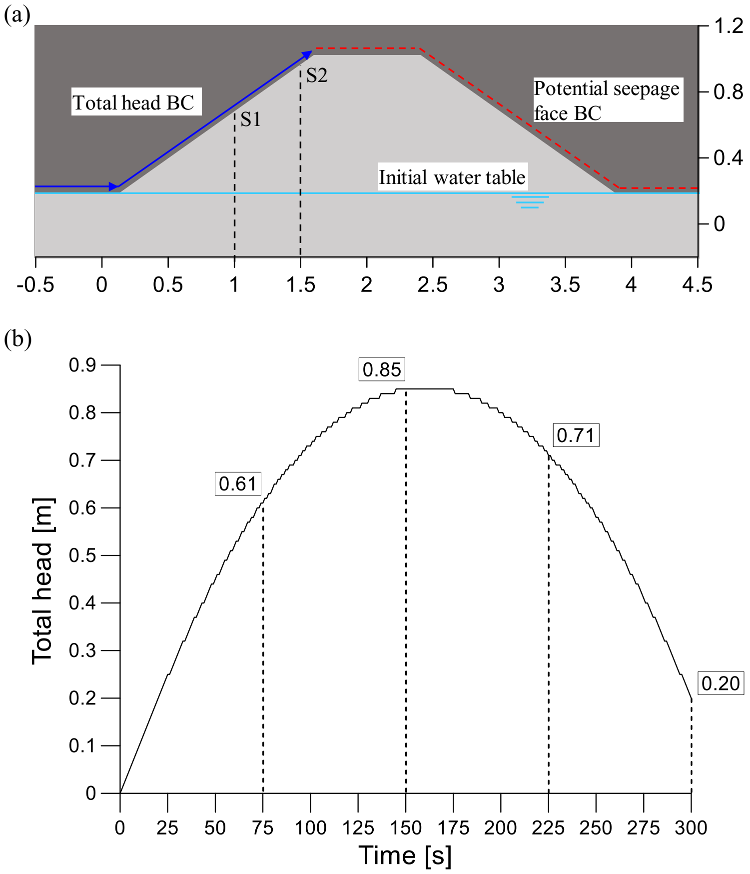

Figure 4.9: (a) 2D seepage problem geometry with outlined initial and BCs, plus sections S1 and S2.(b) Simulated hydrogram, applied as BC on the riverside slope of the numerical model, from [150].

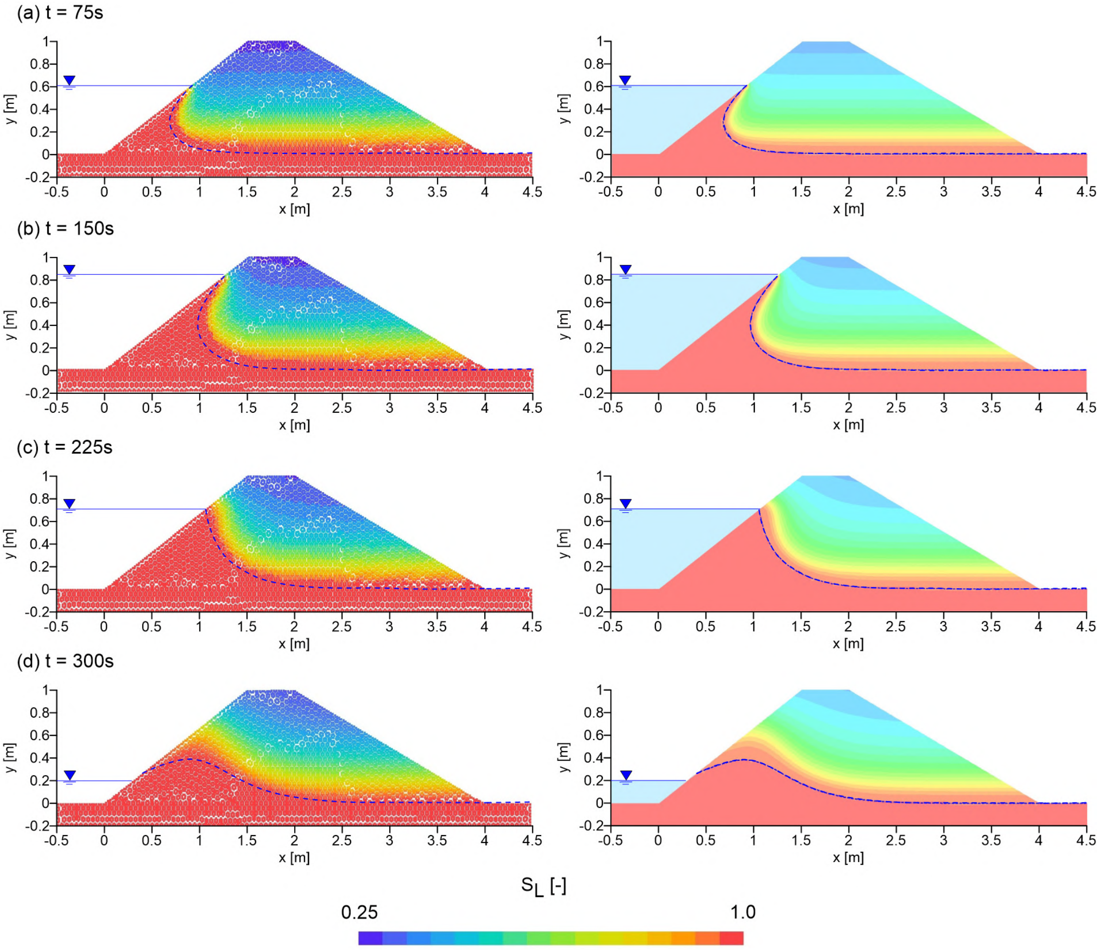

Figure 4.10: Saturation degree S_L contour at four instants, for MPM (left column) and FEM (right column)from [150]. Dashed blue line stands for the phreatic line.

time [90]. The simulation results are presented herein, and compared with those obtained with the FEM code. Figure 4.10 depicts the saturation degree, S_L, contour plot for four particular time instants. These time instants (i.e., 75, 150, 225, and 300s) and their respective total head levels are indicated by the dashed vertical lines in Figure 4.9b. River levels and phreatic surface locations are outlined on the contour plots with blue lines. The spatial distribution of S_L and its evolution with time are in good agreement in MPM and FEM. The phreatic surface curvature at each time instant reflects the crescent and descending phases of the applied hydrograph in an identical manner by both numerical methods. In particular, Figure 4.10d captures the transient nature of this phenomenon,

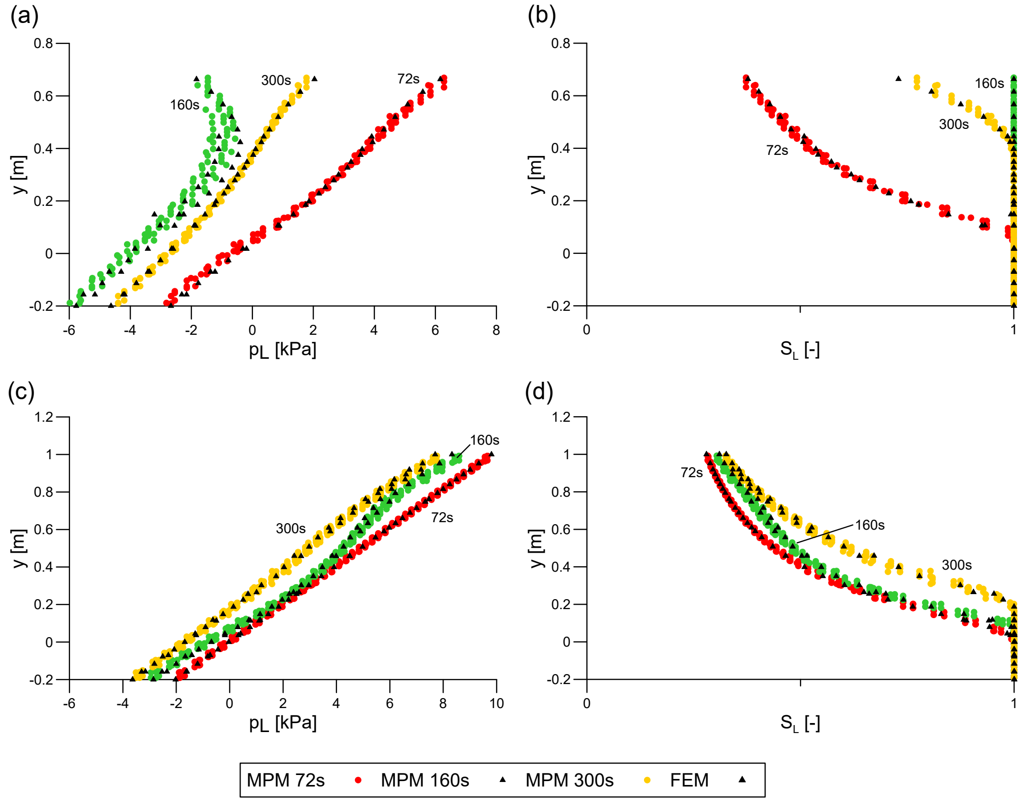

Figure 4.11: Pore pressure p_L and saturation degree S_L along vertical section S1 (panels (a) and (b)) and section S2 (panels (c) and (d)). Black triangles stands for FEM while colored dots for MPM, from [150].

by showing a delay between the effective minimum river level and the phreatic surface exit point on the riverside. This behavior depends on a slower desaturation rate compared with the river level decrease, resulting from the current suction distribution and soil permeability.

To further quantify the MPM formulation efficacy, Figure 4.11 shows the pore pressure p_L and saturation degree S_L along two sections, S1 and S2 (Figure 4.9(a). Figure 4.11a and c correspond to section S1, while Figure 4.11b and d correspond to section S2. Three time instants, 72s, 160s, and 300s are selected to present the temporal seepage flow evolution. These trends highlight the good match between the MPM and FEM results. By comparing curves at 160s and 300s, it is observed that section S1 undergoes full saturation during the rising phase, followed by a desaturation of its upper portion. By contrast, section S2 never reaches complete saturation along most of its vertical extension, which reflects in higher suction values and a saturation degree that never reaches 100% above 0.2m. The trends of pore pressure and saturation degree provide insightful information about the evolving saturation portion of the levee body and the time necessary to return to the initial water table location (not reached during the simulation time).

7 PRELIMINARY STUDY ON NUMERICAL STABILITY IN UNSATURATED CONDITIONS

7.1 REVIEW OF STABILITY CRITERIA

In two-phase problems we can define two time scales of interest, namely that of excess pore pressure dissipation related to consolidation and infiltration and that of compression wave propagation within the solid-fluid mixture. In mathematics, consolidation (infiltration) is seen as parabolic behavior, while wave propagation is hyperbolic behavior. The associated critical time steps are expresses by Eq. 4.61 and Eq. 4.62 respectively, where L_i is a characteristic length, i.e. the element size.

$$\Delta t_c = \frac{L_i^2}{2c} \tag{4.61}$$

$$\Delta t_c = \frac{L_i}{v_c} \tag{4.62}$$

The coefficient c can be written as Eq. 4.63 where E_c' is the effective oedometric modulus. Note that for $S_L = 1$ and $\frac{dS_L}{ds} = 0$ it coincides with the consolidation coefficient.

$$c = \frac{k_L}{\mu_L \left(\frac{1}{E_c'} + \frac{S_L n}{K_L} + n \frac{dS_L}{ds} \right)} \tag{4.63}$$

v_c in Eq. 4.62 represents the one-dimensional compressing wave speed propagation and can be estimated with Eq. 4.64, where E_c and ρ are the oedometric modulus and the density of the considered material.

$$v_c = \sqrt{\frac{E_c}{\rho}} \tag{4.64}$$

Eq. 4.64 can be particularized for undrained conditions using $E_c = E'_c + n/K_L$ and $\rho = \rho_{sat}$ or for dry conditions using $E_c = E'_c$ and $\rho = \rho_{dry}$.

[71] and [165] mathematically studied the stability of the two-phase MPM formulation for saturated conditions proposed in [90]. Both analysis highlight the dependency of Δt_c on hydraulic conductivity and characteristic length (i.e. minimum mesh size). In the work of [71], the eigenvalue problem is solved to study the stability of four different equations: (a) the liquid momentum balance $\Delta t_{c,liquid}$, (b) the mixture momentum balance $\Delta t_{c,mixture}$, (c) the coupled hydro-mechanical system ($\Delta t_{c,coupled}$) (i.e. liquid and mixture momentum balances), and (d) the momentum balance of the mixture in undrained conditions ($\Delta t_{c,undrained}$). The equations are all firstly written for a single node and the homogeneous form is considered, obtaining a second order ODE. Then, the Euler-Cromer explicit time discretisation is introduced, thus a system of two first-order ODEs is obtained. The coefficient matrix of this system is considered: by imposing spectral radius equal to 1, it is possible to solve the eigenvalue problem and determine an expression for Δt_c. The critical time step criterion for the undrained analysis is identical to Eq. 4.62, while the other three criteria share the following expression

$$\Delta t_{c,Yerro} = \frac{2}{\omega}\Big[-\xi + \sqrt{\xi^2 + 1}\Big] \tag{4.65}$$

where ω and ξ vary depending on the set of equations considered, and provided in Tab.4.4 (Saturated column). At this point, a series of oedometric tests are performed with the MPM code based on the formulation by [90]. Δt used in the simulation is manually increased until a maximum value, respectful of the analytical solution, is reached. As a last step, the numerical results are graphically compared with the four mathematical expressions. The latter are modified by adjusting Li around the value of the actual mesh size, to make the curves fit as close as possible to the numerical results. By analyzing several cases, considering different porosity, permeability and mesh sizes, the author concludes that the safest criterion is

$$\Delta t_c = min(\Delta t_{c,undrained}; \Delta t_{c,liquid}) \tag{4.66}$$

[165] considered the stability of the coupled hydro-mechanical system concerning liquid and mixture momentum balances. In particular, the dependency of Δt_c on hydraulic conductivity is investigated. This research is motivated by observations

concerning sharp reductions of Δt_c for low permeability values, which can not be explained by both consolidation and CFL criteria. Rigorous mathematical stability analysis were conducted by means of the matrix method [174], and an estimation of Δt_c is proposed as

$$\Delta t_{c,Mieremet} = \frac{-2a + \sqrt{4a^2 + 8(b + \sqrt{b^2 - 4d})}}{b + \sqrt{b^2 - 4d}} \tag{4.67}$$

where terms a, b and d are reported in Tab. 4.5 (Saturated column). The performance of the proposed criterion is verified with 1D FEM-based simulations. Based on the results of this final comparison, the author states that the criterion is safer compared to previous expression proposed by the same author [175] and to the CFL condition. At the current state, the results of this study are implemented in *Anura3D* and for the majority of the simulations performed for this thesis the following criterion is used

$$\Delta t_c = min(\Delta t_{c,consolidation}; \Delta t_{c,Mieremet}) \tag{4.68}$$

where $\Delta t_{c,consolidation}$ is expressed in Eq. 4.61. Regarding the analysis of the critical time step in the unsaturated regime, as far as the authors know, there are no studies in the context of MPM dynamic formulations. In the 3Phase formulation by [176] the estimation of Δt_c is based on the above mentioned analysis by the same author, conducted on saturated media. This choice is based on the fact that Δt_c is inversely proportional to the Bulk modulus of the mixture. Hence, we can expect that Δt_c in saturated conditions is smaller compared to unsaturated ones. For the same reason, the potential increase of the critical time step in the unsaturated regime, makes reasonable to conduct a detailed analysis.

7.2 NEW STABILITY CRITERIA FOR UNSATURATED CONDITIONS

Assuming that saturation can be understood as a particular case of unsaturated conditions, one could expect that the Δt_c for unsaturated formulations is an extension of those obtained for saturated conditions. In this work, the stability of the 2Phase with suction formulation in unsaturated conditions is studied considering the same approach followed by [71]. The stability of (a) the momentum balance of the liquid, (b) the momentum balance of the mixture, and (c) the coupled system is derived. The main passages to obtain the stability criteria are presented in detail in the Appendix (Sec. 7). The obtained expressions for the critical time step follow the same structure as Eq. 4.65. The new terms ω and ξ are reported in Tab. 4.4 (Unsaturated column).

Given the consistent complexities in applying the same rigorous procedure by [165] to the formulation presented in this thesis, a simplified "adaptation" of Eq. 4.67 to unsaturated conditions is proposed. The terms a, b and d are modified in a similar manner to ω and ξ in saturated vs. unsaturated conditions (4.4). In the term a, S_L^2 is added and ρ_{sat} is replaced by ρ_m. In terms b and d, the liquid bulk modulus K_L is replaced by $\frac{S_L}{\left(\frac{dS_L}{ds}\right)+\frac{S_L}{K_L}}$, based on ω_C and ω_M unsaturated expressions. Note that, consistently for all the criteria, the saturated case ($S_L = 1$) is a particular case of the unsaturated expressions.

	Saturated	Unsaturated
Coupled	$\omega_C = \frac{1}{L_i}\sqrt{\frac{K_L}{\rho_L} + \frac{E_c}{\rho_S(1-n)} + \frac{(1-n)}{n}\frac{K_L}{\rho_S}}$ $\xi_C = \frac{n\mu_L}{2k_L\omega_C}\left[\frac{n}{(1-n)\rho_S} + \frac{1}{\rho_L}\right]$	$\omega_C = \frac{1}{L_i}\sqrt{\left[\frac{S_L}{\left(\frac{dS_L}{ds}+\frac{S_L}{K_L}\right)}\right]\left[\frac{1}{\rho_L} + \frac{1}{\rho_S}\left(\frac{1}{n} - S_L\right)\right] + \frac{E_c}{\rho_S(1-n)}}$ $\xi_C = \frac{S_L n\mu_L}{2k_L\omega_C}\left[\frac{S_L n}{(1-n)\rho_S} + \frac{1}{\rho_L}\right]$
Liquid	$\omega_L = \frac{1}{L_i}\sqrt{\frac{K_L}{\rho_L}}$ $\xi_L = \frac{n\mu_L}{2k_L\omega_L}\frac{1}{\rho_L}$	$\omega_L = \frac{1}{L_i}\sqrt{\frac{S_L}{\rho_L\left(\frac{dS_L}{ds}+\frac{S_L}{K_L}\right)}}$ $\xi_L = \frac{S_L n\mu_L}{2k_L\omega_L}\frac{1}{\rho_L}$
Mixture	$\omega_M = \frac{1}{L_i}\sqrt{\frac{E_c}{(1-n)\rho_S} + \frac{(1-n)}{n}\frac{K_L}{\rho_S}}$ $\xi_M = \frac{n^2\mu_L}{2(1-n)\rho_S k_L\omega_M}$	$\omega_M = \frac{1}{L_i}\sqrt{\frac{1}{\rho_S}\left[\frac{E_c}{(1-n)} + \left(-S_L + \frac{1}{n}\right)\frac{S_L}{\left(\frac{dS_L}{ds}+\frac{S_L}{K_L}\right)}\right]}$ $\xi_M = \frac{S_L^2 n^2\mu_L}{2(1-n)\rho_S k_L\omega_M}$

Table 4.4: Parameters ω and ξ used in Δt_c expression by [71]. Left column: original version for saturated conditions. Right column: new development for unsaturated conditions.

Saturated		Unsaturated	
Mieremet	$a = \frac{n\rho_{sat}\mu}{(1-n)\rho_S\rho_L k_L}$ $b = \frac{4(n\rho_{sat}K_L+(1-2n)\rho_L K_L+n\rho_L E_c)}{n(1-n)\rho_S\rho_L L_i^2}$ $d = \frac{16E_c K_L}{(1-n)\rho_S\rho_L L_i^4}$	Mieremet$_{adapted}$	$a = \frac{{S_L}^2 n\rho_m\mu}{(1-n)\rho_S\rho_L k_L}$ $b = \frac{4\left(n\rho_m\frac{S_L}{\left(\frac{dS_L}{ds}+\frac{S_L}{K_L}\right)}+(1-2n)\rho_L\frac{S_L}{\left(\frac{dS_L}{ds}+\frac{S_L}{K_L}\right)}+n\rho_L E_c\right)}{n(1-n)\rho_S\rho_L L_i^2}$ $d = \frac{16E_c\frac{S_L}{\left(\frac{dS_L}{ds}+\frac{S_L}{K_L}\right)}}{(1-n)\rho_S\rho_L L_i^4}$

Table 4.5: Parameters a, b and d used in Δt_c expression by [165]. Left column: original version for saturated conditions. Right column: adapted criterion for unsaturated conditions.

7.3 NUMERICAL ANALYSIS AND DISCUSSION

In this section, the performances of the unsaturated criteria are evaluated. A trial and error procedure is used to explore Δt_c in unsaturated conditions. A series of MPM-based simulations is performed. The objective is to determine Δt_c for different degrees of saturation. The model is a soil column, 1m high and 0.05m wide. At the top of the column, an external load of 100kPa is applied, see Fig. 4.12 (a). An initial suction is imposed to the entire column and the same suction is applied at the top of the column during the rest of the calculation to ensure that the degree of saturation remains as constant as possible in the model. An infiltration problem wouldn't be suitable to this aim. The material is linear elastic and the intrinsic permeability ($k_L = 2 \cdot 10^{-10} m^2$, equivalent to a hydraulic conductivity of $\kappa \approx 2 \cdot 10^{-3} m/s$) is assumed constant. The mesh is made by linear triangular elements of 0.05m side length. The bottom boundary is fully fixed and impervious. The lateral boundaries only allow vertical movement and are impervious.

The same analysis is repeated for three soil types (sand, silt, and clay) to evaluate the effect of the SWRCs on the numerical stability. The Van-Genuchten model is used to describe three reference SWRC from [170] (Fig. 4.12 (b)). The SWRC parameters are provided in Tab. 4.6. The simulations are performed for each soil type ensuring a large range of suction values, covering degrees of saturation from saturated ($S_L = 1.0$) to approximately dry conditions ($S_L = 10^{-2}$).

Moreover, to evaluate the critical time step in diverse conditions, we consider different sets of analysis varying the porosity ($n = 0.4$ and $n = 0.6$) and the Young modulus ($E_1 = 10^4 kPa$ and $E_2 = 5 \cdot 10^4 kPa$). The Poisson ratio is assumed constant for all the simulations, $\nu = 0.2$. The time step of each calculation is manually increased until the simulation does not converge. This iterative process is repeated for each combination of material parameters. The maximum value that

	Sand	**Silt**	**Clay**
S_{max} [-]	1.0	1.0	1.0
S_{min} [-]	0.003	0.001	0.001
p_{ref} [kPa]	9.9	100.0	196.0
λ [-]	0.8	0.75	0.5

Table 4.6: Van-Genuchten parameters for the three SWRCs used in the critical time step numerical analysis.

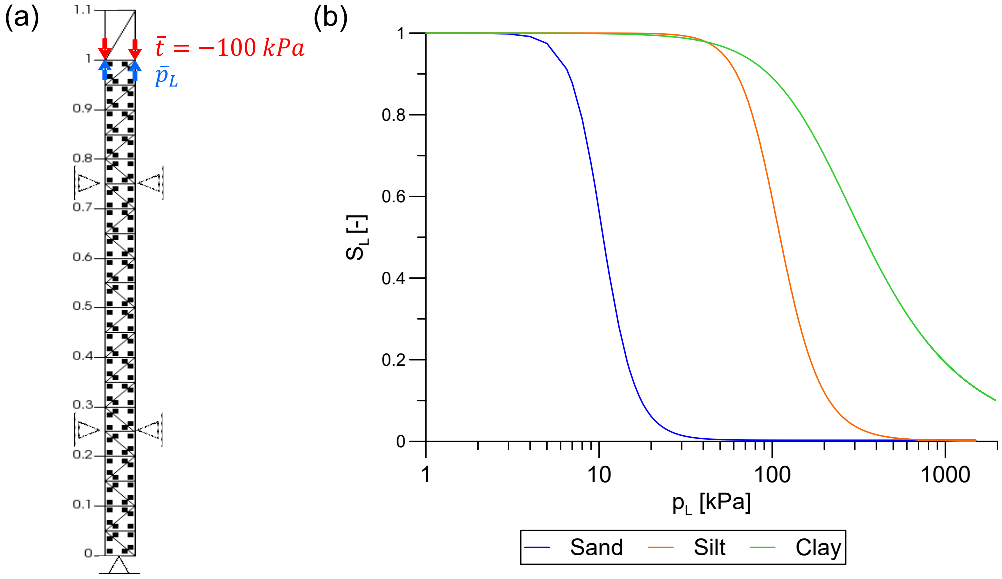

Figure 4.12: Critical time step in unsaturated conditions obtained from numerical simulations: (a) geometry of the problem, (b) SWRCs tested.

ensures the solution convergence is considered the critical time step. Summarizing, for each SWRC a simulation is performed with a constant suction value; in total eight different values of suction (or saturation degree) are considered.

The critical time steps obtained from the numerical tests performed in sand, silt, and clay are presented in Fig. 4.13, Fig. 4.14 and Fig. 4.15, respectively. In all figures, the numerical results plotted together with the stability criteria proposed in this work for unsaturated conditions (Tab. 4.4 and 4.5). In addition, the expressions from the literature, i.e. consolidation and infiltration (Eq. 4.61), and CFL in undrained and dry conditions (Eq. 4.62) are also presented for reference. All the expressions are evaluated considering $L_i = 0.035m$ which corresponds to the minimum altitude of the element. The numerical results show a general increase of Δt_c in the unsaturated regime. The coupled criterion $\Delta t_{c,Coupled}$ appears as the one better fitting the results, however, it overestimates Δt_c near the extremes (dry and saturated conditions). $\Delta t_{c,Mieremet_{adapted}}$ is the second-closest criterion, and it trends to be more conservative than $\Delta t_{c,Coupled}$. It is important to note that near the dry conditions ($S_L \approx 10^{-2}$) a sharp decrease of Δt_c is consistently observed. This decrease is highlighted by $\Delta t_{c,Coupled}$, $\Delta t_{c,Liquid}$ and $\Delta t_{c,Mieremet_{adapted}}$ criteria.

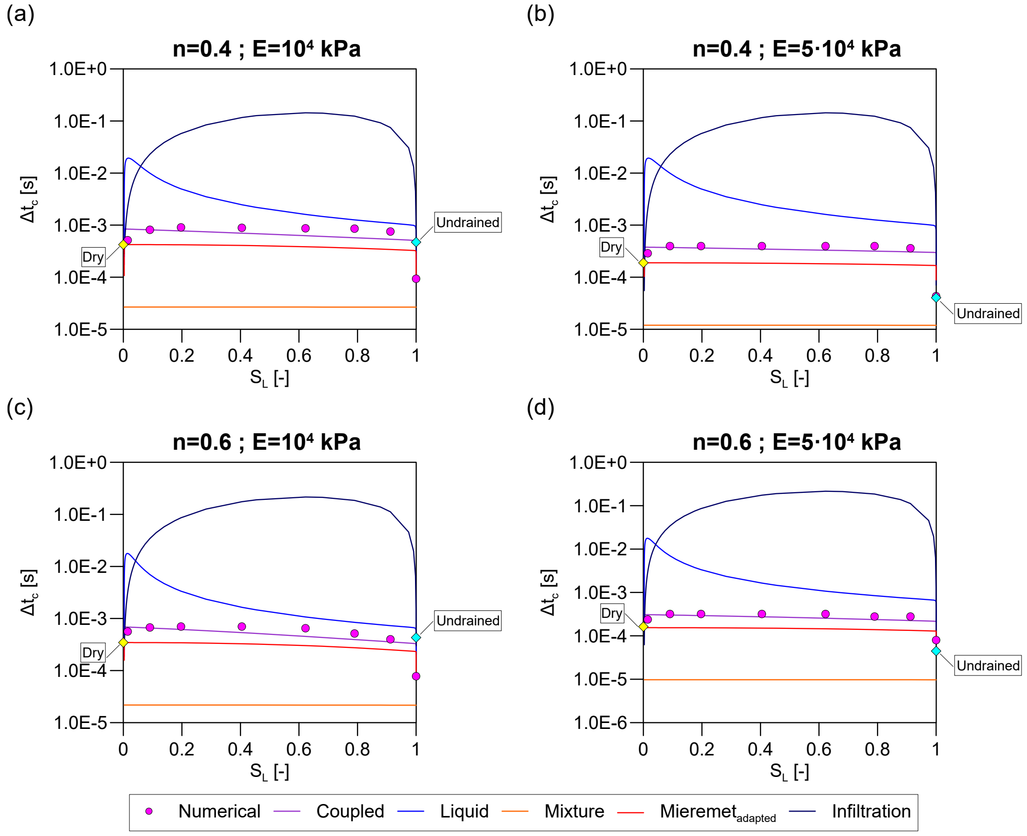

Figure 4.13: Δt_c results from MPM simulations compared with mathematical expressions and literature criteria. Sand SWRC.

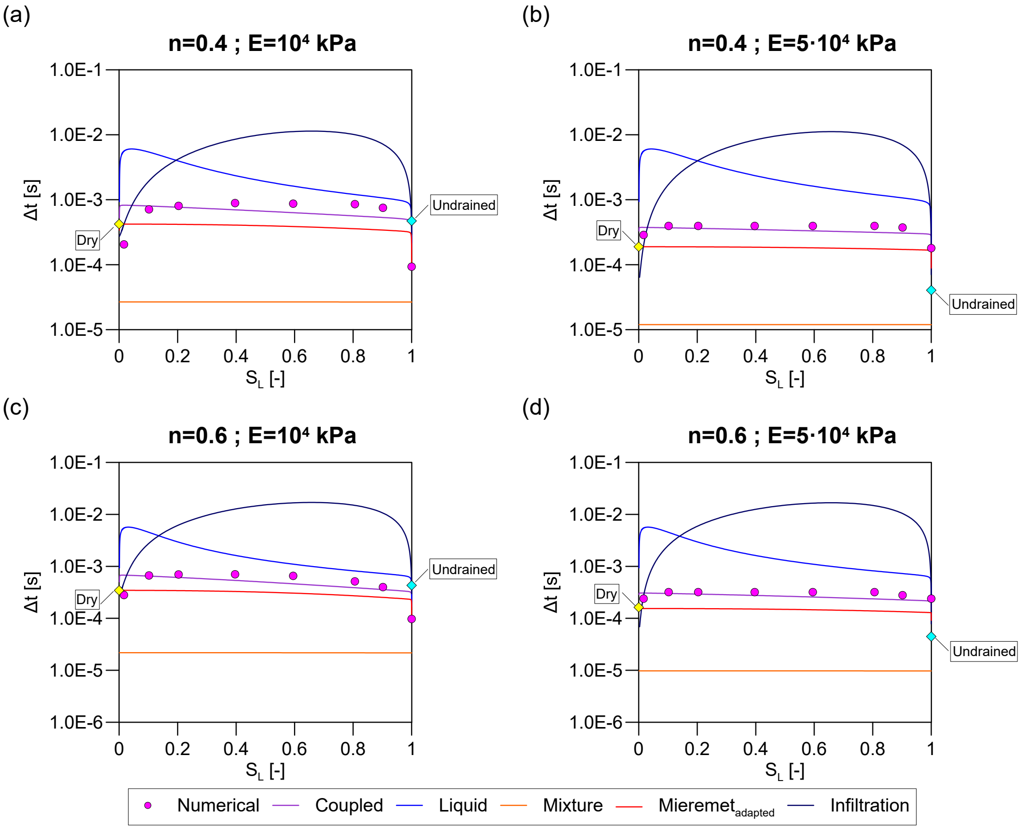

Figure 4.14: Δt_c results from MPM simulations compared with mathematical expressions and literature criteria. Silt SWRC.

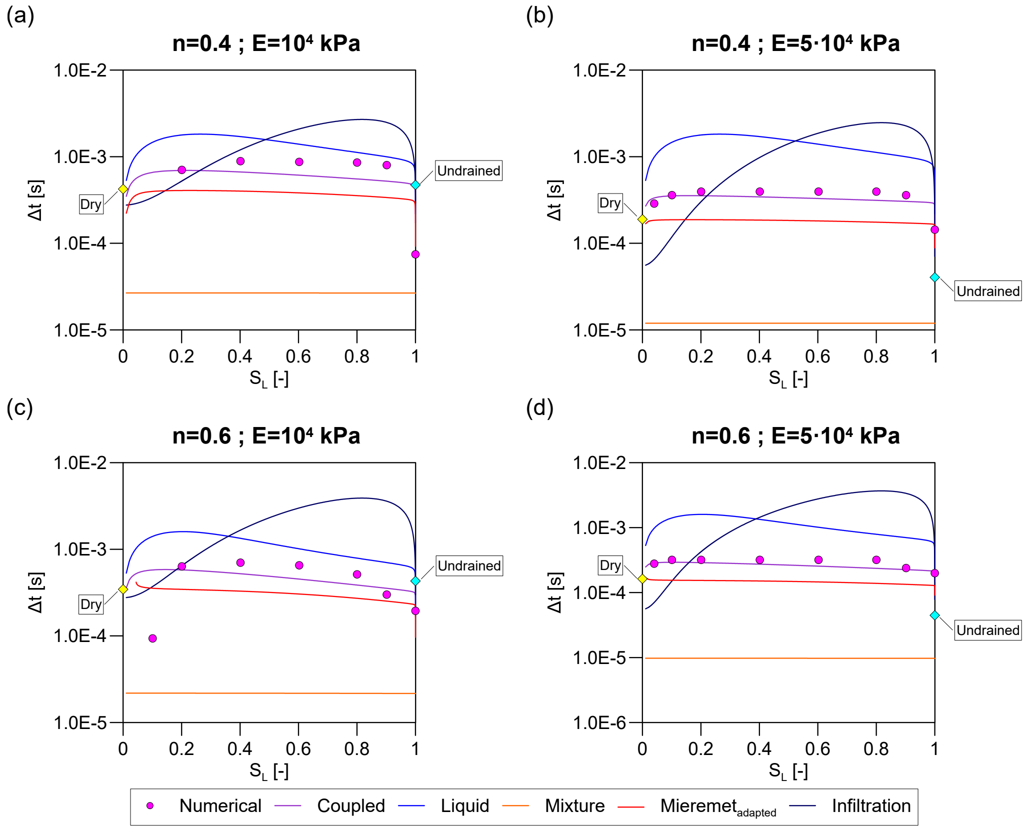

Figure 4.15: Δt_c results from MPM simulations compared with mathematical expressions and literature criteria. Clay SWRC.

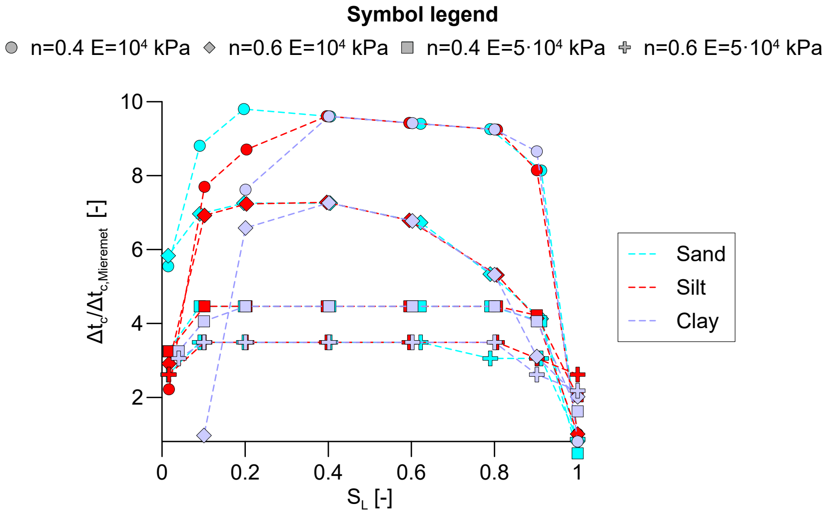

Figure 4.16: Comprehensive numerical results normalized with respect to $\Delta t_{c,Mieremet}$, as function of saturation degree.

It should be noted that the use of $\Delta t_{c,Mieremet_{adapted}}$ is limited by negative values under the square root present at the numerator of this expression (Eq. 4.67). This situation seems to occur when suction values are extremely high (i.e. S_L is very low). This behavior occurs for silt SWRC when $s > 1800kPa$ and for clay SWRC when $s > 4500kPa$ (although it is difficult to appreciate in the figures because of the logarithmic scale). These values of suction are hardly encountered in real geotechnical scenarios.

To better quantify the increase of Δt_c in unsaturated conditions and to visualize the effect of each material parameter on it, in Fig. 4.16(a) the numerical Δt_c values are normalized with respect to $\Delta t_{c,Mieremet}$ (criterion for saturated conditions, Eq. 4.67). We can observe that smaller porosity values result in bigger Δt_c, as highlighted by circle and diamond symbols. On the other side, the higher Young modulus results in lower Δt_c values, visible with square and cross symbols. Furthermore, the higher Young modulus gives a more flat trend in the interval between $S_L = 0.2$ and $S_L = 0.8$. It is interesting to observe the comparable (in some cases identical) increase in Δt_c among the different materials for the same combination of porosity and Young modulus. The major differences occur when approaching dry conditions.

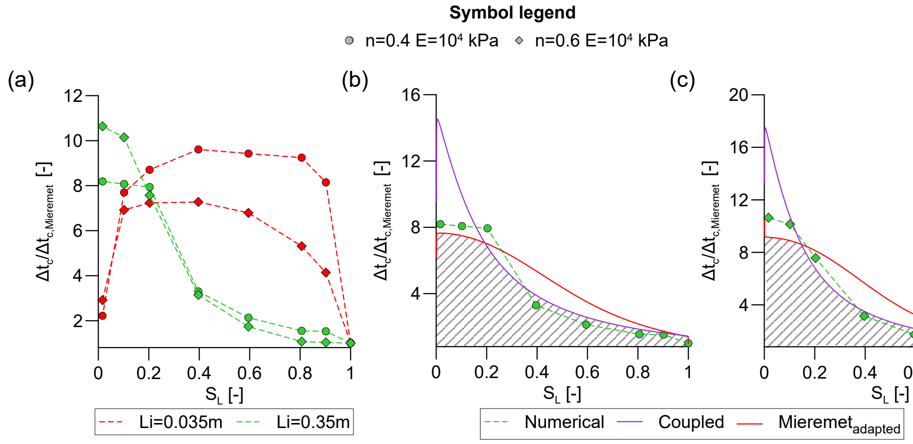

Figure 4.17: (a) Comparison of normalized Δt_c numerical results for different mesh sizes using silt SWRC. Δt_c results numerical and analytical for $L_i = 0.35m$ for porosity values (b) $n = 0.4$ and (c) $n = 0.6$.

7.3.1 Mesh size effect on Δt_c in unsaturated conditions

In Fig. 4.17(a), the numerical outcomes using the same model scaled up 10 times (mesh size 0.5m and $L_i = 0.35m$) are introduced to emphasize the mesh size effect on Δt_c. The comparison with the previous $Li = 0.035m$ is related to the silt material. It is clear that Δt_c depends on the mesh size, in fact results with the coarser mesh have a different trend of critical time step. The sharp reduction of Δt_c near dry conditions seems no more present, on the contrary, in this normalization, Δt_c is continuously increasing. This behavior of Δt_c is explained to a good extent by the proposed $\Delta t_{c,Coupled}$ and $\Delta t_{c,Mieremet_{adapted}}$ criteria, as visible in Fig. 4.17(b) and (c). In particular, if the minimum between the two criteria is considered, as highlighted with the hatch below the two curves, a very similar trend emerges compared with the numerical results. Fig. 4.17(b) and (c) are respectively related to porosity values $n = 0.4$ and $n = 0.6$. The analytical criteria show in a more definite manner, compared to the numerical results, a sharp reduction of Δt_c for the dry conditions, according to the results for the smaller mesh. Given the satisfying but still partial explanation of this behavior by the two criteria, more extensive investigation is further necessary to understand the different trends of Δt_c for various mesh sizes.

7.3.2 PERMEABILITY EFFECT ON Δt_c IN UNSATURATED CONDITIONS

Lastly, the impact of different permeability values is investigated. For this purpose, three additional set of simulations are performed using intrinsic permeabilities of $k_L = 1 \cdot 10^{-9}$, $8 \cdot 10^{-11}$, and $7 \cdot 10^{-12} m^2$). In all simulations, k_L is kept constant during the calculation. Δt_c trends as function of k_L are plotted in Fig. 4.18 for the silt SWRC. The numerical results are presented as well as the infiltration criterion (Eq. 4.61, dashed line), $\Delta t_{c,Coupled}$ (solid lines in Fig. 4.18a) and $\Delta t_{c,Mieremet_{adapted}}$ (solid lines in Fig. 4.18b). It is evident from the simulations that the critical time step first increases with permeability and then decreases. For relatively low permeability values, $\Delta t_{c,Mieremet_{adapted}}$ is a safe underestimation, while $\Delta t_{c,Coupled}$ is closer to them. For higher permeability values, the infiltration criterion can explain the reduction of critical time step, but it offers only an overestimation of it. Nevertheless, both criteria are not able to explain the reduction of Δt_c for high permeability values. This behavior could be explained by considering that high permeability determines a reduction of coupling between phases, the drag force is reduced. Therefore, in this condition the momentum balance equations used to evaluate the numerical stability scheme can become less efficient in explaining the mixture behavior compared to the mass balance equation. Alternatively to this analysis, the stability of the mass balance equation could have been studied, or the stability of the entire system of governing equations, considering mass balance and momentum balance equations.

These preliminary results can encourage future studies and provide an indicative support to stimulate researchers using MPM unsaturated formulations in testing higher values of Δt_c in situations where significant variations of S_L or extreme values in the unsaturated regime, i.e. full saturation or dry conditions, are not encountered. Further studies need to be performed to investigate the effect of other material parameters, such as permeability on the stability of the solution, or numerical parameters, like particle position and interaction between elements. In this regard, a recent study by [177] has highlighted the effect of these parameters on the critical time step in a single phase MPM formulation. This study can be considered in future developments of this work to enrich and make more accurate the proposed criteria.

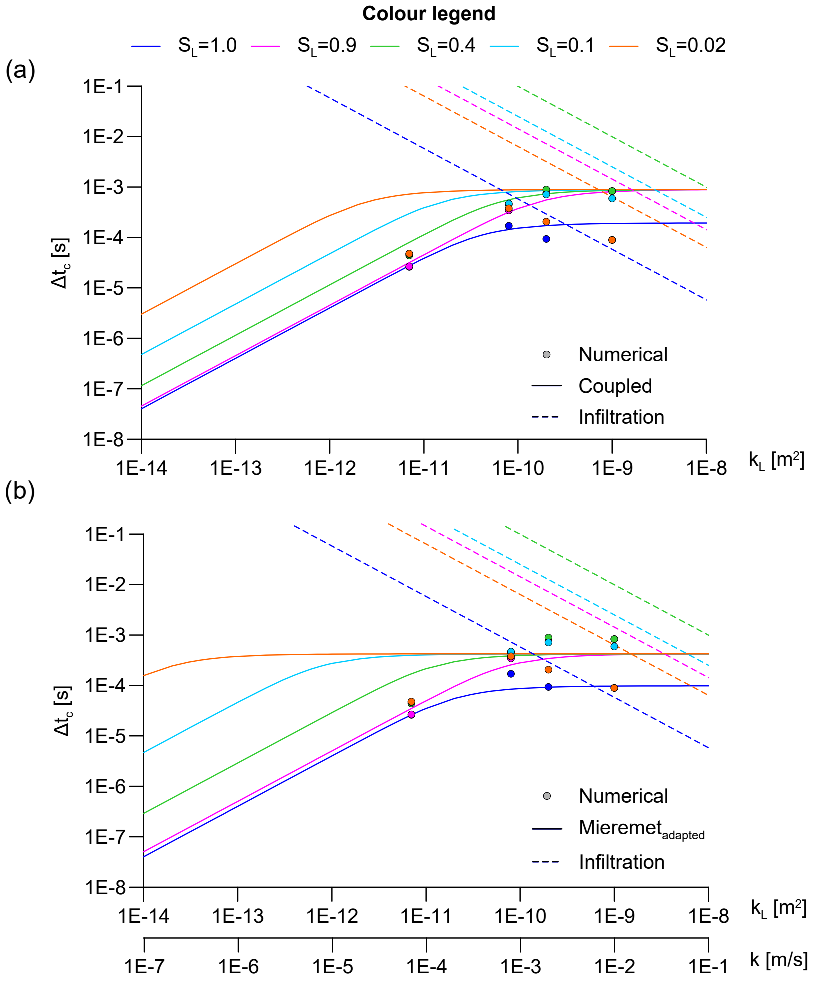

Figure 4.18: Δt_c as function of intrinsic permeability (hydraulic conductivity is indicated in a secondary axis). Comparison between numerical results and analytical expressions: infiltration and $\Delta t_{c,Coupled}$ (a) or $\Delta t_{c,Mieremet_{adapted}}$ (b).

5

Applications: global instability mechanisms in river levees and additional slope stability cases

1 INTRODUCTION

In this chapter the newly developed unsaturated MPM formulation, presented in the previous Chapter 4, is used to analyze different slope stability problems, to investigate failure onset and full post failure behavior. Levees failure mechanisms and more generally the ones determining natural and artificial slope failure are explored; particular attention is given to the alteration of saturation regimes, induced by the transient hydraulic boundary conditions.
Firstly some theoretical cases are considered, then the numerical method is applied to several small and large-scale experiments. Where appropriate, a comparison of results coming from the *2Phase with suction* formulation with the 2Phase Double Point formulation is presented.

Complex failure mechanisms occurring in levees built on top of permeable layers hydraulically interconnected with the river are analyzed by considering centrifuge experiments and MPM simulations. In this case, the MPM model is at prototype scale.

Some of the applications presented in this chapter are taken from two papers coauthored by the thesis author [136, 150].

2 EXPLORING TYPICAL LEVEE'S FAILURE MECHANISMS WITH THEORETICAL SLOPES

Failure of dams and levees can be caused by several mechanisms, e.g. macro-instability, overtopping, erosion (internal and external) [1, 2, 178]. Here the focus is on the macro-instabilities due to changes in the pore pressure regime induced by two typical phenomena schematically represented in Fig. 5.1a: (i) infiltration due to heavy rainfall on the land side (Sec. 2.1) and (ii) a rapid drawdown of the water level on the riverside (Sec. 2.2). MPM results are compared with the ones obtained by FEM seepage analysis coupled with LEM analysis to evaluate FS.

The second case, the drawdown induced instability, differs from the example presented in Sec. 3 of Chapter 3, in two fundamental aspects: first one, the boundary condition above the current water level, having the chance of accounting for suction in this case. Second, the storage term provided by changes in saturation degree, which is among the most impacting factors in pore pressure distribution and evolution in slopes subjected to a drawdown (together with the deformation of the solid skeleton) [179]. Because of these features accounted for in this formulation, the expected results may be more realistic. On the contrary, one of the strong points of the 2P-DP formulation is the ability to reproduce (in a simplified manner) fluidization. This aspect has impact on the shallow propagation, but potentially not on shape and depth of the major slip surface involved in this phenomenon, which can be captured with the unsaturated formulation. Reproduction of fluidization is a complex and advanced modeling topic which can represent an important feature requiring in-depth study and implementation strategies for future developments of this work.

The considered levee is 3m-high with a slope inclination of 2/3. A low-permeability layer is assumed to lie at a depth of 0.5m, here simulated with an impermeable boundary. The levee is assumed to be symmetric, thus the same geometry and discretization is used in both the drawdown and the rainfall case. The geometry and mesh discretization is shown in Fig. 5.1b. For computational efficiency, only half of the levee section is discretized. The model counts a total

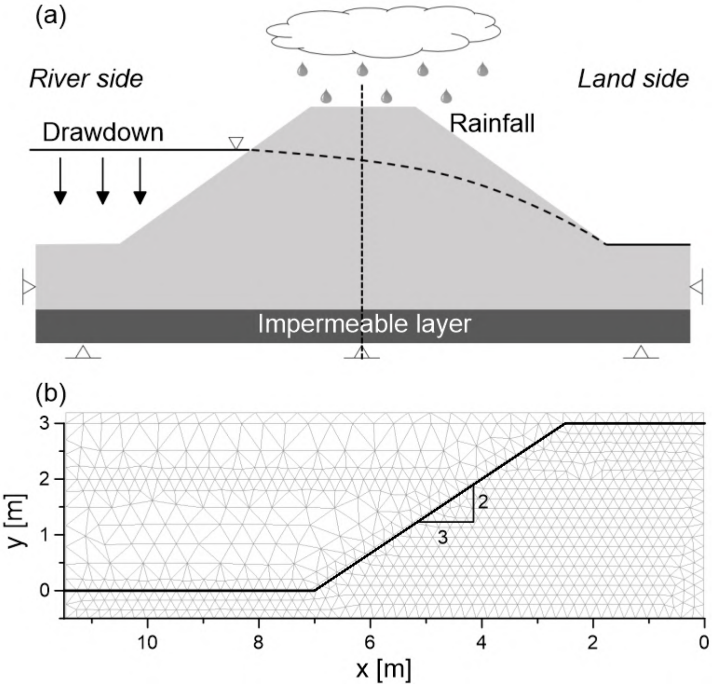

Figure 5.1: (a) Simplified representation of the levee example. (b) Geometry and discretization of the MPM model, from [116].

of 1669 linear triangular elements and 897 nodes. The average element size on the slope is 0.2m. 3 MPs are placed inside each initially active element. For the seepage analysis, a mesh of the same average size and type is used in the FEM model, for a total of 1158 elements. LEM analysis applies Bishop method and the entry and exit option for the slip surface search. A linear SWRC, with slope coefficient $a_v = 4.0 \cdot 10^{-4}$ 1/kPa is used, and the hydraulic conductivity is assumed constant. This permeability is higher than commonly found in these structures, and allows reducing the simulated time and computational cost. As presented in Sec.7, given the explicit nature of the numerical scheme used in *Anura3D*, the critical time step is strongly affected by the hydraulic conductivity. Therefore, it is very hard to currently assign values of hydraulic conductivity typical for silts or clays to a real scale embankment, and with these values be able to reproduce a phenomenon with hours duration in an acceptable computational time. For example, depending not only on the material properties but also on the mesh size, it may take months to simulate a physical phenomenon lasting few hours in a real scenario. An elastic-perfectly plastic Mohr-Coulomb constitutive model,

Solid density $[kg/m^3]$	ρ_S	2700
Liquid density $[kg/m^3]$	ρ_L	1000
Porosity [-]	n	0.4
Liquid bulk modulus $[kPa]$	K_L	80000
Liquid dynamic viscosity $[1/kPa]$	μ_L	$1 \cdot 10^{-6}$
Intrinsic permeability $[m^2]$	κ_L	$4 \cdot 10^{-11} m^2$
Young modulus $[kPa]$	E	50000
Poisson ratio [-]	ν	0.30
Friction angle [°]	ϕ	27
Cohesion $[kPa]$	c'	2

Table 5.1: Material parameters for levee collapse example.

defined in terms of effective stress, is adopted to model the soil behavior, with the material parameters listed in Tab. 5.1. Cohesion and friction angle in unsaturated soils are function of suction, but this effect is assumed negligible in this example. Although the constitutive model is simple, it can provide a realistic representation of the levee response; more advanced constitutive models are used in following examples of this chapter.

2.1 Reproduction of slope instability due to rainfall and high river level

Enduring high water level on the riverside and heavy rainfall can sometimes concur leading to rapid saturation of the levee and potential instability. The geometry and boundary condition of the numerical model are shown in Fig. 5.2. At the right-end, a liquid pressure linearly increasing with depth (hydrostatic pressure distribution) is applied to reproduce in a simplified way a water level of 2.0m on the riverside. The levee surface is a potential seepage face during the initialization phase, and then an infiltration rate $\widehat{w}_y = 1 \cdot 10^{-4} m/s$ is applied to simulate a heavy rainfall in the following steps. Horizontal fixities are applied to the solid phase at the lateral boundaries and the bottom is fully fixed. To generate the initial stress distribution, liquid pressure, seepage face and gravity load are applied assuming an initially high material cohesion (20kPa). Then, cohesion is reduced to 2kPa and the slope is stable with a stress distribution in equilibrium with the applied initial loads.

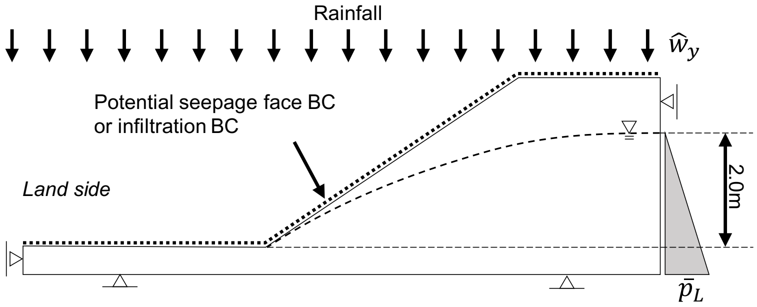

Figure 5.2: Geometry and boundary condition of the model simulating rainfall infiltration on a levee, from [116].

2.1.1 RESULTS

The initial pore pressure distribution obtained with MPM and FEM is in very good agreement (Fig. 5.3). FS evaluated with Bishop method is higher than 1, and indeed the slope is stable and deformations are very small. After stress initialization, rainfall infiltration is applied at the top surface, soil suction decreases and the slope fails. LEM analyses give $FS < 1$ for a time $t = 2s$, which means that the failure surface is fully developed at this moment (Fig.5.4). The MPM results are now presented.

A small decrease of suction is sufficient to trigger the failure, as shown in Fig. 5.5a-c. During soil movement, pressure oscillations are observed. Fig. 5.5d-f plots the evolution of shear strain at significant time instants, showing that a circular failure surface develops rapidly from the bottom of the slope and propagates upward. The shape of the failure surface is in agreement with LEM; however, in MPM it is a result of the calculation, while in LEM it is an hypothesis of the analysis.

Displacements increase suddenly between 5 and 20s (Fig. 5.6). At t=20s the slope finds a new equilibrium configuration measuring 17cm of displacement of the toe and 25cm at the crest. At about 100s there is a further increase of displacement of 2cm due to enduring rainfall infiltration. The crest of the levee moves downward approximately 22cm, which means that the levee in its deformed configuration is probably still able to fulfill its retaining function. This consideration, impossible

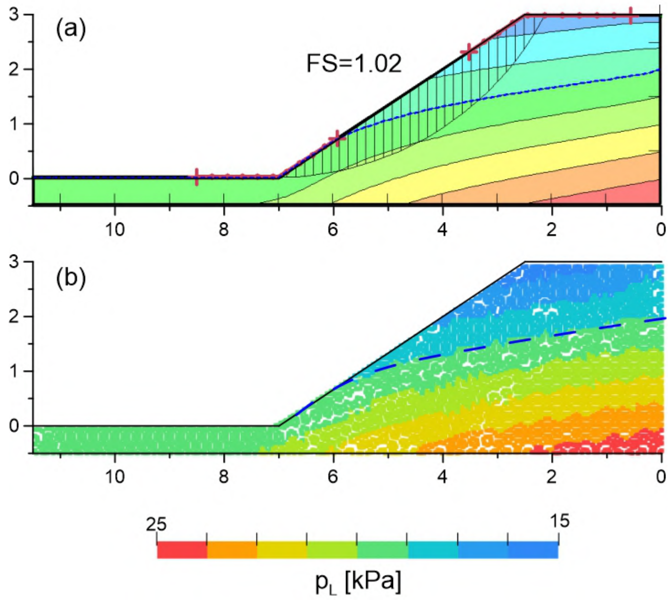

Figure 5.3: Initial pore pressure distribution with (a) FEM and (b) MPM. Safety factor with LEM, from [116].

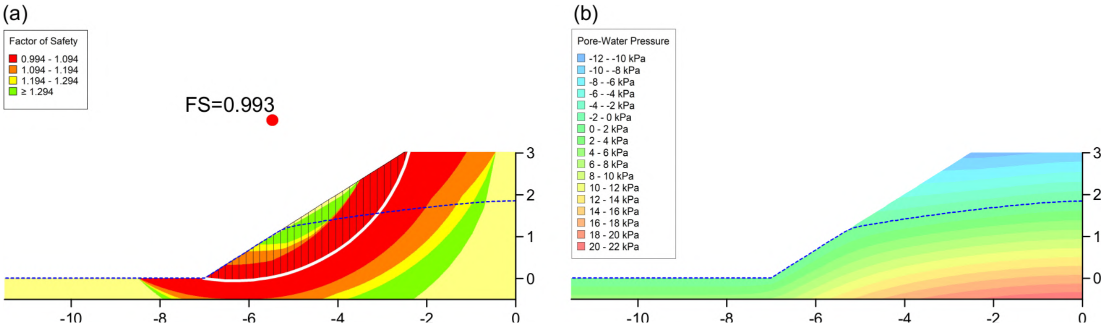

Figure 5.4: First occurrence of $FS < 1$ in LEM analysis (a). Critical slip surface and safety map. Contour of pore pressure from parent seepage analysis (b). Dashed blu line stands for the phreatic line.

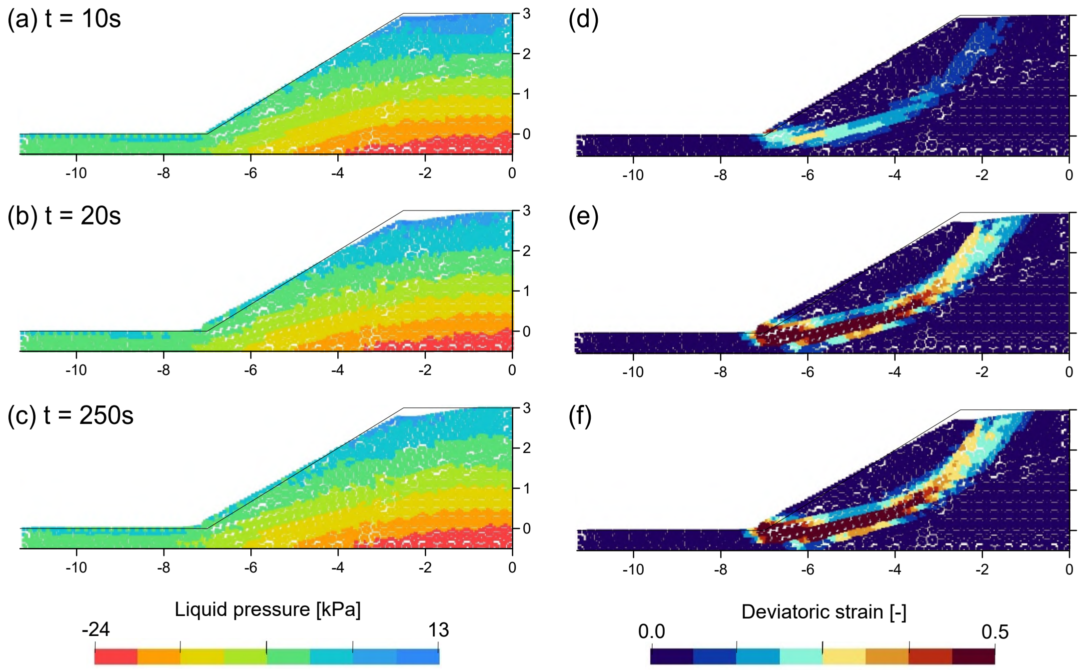

Figure 5.5: Pore pressure (a-c) and deviatoric strain (d-f) contours at different time instant (10s, 20s and 250s)

to get with FEM or LEM, can have significant practical consequences for planning of cost-effective remedial measures.

2.2 REPRODUCTION OF SLOPE INSTABILITY DUE TO RAPID DRAWDOWN

In this case, the initial stress distribution is generated with $K0$-procedure, assuming a river level at 2.0m and $K0 = 0.5$. Then, the applied total head is rapidly decreased to the low water level of 0.5m (Fig. 5.7). As introduced in Sec. 4.1, handling pore pressure in the boundary above the current river level has been progressively improved during this thesis work. In this section, the results of the initial implementation with constant pore pressure imposed are firstly presented. Then, the subsequent (and current) implementation is tested, where the potential seepage face is applied above the current river level boundary nodes. Note that, if measurements of suction data collected on river levee with time are available for a real case study, it is possible to set the constant approximated value based on the real initial condition.

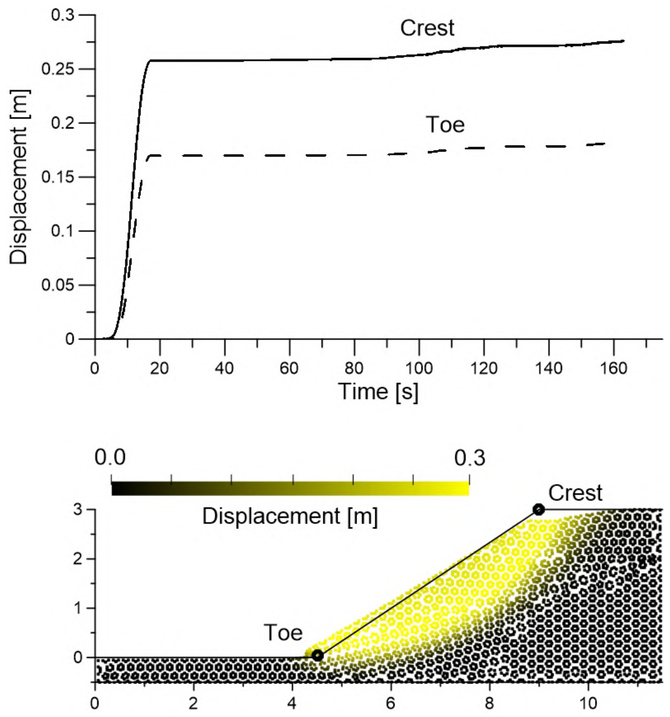

Figure 5.6: Evolution of displacement with time and final displacement contour, from [116].

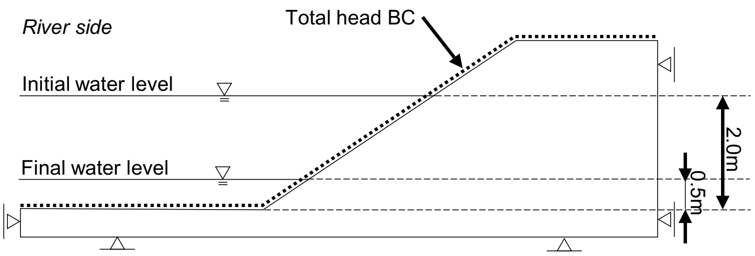

Figure 5.7: Geometry and boundary condition of the model simulating drawdown on a levee, from [116].

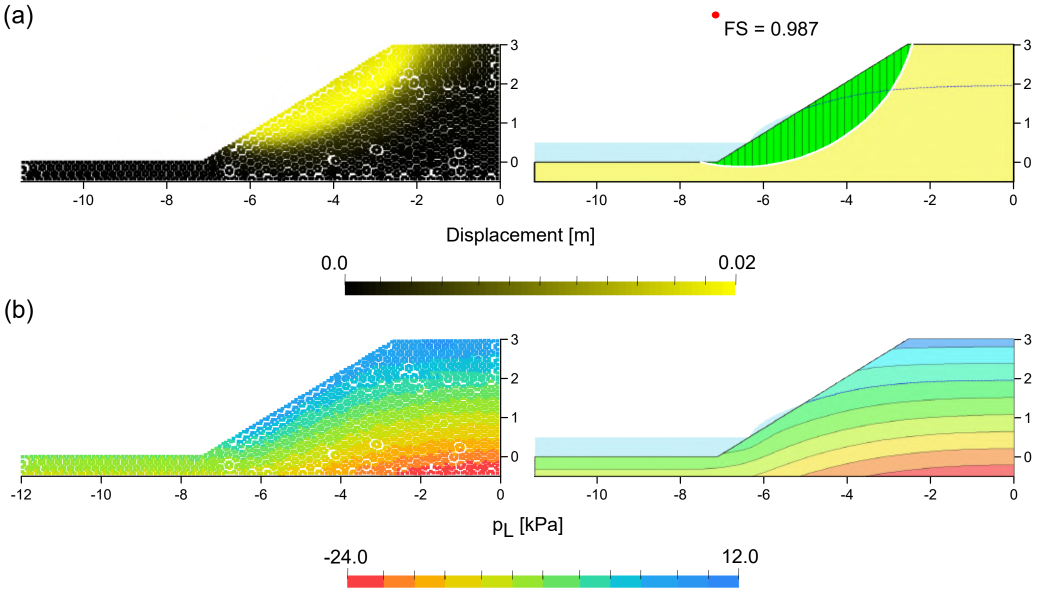

Figure 5.8: Onset of failure: a) Solid displacement norm for MPM and critical slip surface for FEM-LEM b) Concurrent liquid pressure in the same moment, from [116]. Dashed blue line stands for the phreatic line.

2.2.1 RESULTS

In order to emphasize the hydromechanical character of the depicted process, the onset of failure and the concurrent pore pressure distribution for MPM and FEM-LEM analyses are presented in Fig.5.8. For MPM, the norm of solid displacement is used to show the development of the slip surface, while in the LEM the circular surface is automatically generated, just by imposing ranges of entry and exit, and the relative FS is obtained. The failure onset is identified in LEM by the FS passage to a value lower than one, while in MPM it is here identified when the deviatoric strain assumes a value equal to 0.05 and at the same time vertical displacements of the cm-order can be detected at the MPs on the levee crest. The shape of the slip surface is consistent among the two models. The occurrence time of the failure onset differs for a few seconds, which can be explained by looking at the pore pressure distribution above the current river level, as visible in the sketch of Fig.5.8. This difference can be explained because in the MPM simulation, a constant pressure is imposed along the boundary portion above the river height, while in FEM a potential seepage BC is applied instead [46]. Only for MPM it is possible to track the river bank collapse progression during time. The post-failure

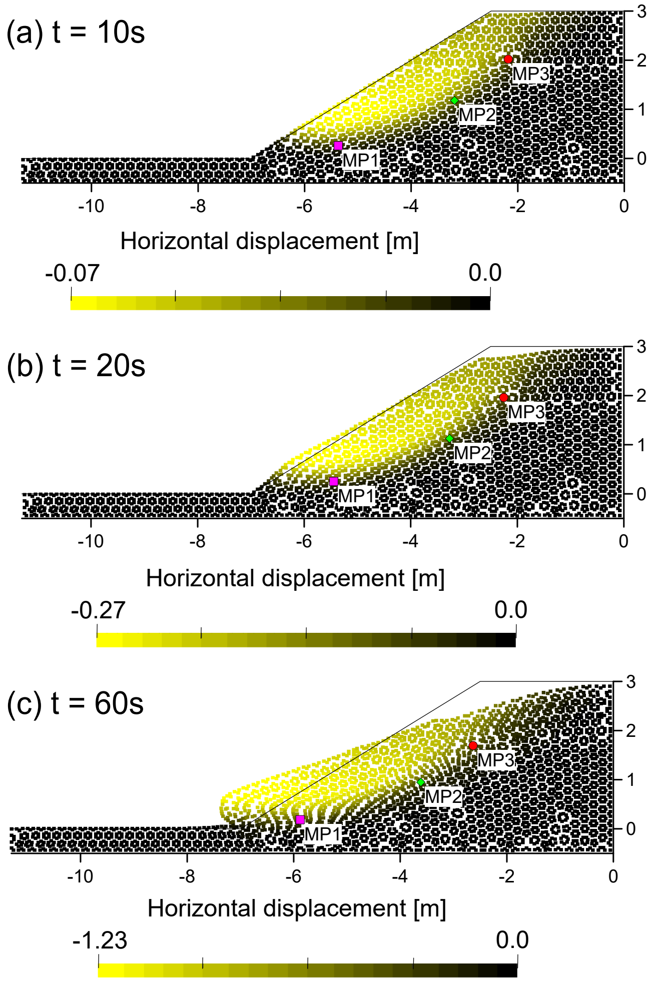

Figure 5.9: Horizontal displacement contours at 10s, 20s and 60s. Identification of MP1, MP2, MP3 along the slip surface, from [116].

behavior is captured in Fig. 5.9 by plotting the horizontal solid displacements at three time instants, together with the initial soil surface elevation reference.

The phenomenon is clearly characterized by large displacements, at the end exceeding 1m (Fig. 5.9c); thus the irreversible collapse of the internal bank is determined. Three MPs nearby the slip surface (MP1, MP2, MP3) are tracked during the slope motion in Fig. 5.9 and used to analyze the evolution of liquid pressure (Fig. 5.10a) and deviatoric strain (Fig. 5.10b) with time. In the first 3 seconds, all the MPs experience a sudden reduction of liquid pressure as a result of the dynamics induced by the rapid drawdown. It is followed by a gentle pressure increase till 20s, and a subsequent interval of pressure oscillations. In general,

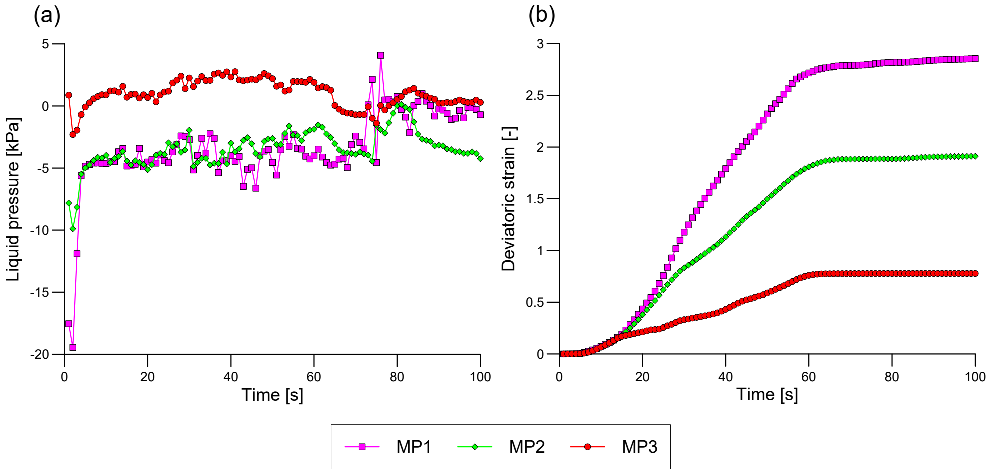

Figure 5.10: Liquid pore pressure (a) and deviatoric strain (b) evolution with time for three selected MPs nearby the slip surface, from [116].

the pore pressure values reflect the overall state of slow desaturation of the slope, antithetic to the rapid kinematic process of slope instability. Concerning this last, the deviatoric strain curves which represent the progressive increase of MPs undergoing plastification around the slip surface area, follow a continuous increase till maximum values are reached at 60s. In addition, the graph shows that from the slope crest towards the toe, the MPs deformation magnitude coherently increases.

2.2.2 Results of new implementation of hydraulic head BC

The results of the same drawdown case with the new implementation of the total head boundary condition are now presented. Dynamic and run out distance result quite different from the previous case. In fact, case all the collapse and final displacements develops in the first 10 seconds, and the maximum displacements of occurs at 6s and remain constants until the end of the simulated time (100s). This behavior is in agreement with a significantly higher pore pressure distribution in the top portion of the slope. Contour of displacements and pore pressure at three significant time instants are plotted in Fig.5.11. These values of suction are in better agreement with the results provided by *Geostudio*. Therefore, when a validation with this software is under treatment, this implementation of the boundary condition is more suitable to compare the results. However, in real case scenarios the pore pressure above the current river level is determined by the

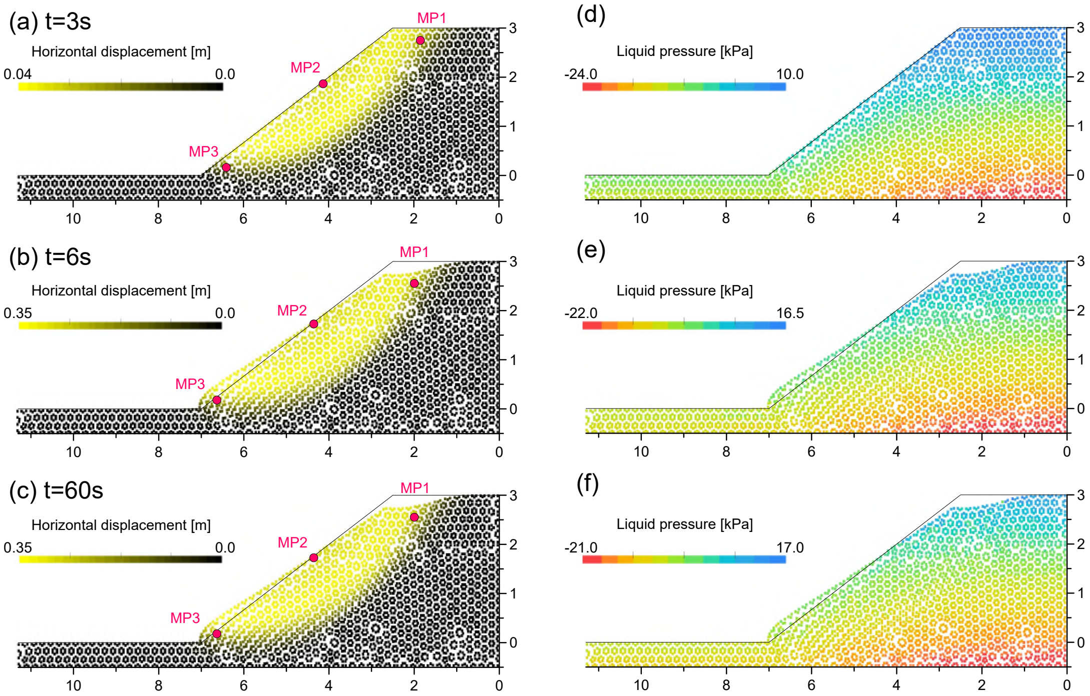

Figure 5.11: Displacements (a-c) and liquid pressure (d-f) contours for three time instants (t=3s, 6s and 60s).

atmospheric conditions and the retention properties of the soil, as explained in Chapter 4.

In Fig.5.12 the quantities pore pressure, deviatoric strain and saturation degree are tracked for three MPs (MP1,MP2 and MP3) indicated in the previous Fig.5.11. On the contrary respect to the previous case, pressure and strain change immediately after the river level reduction, then settle on the new value for the rest of the simulation time.This is particularly true when looking at the deviatoric strain graph, while for the pore pressure slight modifications are visible, depending on the seepage face boundary conditions imposed. In agreement with this, it is possible to observe that the MP undergoing greater modifications along time is the one at the crest, MP1. Indeed, from Fig.5.12 it is visible that the saturation degree keeps reducing after the drawdown, never stabilizing. It is important to keep in account the effect of high suction values developing along the slope surface when the seepage face condition is used. Effective stress distribution and strength parameters of the soil can be impacted, resulting in a over estimation of the actual slope stability. It is always advisable, when for example monitoring data

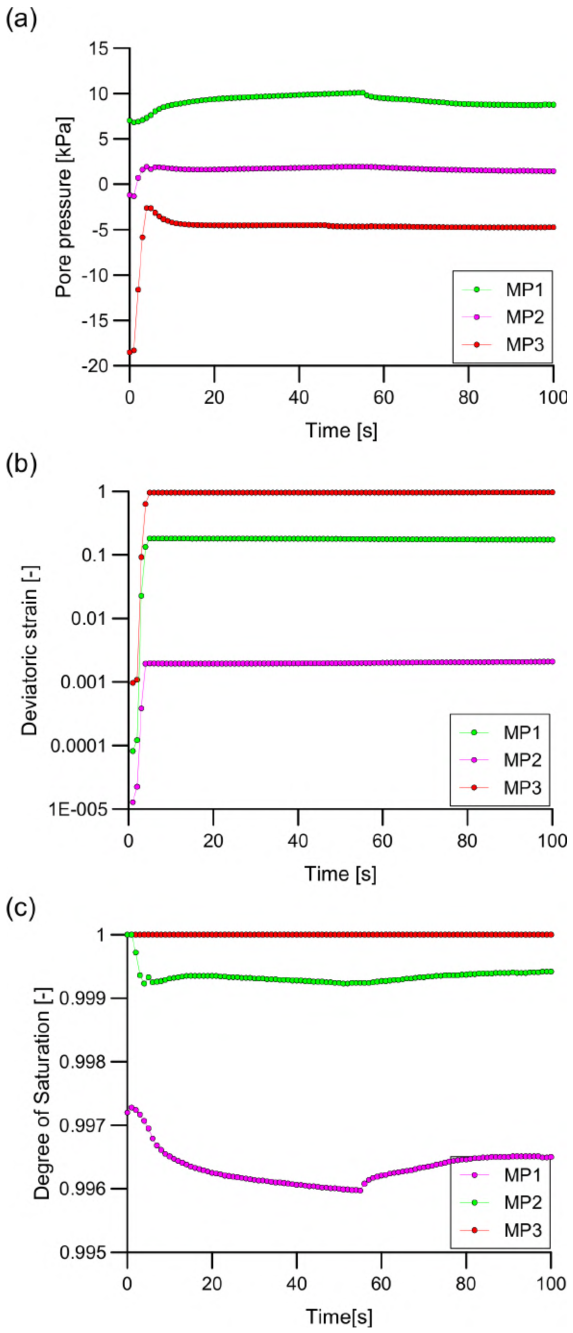

Figure 5.12: Liquid pore pressure (a), deviatoric strain (b) and saturation degree (c) along time for three selected MPs nearby the slip surface.

from tensiometers are available, to set the suction distribution above the phreatic surface in agreement with them.

3 Collapse of an experimental slope due to water table variations

A large-scale human-made slope stability problem inspired by [22] is now considered to highlight the potential of unsaturated MPM as a computational tool for large strain analysis. The sequence of hydraulic loads acting on the slope mimics real field scenarios, thus giving the chance to model the failure mechanism and perform a comparison of the shape of the failure surface. LEM and MPM analyses are performed.

3.1 Experimental test description

The presented case is inspired by the work of [22], focused on the experimental collapse of a 6m high slope. The test explores a slope collapse due to rising and lowering of the water table, which is one of the primary causes of landslides and human-made earth structure failures [41]. The collapse mechanism in this experimental case depends on two factors: (i) firstly, a wetting-induced collapse of the loose slope material which induces progressive settlements; (ii) secondly, shear strength reduction due to suction decrease, which caused the generation of the slip surface and slope collapse. In this work, the focus is on this second mechanism.

The model dimensions are 6x15x5m. The slope inclination is 45°, with a crest width of 5m. A silty-sand mixture is used. Local measurements of soil density indicate some degree of inhomogeneity and that the material is in loose state. Consistently, an average value of porosity $n = 0.5$ is assigned in the numerical model. The strength parameters obtained with consolidated-undrained triaxial tests are a cohesion of $c' = 1\ kPa$, and a friction angle of $\phi = 30°$. The parameters of the SWRC (Tab. 5.2) are calibrated by fitting the adsorption branch found by [22] (Figure 5.13) with the use of a volumetric pressure plate extractor.

In the experiment, the water table variations are produced by a network of holed tubes in a sand layer at the base of the slope. The tubes are linked to an external water storage tank which controls the applied total head.The slope model and water level regulation system are reported in Fig. 5.14. The total head history is divided in three main phases: (i) water table rising in 6 steps, (ii) maximum

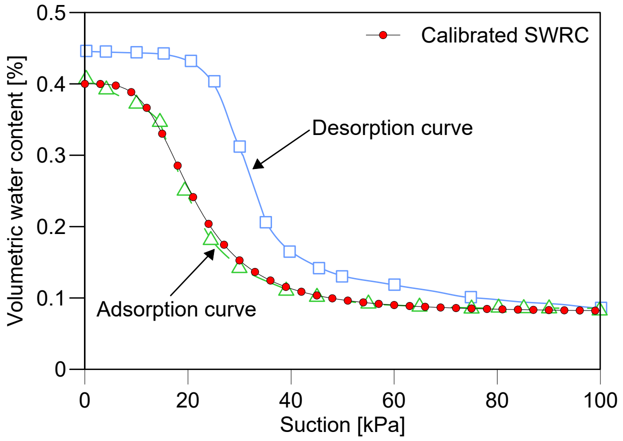

Figure 5.13: SWRC calibration by fitting the adsorption branch from [22].

S_{max}	0.8	[-]
S_{min}	0.16	[-]
p_{ref}	19.0	$[kPa]$
λ	0.75	[-]

Table 5.2: SWRC parameters for the numerical slope

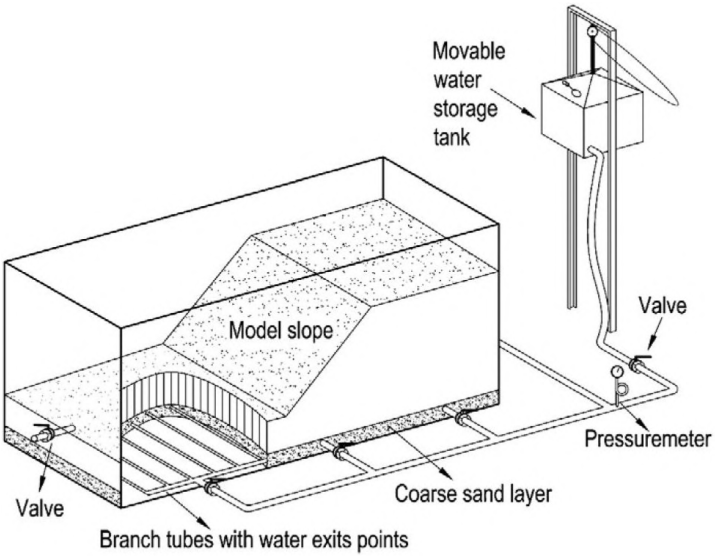

Figure 5.14: Experimental set up: slope physical model and water level control system, from [22].

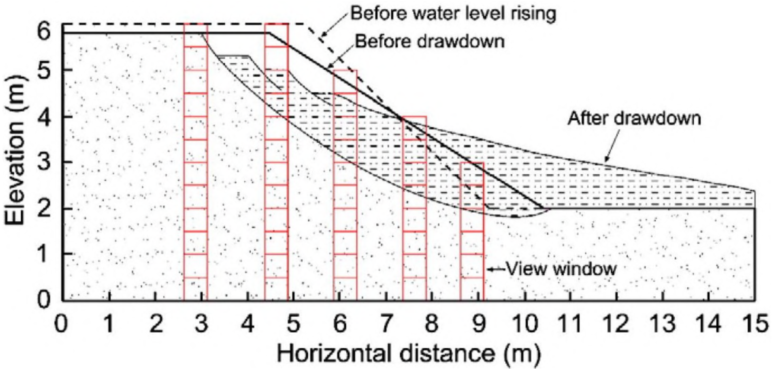

Figure 5.15: Slip surfaces sketch, associated to the two experimental phases, from [22].

level maintenance, corresponding to a fully submerged condition, and (ii) sudden drawdown that brings the water table to 3m.

Two phenomena were observed while raising the water level. First, the crest of the slope model settled.The observed settlements are likely attributable to wetting-induced collapse of the unsaturated loose silt. Second, the loose fill under the sloping surface collapsed gradually as the water level rose, as a consequence of the reduction in shear strength. Only this second aspect can be captured by the MPM model which will be presented in the following sections. The initial slope angle of 45° was reduced to approximately 33° as the water level rose to near the crest of the slope model, as visible in Fig. 5.15. In this sketch, the authors present the slip surfaces identified at the end of the two phases of the experiment.

If on a side, the instability induced by the wetting progress doesn't undermine the overall safety of the slope, which finds a new stable configuration during the level maintenance time, on the other the rapid drawdown generate a catastrophic collapse of the model slope. This is visible in some pictures captured by the authors during the collapse phase (see Fig. 5.16), where it is evident the formation of cracks, detachment and rotation of blocks in series and significant propagation of saturated soil masses. Despite the complexity of this experimental case, it still represents a challenging situation to test the applicability of the unsaturated formulation in reproducing large displacements in unsaturated slopes like water retention earth structures.

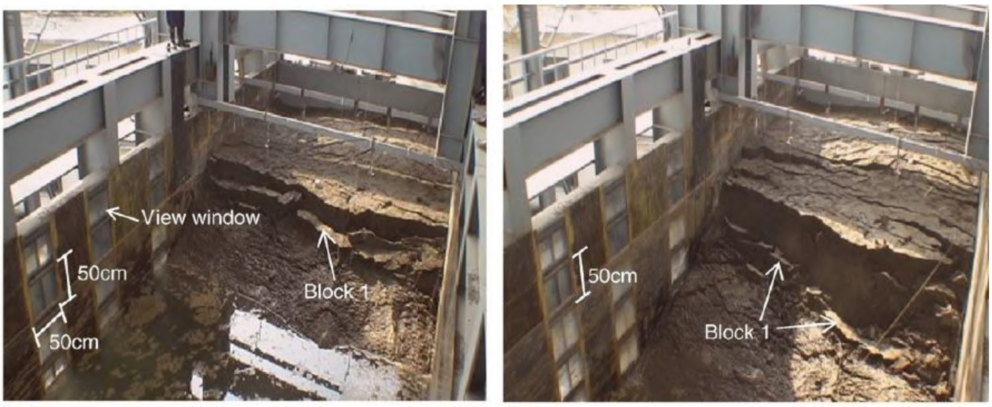

(a) *The water level was drawdown for 0.7m* (b) *The water level was drawdown for 1.5m*

(c) *The water level was drawdown for 1.9m* (d) *General view of the final landslide*

Figure 5.16: Pictures of experimental collapse evolution after rapid drawdown, from [22].

3.2 NUMERICAL MODEL DESCRIPTION

The geometry is built considering two-dimensional plane strain conditions consistent with the dimensions of the experiment (Figure 5.19a). The overall discretisation is conducted with triangular 3-node elements of 0.3m length, each assigned with 3 MPs. A local mesh refinement was applied along the slope surface reducing element length to 0.2m. The total number of elements is 2679. Linear elements are used in this study, thus an appropriate h-type mesh refinement is considered to reach an adequate level of accuracy. Although the use of higher order shape functions has been explored to improve accuracy in MPM [74, 180], their applicability in complex problems is still under investigation.

The material properties are summarized in Tab. 5.3. The intrinsic permeability corresponds to a saturated hydraulic conductivity of $k_{sat} = 5.3 \cdot 10^{-5}\, m/s$, which is one order of magnitude higher than the one reported in the experiment. This is done to reduce the computational cost of the simulation. The numerical time scheme employed in the MPM is explicit. Therefore, the use of extremely small time step increments (e.g., 0.0001s) is required to ensure the stability of the calculation. In these conditions, the computational resources needed to simulate long timescale problems (e.g. days) are very large. The critical time step depends on the hydraulic conductivity; the larger the hydraulic conductivity, the larger the critical time step ([110, 175]). The approach of increasing the hydraulic conductivity to speed up the calculation has been used previously ([159, 181]) when reproducing slope failures. Increasing the hydraulic conductivity will also speed up the pore pressure dissipation and the water front progressing through the slope. However, if the pore water pressures before the collapse obtained in the numerical model are similar to those in the reference problem, it is expected that the impact of using a larger hydraulic conductivity on the failure mechanism is small. In the simulation presented herein, the pore pressures just before the collapse obtained with the MPM simulations (i.e., $H = 6m$ in Figure 5.20g) are consistent with the laboratory measurements ($t = 192$ from [22]) and the FEM calculations (i.e. Figure 5.21). Therefore, it is possible to conclude that using a hydraulic conductivity one order of magnitude higher than the experimental value is an acceptable approximation.

In addition to the saturated conductivity value, a HCC is specified. Since no

ρ_S	2639	$[kg/m^3]$
ρ_L	1000	$[kg/m^3]$
n	0.5	[-]
K_L	80000	$[kPa]$
μ_L	$1.0 \cdot 10^{-6}$	$[kPa \cdot s]$
κ_L	$5.4 \cdot 10^{-11}$	$[m^2]$
E	39000	$[kPa]$
ν	0.30	[-]

Table 5.3: Material parameters for the slope numerical model.

experimental data are reported, three different curves available in *Anura3D* code are tested (Figure 5.17): a suction-independent HCC (i.e., constant and equal to k_{sat}), Hillel expression (Eq. 4.30), and Mualem expression (Eq. 4.31). In the expression by Hillel, a reasonable value of 2 is assigned to the exponent r (usually variable in the range 2-4) while the parameters for Mualem model are specified in Tab. 5.2.

As for the soil constitutive model, an extension of the elastic-perfectly-plastic Mohr-Coulomb model for unsaturated soils proposed by [159], introduced in Chapter 4 Sec. 2.4 is adopted. The beneficial effect of suction on strength parameters is included. The shape and evolution of the slip surface is influenced by the evolution of the degree of saturation because the shear strength is non-linearly dependent on suction. In the selected model, the non-linearity is accounted in the cohesion variation, while the friction angle changes in a linear manner. In absence of experimental data about the shear strength in unsaturated condition, and in order to compare the results of LEM and MPM, the parameters of the constitutive model are calibrated to define a reasonable strength variation in the expected suction range. The LEM analysis is preceded by a transient seepage analysis, considering the same hydraulic load history of the experiment. Two different shear strength suction-dependent models are available in *Geostudio* software to perform the LEM analysis: the non-linear equation depending on the SWRC proposed by [154]

$$\tau = c' + (\sigma - p_G)\tan(\phi') + s\left[\left(\frac{\theta_w - \theta_r}{\theta_s - \theta_r}\right)\tan(\phi')\right] \tag{5.1}$$

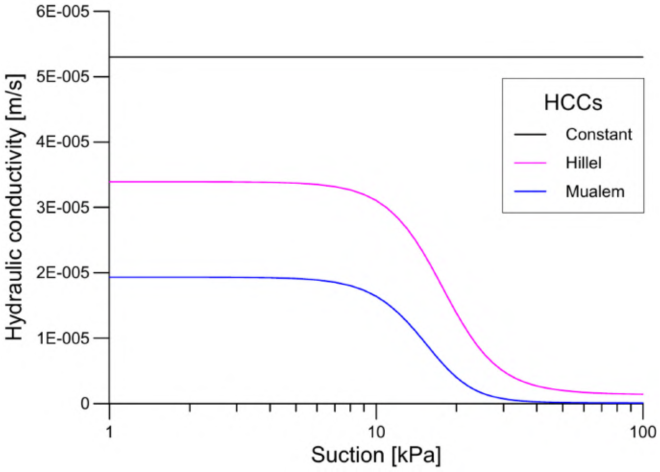

Figure 5.17: HCCs tested in the slope numerical model, from [150].

Combination	$\Delta c_{max}\,[kPa]$	$B\,[-]$
MC_1	15	0.04
MC_2	12	0.07

Table 5.4: Suction dependent elasto-plastic Mohr-Coulomb model parameters for two analyzed combinations.

and the linear law by [182] depending on the parameter ϕ^b

$$\tau = c' + (\sigma - p_G)\tan(\phi') + s\tan(\phi^b) \tag{5.2}$$

In the two equations, suction strength is the last term on the right-hand side, which is plotted as a function of suction in Fig. 5.18. In the experiment, the progressive onset of failure was observed when the water level was approximately between 5 and 6m. Consistently, the shear strength parameters in Eq. 5.1 and 5.2 are calibrated in order to reach a value of FS slightly lower than one around the time consistent with the observations. Then, the parameters of MCSS with suction are obtained by fitting the shear strength vs suction behavior given by previous models in the reference suction range (Fig. 5.18). The variation of friction angle due to suction is typically smaller than the one in cohesion and has less impact on the overall shear strength increment. In this particular example, the friction angle is assumed constant ($A = 0$ in Eq. 4.26) and only the cohesion depends on suction. The results from Fig. 5.18 lead to explore two different plausible combinations of B and Δc_{max}, reported in Tab. 5.4.

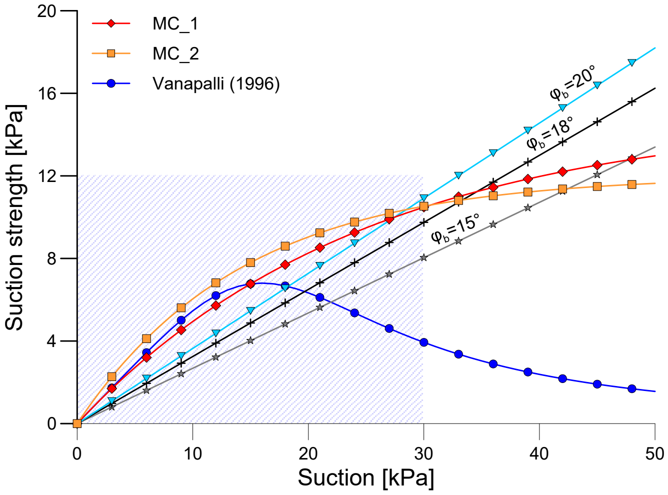

Figure 5.18: Soil model calibrated curves (MC_1 and MC_2) and reference curves: Vanapalli (1994) and Fredlund (1978), from [150].

3.3 Boundary conditions and calculation phases

Solid skeleton BCs include: (a) fixities along x-axis on the vertical lateral boundaries, (b) fixities along y-axis on the top edge, and (c) both x and y-axis fixities along the slope base (fully fixed BC). The hydraulic BCs are a key aspect in the reproduction of complex hydromechanical processes in the earth structure. To reproduce the wetting process, we need to capture the water table rising from the base of the model, whilst simultaneously considering the progressive water filling in front of the slope. After this step, the rapid drawdown phase is simulated, which triggers a rapid soil mass movement, until the entire slope collapses. Keeping in mind this sequence, the numerical simulation phases are presented and explained as follows:

Phase 1: Initialization A quasi static procedure is used to initialize pore pressure and solid stress in the slope. Matching the actual initial condition as seen in the experiment has a crucial impact on the subsequent reproduction of coupled pore pressure-deformation phenomena. To set up suitable BCs, the initial suction values provided by five tensiometers installed in the experimental slope, ranging from 1 to 30kPa, bottom to top, can be considered as a reference. Consistently, pressures from 30kPa to 5kPa are imposed along the slope surface, whereas a uniform value of 0kPa is applied along the lower boundary. In addition, the lateral boundaries are impermeable to the flux. The hydraulic BCs for this phase are presented in Fig. 5.19a.

Phase 2: Water table rising In the second phase, BCs are changed in time and space: the slope undergoes a progressive increase of pore pressure from the bottom, from -20kPa to -60kPa, in agreement with the experimental step sequence. Every pressure increment is reached in 2s and maintained for 60s. Simultaneously, along the surface nodes with initial imposed pressure, the condition is replaced with the hydraulic head BC. This ensures that values are in agreement with the bottom pressure, considering the hydrostatic gradient, as pointed out in Fig. 5.19b. In this way, it's straightforward to account for the water weight accumulating in front of the slope, as seen in the photographic documentation in the publication by [22]. Above the current water level, the seepage face condition gradually replaces the imposed pressure values. The final value of -60kPa along the bottom, corresponding to a complete submerged condition, is maintained for 112s, in analogy with the experimental procedure.

Phase 3: Rapid drawdown This phase investigates the slope failure mechanism. A rapid draining is put in place by suddenly (within 1s) reducing the bottom pressure to 30kPa and the hydraulic head BC is adjusted to a value of 3m. The corresponding BCs are illustrated in Fig. 5.19c. The simulation is then run for a sufficient time to observe the entire post-failure progression, until the soil mass stops moving.

Finally, a mass scaling factor of 100 is used to optimize the computational time and volumetric locking in triangular elements is mitigated by using a strain-smoothing procedure as described in [142].

3.4 RESULTS

In this section, the simulated results are described, focusing on the pore pressure variation, failure mechanism, and post-failure behavior. First, general observations from the numerical results obtained using the second combination of mechani-

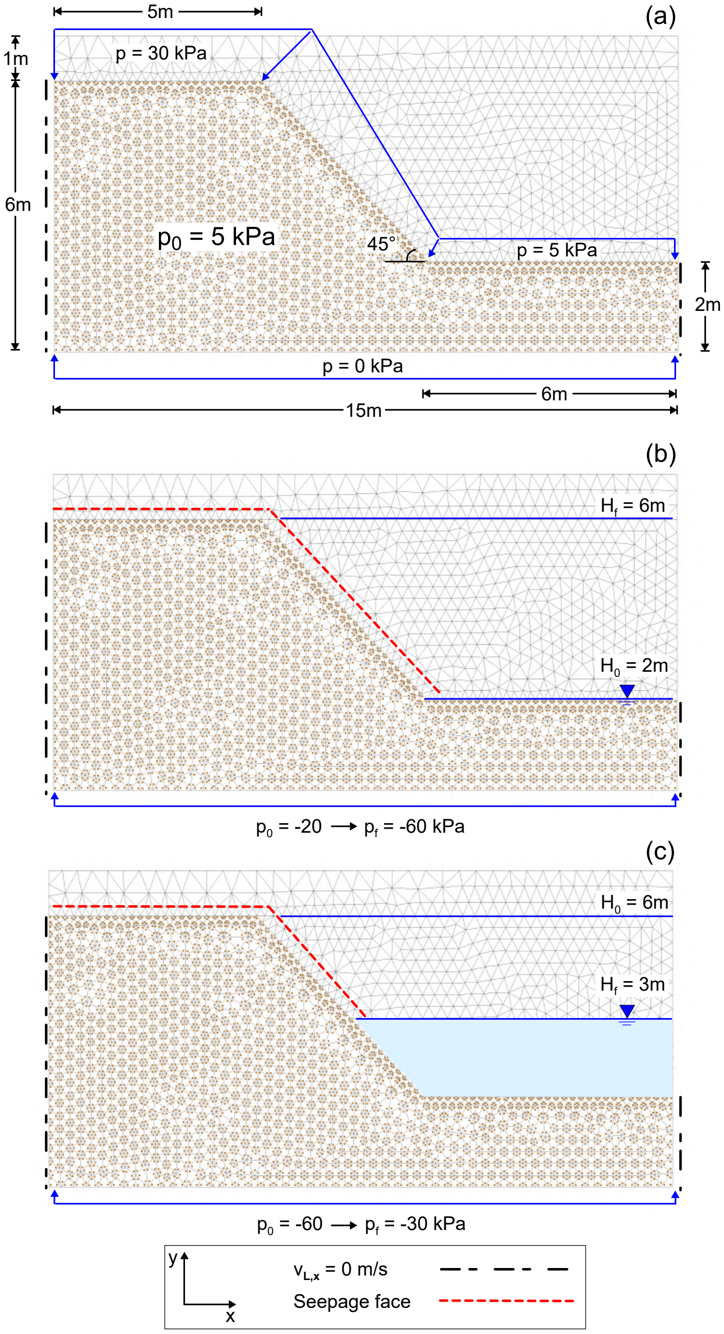

Figure 5.19: Hydraulic BCs for (a) initialization phase, (b) water table rising phase, and (c) rapid drawdown phase, from [150].

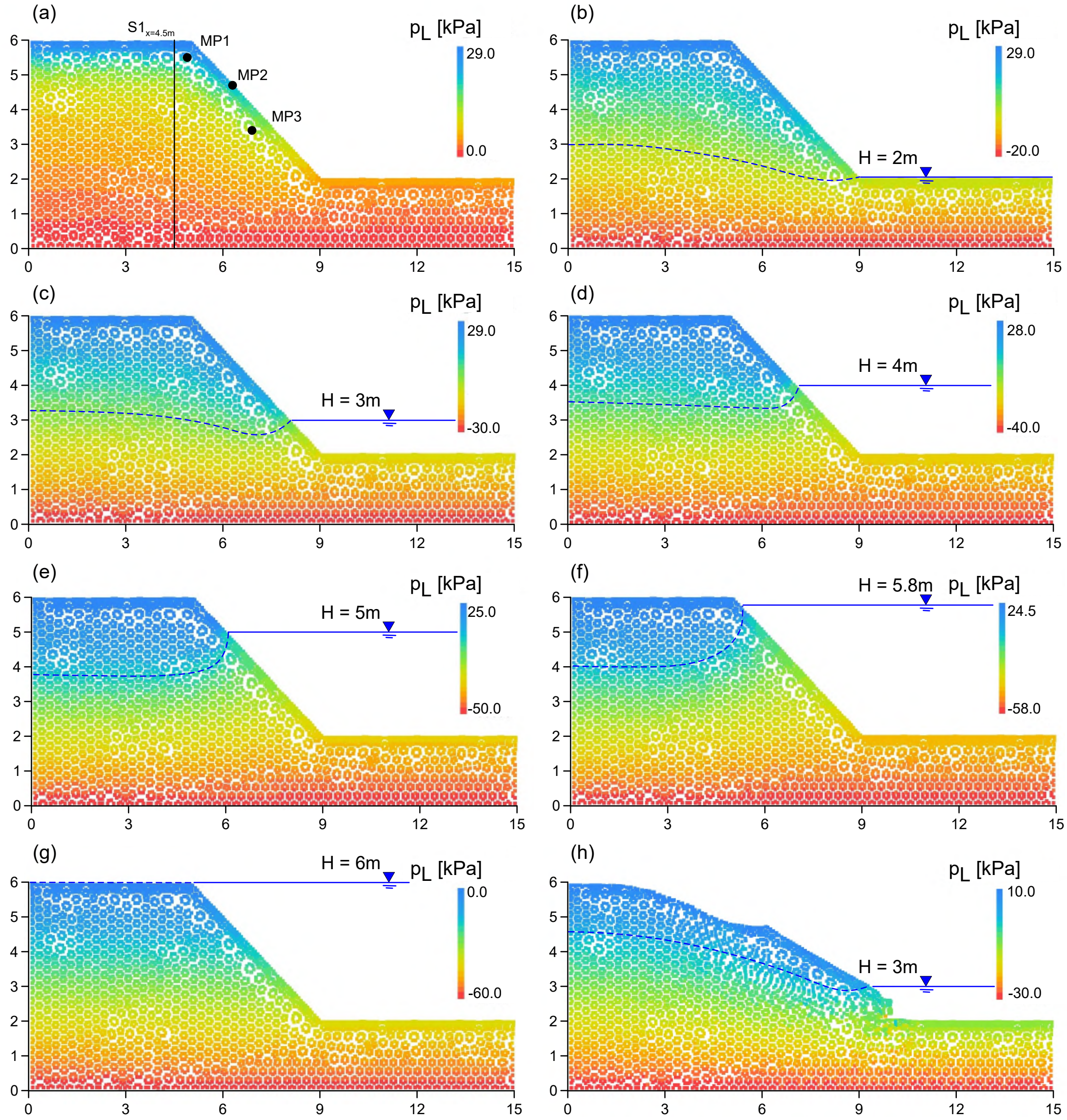

Figure 5.20: Pore pressure contour during the water table rising phase, (a) to (g) and at the simulation end (h). Dashed blue line stands for the phreatic line. Note that p_L range in color legends are different for every panel, to highlight the pressure increment series, from [150].

cal parameters, named MC_2. Then,a comparison of the outcome of different simulations to assess the impact of:

- The input parameters in the constitutive model, i.e. by testing the combinations presented in Tab. 5.4, while keeping constant the HCC;
- The different HCCs, while maintaining the same constitutive model parameter (in this case, MC_2).

The progressive water table rise directly impacts the pore pressure distribution in the slope. Fig. 5.20 presents pore pressure contours corresponding to each pressure increment, from (a) to (g), corresponding to the rising water table phase, and (h), corresponding to the end of the simulation. Note that the rising of the phreatic surface inside the slope shows a delay compared to the external water level. This effect is coherent with the resistance offered by the solid skeleton to the water propagation in the pores. With the rapid drawdown phase, the slope collapse is triggered as shown in Fig. 5.20h.

It is possible to observe that at the end of the rising water table phase, a shear surface develops (Fig. 5.21c), but this does not lead to large deformations because the slope finds a new equilibrium with small displacements. The geometry of the slip surface coincides with the mechanism obtained when $FS < 1$ in LEM analyses, as seen in Fig. 5.21a and b, using Fredlund and Vanapalli models respectively. Despite the three models reach failure at slightly different water tables (5.8m LEM and 6m MPM) the results are acceptable, especially considering the fact that in the experiment, the failure develops when the water level raises between 5 and 6m.

Fig. 5.22 reports the velocity of three MPs, whose initial position is visible in Fig. 5.20a. From this graph, it is possible to assess that the slope undergoes an initial acceleration, but it rapidly stops and large displacements are not observed before the drawdown. This behavior is not predictable by considering the LEM analyses and highlights the advantages of MPM in front of LEM to provide information of the extent of the slope run out. After this small movement, the initiation of the rapid drawdown phase triggers an acceleration increase which determines the large and irreversible soil mass movement. At the end, it can be observed that a deceleration phase occurs until the slope stops moving.

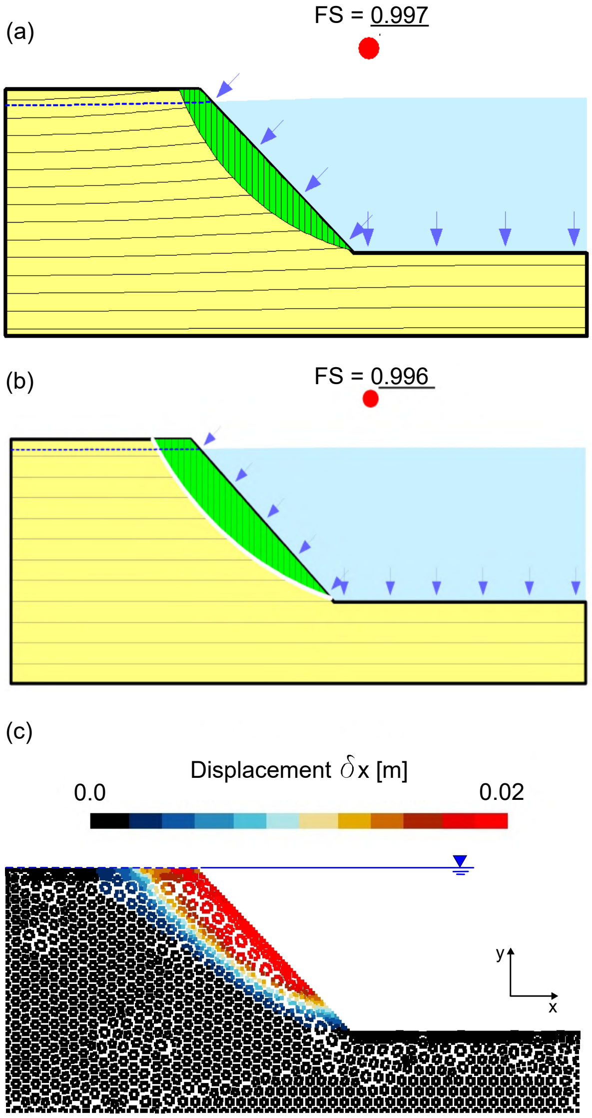

Figure 5.21: Slip surface occurrence before drawdown. LEM analysis (a) Fredlund model with $\phi_b = 20°$, and (b) Vanapalli model with FS indication. For MPM (c), the contour of horizontal displacements δ_x is depicted, from [150].

The two combinations of material parameters give similar results in the first phase. The calculated final displacements are different by approximately 30cm, whereby the combination MC_1 results in a final value of 2.17m, whilst MC_2 results in a final value of 1.83m. The final deposit for the two combinations is outlined in Fig. 5.23, depicting MC_1 in red and MC_2 in blue.

The experimental slope undergoes a complex failure mechanism: a combination of rotation and detachment of single massive blocks, resulting in more than one slip surfaces. More precisely, three slip surfaces can be observed and interpreted through the collapse dynamics. By plotting in Fig. 5.23 the final displacements of combination MC_1 and overlapping the deepest experimental failure surface, a good agreement is visible. The rotational movement occurring in the real case is well captured. However, our model is limited by its inability to fully capture the soil fluidization, since free water is not explicitly simulated by the 2Phase Single-Point approach. The fluidization during the experimental slope collapse is a consequence of the interaction with the free water accumulated at the toe of the slope. In the experiment, the slope toe reaches the model boundary, whereas the numerical slope stops moving after a maximum displacement of approximately 2m. In particular, all the performed simulations using both the constitutive parameter combinations and the different HCCs, end up with a maximum displacement value in the range between 1.8 and 2.3m. Finally, the impact of different HCCs is assessed. All the simulations start from the same initial pore pressure distribution. The models based on the constant and Hillel HCCs (Eq. 4.29 and 4.30) do not show significant differences in terms of duration. On the other hand, the simulation performed using Mualem (Eq. 4.31) requires more time to reach the full saturation prior to drawdown, due to the lower permeability in the unsaturated upper slope portion predicted by this approach. In Fig. 5.24, the pore pressure along a vertical section at x=4.5m (indicated in Fig. 5.20) is depicted for three time instants using the different HCCs. These three instants correspond to: (a) bottom pressure equal to -30kPa, (b) bottom pressure equal to -58kPa and (c) bottom pressure equal to -60kPa. Fig. 5.20c shows the slope saturation delay when using Mualem law. The final slip surface shape turns out to be similar for all the various simulations. As such, it is concluded the permeability law (HCC) has a substantial impact on the timescale but not on the rupture mechanism and the subsequent propagation phase.

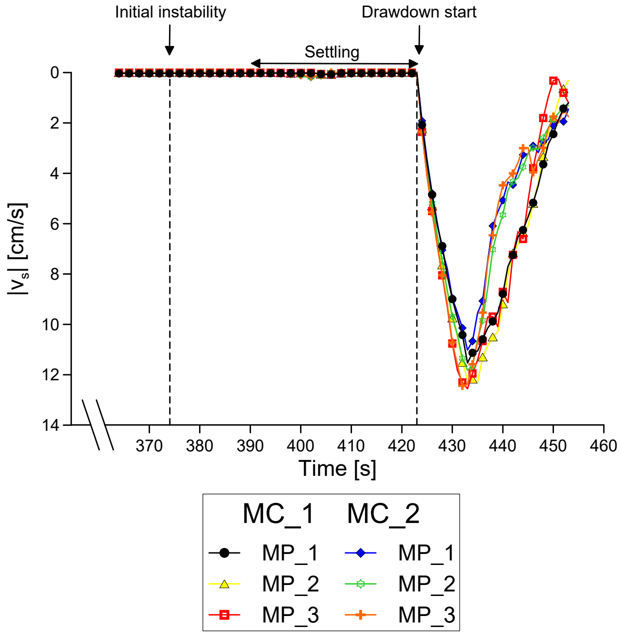

Figure 5.22: Kinematics of the slope model. Velocity norm vs time for three MPs using the two constitutive parameter's combinations. Initial time corresponds to the beginning of the maximum level constant phase, from [150].

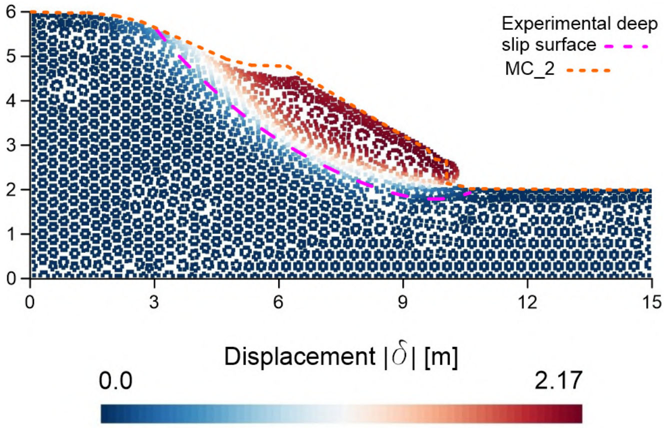

Figure 5.23: Norm of displacement at the end of the drawdown phase using MC_1. The final surface profile of MC_2 is also reported (orange line), together with the experimental slip surface (pink line), from [150].

(a) t=124s

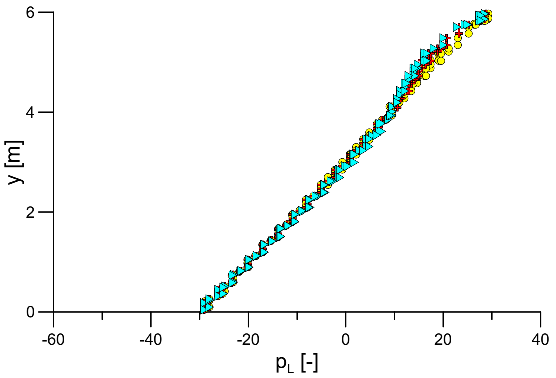

(b) t=310s

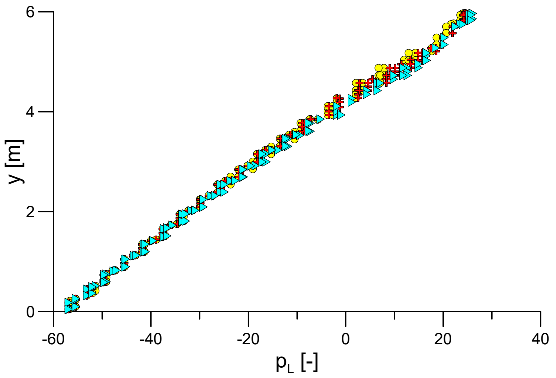

(c) t=420s

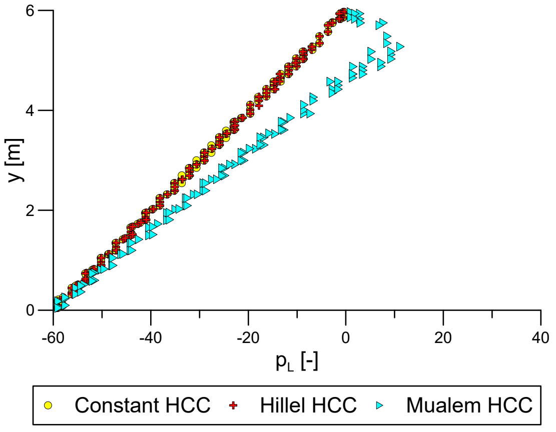

Figure 5.24: Comparison between different HCCs by plotting pore pressure p_L along vertical section S1 for three different time instants, from [150].

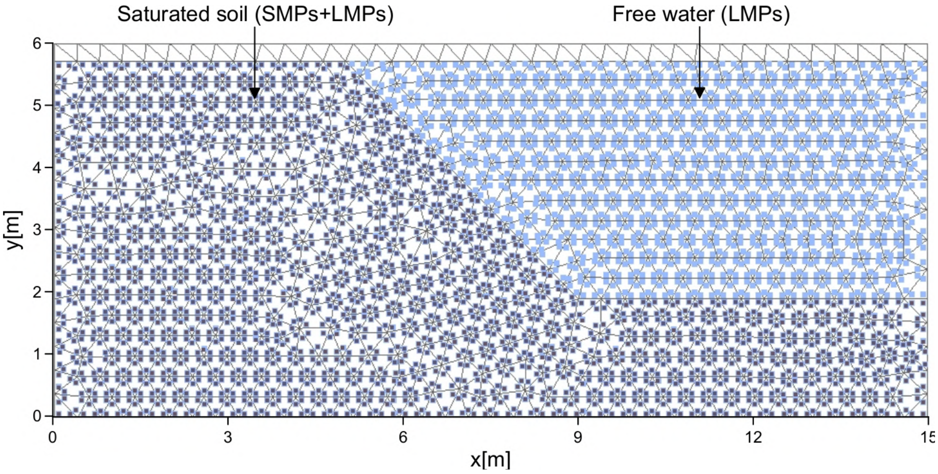

Figure 5.25: Geometry, discretization and MPs assignment related to the 2P-DP model reproducing the experiment by [22].

3.4.1 COMPARISON WITH DOUBLE POINT APPROACH: IMPACT OF FLUIDIZATION ON FINAL RUN OUT

A model with the same geometrical features as the previous is built considering the 2Phase-DP formulation. Only the drawdown phase is captured, with the aim of employing an MPM formulation more suitable to reproduce fluidization resulting from dynamic processes in saturated soils. In this case the initial condition is the one corresponding to full saturation of the experimental slope, i.e. fully submerged, with a water table as high as the slope crest. Based on the experience collected with the model presented in Sec. 3, the model is set up considering a region of free water in front of the slope, and a region of saturated soil corresponding to the slope domain. The average mesh size of the mesh, made by triangular elements, is 0.3m. 12 LMPs are assigned to the free water domain, while 12LMPs + 12SMPs to the solid domain. Mesh discretization and MPs assignment at the beginning of the simulation are visible in Fig. 5.25. The only material property changing is the Bulk modulus of the liquid which is imposed equal to 25000 kPa, for computational speed up. The other material parameters are the same as in Tab. 5.3. In addition, in the double point formulation it is necessary to specify a permeability update law, in this case Darcy law is use, for a better comparison with the previous model. The parameter that control the fluidization process is the maximum porosity. Usually it is defined based on laboratory data, in terms of e_{max} and e_{min}, respectively, maximum and minimum void ratio. In this case these data were not present, so different values of maximum porosity are tested, and the results compared with the final slope profile as a calibration. A value of 0.5 is finally chosen. The initialization of stress and pressure is done with *K0-procedure*, considering a value of K0=0.5. After the initialization, the water table is drop to 3m by removing LMPs in a time of 1.2s, similar to the previous model. Subsequently, the simulation is run until the slope stops moving, which corresponds to a duration of 148s.

3.4.2 RESULTS

The dynamic of the collapse is shown by plotting deviatoric strain of SMPs together with LMPs (blue dots) in Fig. 5.26.The selected five instants of time to plot the results are all after the level drawdown: at (a) 2.7s, (b) 10.2s,(c) 22.7s, (d) 72.7s and (e) 148s (end of simulation).The slope failure starts with a shallow localization as visible in Fig. 5.26(a) which deepens and spread laterally in a few seconds, as visible in Fig. 5.26(b). After this instant, the slip surface doesn't grow deeper while it just involve a slightly bigger portion of the slope, in the direction of the crest, while the slope front tends to propagate in the opposite direction (see Fig. 5.26(c)). When looking at the LMPs, it appears that the slope collapse is inducing a very turbulent behavior, with waves generation. As time progresses, while an imposed external water level reduction occurs, with a consequent progressive reduction of the phreatic surface in the slope, the free water in front of the slope tends to accumulate and its level increases. Concerning this aspect, it's hard to compare it with the experimental results since the pictures captured in the second phase, see Fig. 5.16, cut the lower portion of the slope. Given the numerical boundaries assigned to LMPs and SMPs, the result looks physically coherent. The evolution of collapse shows that the majority of the soil mass failure is concentrated in the first 23s, slightly longer compared to the previous model results, but still very rapid. The following part consists in a slower soil and water settlement toward a new equilibrium configuration. This final configuration is reported in Fig. 5.27. The norm of displacement contour is used and the final profile of the experimental slope is also reported with a dashed red line. It is possible to appreciate that the final run out is significantly greater compared to the previous model results (see Fig. 5.23), with maximum displacements of the SMPs equal to 7.43m along x

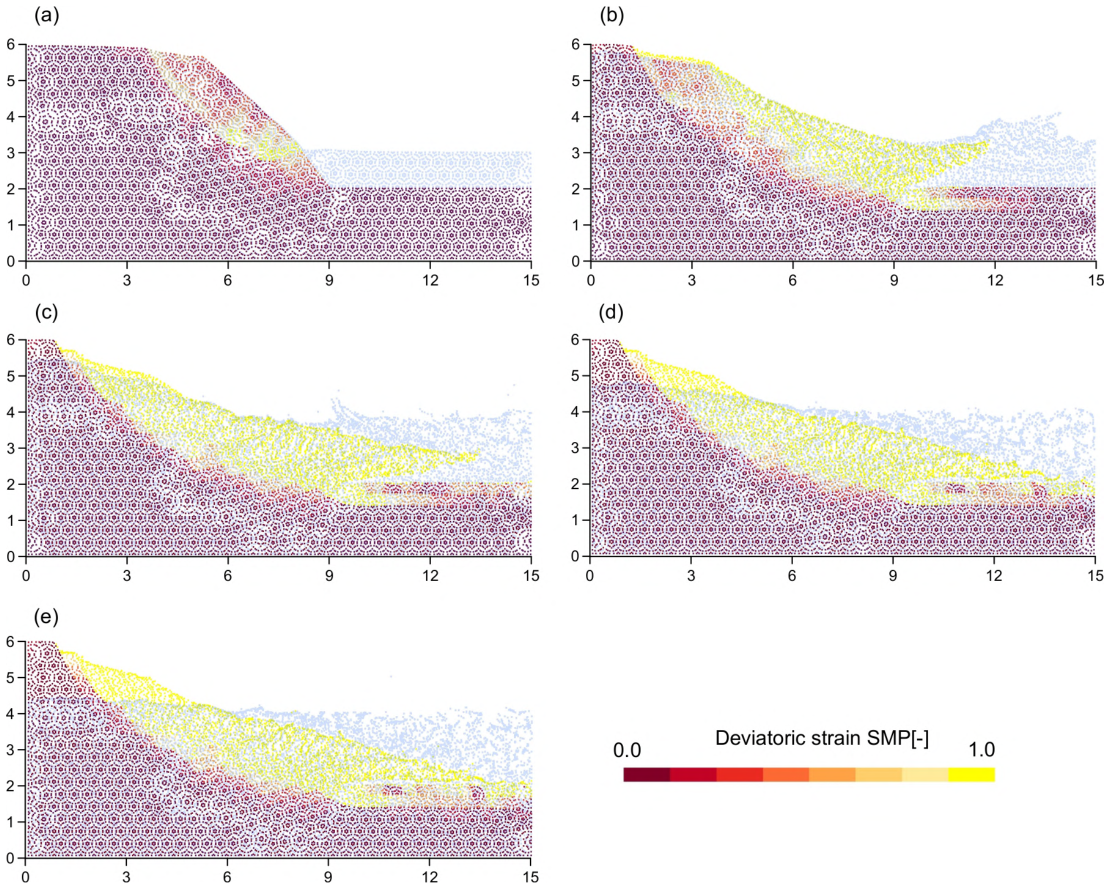

Figure 5.26: Temporal evolution of SMPs deviatoric strain and tracking of LMPs (blue dots) after the rapid drawdown of the water level.

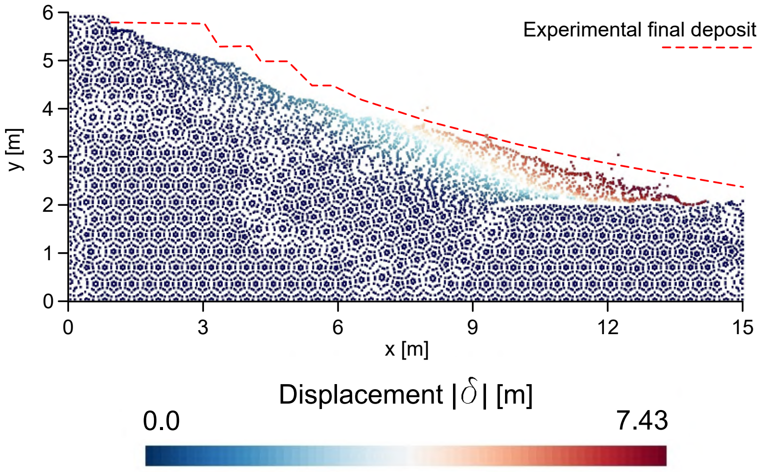

Figure 5.27: Norm of displacements at the end of the drawdown phase with the 2P-DP model. The final experimental profile is reported with a dashed red line.

direction and -3.31m along y direction. The final profile is on average closer to the experimental one, however the top portion appears lower and not characterized by distinct blocks, when compared to experiment. This behavior is most probably due to the rapid desaturation of the experimental slope and the suction increase, which tends to give more cohesion to the top part and to result in the blocks configuration. The use of a multipoint approach, able to consider also the variation in saturation degree, could represent the turning point to explain this complex physical behavior.

4 Levees' instability induced by toe uplift

4.1 Background studies

One of the most critical failure mechanisms is represented by the instability of the landside slope triggered by the development of high uplift pressures at the toe of the embankment, often accompanied by the formation of sand boils. This is frequently the case when embankments are built on top of foundation layers having significantly higher hydraulic conductivity. The development of uplift pressure at the toe of the embankment can lead to failure by triggering two different failure mechanisms: one is the piping process, caused by seepage and internal erosion, while the other is the instability caused by the increase of pore-water pressure and consequent decrease of shear strength of the soil.

The focus of this section is on this second mechanism.

When the river level increases, the pressure in the coarse layer rises accordingly, and high overpressure can be reached if the layer is confined above by a low permeability layer. The latter, a typically soft material like clay or peat, is characterized by very low mechanical strength. Due to the overpressure in the coarse layer, the effective stresses at the interface between coarse and soft layer is almost annulled. The effective stress annulment occurs when overpressure approaches the overburden stress value, depending on thickness, specific weight and saturation degree of the clay layer at the landside. As a consequence of stress annulment, shear strength of the soft layer significantly reduces. In these conditions, sliding occurs along the interface between the two materials, while uplift near the toe area occurs. As a consequence, when the contribution of the toe is missing from the overall strength, the levee external slope starts translating toward the landside, with displacement of even the meter entity ([183]).

It is conventional to define as *uplift length* the thin water zone forming between coarse and soft layer, characterized by constant pore pressure, equal to the overburden weight of the soft layer. This length has been analytically computed by [184] considering either stationary and non-stationary flow below the embankment, and infinite or finite extension of the landside.

[184] concludes that the analytical expression provides only an order of magnitude for the uplift length, since it tends to overestimate it from 25% to either 100% the actual length. This specific collapse mechanism is dominant only if the levee is high enough to withstand other failure mechanisms like overtopping and shallow slope failure [185].

Previous studies about the toe-uplift failure mechanism fall into two categories: experimental, using geotechnical centrifuges, and numerical, aimed at explaining real cases of occurred instabilities or experimental results, even adopting probabilistic approaches ([31] based on LEM analysis). The first studies have been performed in geotechnical centrifuge in the late 1900 and beginning of 2000, [18, 186, 187]. In these tests the control of geometry, materials and boundary conditions allows to better understand the type of mechanism developing under certain gravity levels and head/pressure conditions. Moreover, evolution of collapse can be followed thanks to continuous image recording. The use of reinforcements, like berms, can also be tested (see [18]) to provide design orientation for practitioners.

On the other side, the study of real failure cases, like the famous case of Wilnis in the Netherlands (2003) [40, 183], pushed the development of analytical and numerical methods [185, 188], and to even perform in-site tests [185].

Experiences gained with the use of the Finite Element Method (FEM) have shown its limitations in reproducing this mechanism for two main reasons: for situations with a vertical safety factor (defined as the vertical weight divided by the water pressure in the sand layer) lower than 1.04 [185], it is not possible to apply FEM, since numerical difficulties occur. Moreover, as FEM is basically a stiffness approach, additional parameters and schematisations are required, like moduli, element type/size, initial stress state, acceptable error level– which makes design more time-consuming [185].

Based on these considerations, a simplified analytical method based on the Limit Equilibrium Method (LEM), named Van Method [185], (initially developed in 1999) has progressively gained popularity in the geotechnical community.
Van Method is developed in agreement with Bishop method. According to Van Method, the toe uplift instability is characterized by a triple sliding zone: an active circular, a straight and a passive circular. A schematization is reported in Fig. 5.28 with the reference symbology. The interslice forces of the active and passive zones, I_a and I_p are computed separately considering a momentum equilibrium, and including Mohr-Coulomb failure criterion. The third force which comes into play is the friction force F_s along the straight segment. F_s is computed by considering the expression of the factor of safety FS according to Bishop method

$$FS = -\frac{\tau_s}{FS} \cdot L \tag{5.3}$$

The length of the uplift zone L can be defined with a groundwater analysis, considering quasi-steady state flow conditions. Finally, the factor of safety FS is computed by solving the horizontal forces equilibrium (Eq. 5.4)

$$I_a + I_p + F_s = 0 \tag{5.4}$$

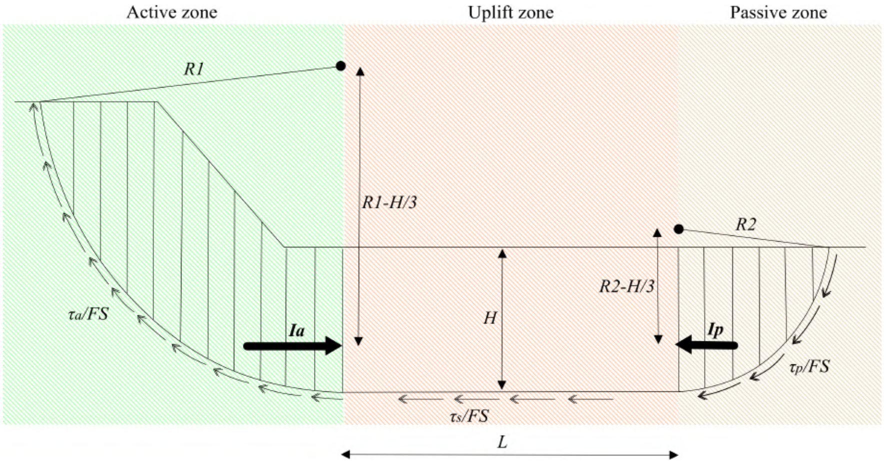

Figure 5.28: Triple sliding zone scheme according to Van Method (adapted from [185]).

Eq. 5.4 is implicit in FS, hence the solution is found by iteration. For $R_1 = R_2$ and $L = 0$ a completely circular slip plane is obtained, and Van Method reduces to Bishop method. Despite its ease of use, Van method has also limitations: it is based on a force approach, which doesn't allow post-failure description. Consequently, it is necessary to employ a large strain approach, like MPM, to capture the full behavior, thus provide new insights about the mechanism. In particular, the ratio between overpressure and vertical total stress near the toe area can be investigated in detail during the entire failure process, without being limited by FEM assumptions.

The kinematic behavior after the onset of failure can be determined, understanding the impact of pressure evolution on the earth structure movements. In this manner, the problems doesn't need to be simplified with the preselection of a critical slip surface, like in LEM, because it is the result of the MPM computation. Given the significant contribution of centrifuge tests to the understanding of the toe-uplift failure mechanism, an experiment performed in 2003 by [18] is selected to be reproduced with MPM. In this manner, it is possible to investigate the kinematic of the phenomenon in well-controlled conditions and to test the capability of MPM as prediction tool for events at the real scale.

4.2 Investigation of levee failure and post-failure with centrifuge tests and MPM simulations

4.2.1 Baseline physical test

In this section, the main aspects of the physical test, used as a reference to apply MPM in the study of the toe uplift mechanism, are introduced. The reference experiment is part of a series of tests conducted by [18] in a geotechnical centrifuge at Delft University of Technology, in 2003. These experiments aimed at reproducing in a controlled environment the conditions triggering toe uplift collapse mechanism, thus improving the understanding of the phenomenon. In addition, the presence of berms and trenches were tested experimentally. The standard dike test is considered here as reference for the MPM model.

In the centrifuge, the levee is built at model scale, with dimensions reported in the sketch of the experimental configuration in Fig. 5.31 (to facilitate reading, also dimensions of the levee at prototype scale are added). In the selected case, the levee and the shallow foundation layer are built with the same material, kaolin clay, while the deep layer is made of sand. Strength parameters are computed based on consolidated undrained triaxial tests (see Tab. 5.5).

The reservoir representing the riverside is progressively filled with water; this is hydraulically disconnected from the levee body because of the presence of a plastic membrane that prevents the seepage in the levee body and in the clay foundation. On the contrary, the reservoir is connected to the deep sandy layer with a tube. A small vertical polystyrene wall is placed on top of the levee, thus allowing water levels higher than the levee's crest to generate higher pressure in the sand layer. On the other end of the layer, the total head in the sand is controlled with a height-adjustable drain, at a fixed height of 2cm above the ground level [189].

The centrifuge is accelerated in steps of 10g until the final value of 120g is reached in approximately 15min. The reservoir level is initially at half the levee height, and it is progressively raised to the maximum value, along with the gravity increment. From the pictures of the experiment, it results that the maximum level H is between 6.5 and 7cm.

In Fig. 5.30 it is reported the evolution of collapse in the centrifuge test with respective gravity levels. This graphical representation (adapted from [189]) is done by subtracting greyscale values of the current phase from the previous phase to highlight deformations. In Fig. 5.30(a), the displacements resulting from accelerating from 1g to 90g are shown. At this step, the slip surface is still not visible and the water level is low (half the dike height). In Fig. 5.30(b), the displacements caused by the acceleration from 90g to 100g can be seen. A sliding mass is now visible, bounded by an active sliding surface. Fig. 5.30(c) the displacements between 100g and 120g are shown. Meanwhile, the water level has also increased at crest height. A secondary shallow slip plane is created over which the levee slides. Afterwards, a passive slip plane arises due to the increasing horizontal deformation. This slip plane forms an approximate straight line. To the right of this line, no deformation can be recognized anymore.

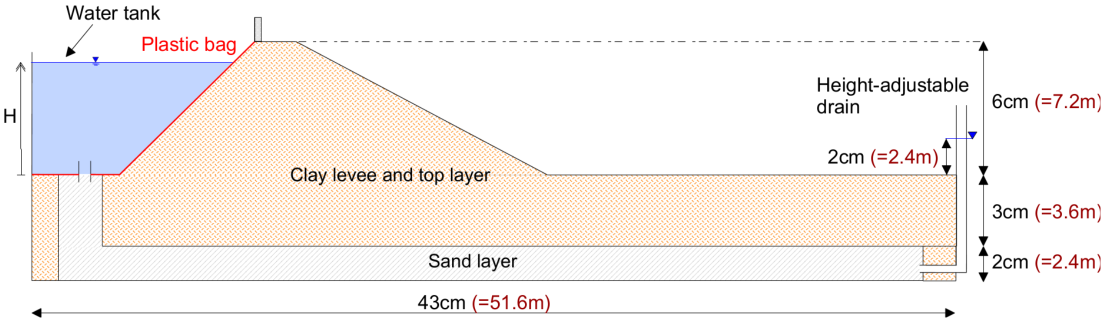

Figure 5.29: Sketch of the principal features of the baseline centrifuge test (model scale). The dimensions at prototype scale are reported in red.

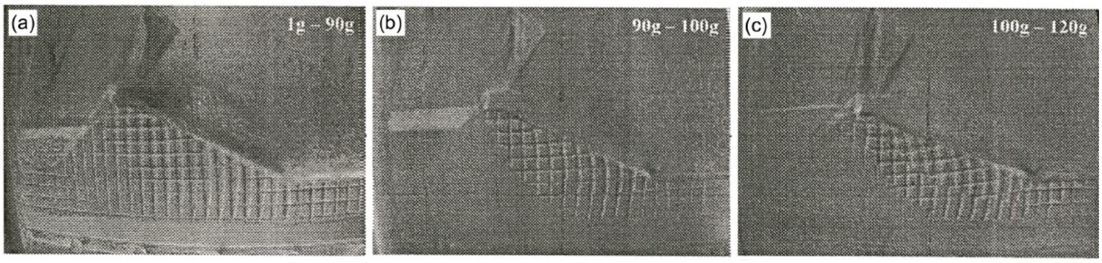

Figure 5.30: Experimental results. Relative displacements at three progressive increments of the gravity level in the centrifuge test. Adapted from [189].

4.2.2 Numerical model set up

The MPM model is built considering the main geometrical features of the experiment at the prototype scale, following the well known similitude ratio (Eq. 5.5).

$$\frac{L_m}{L_p} = \frac{1}{N} \tag{5.5}$$

In Eq. 5.5, N is the amplification factor of gravity, which in the reference experiment assumes a final value of 120, and L_m and L_p are geometrical lengths in the model and the prototype. In addition, plain strain conditions are assumed.

The geometry of the model and the mesh discretization are reported in Fig. 5.31. The mesh is made of 3-noded triangular elements with an average edge size of 0.8m. At the beginning of the simulation, 3MPs are assigned to each element.

The material properties for the two materials are listed in Tab. 5.5. The retention properties were not reported in the reference paper, so simplified linearized SWRCs are used according to Eq. 5.6.

$$S_L = 1 - a_v \cdot (p_L) \tag{5.6}$$

The values of the calibration parameter a_v are based on the literature for similar materials.

The hydraulic conductivity function for each material is assumed constant (not changing with the saturation degree), equal to the saturated hydraulic conductivity value. In the experiment, the saturated hydraulic conductivity of clay is $k_c = 1.16 \cdot 10^{-9} m/s$, while in the numerical model a higher value is used, as reported in Tab. 5.5. The final value of clay hydraulic conductivity of Tab. 5.5 represents a compromise between minimizing the computational cost and best matching with the experimental outcome. In Sec. 4.3 the impact of hydraulic conductivity of the clay layer on the MPM simulation is investigated.

Regarding soil strength, an elastic perfectly plastic Mohr-Coulomb model is used for both materials, considering parameters in agreement with the experimental values [18]. Young modulus is selected considering the unloading path, more representative of the phenomenon under analysis. A mass scaling of 100 is used to reduce the computational cost and a small value of damping, equal to 0.05, is used to guarantee numerical stability [115].

The boundary conditions (BCs) are specified as follows. The BCs for the solid phase are reported in Fig. 5.31(a) and they remain constant for the entire simulation. The choice of fixing the inner slope is related to the experimental configuration, where the reservoir, progressively filled, is acting in a stabilizing manner for the riverside slope, which otherwise would tend to collapse before the maximum water level is reached. The bottom edge of the model is fully fixed, while

	Sand	**Clay**
ρ_S $[kg/m^3]$	2610	2542
ρ_L $[kg/m^3]$	1000	1000
n $[-]$	0.355	0.3
K_L $[kPa]$	60000	60000
μ_L $[kPa \cdot s]$	10^{-6}	10^{-6}
a_v $[1/kPa]$	$6 \cdot 10^{-3}$	$4 \cdot 10^{-4}$
k_{sat} $[m/s]$	$7.44 \cdot 10^{-3}$	$7.44 \cdot 10^{-5}$
E $[kPa]$	55860	5520
ν $[-]$	0.33	0.15
ϕ $[°]$	37	22
c' $[kPa]$	0.0	10

Table 5.5: Material parameters for the MPM model of toe uplift induced instability.

the other lateral edges are normally fixed. Pressure and stress are initialized with the *K0*-procedure ($K0 = 0.5$), assuming that the water table is at the interface between sand and clay. The water table initial location guarantees unsaturated conditions of the levee body and the clay foundation layer. One step of quasi-static gravity loading is run after *K0*-procedure to improve the stress distribution. During the initialization, the bottom is impermeable, as visible in Fig. 5.31(b). The hydraulic condition on the inner slope is impermeable, resembling the plastic membrane effect, while on the land side a potential seepage face is assigned.

After initialization, only the bottom BC for the liquid is changed to an imposed pressure (Fig. 5.31c). The applied pressure has a linear distribution with a maximum on the left side $\bar{p}_L|_{x=0m}$ and a minimum on the right side $\bar{p}_L|_{x=50m}$. The first changes in its magnitude during the simulation, resembling the water table rising in the reservoir, while the latter is constant as the drain height is kept fixed in the experiment. The term "Phase" in the following is used to define a part of the simulation characterized by a specific distribution of nodal pressure at the bottom.

In the MPM model, a uniform initial distribution of imposed nodal pressure equal to -82kPa is assigned (Phase 1), which corresponds to a water column of 2.4m above ground level, equal to the height of the drain. This condition is maintained for 8 min. The values at the extreme nodes of the model which bound the linear distribution, i.e. $x = 0m$ and $x = 50m$, are reported in Tab. 5.6. Each new pressure distribution defines a new *phase* of the simulation with a certain

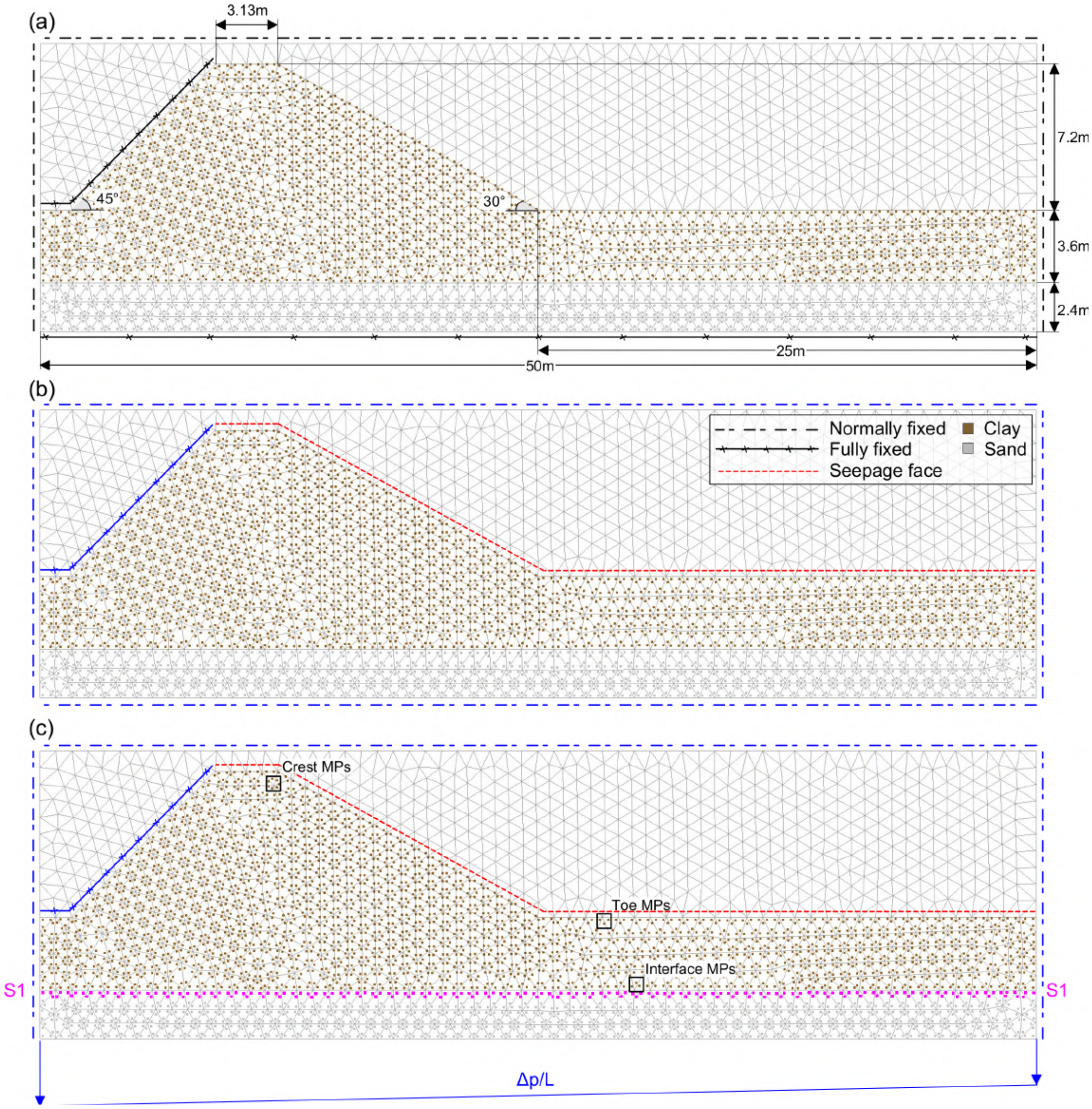

Figure 5.31: MPM model of centrifuge test (prototype scale). (a) BCs for the solid. (b) BCs for the liquid during initialization, (c) BCs for the liquid after initialization.

duration, also reported in Tab. 5.6. The horizontal gradient of pressure at the bottom boundary tends to become progressively steeper, as visible in Fig. 5.32.

ID	$\Delta t\ [min]$	$\bar{p}_L\|_{x=0m}\ [kPa]$	$\bar{p}_L\|_{x=50m}\ [kPa]$
Phase 1	8	-82	-82
Phase 2	45	-102	-82
Phase 3	116	-122	-82
Phase 4	182	-142	-82
Phase 5	202	-162	-82

Table 5.6: Boundary values of the imposed nodal pressures at the model bottom edge.

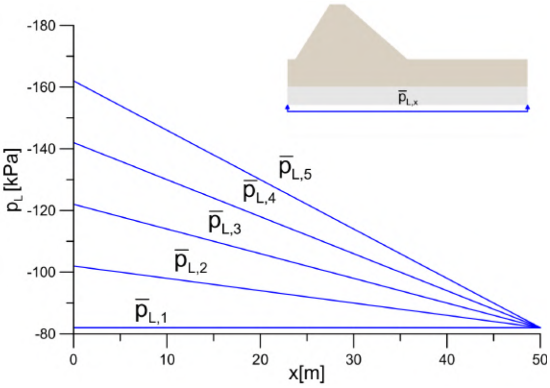

Figure 5.32: Imposed nodal pressure along the bottom edge of the model, in the five subsequent phases.

The sequence of pressure increments and each duration is schematized as follows. From Fig. 5.30, it is identified the position of the maximum water level reached during the experiment ($H = 7.8 - 8.4m$), which corresponds to a pressure of approximately -120 kPa at the interface between sand and clay. This means that the critical pressure distribution able to trigger the instability should be between Phase 3 and Phase 4. Phase 5 does not have an experimental counterpart, and it is carried out to explore numerically the evolution of failure in the event of an additional pressure increase.

To monitor the stresses and pressures at the interface between sand and clay, the MPs nearby section S1 are highlighted in Figure 5.31(c). Furthermore, in the same figure, three locations are selected, crest, interface, and toe, to track the evolution of MPs kinematic variables in the next section.

4.2.3 RESULTS

As introduced in the previous sections, the problem under analysis is strongly controlled by three main aspects: stratigraphy, material properties, and variation of hydraulic boundary conditions (mainly the pressure in the sand layer). Among the objectives of the MPM model, there is the identification of the critical pressure gradient at the interface between sand and clay, triggering failure, and the following displacements. These displacements can be entirely reproduced by the MPM model, in response to each modification of the boundary conditions. This is a major aim when employing MPM in the investigation of toe uplift.

Two figures are herein presented to explain the main outcomes of the simulation: Fig. 5.33 and Fig. 5.34. These figures illustrate stress and deformation behavior respectively. It has to be noted that the pressure at the interface between sand and clay does not correspond to the bottom imposed pressure, it is necessarily decreased by a factor $(\gamma_w \, h)$, where h is the sand layer thickness. This pressure, stored at the MPs, is computed along the interface section S1 at every computational step and compared with the total vertical stress along the same section in Fig. 5.33. The overburden stress on the landside, considering a clay thickness of 3.6m, outside the load footprint of the levee, is equal to 73.44kPa. As a reference, this value is reported in Fig. 5.33 with a horizontal red line.

Each panel of Fig. 5.33 depicts the stresses along S1 at instants corresponding to the end of each Phase. It is visible that, starting from t=169min (end of Phase 3), the liquid pressure values approach the total vertical stress values near the toe (around $x = 30 - 35m$), thus uplift occurs and consequently a shear failure surface develops and an acceleration of the displacements is observed. This is visualized in Fig. 5.34 which reports contours of deviatoric strain and norm of displacements. At t=169min, high deviatoric strains are observed near the interface between sand and clay and extend both toward the landside toe and the riverside crest. The corresponding situation in terms of displacements is the following: the vectors near the landside slope are oriented upward and toward the landside, with maximum displacements equal to 13cm. The direction of movement appears as the onset of a rotation. At the same time, along the interface, between $x = 20m$ and $x = 25m$, vectors are horizontal and directed toward the landside, showing a translational movement. Lastly, the vectors along the landside surface display an uplift movement.

At t=170min (beginning of Phase 4), pressure increases and the failure process is fully triggered (Fig. 5.34). At this time, the slip surface is more marked and continuous, with an overall increment of strain. The displacement vectors show that the movement is characterized by a translation in the foundation, near the levee's toe, and a roto-translation of the levee slope. This result is distinctive of the phenomenon under analysis, well captured by MPM.

During Phase 4, the process evolves, reaching displacements even higher than 1m. Consistently, in the range $25 < x < 35$, total stress and pressure are approximately equal along S1, as visible in Fig. 5.33 at the end of Phase 4 (t=351min).

The subsequent increment of pressure (Phase 5) triggers additional movements and larger displacements, which impact on a more irregular stress distribution on the landside, with oscillations typical of MPM (see Fig. 5.33). At the end of Phase 5 (t=553min), the levee crest settled about 2m, while the toe reached a vertical displacement of approximately 0.8m (Fig. 5.34). The entity of these displacements provide a clear picture of the damage to the earth structure, and this quantification has never been possible until now with other numerical techniques.

The impact of pressure increments of Phases 3, 4, and 5 on the displacements is reported in Fig. 5.35 with relative displacements. Relative displacements are computed for consecutive instants, thus, for instance, relative displacement vectors at t=54min are obtained by subtracting displacement vectors at 53min from displacement vector at 54min. With this graphical representation, it is quantifiable the boost in movement of each new pressure distribution and the progressive development of the instability mechanism.

As previously mentioned, the pressure distribution of Phase 3 is critical, in the sense that uplift and translational movement near the toe occur at the beginning of it. In Phases 4 and 5, large displacements characterize the levee movement with crest height lowering. This behavior may favour overtopping but also relevant damage to infrastructures and private buildings on the landside.

The dynamic process of levee failure can be additionally analyzed by considering the kinetic energy of the system (Fig. 5.36a). Two peaks of major intensity can be recognized at approximately 180min and 360min, immediately after applying bottom pressures of Phases 4 and 5. The peaks correspond to a rapid acceleration of the soil masses, in response to the applied pressure.In Fig. 5.36(b) liquid pressure

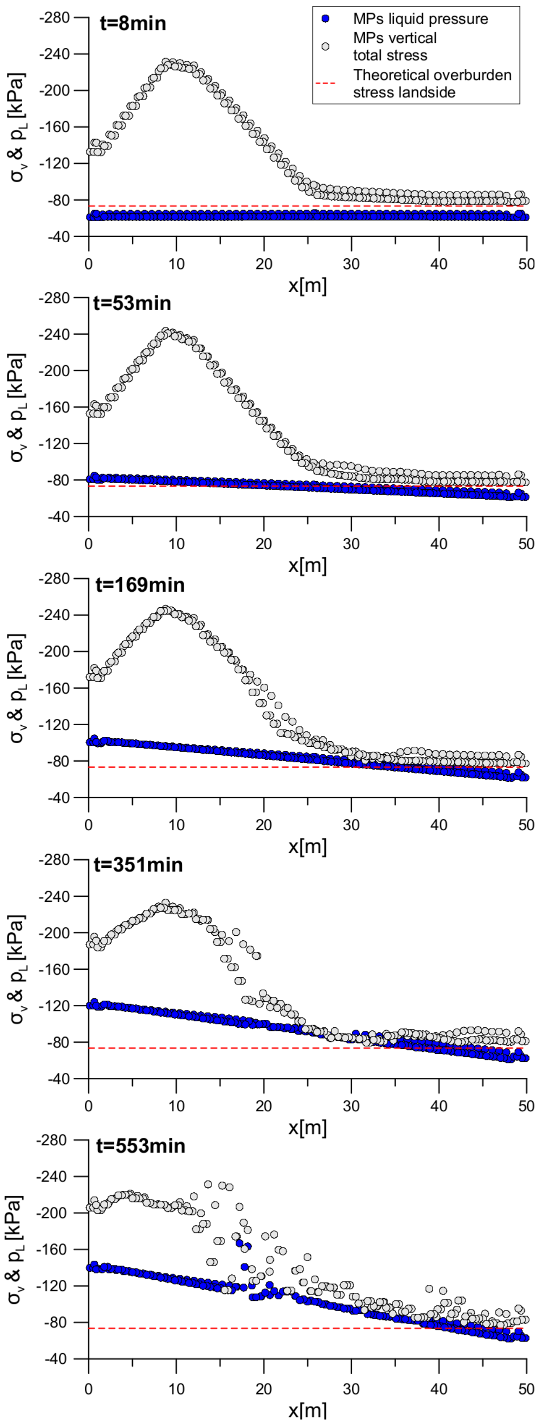

Figure 5.33: MPs stress variables along section S1 at five instants, corresponding to the end of each Phase.

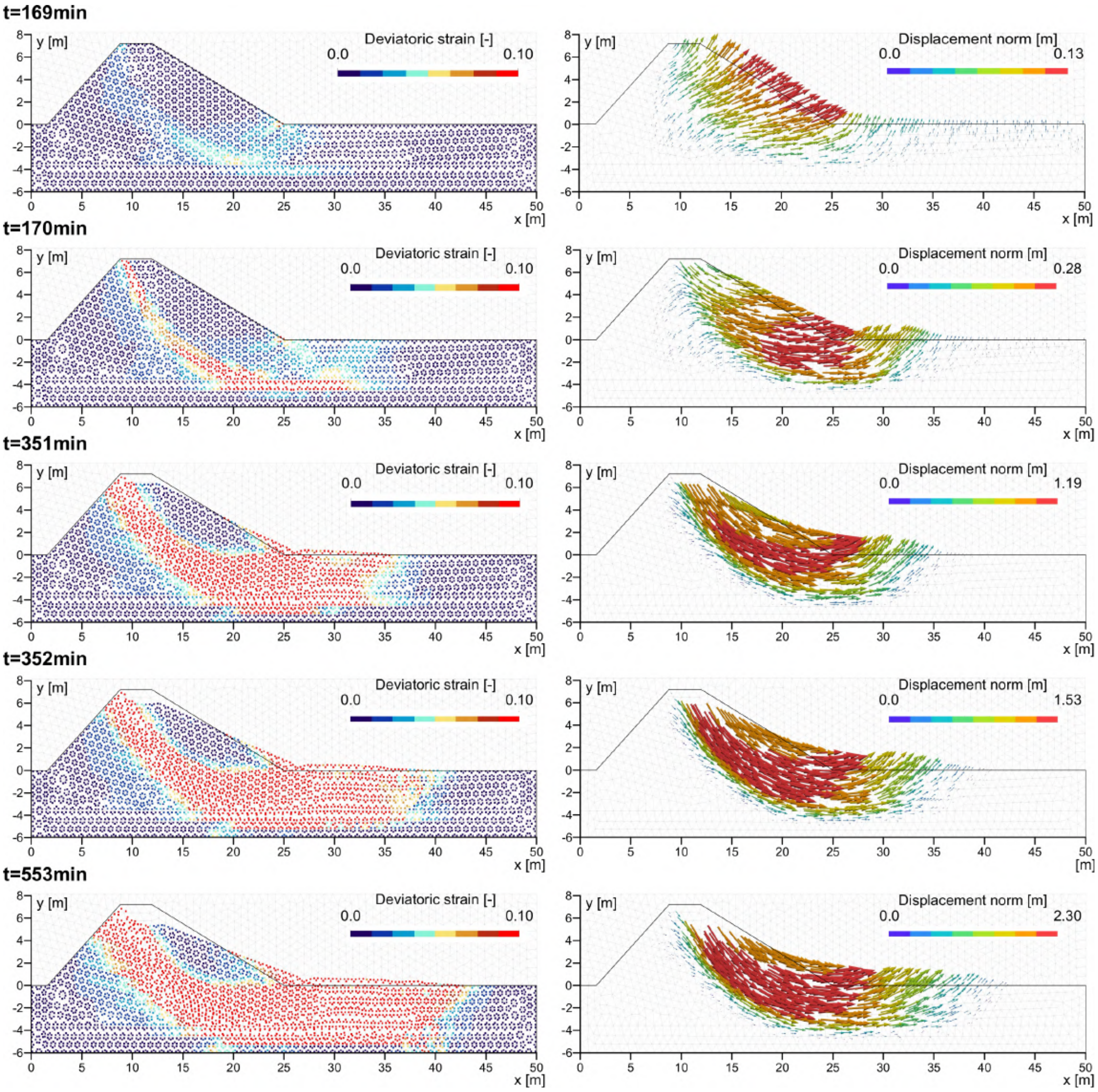

Figure 5.34: Contours of deviatoric strain (left column) and norm of displacements (right column) for five instants of time.

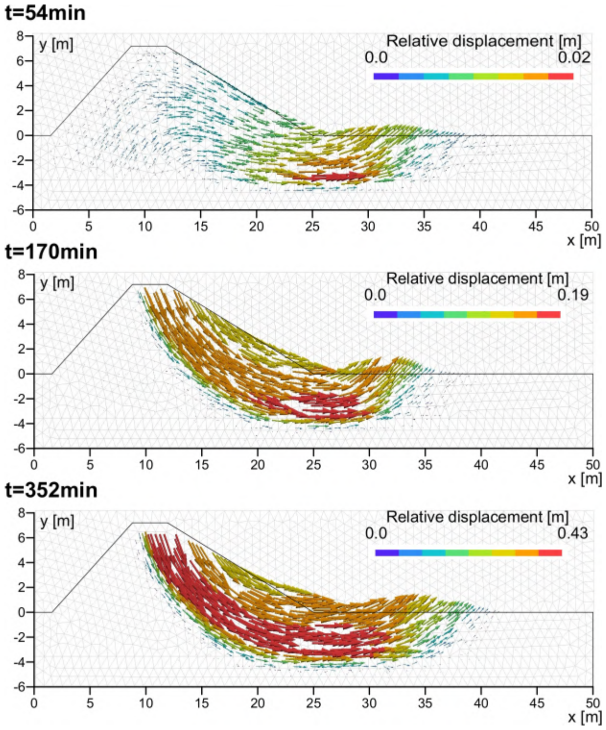

Figure 5.35: Relative displacements at three selected instants of time, corresponding to the passage between Phases 2 and 3 (t=54min), between Phases 3 and 4 (t=170min), and between Phases 4 and 5 (t=352min).

and vertical stresses at MPs on S1 (in the sand layer) with coordinate $x \approx 30m$, are plotted. Liquid pressure increases in each phase and remains almost constant for the entire phase. For the first three phases total vestical stress is approximately constant, while effective stress decreases. At t=70s, liquid pressure and total stress are approximately equal in this location, thus effective stress is nearly zero. Subsequently, while time progress, the slope deforms, thus increasing the total and effective stresses. A similar process is observed in phase 5. Mild oscillations are visible in the solid stress graphs in correspondence of phases 4 and 5.

In Fig. 5.36(c)the uplift length at prototype scale, computed from the simulation outcome, is reported. The numerical uplift length is computed considering a set of MPs near the interface S1, in a range $11 < x < 50m$, and evaluating the position of those MPs having vertical effective stress $\sigma'_y \approx 0$. Since t=54min (Phase 3), the uplift length increases progressively, reaching a maximum value of 7.6m at t=180min. This value is very close to the experimental uplift length measured $\approx$ 6cm [189] (=7.2m at the prototype scale, see Fig. 5.36(c)). After this peak, during the dynamic motion of the slope, the uplift length oscillates and it initially decreases during Phase 4, and then progressively increases. During Phase 5, the uplift reaches a maximum value of 13.5m, followed by a decrease around the value of 9m. This response is the result of both numerical and physical factors. In fact, stress oscillations are observed in MPM during the highly dynamic motion and since stresses are used to compute the uplift length, as a consequence, the calculated uplift length oscillates too. Therefore, the computation is indicative and provides a general order of magnitude for Phases 4 and 5, while it is more meaningful in the previous part of the simulation. Concerning the physical aspects impacting on the trend of the uplift length during post-failure, i.e. Phases 4 and 5, it is possible to find an explanation considering Fig. 5.33 and Fig. 5.36(b): during collapse, the effective stress increases again, thus decreasing the uplift length.

Fig. 5.36(d) reports the time evolution of some components of displacement at three locations (indicated in Fig. 5.31(c)): at the levee crest, at the interface at depth (but considering MPs in the clay) and at the toe, near the soil surface. These trends aid in a precise quantification of the large displacements affecting the levee collapse.

In Fig. 5.37 the experimental result (a) is compared with the simulated norm of displacement (b) at the end of Phase 4. As previously mentioned, in Phase 5

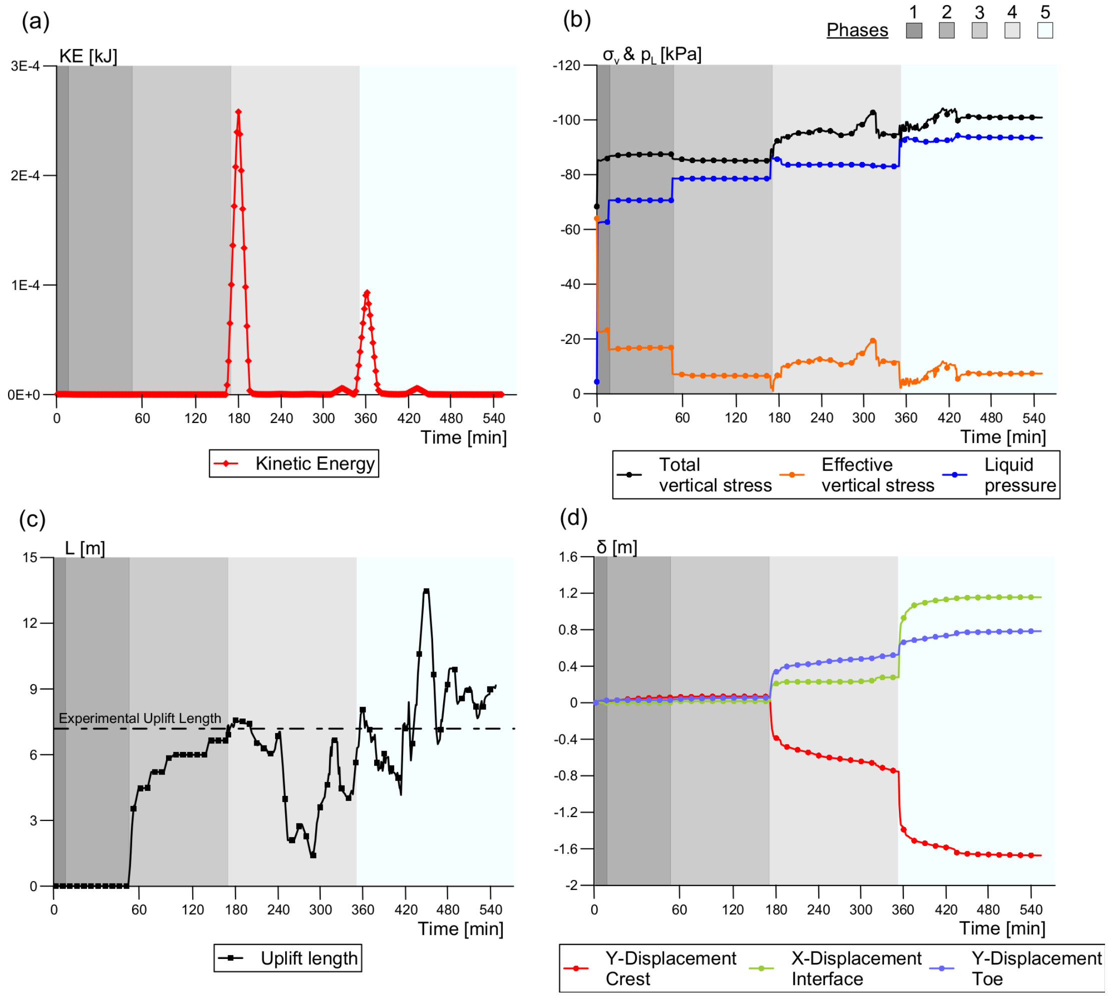

Figure 5.36: Time evolution of kinetic energy of the system (a). Liquid pressure and stress for a MP at the interface between sand and clay (in sand) (b). Time evolution of uplift length (c), and components of MPs displacement at three locations (d) (negative values stand for settlement of the levee crest).

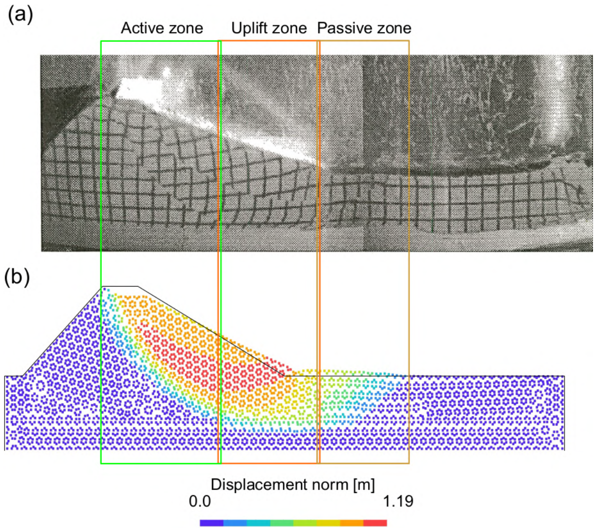

Figure 5.37: Comparison between experimental (a) and numerical (b) final configurations.

boundary pressures higher than the experiment are applied to the model, thus it is not considered here. It is possible to identify the typical triple sliding surface and the zones bounded by it: the active zone, the uplift length, and the passive zone. The extension of the zones is very similar between experiment and numerical results. The magnitude and direction of displacements aid in visualizing the types of movement, showing a rotation in the active area, horizontal translation along the uplift length, and a roto-traslation in the passive area. The shallower slip surface, visible in the experimental picture, is responsible for some material accumulation at the toe, visible as a small bulging at the end of the slope. This slip surface and its impact on the final profile can not be accounted for in the MPM model. This is probably due to the difference in the loading path between numerical and experimental models. In fact, in the experiment, a rise in g-level with the progressive rise of water level is carried out, while the numerical model is already at the final g-level and only the pressure is progressively increasing. Unlike the numerical model, the initial vertical settlement of the experimental levee after construction may also have impacted on the formation of this shallow slip surface.

4.3 Effect of permeability ratio on MPM

The effect of foundation soils' hydraulic conductivity on the collapse mechanism is investigated in this section. Fig. 5.38 reports deviatoric strain and liquid pressure contours for three MPM models with different hydraulic conductivity ratios (k_c/k_s, where k_c and k_s respectively stand for clay and sand hydraulic conductivities). In each model, k_c is varying, while k_s is kept constant. Deviatoric strain and liquid pressure contours at the beginning of Phase 4 (t=170min) are presented in Fig. 5.38.

In the investigated cases, high shear strains initially localize at the interface between sand and clay, and the location of this area is similar. However, the reduction of hydraulic conductivity ratio modifies the temporal development of the entire slip surface in the active and passive zones. At t=170min, for $k_c/k_s = 10^{-1}$ the slip surface is well developed on both sides of the levee (Fig. 5.38). The slope collapse has been triggered and the crest settled slightly. In this scenario, the mechanism is more rapid and less extended toward the landside. For $k_c/k_s = 10^{-2}$, the slip surface on the passive zone is not clearly developed yet. For $k_c/k_s = 10^{-3}$, high shear strains are visible only in the uplift zone at this stage, and additional time is necessary to appreciate the entire slip surface formation. The reduction of hydraulic conductivity ratio implies a slower development of the slip surface and evolution of post-failure displacements, plus a slightly more extended uplift length zone.

This behavior is directly linked to the liquid pressure distribution, which depends on the hydraulic conductivity. Indeed, as expected, the sand layer is characterized by similar values in the three investigated cases, thus favouring the localization of shear at depth. On the other side, the levee body and the clay layer record different values of pressure in the three investigated scenarios. To this aim, the pressure distribution at two sections, S2 and S3, is indicated in Fig. 5.38. The higher suctions in the case with smaller hydraulic conductivity ratio ($k_c/k_s = 10^{-3}$) are counteracting the development of the slip surface in the levee body. This phenomenon is of transient nature and the hydraulic conductivity of the clay layer seems to be playing a major role in delaying the progression of movement.

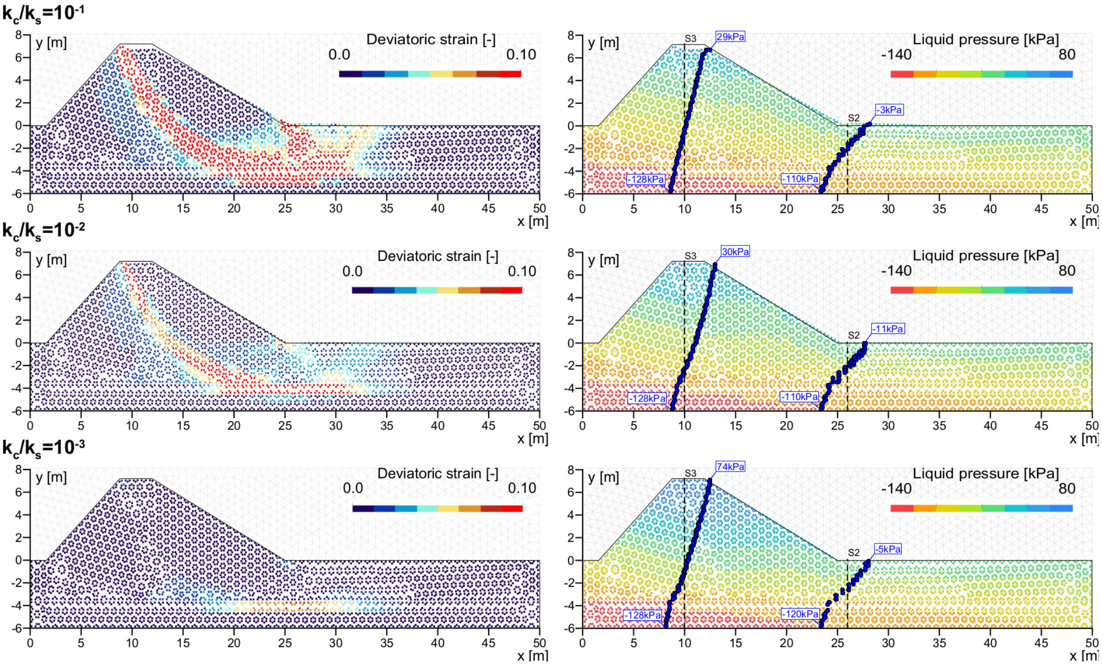

Figure 5.38: Impact of hydraulic conductivity on uplift failure mechanism. Deviatoric strain and liquid pressure contours at the beginning of Phase 4 (t=170min) for numerical models with three different permeability ratios.

4.4 Conventional numerical analysis

In this section, conventional numerical methods, based on force approach, are used to analyze the same case. Once again, it is possible to understand the innovation of using MPM to investigate failure mechanisms of levees, and the benefits in terms of supporting risk assessments. LEM based analysis are carried out with the software *Geostudio*. while Van Method based analysis are run with the software *D-Stability* [190].

The LEM analysis is based on a simplified distribution of pore pressure depending on a phreatic surface drawn by the user. No seepage analysis is run. The pore pressure is applied only on the sand layer. Two distribution of pressure are considered: one corresponding to the pressures of the MPM model at the end of Phase 3 and the other one at the end of Phase 4. The materials are assigned the same constitutive model as in the MPM model, i.e. Mohr-Coulomb with parameters as specified in Tab. 5.5. An entry and exit specification of the slip surface is used and Morgenstern-Price method is considered. The results of the analysis are reported in Fig. 5.39. In contrast to the MPM outcomes, the

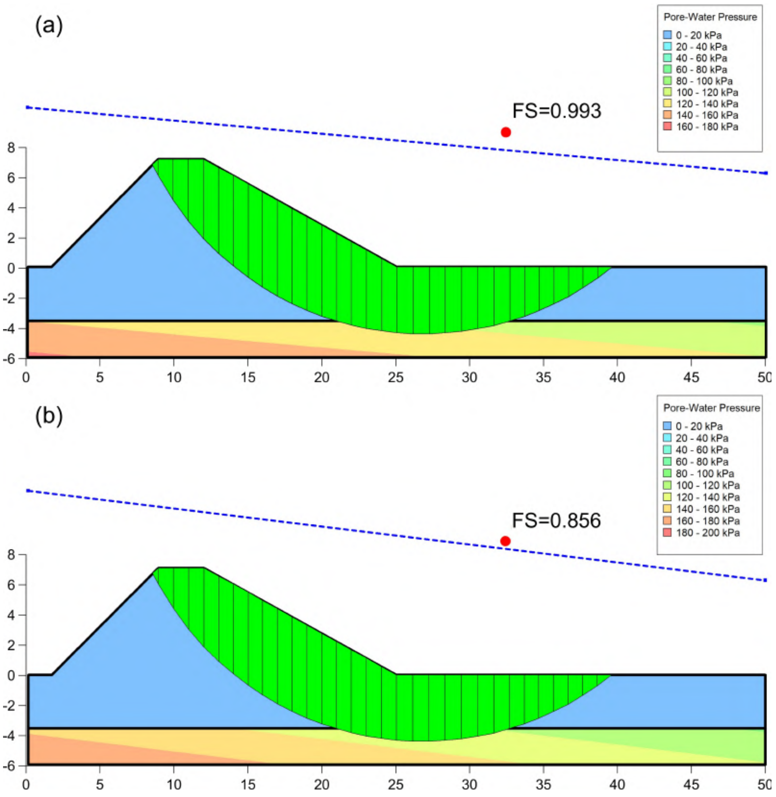

Figure 5.39: Results of LEM analysis for a pore pressure distribution corresponding to Phase 3 (a) and Phase 4 (b).

LEM analysis shows an instability at the end of Phase 3 with a slip surface fully developed at depth. This is due to an imprecise distribution of effective stress in this analysis, which is not physically consistent. However, the shape of the slip surface on the riverside (the circular part before the uplift zone) is very similar to the MPM localization of strain and the overall dimension of the potentially unstable mass, inferiorly bounded by the slip surface, is similar to the one visible in the MPM analysis at the end of Phase 4 (see Fig. 5.34). The values of the FS clearly identify a potential instability, but no movement quantification and no information concerning the toe uplift are retrievable from this kind of analysis.

Concerning the model with Van method, the uplift pressure is applied assigning a total head level to the sand layer with values corresponding to the applied pressure. A horizontal phreatic surface is applied at the ground level for the clay. Only material unit weight and strength parameters are necessary for this analysis.

Fig. 5.40 shows the results obtained with Van method. In Phase 2, FS is greater than one, thus the slope is stable. In Phase 3, FS is slightly lower than one, meaning that failure can occur. This result agrees with the MPM simulation, in which an increase of Kinetic Energy and large displacement are observed at the end of this phase. Even lower FS are obtained for Phases 4 and 5 due to the increase of pressure in the sand layer, but these results are not representative of real conditions because the geometry of the slope will change during the collapse as can be observed with MPM.

The Van method has the advantage of requiring a limited number of parameters and allows to determine the slip surface with the lowest safety factor (critical slip surface). Since it enforces only force equilibrium disregarding the slope deformation, FS lower than 1 can be obtained as an output, but post-failure displacement cannot be inferred. The method is very simple and computationally inexpensive, thus well suited for projects requiring a large number of simulations.

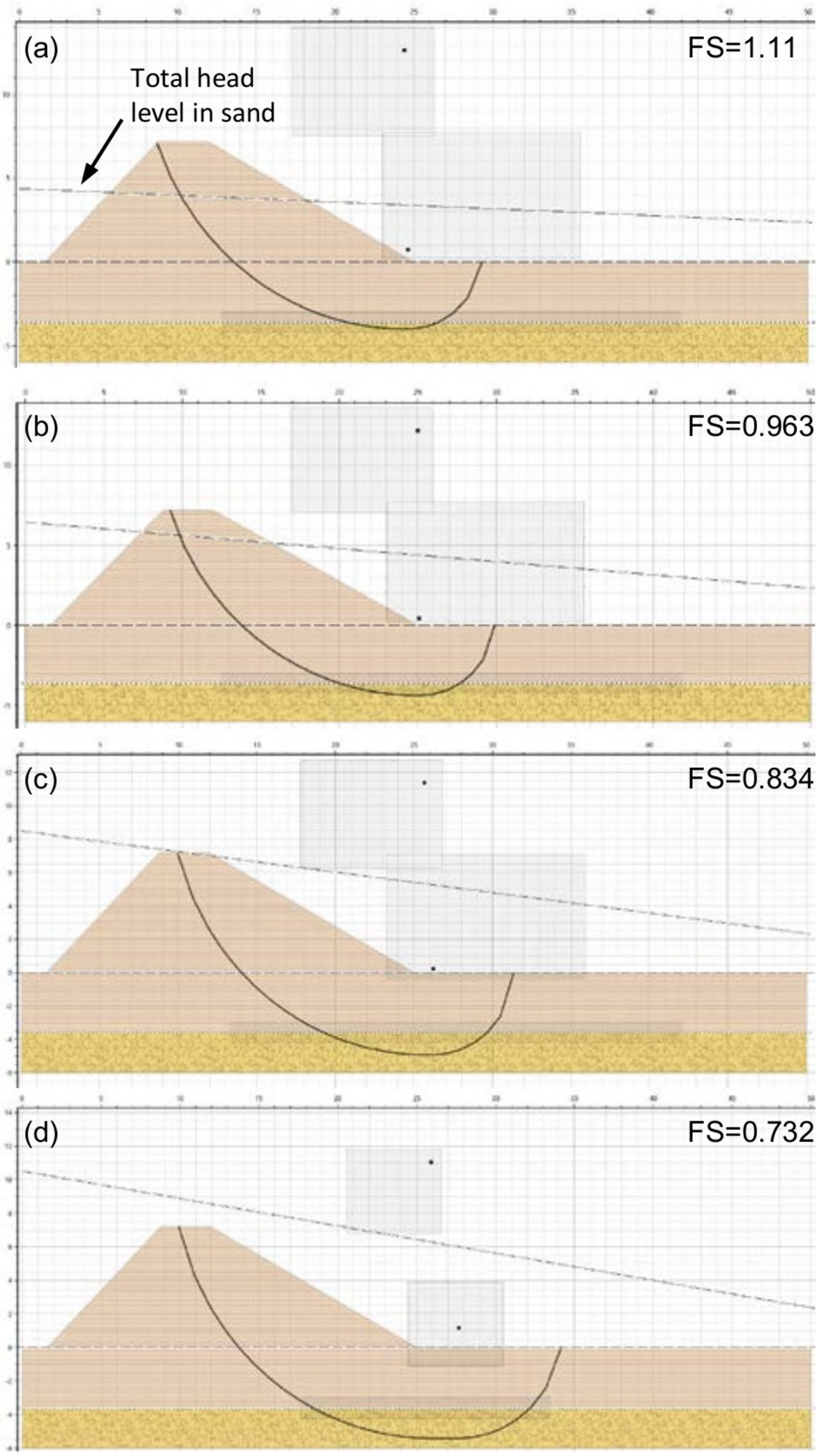

Figure 5.40: Slip surface and FS with Van Method for (a) Phase 2, (b) Phase 3, (c) Phase 4 and (d) Phase 5.

6

Conclusions

In the research work object of this thesis, a new approach to investigate and predict macro-instability in river levees is proposed: the use of multiphase MPM formulations. MPM is a powerful large strain approach with the capability of modelling failure and post-failure behavior of geotechnical structures. This aspect is fundamental and innovative in the realm of risk assessment associated to slope stability of river levees.

In fact, in the current practice, numerical approaches based on forces, resulting in the computation of the factor of safety, are used to predict the behavior of these earth structures. Only the onset of failure can be identified and evolution of a collapse mechanism, thus of the levee safety with time, can not be fully quantified. The importance of improving numerical predictions is even more significant if we consider the difficulties and economical limitations associated to physical modelling of levees and the use of monitoring techniques. The experience with the design of a complete investigation campaign on a levee stretch in the lower Tagliamento river in Italy and the consequent conventional safety analysis based on the Limit Equilibrium Method, allows understanding peculiarities of these water retention earth structures, like the construction materials and the natural ones, the spatial heterogeneity and their impact on the overall behavior, the impact of variable saturation and the importance of quantifying the transient hydrodynamic load system acting, and finally the necessity of optimizing resources in these long extension structures.

After the review of the current knowledge and techniques put in place to predict the behavior of levees, a state of the art about multiphase MPM formulations is carried out. The review of the major features of each formulation and the following testing activity using the 2Phase Double Point formulation (the more advanced formulation at the beginning of this research work) aided in the selection of the formulation to develop for the scopes of this study.

An unsaturated MPM formulation, computationally efficient, based on the approximation of gas pressure equal to the atmospheric pressure and constant, hence accounting for only two phases, is the focus of this research activity. The formulation features a full set of hydraulic boundary conditions which guarantee the reproduction of river level oscillations near levee banks, rainfall and the potential seepage face condition at the landside. This is among the most innovative aspects of this research work. A study about numerical stability is additionally carried out at a preliminary level, showing the potential increase in critical time step, thus potentially reduced simulation times, in unsaturated conditions. The formulation development and study about the critical time step have a strong general validity for MPM users. The formulation is validated with two examples, but additional cases can be found in the publication list reported at the end of this thesis. The comparison with already validated FEM codes provides very satisfying results. It is nevertheless important to underline that the validation doesn't consider any large strain example, since analytical cases with this characteristic are not available.

After validation, the formulation is tested in several applied cases: theoretical slopes, large scale experimental slopes, centrifuge tests. As a result, new insights are provided about the instability in levees by quantifying the actual movement and subsequent evolution of a collapse mechanism under different hydraulic load combinations. The ease in employing the formulation in different cases, and the chance to perform whatever parametrical analysis, appears as a strong feature to extend in the future the use of this MPM formulation to several other applied cases where partially saturated slopes, artificial or natural, and other geotechnical problems of soil-water-structure interactions are investigated.

To this aim, the implemented code should be included in the open source version of *Anura3D*; this activity can be carried on in the immediate future. On a general basis, some additional improvements may be done. Indeed, based on the outcomes of the different applied cases treated in this research work, some potential future developments can be foreseen.

- Improve the physical description of fluidization. This aspect is particularly relevant when propagation of highly saturated soil masses are present. It was particularly evident in the large scale slope reproduced in Chapter 5. To this aim, more advanced constitutive models should be explored.
- Further investigation about numerical stability in unsaturated conditions. The preliminary study at the end of Chapter 5 can be enriched with more numerical results and a detailed treatment considered also MPs location.
- Improve the efficiency by implementing strategies able to account for large timescale events. Among them, the use of an implicit in time integration scheme may represent the most efficient way to tackle this issue. However, other approaches, for example by coupling implicit FEM and MPM in the same simulation, may be explored.
- Improve the pressure oscillations. On a general level, this problem requires higher order shape functions, thus a new consistent and robust implementation.

7

Appendix

In this appendix, the steps followed to study the numerical stability of the formulation presented in Chapter 4 are presented. Three different Δt_c criteria are obtained taking into account the stability of (a) the coupled system of momentum balance equations, (b) the momentum balance of the liquid phase, and (c) the momentum balance of the mixture.

1 STABILITY OF THE COUPLED SYSTEM OF MOMENTUM BALANCE EQUATIONS

The governing equations in the strong form considered are the liquid momentum balance and the mixture momentum balance as in

$$\rho_L \mathbf{a}_L = \nabla p_L - \mathbf{f}_L^d + \rho_L \mathbf{g} \tag{7.1}$$

$$n_S \rho_S \mathbf{a}_S + n_L \rho_L \mathbf{a}_L = \nabla \cdot \boldsymbol{\sigma} + \rho_m \mathbf{g} \tag{7.2}$$

Additionally, the mass balance equation is considered to express the liquid pressure as function of velocity (Eq. 7.3). A linear elastic solid constitutive law (Eq. 7.4) is assumed to express effective stress as function of solid displacements.

The sign convention used expresses suction s as $s = -p_L$.

$$n\left(S_{\mathrm{L}}\frac{\partial \rho_{\mathrm{L}}}{\partial p_{\mathrm{L}}} + \rho_{\mathrm{L}}\frac{\partial S_{\mathrm{L}}}{\partial p_{\mathrm{L}}}\right)\frac{\mathrm{D^S} p_{\mathrm{L}}}{\mathrm{D}t} = \rho_{\mathrm{L}} n S_{\mathrm{L}} \mathrm{div}(\mathbf{v}_{\mathrm{S}} - \mathbf{v}_{\mathrm{L}}) - \rho_{\mathrm{L}} S_{\mathrm{L}} \mathrm{div}(\mathbf{v}_{\mathrm{S}}) \tag{7.3}$$

$$d\boldsymbol{\sigma'} = \mathbf{E_c} \cdot d\boldsymbol{\varepsilon} \tag{7.4}$$

If a single node i is considered, the momentum balances per unit volume at time t_k can be written as a system of second-order ordinary differential equations (ODE). The homogeneous form for both equations follows

$$\rho_L a_L^k + q_L v_L^k - q_L v_S^k + K_L u_L^k + \frac{(1-n)}{n} K_L u_S^k = 0 \tag{7.5}$$

$$(1-n)\rho_s a_S^k + n S_L \rho_L a_L^k + K_S u_S^k + \frac{(1-n)}{n} K_L u_S^k + K_L u_L^k = 0 \tag{7.6}$$

where

$$q_L = \frac{S_L n \mu_L}{k_L} \tag{7.7}$$

$$K_L = \frac{S_L}{L_i^2} \cdot \frac{1}{\left(\frac{dS_L}{ds} + \frac{S_L}{K_w}\right)} \tag{7.8}$$

$$K_S = \frac{E_c}{L_i^2} \tag{7.9}$$

In this notation K_w is the bulk modulus of the liquid, while K_L is a term which includes K_w, S_L (the saturation degree), $\frac{dS_L}{ds}$, the derivative of S_L respect to suction, and L_i as the characteristic length of a mesh element.
The use of an Euler-Cromer time scheme leads to the following set of equations (introduced in Chapter 2)for the kinematic variables of liquid and solid phases.

$$v_L^{k+1} = v_L^k + \Delta t \ a_L^k \tag{7.10}$$

$$v_S^{k+1} = v_S^k + \Delta t \ a_S^k \tag{7.11}$$

$$u_L^{k+1} = u_L^k + \Delta t\ v_L^{k+1} \tag{7.12}$$

$$u_S^{k+1} = u_S^k + \Delta t\ v_S^{k+1} \tag{7.13}$$

From Eq. 7.5 and Eq. 7.6 it is possible to express accelerations as function of all the other terms as follows.

$$a_L^k = -\frac{q_L}{\rho_L}\ v_L^k + \frac{q_L}{\rho_L}\ v_S^k - \frac{K_L}{\rho_L}\ u_L^k - \frac{(1-n)}{n\rho_L} K_L u_S^k \tag{7.14}$$

$$a_S^k = -\frac{nS_L\rho_L}{(1-n)\rho_s} a_L^k - \frac{K_S}{(1-n)\rho_s} u_S^k - \frac{K_L}{n\rho_S} u_S^k - \frac{K_L}{(1-n)\rho_s} u_L^k \tag{7.15}$$

Now, the acceleration expressions (Eqs. 7.14 and 7.15) are substituted in the explicit time scheme set (Eqs. 7.12, 7.10, 7.13, 7.11).

$$u_L^{k+1} = u_L^k + \Delta t\Big[v_L^k + \Delta t\Big(- \frac{q_L}{\rho_L}\ v_L^k + \frac{q_L}{\rho_L}\ v_S^k - \frac{K_L}{\rho_L}\ u_L^k - \frac{(1-n)}{n\rho_L} K_L u_S^k\Big)\Big] \tag{7.16}$$

$$v_L^{k+1} = v_L^k + \Delta t\Big(- \frac{q_L}{\rho_L}\ v_L^k + \frac{q_L}{\rho_L}\ v_S^k - \frac{K_L}{\rho_L}\ u_L^k - \frac{(1-n)}{n\rho_L} K_L u_S^k\Big) \tag{7.17}$$

$$u_S^{k+1} = u_S^k + \Delta t\Big[v_s^k + \Delta t\Big(- \frac{nS_L\rho_L}{(1-n)\rho_s} a_L^k - \frac{K_S}{(1-n)\rho_s} u_S^k - \frac{K_L}{n\rho_S} u_S^k - \frac{K_L}{(1-n)\rho_s} u_L^k\Big)\Big] \tag{7.18}$$

$$v_S^{k+1} = v_S^k + \Delta t\Big(- \frac{nS_L\rho_L}{(1-n)\rho_s} a_L^k - \frac{K_S}{(1-n)\rho_s} u_S^k - \frac{K_L}{n\rho_S} u_S^k - \frac{K_L}{(1-n)\rho_s} u_L^k\Big) \tag{7.19}$$

The coefficients' matrix of the system of Eqs. 7.16, 7.17, 7.18, 7.19 is evaluated to solve the eigenvalues problem

$$det(A - \lambda I) = 0 \tag{7.20}$$

Thus, a quadratic equation for λ is obtained (Eq. 7.21). In this equation, the terms $\geq \Delta t_c^3$ are neglected

$$\lambda^2 + \lambda\Big(\Delta t_c q_L Q - \frac{c\Delta t_c^2}{\rho_s} + \frac{K_L \Delta t_c^2}{\rho_L} - 2\Big) + \Big(1 - \Delta t q_L Q\Big) = 0 \tag{7.21}$$

If Eq. 7.21 is solved for Δt_c by imposing $|\lambda| = 1$, it results in

$$\Delta t_c = \frac{-q_L Q + \sqrt{(q_L Q)^2 + 4\Big(\frac{K_L}{\rho_L} - \frac{c}{\rho_s}\Big)}}{\Big(\frac{K_L}{\rho_L} - \frac{c}{\rho_s}\Big)} \tag{7.22}$$

Eq. 7.22, rearranged in a more general form, is equivalent to Eq. 4.65 proposed by [71],

$$\Delta t_c = \frac{2}{\omega}\Big[-\xi + \sqrt{\xi^2 + 1}\Big] \tag{7.23}$$

where the parameters ω and ξ have a new expression

$$\omega_c = \sqrt{\Big(\frac{K_L}{\rho_L} - \frac{c}{\rho_s}\Big)} = \frac{1}{L_i}\sqrt{\Big[\frac{S_L}{\Big(\frac{dS_L}{ds} + \frac{S_L}{K_w}\Big)}\Big]\Big[\frac{1}{\rho_L} + \frac{1}{\rho_S}(\frac{1}{n} - S_L)\Big] + \frac{E_c}{\rho_S(1-n)}} \tag{7.24}$$

$$\xi_c = \frac{q_L Q}{2\omega_c} = \frac{S_L n \mu_L}{2k_L \omega_c}\Big[\frac{S_L n}{(1-n)\rho_S} + \frac{1}{\rho_L}\Big] \tag{7.25}$$

2 STABILITY OF THE MOMENTUM BALANCE OF THE LIQUID PHASE

The same procedure presented for the coupled system can be applied to study the stability of the momentum balance of the liquid phase. By considering the homogeneous form of Eq. 7.5 (without the terms referring to the solid phase), we obtain

$$\rho_L a_L^k + q_L v_L^k + K_L u_L^k = 0 \tag{7.26}$$

The set of two ODEs (by considering the Euler-Cromer time scheme) is now

$$u_L^{k+1} = u_L^k + \Delta t\Big[v_L^k + \Delta t\Big(-\frac{q_L}{\rho_L}\, v_L^k - \frac{K_L}{\rho_L}\, u_L^k\Big)\Big] \tag{7.27}$$

$$v_L^{k+1} = v_L^k + \Delta t\Big(- \frac{q_L}{\rho_L}\ v_L^k - \frac{K_L}{\rho_L}\ u_L^k\Big) \tag{7.28}$$

The characteristic polynomial based on the resolution of the eigenvalues problem for Eqs. 7.27 and 7.28 is

$$\lambda^2 + \lambda\Big(\frac{\Delta t_c q_L}{\rho_L} + \frac{K_L \Delta t_c^2}{\rho_L} - 2\Big) + \Big(1 - \frac{\Delta t_c q_L}{\rho_L}\Big) = 0 \tag{7.29}$$

Eq. 7.29 solved for Δt_c gives

$$\Delta t_c = \frac{-\frac{q_L}{\rho_L} + \sqrt{\left(\frac{q_L}{\rho_L}\right)^2 + 4\frac{K_L}{\rho_L}}}{\frac{K_L}{\rho_L}} \tag{7.30}$$

Arranged in a more general form, it is equivalent to 4.65, where

$$\omega_L = \sqrt{\frac{K_L}{\rho_L}} = \frac{1}{L_i}\sqrt{\frac{S_L}{\rho_L\left(\frac{dS_L}{ds} + \frac{S_L}{K_w}\right)}} \tag{7.31}$$

$$\xi_L = \frac{\left(\frac{q_L}{\rho_L}\right)}{2\omega_L} = \frac{S_L n \mu_L}{2k_L\omega_L}\frac{1}{\rho_L} \tag{7.32}$$

3 STABILITY OF THE MOMENTUM BALANCE OF THE MIXTURE

Same procedure presented for the coupled system can be applied to study the stability of the momentum balance of the mixture. By considering the homogeneous form of Eq. 7.6, we obtain

$$(1-n)\rho_S a_S^k + nS_L q_L v_S^k + \Big[K_S + (1-n)\Big(- S_L + \frac{1}{n}\Big)K_L\Big]u_S^k = 0 \tag{7.33}$$

The set of 2 ODEs (by considering the Euler-Cromer time scheme) is now

$$u_S^{k+1} = u_S^k + \Delta t(v_s^k + \Delta t a_s^k) \tag{7.34}$$

$$v_S^{k+1} = v_s^k + \Delta t a_s^k \tag{7.35}$$

The characteristic polynomial (related to Eqs. 7.34 and 7.35) is now

$$\lambda^2 + \lambda\Big[P\Delta t_c^2 + \frac{S_L \Delta t_c n q_L}{(1-n)\rho_S} - 2\Big] + \Big[1 - \frac{S_L \Delta t_c n q_L}{(1-n)\rho_S}\Big] = 0 \tag{7.36}$$

where the term P is expressed as

$$P = \frac{1}{\rho_S}\Big[\frac{K_S}{(1-n)} + \Big(-S_L + \frac{1}{n}\Big)K_L\Big] \tag{7.37}$$

If we solve Eq. 7.36 for Δt_c we obtain

$$\Delta t_c = \frac{\Big(-\frac{nS_L q_L}{(1-n)\rho_s} + \sqrt{\Big(\frac{nS_L q_L}{(1-n)\rho_s}\Big)^2 + 4P}\Big)}{P} \tag{7.38}$$

Arranged in a more general form, it is equivalent to Eq. 4.65, where

$$\omega_M = \sqrt{P} = \frac{1}{L_i}\sqrt{\frac{1}{\rho_S}\Big[\frac{E_c}{(1-n)} + \Big(-S_L + \frac{1}{n}\Big)\frac{S_L}{\Big(\frac{dS_L}{ds} + \frac{S_L}{K_w}\Big)}\Big]} \tag{7.39}$$

$$\xi_M = \frac{\Big(\frac{nS_L q_L}{(1-n)\rho_s}\Big)}{2\omega_M} = \frac{S_L^2 n^2 \mu_L}{2(1-n)\rho_s k_L \omega_M} \tag{7.40}$$

References

[1] P. Simonini, S. Cola, and S. Bersan, “Caratterizzazione geotecnica, meccanismi di collasso e monitoraggio degli argini fluviali - relazione generale,” 2014.

[2] Y. Deniaud, H. van Hemert, J. McVicker, A. Bernard, B. Beullac, R. Tourment, M. Igigabel, R. Pohl, M. Sharp, J. Simm *et al.*, “Functions, forms and failure of levees.” CIRIA, 2013.

[3] T. Dezert, Y. Fargier, S. Palma Lopes, and P. Côte, “Geophysical and geotechnical methods for fluvial levee investigation: A review,” *Engineering Geology*, vol. 260, p. 105206, 2019. [Online]. Available: https://www.sciencedirect.com/science/article/pii/S0013795218304903

[4] S. Bonelli and F. Nicot, *Erosion in Geomechanics Applied to Dams and Levees*. John Wiley Sons, Ltd, 2013.

[5] S. Cola, V. Girardi, S. Bersan, P. Simonini, L. Schenato, and F. De Polo, “An optical fiber-based monitoring system to study the seepage flow below the landside toe of a river levee,” *Journal of Civil and Structural Health Monitoring*, vol. 11, p. 691–705, 2021. [Online]. Available: https://doi.org/10.1007/s13349-021-00475-y

[6] B. Cosanti, N. Squeglia, and D. Lo Presti, “Analysis of existing levee systems: The Serchio river case,” *Rivista Italiana di Geotecnica*, vol. 48, pp. 49–67, 2014.

[7] A. Pozzato, A. Tarantino, and F. Polo, “Analysis of the effects of the partial saturation on the adige river embankment stability,” in *Unsaturated Soils: Research Applications*, 2014, pp. 1367–1372.

[8] G. Gottardi and C. Gragnano, “On the role of partially saturated soil strength in the stability analysis of a river embankment under steady-state

and transient seepage conditions," *E3S Web Conf.*, vol. 9, p. 19002, 2016. [Online]. Available: https://doi.org/10.1051/e3sconf/20160919002

[9] C. Zwanenburg, N. López-Acosta, R. Tourment, A. Tarantino, A. Pozzato, and A. Pinto, "Lessons learned from dike failures in recent decades," vol. 4, pp. 203–229, 2018.

[10] C. Zwanenburg, "Potential head response to river fluctuations," in *A feeling for soil and water. A tribute to Prof. Frans Barends*, M. Van, E. Den Haan, and J. Van Deen, Eds. Deltares Select Series, 2011, ch. 3, pp. 29–48.

[11] J. M. Duncan, "State of the art: Limit equilibrium and finite-element analysis of slopes," *Journal of Geotechnical Engineering*, vol. 122, no. 7, pp. 577–596, 1996.

[12] J. Krahn, "The 2001 R.M. Hardy Lecture: The limits of limit equilibrium analyses," *Canadian Geotechnical Journal*, vol. 40, pp. 643–660, 2003.

[13] D. V. Griffiths and P. A. Lane, "Slope stability analysis by finite elements," *Géotechnique*, vol. 49, no. 3, pp. 387–403, 1999. [Online]. Available: https://doi.org/10.1680/geot.1999.49.3.387

[14] M. Budhu and R. Gobin, "Slope instability from ground-water seepage," *Journal of Hydraulic Engineering*, vol. 122, 07 1996.

[15] H. Worsching, R. Becher, S. Schlaeger, A. Bieberstein, and P. Kudella, "Spatial-TDR moisture measurement in a large scale levee model made of loamy soil material," in *Proceedings TDR 2006, Purdue University, West Lafayette*, 2006.

[16] R. Orense, S. Shimoma, K. Maeda, and I. Towhata, "Instrumented model slope failure due to water seepage," *Journal of Natural Disaster Science*, vol. 26, pp. 15–26, 2004.

[17] A. Tohari, M. Nishigaki, and M. Komatsu, "Laboratory rainfall-induced slope failure with moisture content measurement," *Journal of Geotechnical and Geoenvironmental Engineering*, vol. 133, no. 5, pp. 575–587, 2007.

[18] H. Allersma and A. Rohe, "Centrifuge tests on the failure of dikes caused by uplift pressure," *International Journal of Physical Modelling in Geotechnics*, vol. 3, no. 1, pp. 45–53, 2003. [Online]. Available: https://doi.org/10.1680/ijpmg.2003.030104

[19] P. Hudacsek, M. F. Bransby, P. D. Hallett, and A. G. Bengough, "Centrifuge modelling of climatic effects on clay embankments," *Proceedings of the Institution of Civil Engineers - Engineering Sustainability*, vol. 162, no. 2, pp. 91–100, 2009. [Online]. Available: https://doi.org/10.1680/ensu.2009.162.2.91

[20] R. Saran and B. Viswanadham, "Centrifuge model tests on the use of geosynthetic layer as an internal drain in levees," *Geotextiles and Geomembranes*, vol. 46, no. 3, pp. 257–276, 2018. [Online]. Available: https://www.sciencedirect.com/science/article/pii/S0266114417301735

[21] G. Calabresi, F. Colleselli, D. Danese, G. Giani, C. Mancuso, L. Montrasio, A. Nocilla, L. Pagano, E. Reali, and A. Sciottia, "Research study of the hydraulic behaviour of the Po River embankments," *Canadian Geotechnical Journal*, 2013.

[22] G. Jia, T. L. Zhan, Y. Chen, and D. Fredlund, "Performance of a large-scale slope model subjected to rising and lowering water levels," *Engineering Geology*, vol. 106, no. 1, pp. 92–103, 2009. [Online]. Available: https://doi.org/10.1016/j.enggeo.2009.03.003

[23] G. J. C. M. Koelewijn, André R.and Hoffmans and M. A. Van, "Lessons learned from a full-scale dyke failure test," *International Conference on Case Histories in Geotechnical Engineering*, vol. 33, 2004. [Online]. Available: https://scholarsmine.mst.edu/icchge/5icchge/session02/33

[24] X. Rivera-Hernandez, G. Ellithy, and F. Vahedifard, "Integrating field monitoring and numerical modeling to evaluate performance of a levee under climatic and tidal variations," *Journal of Geotechnical and Geoenvironmental Engineering*, vol. 145, 10 2019.

[25] M. Rinaldi, N. Casagli, S. Dapporto, and A. Gargini, "Monitoring and modelling of pore water pressure changes and riverbank stability during

flow events," *Earth Surface Processes and Landforms*, vol. 29, no. 2, pp. 237–254, 2004. [Online]. Available: https://onlinelibrary.wiley.com/doi/abs/10.1002/esp.1042

[26] H. Su, H. Li, Y. Kang, and Z. Wen, "Experimental study on distributed optical fiber-based approach monitoring saturation line in levee engineering," *Optics Laser Technology*, vol. 99, pp. 19–29, 2018. [Online]. Available: https://www.sciencedirect.com/science/article/pii/S0030399217303778

[27] G. Tresoldi, D. Arosio, A. Hojat, L. Longoni, M. Papini, and L. Zanzi, "Long-term hydrogeophysical monitoring of the internal conditions of river levees," *Engineering Geology*, 05 2019. [Online]. Available: https://www.sciencedirect.com/science/article/pii/S0013795218313656

[28] N. Melnikova, D. Jordan, V. Krzhizhanovskaya, and P. Sloot, "Slope Instability of the Earthen Levee in Boston, UK: Numerical Simulation and Sensor Data Analysis," 01 2014.

[29] M. Martinelli, A. Rohe, and K. Soga, "Modeling dike failure using the material point method," *Procedia Engineering*, vol. 175, pp. 341–348, 2017, proceedings of the 1st International Conference on the Material Point Method (MPM 2017). [Online]. Available: https://www.sciencedirect.com/science/article/pii/S1877705817300425

[30] E. J. Fern, D. A. de Lange, C. Zwanenburg, J. A. M. Teunissen, A. Rohe, and K. Soga, "Experimental and numerical investigations of dyke failures involving soft materials," *Engineering Geology*, vol. 219, pp. 130–139, 2017. [Online]. Available: https://www.sciencedirect.com/science/article/pii/S0013795216302198

[31] R. Lanzafame and N. Sitar, "Reliability analysis of the influence of seepage on levee stability," *Environmental Geotechnics*, vol. 6, no. 5, pp. 284–293, 2019. [Online]. Available: https://doi.org/10.1680/jenge.18.00060

[32] M. Marchi, G. Gottardi, M. Ranalli, M. Tonni, C. Madiai, and G. Vanucchi, "Probabilità di collasso di un tratto di argine maestro del fiume Po," in *Incontro Annuale dei Ricercatori di Geotecnica 2021 – IARG2014 Chieti*, 2014.

[33] G. Gottardi, C. G. Gragnano, M. Ranalli, and L. Tonni, “Reliability analysis of riverbank stability accounting for the intrinsic variability of unsaturated soil parameters,” *Structural Safety*, vol. 86, p. 101973, 2020. [Online]. Available: https://www.sciencedirect.com/science/article/pii/S0167473020300527

[34] N. Rossi, M. Bačić, M. S. Kovačević, and L. Librić, “Development of fragility curves for piping and slope stability of river levees,” *Water*, vol. 13, no. 5, 2021. [Online]. Available: https://www.mdpi.com/2073-4441/13/5/738

[35] J. Nuttall, “Stochastic approach to slope stability analysis with in-situ data,” 2013, pp. 527–538.

[36] T. Xiao, D.-Q. Li, Z.-J. Cao, S.-K. Au, and K.-K. Phoon, “Three-dimensional slope reliability and risk assessment using auxiliary random finite element method,” *Computers and Geotechnics*, vol. 79, pp. 146–158, 2016. [Online]. Available: https://www.sciencedirect.com/science/article/pii/S0266352X16301240

[37] S. H. H. Z. e. a. Fu, Z., “Multiple failure modes-based practical calculation model on comprehensive risk for levee structure,” *Stoch Environ Res Risk Assess*, vol. 32, p. 1051–1064, 2018. [Online]. Available: https://doi.org/10.1007/s00477-017-1448-2

[38] M. A. Hicks and Y. Li, “Influence of length effect on embankment slope reliability in 3d,” *International Journal for Numerical and Analytical Methods in Geomechanics*, vol. 42, no. 7, pp. 891–915, 2018. [Online]. Available: https://onlinelibrary.wiley.com/doi/abs/10.1002/nag.2766

[39] A. Amabile, A. Pozzato, and A. Tarantino, “Instability of flood embankments due to pore-water pressure build-up at the toe: lesson learned from the Adige River case study,” *Canadian Geotechnical Journal*, vol. 57, no. 12, pp. 1844–1853, 2020.

[40] S. Van Baars, “The horizontal failure mechanism of the Wilnis peat dyke,” *Géotechnique*, vol. 55, no. 4, pp. 319–323, 2005. [Online]. Available: https://doi.org/10.1680/geot.2005.55.4.319

[41] J. Kool, W. Kanning, T. Heyer, C. Jommi, and S. N. Jonkman, “Forensic analysis of levee failures: The *B*reitenhagen case,” *International Journal of Geoengineering Case Histories*, vol. 5, no. 2, pp. 70–92, 2019.

[42] R. B. Seed, R. G. Bea, A. Athanasopoulos-Zekkos, G. P. Boutwell, J. D. Bray, C. Cheung, D. Cobos-Roa, J. Cohen-Waeber, B. D. Collins, L. F. Harder, R. E. Kayen, J. M. Pestana, M. Riemer, J. D. Rogers, R. Storesund, X. Vera-Grunauer, and J. Wartman, “New Orleans and Hurricane Katrina. IV: Orleans East Bank (Metro) Protected Basin,” *Journal of Geotechnical and Geoenvironmental Engineering*, vol. 134, pp. 762–779, 2008.

[43] I. E. Özer, M. van Damme, and S. N. Jonkman, “Towards an International Levee Performance Database (ILPD) and Its Use for Macro-Scale Analysis of Levee Breaches and Failures,” *Water*, vol. 12, no. 1, 2020. [Online]. Available: https://www.mdpi.com/2073-4441/12/1/119

[44] M. T. Perri, J. Boaga, S. Bersan, G. Cassiani, S. Cola, R. Deiana, P. Simonini, and S. Patti, “River embankment characterization: The joint use of geophysical and geotechnical techniques,” *Journal of Applied Geophysics*, vol. 110, pp. 5–22, 2014. [Online]. Available: https://doi.org/10.1016/j.jappgeo.2014.08.012

[45] *Norme Tecniche per le Costruzioni.* DEI, 2018.

[46] I. GEO-SLOPE, “Seepage Modeling with SEEP/W,” 2012. [Online]. Available: http://www.geo-slope.com

[47] M. Mbonimpa, A. M, B. Bussière, and R. Chapuis, “A model to predict the water retention curve from basic geotechnical properties,” *Canadian Geotechnical Journal*, vol. 40, pp. 1104–1122, 12 2003.

[48] A. Maqsoud, B. Bussière, A. Michel, and M. Mbonimpa, “Conversion of the Modified Kovács Model Parameters to the Brooks and Corey and van Genuchten Model Parameters for the Water Retention Curve of Sandy and Silty Soils,” *Journal of Irrigation and Drainage Engineering*, vol. 139, pp. 388–398, 2013.

[49] B. G. Galerkin, “Rods and plates: Series in some questions of elastic equilibrium of rods and plates,” *Springfield, Va: National Technical Information Service*, 1968.

[50] O. Zienkiewicz and I. Cheung, *The Finite Element Method in Engineering Science*, ser. McGraw-Hill European Publishing Programme. McGraw-Hill, 1971. [Online]. Available: https://books.google.it/books?id=_d1RAAAAMAAJ

[51] R. A. Gingold and J. J. Monaghan, “Smoothed particle hydrodynamics: theory and application to non-spherical stars,” *Monthly Notices of the Royal Astronomical Society*, vol. 181, no. 3, pp. 375–389, 1977. [Online]. Available: https://doi.org/10.1093/mnras/181.3.375

[52] H. H. Bui, R. Fukagawa, K. Sako, and S. Ohno, “Lagrangian meshfree particles method (SPH) for large deformation and failure flows of geomaterial using elastic–plastic soil constitutive model,” *International Journal for Numerical and Analytical Methods in Geomechanics*, vol. 32, no. 12, pp. 1537–1570, 2008. [Online]. Available: https://onlinelibrary.wiley.com/doi/abs/10.1002/nag.688

[53] M. Pastor, A. Yague, M. Stickle, D. Manzanal, and P. Mira, “A two-phase SPH model for debris flow propagation,” *International Journal for Numerical and Analytical Methods in Geomechanics*, vol. 42, no. 3, pp. 418–448, 2018. [Online]. Available: https://onlinelibrary.wiley.com/doi/abs/10.1002/nag.2748

[54] D. Sulsky, Z. Chen, and H. Schreyer, “A particle method for hystory-dependent materials,” *Computer Methods in Applied Mechanics and Engineering*, vol. 118, no. 1-2, pp. 179–196, 1994.

[55] E. Onate, S. R. Idelsohn, F. Del Pin, and R. Aubry, “The particle finite element method — an overview,” *International Journal of Computational Methods*, vol. 01, no. 02, pp. 267–307, 2004. [Online]. Available: https://doi.org/10.1142/S0219876204000204

[56] L. Monforte, J. Carbonell, M. Arroyo, and et al., “Performance of mixed formulations for the particle finite element method in soil mechanics

problems," *Comp. Part. Mech.*, vol. 04, p. 269–284, 2017. [Online]. Available: https://doi.org/10.1007/s40571-016-0145-0

[57] L. Moresi, F. Dufour, and H. Muhlhaus, "A lagrangian integration point finite element method for large deformation modeling of viscoelastic geomaterials," *Journal of Computational Physics*, vol. 184, 01 2003.

[58] X. Zhang, Z. Chen, and Y. Liu, "Chapter 1 - introduction," in *The Material Point Method*, X. Zhang, Z. Chen, and Y. Liu, Eds. Oxford: Academic Press, 2017, pp. 1–9. [Online]. Available: https://www.sciencedirect.com/science/article/pii/B9780124077164000016

[59] J. Donea, A. Huerta, J.-P. Ponthot, and A. Rodríguez-Ferran, "Arbitrary lagrangian–eulerian methods," in *Encyclopedia of Computational Mechanics*. American Cancer Society, 2004, ch. 14. [Online]. Available: https://onlinelibrary.wiley.com/doi/abs/10.1002/0470091355.ecm009

[60] A. Alsardi, J. Copana, and A. Yerro, "Modelling earthquake-triggered landslide runout with the material point method," *Proceedings of the Institution of Civil Engineers - Geotechnical Engineering*, vol. 174, no. 5, pp. 563–576, 2021. [Online]. Available: https://doi.org/10.1680/jgeen.20.00235

[61] F. Ceccato, L. Beuth, P. A. Vermeer, and P. Simonini, "Two-phase material point method applied to the study of cone penetration," *Computers and Geotechnics*, vol. 80, pp. 440–452., 2016.

[62] L. Zambrano-Cruzatty and A. Yerro, "Numerical simulation of a free fall penetrometer deployment using the material point method," *Soils and Foundations*, vol. 60, no. 3, pp. 668–682, 2020. [Online]. Available: https://www.sciencedirect.com/science/article/pii/S0038080620336179

[63] M. Martinelli and V. Galavi, "Investigation of the material point method in the simulation of cone penetration tests in dry sand," *Computers and Geotechnics*, vol. 130, p. 103923, 2021. [Online]. Available: https://www.sciencedirect.com/science/article/pii/S0266352X20304869

[64] A. Yerro, A. Rohe, and K. Soga, “Modelling internal erosion with the material point method,” in *1st International Conference on the Material Point Method, MPM 2017*, 2017, pp. 1–8.

[65] A. Yerro, K. Soga, and J. Bray, “Runout evaluation of Oso landslide with the material point method,” *Canadian Geotechnical Journal*, vol. 14, no. December, pp. 1–14, 2018.

[66] X. Lei, S. He, X. Chen, H. Wong, L. Wu, and E. Liu, “A generalized interpolation material point method for modelling coupled seepage-erosion-deformation process within unsaturated soils,” *Advances in Water Resources*, vol. 141, p. 103578, 2020.

[67] E. J. Fern, “Modelling tunnel-induced deformations with the material point method,” *Computers and Geotechnics*, vol. 111, no. January, pp. 202–208, 2019. [Online]. Available: https://doi.org/10.1016/j.compgeo.2019.03.017

[68] O. C. Zienkiewicz, a. H. C. Chan, M. Pastor, B. A. Schrefler, and T. Shiomi, *Computational Geomechanics*. New York: Wiley & Sons, 1999.

[69] C. Detournay and E. Dzik, “Nodal mixed discretization for tetrahedral elements,” in *4th international FLAC symposium, numerical modeling in geomechanics. Minnesota Itasca Consulting Group*, vol. Paper No. 07-02. R. Hart and P. Varona, Eds. Minneapolis, Minnesota: Itasca Consulting Group, Inc., 2006, 2006.

[70] F. Ceccato, G., J. Fern, M. Martinelli, A. Rohe, and A. Yerro, “MPM Research Community - Anura3D MPM Software - Scientific Manual,” 2019. [Online]. Available: https://github.com/Anura3D/Anura3D_OpenSource

[71] A. Yerro, “MPM modelling of landslides in brittle and unsaturated soils,” Ph.D. dissertation, Ph.D thesis, Univestitat Politecnica de Catalunya, Spain.

[72] S. G. Bardenhagen and E. M. Kober, “The generalized interpolation material point method,” *Computer Modeling in Engineering & Sciences*, vol. 5, no. 6, pp. 477–496, 2004. [Online]. Available: http://www.techscience.com/CMES/v5n6/33378

[73] A. Sadeghirad, R. M. Brannon, and J. Burghardt, “A convected particle domain interpolation technique to extend applicability of the material point method for problems involving massive deformations,” *International Journal for Numerical Methods in Engineering*, vol. 86, no. 12, pp. 1435–1456, 2011. [Online]. Available: https://onlinelibrary.wiley.com/doi/abs/10.1002/nme.3110

[74] M. Steffen, P. C. Wallstedt, J. E. Guilkey, R. M. Kirby, and M. Berzins, “Examination and analysis of implementation choices within the Material Point Method (MPM),” *CMES - Computer Modeling in Engineering and Sciences*, vol. 31, no. 2, pp. 107–127, 2008.

[75] D. Z. Zhang, X. Ma, and P. T. Giguere, “Material point method enhanced by modified gradient of shape function,” *J. Comput. Phys.*, vol. 230, no. 16, p. 6379–6398, Jul. 2011. [Online]. Available: https://doi.org/10.1016/j.jcp.2011.04.032

[76] J. González-Acosta, P. Vardon, G. Remmerswaal, and M. Hicks, “An investigation of stress inaccuracies and proposed solution in the material point method,” *Computational Mechanics*, vol. 65, 02 2020.

[77] Z. Wieckowski, “The material point method in large strain engineering problems,” *Computer Methods in Applied Mechanics and Engineering*, vol. 193, no. 39, pp. 4417–4438, 2004, the Arbitrary Lagrangian-Eulerian Formulation. [Online]. Available: https://www.sciencedirect.com/science/article/pii/S0045782504002282

[78] A. Stomakhin, C. Schroeder, L. Chai, J. Teran, and A. Selle, “A material point method for snow simulation,” *ACM Trans. Graph.*, vol. 32, no. 4, Jul. 2013. [Online]. Available: https://doi.org/10.1145/2461912.2461948

[79] S. Bandara and K. Soga, “Coupling of soil deformation and pore fluid flow using material point method,” *Computers and Geotechnics*, vol. 63, pp. 199–214, 2015. [Online]. Available: https://www.sciencedirect.com/science/article/pii/S0266352X14001839

[80] X. Zheng, F. Pisanò, P. J. Vardon, and M. A. Hicks, “An explicit stabilised material point method for coupled hydromechanical problems in

two-phase porous media," *Computers and Geotechnics*, vol. 135, p. 104112, 2021. [Online]. Available: https://www.sciencedirect.com/science/article/pii/S0266352X21001166

[81] J. E. Guilkey and J. A. Weiss, "Implicit time integration for the material point method: Quantitative and algorithmic comparisons with the finite element method," *International Journal for Numerical Methods in Engineering*, vol. 57, no. 9, pp. 1323–1338, 2003. [Online]. Available: https://onlinelibrary.wiley.com/doi/abs/10.1002/nme.729

[82] D. Sulsky and A. Kaul, "Implicit dynamics in the material-point method," *Computer Methods in Applied Mechanics and Engineering*, vol. 193, pp. 1137–1170, 03 2004.

[83] B. Wang, P. J. Vardon, M. A. Hicks, and Z. Chen, "Development of an implicit material point method for geotechnical applications," *Computers and Geotechnics*, vol. 71, pp. 159–167, 2016. [Online]. Available: https://www.sciencedirect.com/science/article/pii/S0266352X15001858

[84] I. Iaconeta, A. Larese, R. Rossi, and E. Oñate, "An implicit material point method applied to granular flows," *Procedia Engineering*, vol. 175, pp. 226–232, 2017, proceedings of the 1st International Conference on the Material Point Method (MPM 2017). [Online]. Available: https://www.sciencedirect.com/science/article/pii/S1877705817300176

[85] A. Larese, I. Iaconeta, B. Chandra, and V. Singer, "Implicit mpm and coupled mpm-fem in geomechanics," in *Point based numerical methods in geomechanics*. ALERT School In geomechanics, 2020, pp. 1534–188.

[86] S. Kularathna, W. Liang, T. Zhao, B. Chandra, J. Zhao, and K. Soga, "A semi-implicit material point method based on fractional-step method for saturated soil," *International Journal for Numerical and Analytical Methods in Geomechanics*, vol. 45, pp. 1405—-1436, 2021.

[87] D. Sulsky, S.-J. Zhou, and H. L. Schreyer, "Application of a particle-in-cell method to solid mechanics," *Computer Physics Communications*, vol. 87, no. 1-2, pp. 236–252, 1995. [Online]. Available: http://linkinghub.elsevier.com/retrieve/pii/0010465594001707

[88] A. Yerro and A. Rohe, "Fundamentals of the Material Point Method," in *The Material Point Method for Geotechnical Engineering*, J. Fern, A. Rohe, K. Soga, and E. Alonso, Eds. CRC Press, 2019, ch. 6, pp. 101–124.

[89] F. Zabala and E. Alonso, "Progressive failure of Aznalcóllar dam using the material point method," *Géotechnique*, vol. 61, no. 9, pp. 795–808, 2011.

[90] I. Kafaji, "Formulation of a Dynamic Material Point Method (MPM) for Geomechanical Problems," Ph.D. dissertation, Institut für Geotechnik der Universität Stuttgart, January 2013.

[91] Y. Zhao and J. Choo, "Stabilized material point methods for coupled large deformation and fluid flow in porous materials," *Computer Methods in Applied Mechanics and Engineering*, vol. 362, 2020. [Online]. Available: https://www.sciencedirect.com/science/article/pii/S0045782519306322

[92] S. S. Bandara, "Material Point Method to simulate Large Deformation Problems in Fluid-saturated Granular Medium," Ph.D. dissertation, Ph.D. thesis, Cambridge, UK, 2013.

[93] M. Martinelli, "Soil-water interaction with Material Point Method. Double-Point Formulation," Report on EU-FP7 research project MPM-Dredge PIAP-GA-2012-324522., Tech. Rep., 2016.

[94] Y. Yamaguchi, S. Takase, S. Moriguchi, and K. Terada, "Solid–liquid coupled material point method for simulation of ground collapse with fluidization," *Computational Particle Mechanics*, vol. 7, no. 2, pp. 209–223, Mar. 2020.

[95] K. Feng, D. Huang, and G. Wang, "Two-layer material point method for modeling soil–water interaction in unsaturated soils and rainfall-induced slope failure," *Acta Geotechnica*, vol. 16, pp. 2529–2551, Aug. 2021.

[96] F. Ceccato, A. Yerro, and M. Martinelli, "Modelling soil-water interaction with the material point method. evaluation of single-point and double-point formulations," 06 2018.

[97] I. Jassim, D. Stolle, and P. Vermeer, "Two-phase dynamic analysis by material point method," *International Journal for Numerical and Analytical*

Methods in Geomechanics, vol. 37, pp. 2502–2522, 2013. [Online]. Available: http://onlinelibrary.wiley.com/doi/10.1002/nag.2146/full

[98] H. Zhang, K. Wang, and Z. Chen, "Material point method for dynamic analysis of saturated porous media under external contact/impact of solid bodies," *Computer Methods in Applied Mechanics and Engineering*, vol. 198, no. 17, pp. 1456–1472, 2009. [Online]. Available: https://www.sciencedirect.com/science/article/pii/S0045782508004349

[99] Z. Hu, Y. Liu, H. Zhang, Y. Zheng, and H. Ye, "Implicit material point method with convected particle domain interpolation for consolidation and dynamic analysis of saturated porous media with massive deformation," *International Journal of Applied Mechanics*, vol. 13, no. 02, p. 2150023, 2021. [Online]. Available: https://doi.org/10.1142/S175882512150023X

[100] K. Abe, K. Soga, and S. Bandara, "Material Point Method for Coupled Hydromechanical Problems," *Journal of Geotechnical and Geoenvironmental Engineering*, vol. 140, pp. 1–16, 2013.

[101] M. Martinelli and A. Rohe, "Modelling fluidisation and sedimentation using material point method," in *Proc. 1st Pan-American Congress on Computational Mechanics (PANACM 2015), Buenos Aires, Argentinia*, S. Idelsohn, V. Sonzogni, A. Coutinho, M. Cruchaga, A. Lew, and M. Cerrolaza, Eds., 2015.

[102] I. Vardoulakis, "Fluidisation in artesian flow conditions: Hydromechanically stable granular media," *Géotechnique*, vol. 54, no. 2, pp. 117–130, 2004.

[103] P. Forchheimer, "Wasserbewegung durch Boden," *Zeitschrift des Vereins Deutscher Ingenieure*, 1901.

[104] D. Li, T. W. Engler *et al.*, "Literature review on correlations of the non-Darcy coefficient," in *SPE Permian Basin Oil and Gas Recovery Conference*. Society of Petroleum Engineers, 2001.

[105] O. D. Orodu, F. A. Makinde, and K. B. Orodu, "Experimental study of darcy and non-darcy flow in porous media," *International Journal of Engineering and Technology*, vol. 2, no. 12, pp. 1934–1943, 2012.

[106] S. Ergun, "Fluid flow through packed column," *Chemical Engineering Progress*, 1952.

[107] C. Beenakker, "The effective viscosity of a concentrated suspension of spheres (and its relation to diffusion)," *Physica A: Statistical Mechanics and its Applications*, vol. 128, no. 1-2, pp. 48–81, 1984.

[108] F. M. Hamad, "Formulation of a dynamic material point method and applications to soil–water–geotextile systems," Ph.D. dissertation, Ph.D thesis, University of Struttgart, Germay, 2014.

[109] X. Zhao, M. Bolognin, D. Liang, A. Rohe, and P. J. Vardon, "Development of in/outflow boundary conditions for mpm simulation of uniform and non-uniform open channel flows," *Computers Fluids*, vol. 179, pp. 27–33, 2019. [Online]. Available: https://www.sciencedirect.com/science/article/pii/S004579301830728X

[110] A. Yerro, E. E. Alonso, and N. M. Pinyol, "The material point method for unsaturated soils," *Geotechnique*, vol. 65, no. 3, pp. 201–217, 2015. [Online]. Available: http://www.icevirtuallibrary.com/doi/10.1680/geot.14.P.163

[111] S. Bandara, A. Ferrari, and L. Laloui, "Modelling landslides in unsaturated slopes subjected to rainfall infiltration using material point method," *International Journal for Numerical and Analytical Methods in Geomechanics*, vol. 40, no. 9, pp. 1358–1380, 2016.

[112] B. Wang, P. Vardon, and M. Hicks, "Investigation of retrogressive and progressive slope failure mechanisms using the material point method," *Computers and Geotechnics*, vol. 78, pp. 88–98, 2016. [Online]. Available: http://linkinghub.elsevier.com/retrieve/pii/S0266352X16300891

[113] B. Wang, P. J. Vardon, and M. A. Hicks, "Rainfall-induced slope collapse with coupled material point method," *Engineering Geology*, vol. 239, no. February, pp. 1–12, 2018. [Online]. Available: https://doi.org/10.1016/j.enggeo.2018.02.007

[114] X. Lei and W. Solowski, "Mpm simulation of fine particle migration process within unsaturated soils," in *Proceedings of the 2nd International Conference*

on the Material Point Method for Modelling Soil-Water-Structure Interaction (MPM 2019), 2019.

[115] F. Ceccato, V. Girardi, A. Yerro, and P. Simonini, "Evaluation of dynamic explicit MPM formulations for unsaturated soils," in *Particles 2019*, E. Oñate, M. Bischoff, D. Owen, P. Wriggers, and T. Zohdi, Eds., Barcellona, 2019.

[116] F. Ceccato, A. Yerro, V. Girardi, and P. Simonini, "Two-phase dynamic MPM formulation for unsaturated soil," *Computers and Geotechnics*, vol. 129, no. July 2020, p. 103876, 2021. [Online]. Available: https://doi.org/10.1016/j.compgeo.2020.103876

[117] M. Martinelli, W.-L. Lee, C.-L. Shieh, and S. Cuomo, "Rainfall Boundary Condition in a Multiphase Material Point Method," in *Fifth World Landslide Forum*, 2021, pp. 303–309.

[118] W. Lee, M. Martinelli, and C. L. Shieh, "Modelling rainfall-induced landslides with the material point method: the Fei Tsui Road case," in *Proceedings of the XVII ECSMGE-2019 Geotechnical Engineering foundation of the future ISBN 978-9935-9436-1-3*, no. Knii 1996, 2019.

[119] A. Yerro, A. Rohe, and K. Soga, "Modelling Internal Erosion with the Material Point Method," *Procedia Engineering*, vol. 175, pp. 365–372, 2017. [Online]. Available: http://dx.doi.org/10.1016/j.proeng.2017.01.048

[120] M. Nuth and L. Laloui, "Effective stress concept in unsaturated soils: Clarification and validation of a unified framework," *International journal for numerical and analytical methods in Geomechanics*, vol. 32, no. 7, pp. 771–801, 2008.

[121] A. W. Bishop, "The principle of effective stress," *Teknisk ukeblad*, vol. 39, pp. 859–863, 1959.

[122] E. E. Alonso, A. Gens, and A. Josa, "A constitutive model for partially saturated soils," *Géotechnique*, vol. 40, no. 3, pp. 405–430, 1990. [Online]. Available: https://doi.org/10.1680/geot.1990.40.3.405

[123] N. Phuong, A. van Tol, A. Elkadi, and A. Rohe, "Numerical investigation of pile installation effects in sand using material point method," *Computers and Geotechnics*, vol. 73, pp. 58–71, 2016. [Online]. Available: https://www.sciencedirect.com/science/article/pii/S0266352X15002426

[124] J. Fern, A. Rohe, K. Soga, and E. Alonso, *The Material Point Method for Geotechnical Engineering: A Practical Guide.* CRC Press, 2019.

[125] G. Di Carluccio, N. M. Pinyol, and E. Alonso, "Liquefaction-induced large displacements of caisson quay wall: Barcelona harbor, Spain," in *2nd International Conference on the Material Point Method for Modelling Soil-Water Structure Interaction - Cambridge.*

[126] M. Stapelfeldt, B. Bienen, and J. Grabe, "Insights into suction caisson installation utilising the material point method," in *16th International Conference of the International Association for Computer Methods and Advances in Geomechanics, IACMAG 2021*, 2021, vol. 125, pp. 802–809. [Online]. Available: http://hdl.handle.net/11420/10518

[127] D. Liang, X. Zhao, and K. Soga, "Simulation of overtopping and seepage induced dike failure using two-point mpm," *Soils and Foundations*, vol. 60, no. 4, pp. 978–988, 2020. [Online]. Available: https://www.sciencedirect.com/science/article/pii/S003808062033688X

[128] J. Murphy, A. Yerro, and K. Soga, "A new approach to simulate suffusion processes with mpm," in *Geo-Congress 2020*, pp. 482–490. [Online]. Available: https://ascelibrary.org/doi/abs/10.1061/9780784482803.052

[129] B. Zuada Coelho, A. Rohe, A. Aboufirass, J. Nuttall, and M. Bolognin, "Assessment of dike safety within the framework of large deformation analysis with the material point method," in *NUMGE2018*, 2018.

[130] G. Lube, H. E. Huppert, R. S. J. Sparks, and A. Freundt, "Collapses of two-dimensional granular columns," *Physical Review E - Statistical, Nonlinear, and Soft Matter Physics*, vol. 72, no. 4, pp. 1–10, 2005.

[131] E. Lajeunesse, L. Malverti, and F. Charru, “Bed load transport in turbulent flow at the grain scale: Experiments and modeling,” *Journal of Geophysical Research: Earth Surface*, vol. 115, no. 4, 2010.

[132] R. Artoni, A. C. Santomaso, F. Gabrieli, D. Tono, and S. Cola, “Collapse of quasi-two-dimensional wet granular columns,” *Physical Review E - Statistical, Nonlinear, and Soft Matter Physics*, vol. 87, no. 3, pp. 1–8, 2013.

[133] A. Bougouin and L. Lacaze, “Granular collapse in a fluid: Different flow regimes for an initially dense-packing,” *Physical review fluids*, vol. 064305, no. 3, pp. 1–23, 2018.

[134] A. C. Santomaso, S. Volpato, and F. Gabrieli, “Collapse and runout of granular columns in pendular state,” *Physics of Fluids*, vol. 30, no. 6, 2018.

[135] L. Jing, G. C. Yang, C. Y. Kwok, and Y. D. Sobral, “Dynamics and scaling laws of underwater granular collapse with varying aspect ratios,” *Physical Review E*, vol. 98, no. 4, pp. 1–15, 2018.

[136] F. Ceccato, A. Leonardi, V. Girardi, P. Simonini, and M. Pirulli, “Numerical and experimental investigation of saturated granular column collapse in air,” *Soils and Foundations*, no. xxxx, 2020. [Online]. Available: https://doi.org/10.1016/j.sandf.2020.04.004

[137] F. Ceccato, V. Girardi, and P. Simonini, “Developing and testing multiphase mpm approaches for the stability of dams and river embankments,” in *Conference of the Italian Association of Theoretical and Applied Mechanics*. Springer, 2019, pp. 2179–2195.

[138] L. Brezzi, “Collapse of granular – cohesive soil mixtures on a horizontal plane,” *Acta Geotechnica*, vol. 7, 2018.

[139] C. Meruane, A. Tamburrino, and O. Roche, “On the role of the ambient fluid on gravitational granular flow dynamics,” *Journal of Fluid Mechanics*, vol. 648, pp. 381–404, 2010.

[140] E. Lajeunesse, J. Monnier, and G. Homsy, “Granular slumping on a horizontal surface,” *Physics of fluids*, vol. 17, no. 10, p. 103302, 2005.

[141] P. Li, D. Wang, Y. Wu, and Z. Niu, “Experimental study on the collapse of wet granular column in the pendular state,” *Powder Technology*, vol. 393, pp. 357–367, 2021. [Online]. Available: https://www.sciencedirect.com/science/article/pii/S0032591021006781

[142] F. Ceccato and P. Simonini, “Numerical Features Used in Simulations,” in *The Material Point Method for Geotechnical Engineering*, J. Fern, A. Rohe, K. Soga, and E. Alonso, Eds. CRC Press, 2019, ch. 6, pp. 101–124.

[143] E. J. Fern and K. Soga, “The role of constitutive models in MPM simulations of granular column collapses,” *Acta Geotechnica*, vol. 11, no. 3, pp. 659–678, 2016.

[144] M. Steffen, R. Kirby, and M. Berzins, “Decoupling and balancing of space and time errors in the material point method (MPM),” *International journal for numerical methods in Engineering*, vol. 82, no. December 2009, pp. 1207–1243, 2010.

[145] C. Janßen and M. Krafczyk, “Free surface flow simulations on GPGPUs using the LBM,” *Computers and Mathematics with Applications*, vol. 61, no. 12, pp. 3549–3563, 2011.

[146] X. Zhao, D. Liang, and M. Martinelli, “Numerical simulations of dam-break floods with mpm,” *Procedia Engineering*, vol. 175, pp. 133–140, 2017.

[147] A. Leonardi, M. Cabrera, F. K. Wittel, R. Kaitna, M. Mendoza, W. Wu, and H. J. Herrmann, “Granular-front formation in free-surface flow of concentrated suspensions,” *Physical Review E - Statistical, Nonlinear, and Soft Matter Physics*, vol. 92, no. 5, p. 052204, 2015.

[148] I. Redaelli, F. Ceccato, C. Prisco, and P. Simonini, “MPM simulations of granular column collapse with a new constitutive model for the solid-fluid transition,” *5th International Conference on Particle-Based Methods - Fundamentals and Applications, PARTICLES 2017*, no. September, pp. 539–545, 2017.

[149] T. N. Delft University of Technology Plaxis BV, “Plaxis 2D 2018 manual,” 2018. [Online]. Available: https://www.bentley.com/en/products/product-line/geotechnical-engineering-software/plaxis-2d

[150] V. Girardi, A. Yerro, F. Ceccato, and P. Simonini, “Modelling deformations in water retention structures with unsaturated material point method,” *Proceedings of the ICE - Geotechnical Engineering*, vol. 174(5), 2021.

[151] A. Yerro, E. Alonso, and N. Pinyol, “Modelling large deformation problems in unsaturated soils,” in *E-UNSAT 2016*, vol. 9, no. 08019, 2016, pp. 1–6.

[152] E. E. Alonso and A. Lloret, “Evolution in time of the reliability of slopes in partially saturated soils,” in *Applications of Statistics and Probability in Soil and Structural Engineering*, Pitagora, Ed., Firenze, 1983, pp. 1363–1376.

[153] A. Gens, M. Sánchez, and D. Sheng, “On constitutive modelling of unsaturated soils,” *Acta Geotechnica*, vol. 1, no. 3, pp. 137–147, 2006.

[154] S. K. Vanapalli, D. G. Fredlund, D. E. Pufahl, and A. W. Clifton, “Model for the prediction of shear strength with respect to soil suction,” *Canadian Geotechnical Journal*, vol. 33, no. 3, pp. 379–392, 1996.

[155] B. Loret and N. Khalili, “A three-phase model for unsaturated soils,” *International Journal for Numerical and Analytical Methods in Geomechanics*, vol. 24, no. 11, pp. 893–927, 2000.

[156] D. Mašín and N. Khalili, “A hypoplastic model for mechanical response of unsaturated soils,” *International Journal for Numerical and Analytical Methods in Geomechanics*, vol. 32, no. 15, pp. 1903–1926, 2008.

[157] D. Sheng, S. W. Sloan, and A. Gens, “A constitutive model for unsaturated soils: thermomechanical and computational aspects,” *Computational Mechanics*, vol. 33, pp. 453–465, 2004.

[158] B. Francois and L. Laloui, “Acmeg-ts: A constitutive model for unsaturated soils under non-isothermal conditions,” *International Journal for Numerical and Analytical Methods in Geomechanics*, vol. 32, no. 16, pp. 1955–1988, 2008.

[159] A. Yerro, E. Alonso, and N. Pinyol, “The material point method for unsaturated soils,” *Géotechnique*, vol. 65, no. 3, pp. 201–217, 2015.

[160] M. Van Genuchten, “A closed-form equation for predicting the hydraulic conductivity of unsaturated soils,” *Soil science society of America journal*, vol. 44, no. 5, pp. 892–898, 1980.

[161] R. H. Brooks, *Hydraulic properties of porous media.* Colorado State University, 1965.

[162] D. Fredlund and A. Xing, “Equations for the soil-water characteristic curve,” *Canadian Geotechnical Journal*, vol. 31, no. 4, pp. 521–532, 1994. [Online]. Available: https://doi.org/10.1139/t94-061

[163] D. Hillel, *Soil and water – physical principles and processes.* London (UK): Academic press, 1971.

[164] Y. Mualem, “Hysteretical models for prediction of the hydraulic conductivity of unsaturated porous media,” *Water Resources Research*, vol. 12, no. 6, pp. 1248–1254, 1976. [Online]. Available: http://doi.wiley.com/10.1029/WR012i006p01248

[165] M. M. J. Mieremet, “Numerical stability for velocity-based 2-phase formulation for geotechnical dynamic analysis,” Reports of the Delft Institute of Applied Mathematics, Delft University of Technology, Delft, The Netherlands, Report 15-03, {ISSN} 1389-6520, 2015.

[166] C. Scudeler, C. Paniconi, D. Pasetto, and M. Putti, “Examination of the seepage face boundary condition in subsurface and coupled surface/subsurface hydrological models,” *Water Resources Research*, vol. 53, pp. 1799–1819, 2017.

[167] R. Hu, Y. Chen, C. Zhou, and H.-H. Liu, “A numerical formulation with unified unilateral boundary condition for unsaturated flow problems in porous media,” *Acta Geotechnica*, 2016.

[168] Y.-M. Hong and S. Wan, “Forecasting groundwater level fluctuations for rainfall-induced landslide,” *Natural Hazards*, vol. 57, no. 2, pp. 167–184, 2011.

[169] A. Hendron Jr and F. D. Patton, “The Vaiont slide. A geotechnical analysis based on new geologic observations of the failure surface. Volume 1. Main text,” Army Engineer Waterways Experiment Station Vicksburg MS Geotechnical Lab, Tech. Rep., 1985.

[170] N. Lu and W. Likos, *Unsaturated Soil Mechanics.* Wiley, 2004. [Online]. Available: https://books.google.com/books?id=Rv1RAAAAMAAJ

[171] D. V. Griffiths and N. Lu, “Unsaturated slope stability analysis with steady infiltration or evaporation using elasto-plastic finite elements,” *International Journal for Numerical and Analytical Methods in Geomechanics*, vol. 29, no. 3, pp. 249–267, 2005.

[172] H. Rahardjo, A. Satyanaga, and E. C. Leong, “Effects of flux boundary conditions on pore-water pressure distribution in slope,” *Engineering Geology*, vol. 165, pp. 133–142, 2013. [Online]. Available: http://dx.doi.org/10.1016/j.enggeo.2012.03.017

[173] C. Callari and A. D. Abati, “Finite element methods for unsaturated porous solids and their application to dam engineering problems,” 2009.

[174] C. Hirsch, *Numerical Computation of Internal and External Flows: The Fundamentals of Computational Fluid Dynamics.* Elsevier Science, 2007.

[175] M. M. J. Mieremet, D. F. Stolle, F. Ceccato, and C. Vuik, “Numerical stability for modelling of dynamic two-phase interaction,” *International Journal for Numerical and Analytical Methods in Geomechanics*, vol. 40, no. 9, 2015.

[176] A. Yerro, E. E. Alonso, and N. M. Pinyol, “Modelling progressive failure with MPM,” in *Proc. 8th European Conference on Numerical Methods in Geotechnical Engineering (NUMGE 2014), Delft, The Netherlands*, M. A. Hicks, R. B. J. Brinkgreve, and A. Rohe, Eds., 2014, pp. 319–323.

[177] R. Ni and X. Zhang, “A precise critical time step formula for the explicit material point method,” *International Journal for Numerical and Analytical Methods in Geomechanics*, vol. 121, pp. 4989—-5016, 2020.

[178] P. Peter, Ed., *Canal and River Levees*, ser. Developments in Geotechnical Engineering. Elsevier, 1982, vol. 29. [Online]. Available: https://www.sciencedirect.com/science/article/pii/B9780444997265500078

[179] N. Puigmartí, E. Alonso, and S. Olivella, "Rapid drawdown in slopes and embankments," *Water Resources Research*, vol. 44, 05 2008.

[180] P. de Koster, R. Tielen, E. Wobbes, and M. Möller, "Extension of B-spline Material Point Method for unstructured triangular grids using Powell–Sabin splines," *Computational Particle Mechanics*, 2020. [Online]. Available: https://doi.org/10.1007/s40571-020-00328-3

[181] K. Soga, E. Alonso, A. Yerro, K. Kumar, and S. Bandara, "Trends in large-deformation analysis of landslide mass movements with particular emphasis on the material point method," *Géotechnique*, vol. 66, no. 3, pp. 248–273, 2016. [Online]. Available: https://doi.org/10.1680/jgeot.15.lm.005

[182] D. Fredlund, N. R. Morgenstern, and R. Widger, "The shear strength of unsaturated soils," *Canadian geotechnical journal*, vol. 15, no. 3, pp. 313–321, 1978.

[183] A. Bezuijen, G. Kruse, and M. Van, "Failure of peat dikes in The Netherlands," in *Proceedings of the 16th International Conference on Soil Mechanics and Geotechnical Engineering*, 2005.

[184] F. B. J. Barends, "Uplift of the hinterland at high water levels," GeoDelft, Delft, The Netherlands, Report No. CO-290831/2, 1988.

[185] M. A. Van, A. R. Koelewijn, and F. B. Barends, "Uplift phenomenon: Model, validation, and design," *International Journal of Geomechanics*, vol. 5, no. 2, pp. 98–106, 2005.

[186] C. C. Hird, A. Marsland, and A. N. Schofield, "The development of centrifugal models to study the influence of uplift pressures on the stability of a flood bank," *Géotechnique*, vol. 28, no. 1, pp. 85–106, 1978. [Online]. Available: https://doi.org/10.1680/geot.1978.28.1.85

[187] C. J. Padfield and A. N. Schofield, “The development of centrifugal models to study the influence of uplift pressures on the stability of a flood bank,” *Géotechnique*, vol. 33, no. 1, pp. 57–66, 1983. [Online]. Available: https://doi.org/10.1680/geot.1983.33.1.57

[188] M. Redaelli, A. Cividini, and G. Gioda, “Influence of boundary conditions in a finite-element analysis of river levees,” *International Journal of Geomechanics*, vol. 11, no. 5, pp. 399–405, 2011.

[189] A. Rohe and H. Allersma, “Modelonderzoek naar het optreden van oprdijf-condities achter dijken,” Faculteit Civiele Techniek en Geowetenschappen, Delft Technische Universiteit Delft, Report nr Geo, 490 a, 2000.

[190] R. V. D. Meij, “Slope Stability Software for Soft Soil Engineering - D-Stability,” 2021. [Online]. Available: https://www.deltares.nl/en/software/d-stability/

Acknowledgments

I'd like to express my acknowledgments to many significant people who have contributed to the succeeding completion of this PhD thesis.

First I want to thank my supervisor Professor Paolo Simonini. I have firstly met professor Simonini in 2015 during my bachelor degree, attending his class of Geotechnical Engineering. He was capable of stimulating interest in the subject, which appeared to me as fascinating, challenging and with a variety of applications of current relevance. Since then, Professor Simonini has become the most relevant figure in my education: he has been my supervisor since my bachelor thesis, he has pushed me to carry out a double degree with the University of Grenoble, attending the master course in Geomechanics, Civil Engineering and Risk. This experience had strongly changed my perspective concerning research, and posed the bases for my prosecution of studies with the PhD. I am grateful Professor Simonini has been giving value to international experiences like this one. Along the years I have developed increasing trust in him: he has repeatedly confirmed his professional expertise in several occasions, he is a reference for many people around him in the academic environment and outside it; I am grateful I had the chance to work as closely with him. Moreover, Professor Simonini has always believed in me, even more than what I do, even in times when the research work was hard to carry on, while I was facing the loss of my dad. All his dedication to my education and my personal growth is sincerely appreciated.

I wish to acknowledge my co-supervisors Dr Francesca Ceccato and Dr Alba Yerro. Dr Ceccato has been the person most directly involved in my work and in every technical aspect of it. I have learned a lot from her in terms of being a real researcher, like having discipline, perseverance, optimizing time and prioritization.

Dr Yerro has been supporting me since my second year of PhD, when I spent a period at Virginia Tech working under her supervision. I have been feeling extremely motivated by Dr Yerro. She is a proficient researcher, teacher and a successful supervisor for all her students. I feel a sense of admiration for her work and her efforts.

Thanks to two of the closest friends I met in the academic environment, Antonio and Abdel. Antonio is one of the most brilliant researchers and engineers I have ever met, and a person of strong integrity, and maturity. Abdel is a young researcher at Virginia Tech, with a huge potential and a promising future in front of him. He has been a big a reference during my research period in the US, I keep finding strong inspirations during our work talks.

Thanks to Giulia, Liliana and Michele, friends and PhD students sharing this experience in the last 4 years.

Thanks to all my colleagues from the Geotechnical group in Padova.

Thanks to my closest friends Claudio and Francesca. Despite the distance which separated us during these years, the friendship with each of them has not weakened at all. Long video calls and recorded messages has been saving us on a regular basis, and the few occasions we could spend time together during the year were always the best time for me.

Thanks to my friends Michela, Piervittorio, Filippo and Mario, among many others.

Thanks to my flatmates and friends Francesco, Bruno, Anna Pa, Anna Po, Giulia and Irene. I had a unique life experience with them for the last two years of my PhD. We have been supporting each other, sharing movie nights, working out, playing games, laughing, crying, partying and enjoying long (sometimes all night long) talks.

Last but not least, I wish to express my biggest thanks to my family and to my boyfriend Chris. This research work wouldn't have been possible without them. My family has been close to me and constantly supporting during my studies. I will never be able to thank them enough.

I wish to specially thank Chris for loving me, encouraging me, giving me motivation, revising my English papers and this thesis, understanding me and learning how to deal with me when this work was absorbing all my energy, for bragging about me becoming a doctor one day, for facing with me the difficulties of the long distance and for being the best partner during this journey.

List of publications

At indexed journal

- **Numerical and experimental investigation of saturated granular column collapse in air**
  F. Ceccato, A. Leonardi, V. Girardi, P. Simonini, M. Pirulli
  (2020) Soils and Foundations 60 (3), 683-696

- **Two-phase dynamic MPM formulation for unsaturated soil**
  F. Ceccato, A. Yerro, V. Girardi, P. Simonini
  (2021) Computers and Geotechnics 129, 103876

- **Modelling deformations in water retention structures with unsaturated material point method**
  V. Girardi, A. Yerro, F. Ceccato, P. Simonini
  (2021) Proceedings of the Institution of Civil Engineers–Geotechnical Engineering 174 (5), 577-592

- **An optical fiber-based monitoring system to study the seepage flow below the landside toe of a river levee**
  S. Cola, V. Girardi, S. Bersan, P. Simonini, L. Schenato, F. De Polo
  (2021) Journal of Civil Structural Health Monitoring 11 (3), 691-705

At conference

- **MPM Simulations of the Impact of Fast Landslides on Retaining Dams**
  F. Ceccato, P. Simonini, V. Girardi
  (2019) Proceedings of China-Europe Conference on Geotechnical Engineering, 296-299

- **Evaluation of dynamic explicit MPM formulations for unsaturated soils**
  F. Ceccato, V. Girardi, A. Yerro, P. Simonini
  (2019) Proc. Particles 2019, E. Onate,M. Bischoff, D. Owen, P. Wriggers, and T. Zohdi, Eds., Barcellona.

- **Developing and Testing Multiphase MPM Approaches for the Stability of Dams and River Embankments**
  F. Ceccato, V. Girardi, P. Simonini
  (2019) Proc. XXIV Conference of the Italian Association of Theoretical and Applied Mechanics (AIMETA)

- **Effect of artificial snowing system on the stability of a ski slope in the Dolomites**
  F. Ceccato, S. Cola, V. Girardi, P. Simonini
  (2020) SCG-XIII International Symposium on Landslides. Cartagena, Colombia.

- **Modellazione del collasso di un rilevato arginale con il metodo dei punti materiali per terreni parzialmente saturi.**
  V. Girardi, F. Ceccato
  (2021) IAGIG, Pisa https://doi.org/10.13131/unipi/iagig.x.2021/1.13

- **Valutazione degli effetti di uno svaso rapido sulla stabilità del petto arginale con il metodo dei punti materiali.**
  V. Girardi, F. Ceccato
  (2021) IAGIG, Pisa https://doi.org/10.13131/unipi/iagig.x.2021/3.3

- **Large strain analysis of unsaturated heterogeneous slopes with MPM**
  V. Girardi, F. Ceccato, A. Yerro, P. Simonini, F. Gabrieli
  (2022) Proc. 16th International Conference of the International Association for Computer Methods and Advances in Geomechanics (IACMAG)

Under review at indexed journals

- **Modelling unsaturated soils with the Material Point Method. A discussion of the state-of-the-art**
  A. Yerro, V. Girardi, F. Ceccato, M. Martinelli
  (2022) Geomechanics for Energy and Environment (accepted)

- **Failure of levees induced by toe uplift: investigation of post-failure behavior with the Material Point Method**
  V. Girardi, F. Ceccato, A. Rohe, P. Simonini, F. Gabrieli
  (2022) Journal of Rock Mechanics and Geotechnical Engineering